UNIVERSITAT DE BARCELONA

Antenna Design and Characterization for Biomedical Applications

Aleix Garcia Miquel

UNIVERSITAT DE BARCELONA

Doctoral thesis

ANTENNA DESIGN AND CHARACTERIZATION FOR BIOMEDICAL APPLICATIONS

Aleix Garcia Miquel

UNIVERSITAT DE BARCELONA

ANTENNA DESIGN AND CHARACTERIZATION FOR BIOMEDICAL APPLICATIONS

Aleix Garcia Miquel

Supervised by

Dra. Neus Vidal Martínez

Thesis submitted to the Doctoral Program in Biomedicine from the University of Barcelona

Department of Electronics and Biomedical Engineering

Barcelona, 2018

"Quan pensàvem que teníem totes les respostes,

de sobte, van canviar totes les preguntes"

– Mario Benedetti

Acknowledgments

En primer lloc, i com a figura indispensable i destacada d'aquesta tesi, vull donar les gràcies a la Dra. Neus Vidal. Amb ella vam començar un camí que ha durat gairebé cinc anys. Un camí ple d'obstacles i moments difícils, però sobretot ple d'èxits i d'experiències inoblidables. Ella m'ha donat l'oportunitat, l'empenta i la constància necessàries per realitzar aquesta tesi doctoral, i és gràcies a ella que aquesta tesi ha esdevingut finalment una realitat i una etapa de la meva vida que mai oblidaré. Enrere queda una directora de tesi excepcional; a davant, una amiga per sempre.

Vull fer extensiu aquest agraïment a tot el grup de Radiofreqüència de la Universitat de Barcelona, el GRAF. Gràcies al Dr. Josep Maria López-Villegas per la seva infinita saviesa, al Dr. Javier Sieiro pels seus consells i la seva paciència, a tots els companys de laboratori, començant pel Pau i el Saiyd, i acabant pel més jove, l'Arnau, amb qui hem compartit grans moments durant aquests últims mesos de tesi.

També vull mencionar especialment a altres amistats del departament que estic segur que em quedaran per tota la vida. Laura, gràcies per tot, per acollir-me com un més del vostre grup, per estar sempre allà i sobretot per les teves "laurades". Luís, qué decir de ti... Como echo de menos esas charlas sinceras acompañadas de unes birras mano a mano. Xavi, Jordi, Dani, Romen i Sergio, gràcies per tants bons moments.

Agrair també de tot cor l'ajuda i l'amistat de la Bea, per ensenyar-me el procés de fabricació de les antenes a FAE i per la seva paciència i dedicació. Gràcies també al Dr. Francisco Ramos, i en general a tots els companys de FAE, per donar-me l'oportunitat de conèixer la fabricació de prototips des de dins.

Al Jordi Domingo, per compartir els seus coneixements sobre el disseny de plaques i sobre les mesures amb fibra òptica. A la Bruna, per la seva inspiració en el projecte de RFID. A la Roser, pels seus valuosos consells en el món de la recerca i del "running". Als ex-companys de despatx i als companys del dia a dia, com la Cristina, el Nil, l'Àlex o el Manel. Als companys del Teeti, i en general, a tots els companys i professors del departament. Un agraïment especial als professors amb els que he compartit classes, com el Jaime, el Lorenzo, el Jordi, el Mauri i l'Òscar, entre d'altres.

De la mateixa manera, també vull agrair als estudiants de grau i màster que he dirigit, Nunzio, Noemí, Albert, Meritxell, Marc, Roger, David i finalment Jordi, per encomanar-me la seva motivació en els respectius projectes. Als companys que he anat coneixent al llarg del doctorat, ja sigui assistint a congressos com organitzant-los; un sincer agraïment als amics de les JIPI i del BiomedPhDay per haver

compartit la gran experiència que és organitzar un congrés i haver-ho fet de la millor manera possible.

Gràcies al Dr. Albert Cornet, director del Departament d'Enginyeria Electrònica i Biomèdica, i al Dr. Albert Tauler, coordinador del Programa de Doctorat de Biomedicina, pel seu suport i afecte durant tot el doctorat.

To all the people I met during my stay at Kansas State University, thanks for your hospitality and for the amazing beach volleyball games. Special thanks to Dr. Punit Prakash for being an excellent mentor and person, and one of the brightest minds I have had the pleasure of meeting.

Una mención especial a mi hermano mayor en Kansas, el Dr. Sergio Curto. Gracias infinitas por acogerme en *The little apple* y por toda tu ayuda, especialmente durante los primeros días de adaptación y, en general, por todo lo que he aprendido a tu lado.

Thanks to the colleagues I made from around the world during the Modeling course in Charleston. We had a really good time there. I also would like to thank all the teachers of the course, especially Dr. Dieter Haemmerich, for their inspiring talks.

Un agraïment sincer als companys del curs de Compact Antennas a Barcelona i als seus excepcionals professors, el Dr. Lluís Jofre o el Dr. Jordi Romeu, entre d'altres.

Special thanks to Dr. Anja Skrivervik, for her valuable knowledge in the design of implantable antennas and her motivating explanations. I would also like to thank Dr. Assimina Kiourti, Dr. Stavros Koulouridis and Dr. Marta Cabedo for their suggestions and advice on the subject.

Dar las gracias también al Dr. Juan Córcoles del grupo de Radiofrecuencia de la Universitat Autónoma de Madrid por su implicación y su experiencia en el desarrollo de algoritmos de optimización para el dispositivo de hipertermia.

També volia mostrar el meu agraïment més sincer a tota la gent que ha estat donant-me suport durant aquests quasi cinc anys, com a la Mireia, amb qui portem compartint camí i amistat des de la carrera. Gràcies per tants somriures.

Als amics de la pinya, Saul, Adri, Wark, Tutu i Sobri, pel seu suport incondicional i tots els bons moments que hem compartit.

A la família de telecos i de la Telecogresca, per posar una dosi important d'èpica a la meva vida.

Als del màster, especialment al Xavi i la Núria, per transmetre'm el seu afecte i alegria durant aquests últims anys.

Als erasmus que encara es deixen veure de tant en tant, com l'Augusto i l'Aina. Una cassalla a la vostra salut.

Als companys de viatge i germans de batalles del dia a dia, els cassolencs: David, Albert, Xals, Neus, Blanca, Carla, Mar, Eli, Gerard, Esther, Guillem, Loreidy, Jessica, Jordi, Navas, Nuria, Pau, Pol, Paula, Marc i Uris. Gràcies per ser-hi sempre.

Als vanguards, Ana, Arnim, Gael, Helenas, Isa, Sasha, Marcos, Maria, Marien, Marta, Pau, Sara, Vero i Christian, pel seu amor en tot allò que fan.

Als veïns de l'Esquirol, on tantes pàgines de la tesi he pogut escriure.

Als altres amics i amigues, com l'Àlex, que han anat omplint de moments brillants les diferents etapes de la meva vida.

I sobretot gràcies a la meva família, pel seu afecte, tendresa i comprensió. A la meva mare, per ser un referent i el meu far des del dia que vaig néixer, per aconseguir educar-me i fer de mi la persona que sóc. Al Joan, la inspiració eterna. Allà on siguis, estigues orgullós. Al meu pare, pel seu afecte i per la seva tranquil·litat. A la meva germana, per tot el seu suport i estima constant, l'altre far de la meva vida. Al meu germà, el germà retrobat, per la seva tendresa i sinceritat. A la meva àvia i al meu tiet, pel seu somriure malgrat les adversitats. Als cosins, tiets i a tota la família que m'ha vist créixer i m'ha ajudat a arribar fins aquí.

I finalment, gràcies a la meva companya de vida, la Marina, per la teva màgia en tot allò que fas, perquè amb tu tot és especial, per convertir les coses petites del dia a dia en aventures, pel teu amor i alegria per la vida, pel teu suport constant i per fer de mi una millor persona. Fer la tesi al teu costat ha estat el millor regal d'aquests cinc anys.

ABSTRACT

The use of radiofrequency in biomedical devices is taking on increasing significance due to its contributions to the prevention, diagnosis and treatment of diseases, either for minimally invasive remote monitoring of physiological data or for other applications such as medical imaging and thermal treatments. The advantages provided by radiofrequency fit perfectly inside the new paradigm of predictive, preventive, personalized and participatory medicine (P4 medicine) in which the individual patient is the central focus of the healthcare system.

Although the development of biomedical devices with radiofrequency has been studied in depth in recent years, several challenges still remain. In this context, this thesis deals with one of the most important issues: the design and characterization of antennas in the presence of the human body. The main goal of this thesis is to develop new antenna designs that overcome some of the current limitations, such as miniaturization, efficiency, frequency detuning and integration. This thesis also aims to provide tools and new insights for the development of antenna designs in the presence of the human body by analyzing the interaction between the antennas and the surrounding biological medium.

The research carried out has two main focuses: the wireless transmission of physiological data (biotelemetry) and microwave hyperthermia for cancer treatments. For the first, the study presents a theoretical framework review of in-body antennas followed by an exhaustive study of their miniaturization process, the manufacturing and the experimental characterization, as well as the phantom influence. Based on these studies, a novel multilayered broadband antenna and a miniaturized RFID tag are presented. And with regard to thermal treatment of breast cancer, an on-body, compact and configurable applicator with a phased antenna array has been developed.

In conclusion, the outcomes of this thesis make contributions in two main areas: (1) the antenna design and characterization for use in the presence of human body and (2) the research of new solutions for in-body biomedical devices with biotelemetry and for the treatment of breast cancer through microwave hyperthermia.

Keywords: biotelemetry, antennas in lossy matter, implantable antennas, miniaturized antennas, electrically small antennas, in-body communications, Low-Temperature Co-fired Ceramic (LTCC), Medical Device Radiocommunications Service (MedRadio), broadband antennas, Radio Frequency Identification (RFID), phased antenna array, microwave hyperthermia, breast cancer treatment.

RESUMEN

El uso de la radiofrecuencia en dispositivos biomédicos es cada vez más extendido debido a su contribución a la prevención, diagnóstico y tratamiento de enfermedades, ya sea para el control remoto de datos fisiológicos con mínima invasividad o para otras aplicaciones, como la imagen médica o los tratamientos térmicos. Las ventajas que ofrece la radiofrecuencia a estos dispositivos se adaptan totalmente dentro del nuevo paradigma de medicina basado en la predicción, prevención, personalización y participación, y donde el paciente se sitúa en el eje central del sistema sanitario.

A pesar de que el desarrollo de dispositivos biomédicos con radiofrecuencia ha sido ampliamente estudiado durante los últimos años, aún quedan muchos retos por alcanzar. En este contexto, esta tesis trata de abordar uno de los puntos más relevantes: el diseño y la caracterización de antenas en presencia del cuerpo humano. El objetivo principal de la tesis es el desarrollo de nuevos diseños de antenas que superen algunas de las limitaciones o prestaciones actuales, como la miniaturización, la eficiencia, la desintonización frecuencial o la integración con el dispositivo, entre otros. Esta tesis también pretende proporcionar herramientas y nuevos conocimientos para el desarrollo de diseños de antenas en presencia del cuerpo humano mediante el análisis de la interacción entre las propias antenas y el medio biológico que las rodea.

La investigación llevada a cabo se centra en dos enfoques distintos: la transmisión inalámbrica de datos fisiológicos (biotelemetría) y la hipertermia de microondas para tratamientos de cáncer. Para el primero, el trabajo presentado consta de una revisión del marco teórico actual de las antenas implantables seguido de un estudio exhaustivo de su proceso de miniaturización, fabricación y caracterización experimental, así como también de la influencia del uso de diferentes *phantoms*. En base a estos estudios, se presentan una antena de banda ancha multicapa y una etiqueta RFID miniaturizada basadas en la tecnología LTCC. Por otra parte, se presenta un aplicador de microondas formado por una matriz de antenas configurables para ser utilizado en el tratamiento térmico del cáncer de mama.

En conclusión, los resultados de esta tesis contribuyen principalmente a: (1) el diseño y caracterización de antenas en presencia del cuerpo humano y (2) la búsqueda de nuevas soluciones para dispositivos biomédicos con biotelemetría y para el tratamiento del cáncer de mama mediante la hipertermia de microondas.

Palabras clave: biotelemetría, antenas implantables, antenas miniaturizadas, cerámica tratada a baja temperatura (LTCC), identificación por radiofrecuencia (RFID), matriz de antenas configurables, hipertermia de microondas, tratamiento de cáncer de mama.

RESUM

L'ús de la radiofreqüència en dispositius biomèdics és cada vegada més extens degut a la seva contribució a la prevenció, diagnòstic i tractament de malalties, ja sigui pel control remot de dades fisiològiques amb mínima invasivitat o per altres aplicacions, com la imatge mèdica o els tractaments tèrmics. Els avantatges que ofereix la radiofreqüència a aquests dispositius s'adapten de ple dins el nou paradigma de medicina basat en la predicció, prevenció, personalització i participació, i on el pacient es situa en el focus central del sistema sanitari.

Tot i que el desenvolupament de dispositius biomèdics amb radiofreqüència ha estat àmpliament estudiat durant els últims anys, encara queden molts reptes per assolir. En aquest context, aquesta tesi tracta d'abordar un dels punts més rellevants: el disseny i la caracterització d'antenes en presència del cos humà. L'objectiu principal de la tesi és el desenvolupament de nous dissenys d'antenes que superin algunes de les limitacions o prestacions actuals, com ara la miniaturització, l'eficiència, la desintonització freqüencial o la integració amb el dispositiu, entre d'altres. Aquesta tesi també pretén proporcionar eines i nous coneixements pel desenvolupament de dissenys d'antenes en presència del cos humà mitjançant l'anàlisi de la interacció entre les pròpies antenes i el medi biològic que les envolta.

La investigació duta a terme es centra en dos enfocaments diferents: la transmissió sense fils de dades fisiològiques (biotelemetria) i la hipertèrmia de microones per a tractaments de càncer. Ambdues àrees comparteixen diversos aspectes destacables relacionats amb el disseny d'antenes. Per això, el treball presentat comença amb una recapitulació teòrica dels aspectes més destacables en el disseny d'antenes en presència del cos humà. Pel que fa a la biotelemetria sense fils, es realitza una revisió del marc teòric actual, amb especial èmfasi a les antenes implantables, per tal d'identificar els reptes més significatius en el seu desenvolupament i la manera d'abordar-los. D'aquesta manera, durant la primera part de la tesi, es proposen una sèrie d'estudis, ordenats per capítols, on es tracten diversos punts rellevants en el desenvolupament d'antenes implantables.

En primer lloc, es presenta un estudi sobre la miniaturització d'antenes implantables de tipus PIFA, ja que aquesta tipologia permet el desenvolupament de dissenys amb volums reduïts sense degradar en excés les prestacions de les antenes. A partir d'aquí, es comparen diferents mètodes de miniaturització per als radiadors, (fractals, meandres o espirals) i s'explora la miniaturització 3D mitjançant el disseny multicapa. Els resultats mostren que les antenes implantables amb estructura d'espiral quadrada tenen la millor relació entre el

volum i l'eficiència, especialment en el disseny 3D multicapa i amb el radiador en direcció al pla de massa.

A continuació es presenta un anàlisi de la influència de l'ús de *phantoms* en la caracterització d'antenes implantables de tipus PIFA amb estructura d'espiral quadrada. Es quantifiquen les variacions de l'eficiència de les antenes en funció de certs paràmetres, com la freqüència, la forma i les dimensions dels *phantoms,* o la profunditat de l'implant. En base als resultats obtinguts, es proposa un protocol de caracterització d'antenes implantables amb l'objectiu d'estandarditzar l'ús de *phantoms* en funció de la freqüència i així poder facilitar la comparativa entre diferents antenes.

Un altre aspecte rellevant en el disseny d'antenes implantables és la fabricació dels prototips. En aquesta tesi es detalla el procés de fabricació de les antenes presentades mitjançant la tecnologia LTCC. Aquesta tecnologia, basada en la ceràmica tractada a baixa temperatura, presenta nombroses propietats adequades per a les antenes implantables (estructures multicapa monolítiques, inclusió de vies i cavitats internes, integració amb altres components electrònics, substrats biocompatibles i de baixes pèrdues, etc). Es realitzen una sèrie de proves de sensibilitat per tal de determinar la desintonització freqüencial deguda al procés de fabricació. També es detalla el procés de caracterització experimental dels prototips i es proposen noves tècniques per tal d'eliminar els efectes del cable coaxial en les mesures, com són l'ús d'un *splitter* o d'un enllaç de fibra òptica.

Tot seguit es presenten tres demostradors o dissenys d'antenes orientats a tres aplicacions. En primer lloc, es presenta una antena implantable de banda ampla multicapa per a la biotelemetria sense fils. Els seus punts forts consisteixen en una mida reduïda, un ample de banda capaç de compensar la desintonització freqüencial ocasionada pels teixits biològics adjacents i una estructura que permet la integració d'altres components electrònics. L'antena és fabricada en tecnologia LTCC i els resultats concorden satisfactòriament amb les simulacions.

El segon demostrador consisteix en el disseny d'una etiqueta implantable RFID per a la monitorització sense fils de pacients. En aquest cas, el disseny també es realitza tenint en compte la miniaturització i la integració amb el xip RFID, així com un ample de banda suficientment gran. Les simulacions i la realització experimental mostren resultats similars.

Finalment, es presenta un aplicador de microones compacte format per una matriu d'antenes configurables en fase per ser utilitzat en el tractament tèrmic del càncer de mama. S'estudia el comportament del dispositiu davant de diferents escenaris, com ara en models de mama de diferents dimensions o en tumors a diferents localitzacions i en diferents estats d'evolució. També s'avalua l'impacte de canviar la separació entre les antenes i la quantitat d'antenes en la potència absorbida pel model. Per tal de focalitzar adequadament la potència entregada per les antenes en

cada cas, s'implementa un algoritme basat en la superposició dels camps elèctrics amb l'objectiu de trobar les fases òptimes de les alimentacions de cada antena. Finalment, es realitza una prova de concepte mitjançant la fabricació d'un prototip amb quatre antenes de fase variable. La monitorització dels canvis de temperatura en un model *ex-vivo* indiquen una bona viabilitat del dispositiu per tractar càncers de mama de diferents característiques.

En conclusió, els resultats d'aquesta tesi contribueixen principalment als següents punts: (1) el disseny i caracterització d'antenes en presència del cos humà i (2) la recerca de noves solucions per a dispositius biomèdics amb biotelemetria i per al tractament del càncer de mama mitjançant la hipertèrmia de microones.

Paraules clau: biotelemetria, antenes implantables, antenes miniaturitzades, ceràmica tractada a baixa temperatura (LTCC), servei de radiocomunicacions de dispositius mèdics (MedRadio), identificació per radiofreqüència (RFID), matriu d'antenes configurables, hipertèrmia de microones, tractament de càncer de mama.

Contents

List of Figures

List of Tables

Acronyms

ADS	Advanced Design System
ANSI	American National Standards Institute
BW	Bandwidth
CENELEC	European Committee for Electrotechnical Standardization
CST	Computer Simulation Technology
DE	Differential Equation
DFB	Distributed Feedback Laser
EIRP	Effective Isotropic Radiated Power
EM	Electromagnetic
ESA	Electrically Small Antennas
FAE	Francisco Albero SAU
FCC	Federal Communication Commission
FDTD	Finite-Difference Time-Domain
FEM	Finite-Element Method
FIT	Finite Integration Technique
FO	Optical Fiber
GPU	Graphics Processing Unit
GRAF	Radiofrequency Group
HF	High Frequency
IC	Integrated Circuit
IE	Integral Equation
ICNIRP	International Comission on Non-Ionizing Radiation Protection
IEEE	Institute of Electrical and Electronics Engineers

IFAC	Institute of Applied Physics Nello Carrara
IMD	Implantable Medical Device
IoT	Internet of Things
ISM	Industrial, Scientific and Medical
KSU	Kansas State University
LF	Low Frequency
LTCC	Low Temperature Co-fired Ceramics
MedRadio	Medical Device Radio Communication Service
MoM	Method of Moments
MRI	Magnetic Resonance Imaging
P4	Predictive, Preventive, Personalized and Participatory
PA	Power Absorption
PBA	Perfect Boundary Approximation
PCB	Printed Circuit Board
PDMS	Polydimethylsiloxane
PEEK	Polyether Ether Ketone
PIFA	Planar Inverted-F Antenna
PML	Perfectly Matched Layer
PTFE	Polytetrafluoroethylene
RA	Reference Antenna
RF	Radiofrequency
RFID	Radio Frequency Identification
RTLS	Real Time Location System
SAM	Specific Anthropomorphic Mannequin
SAR	Specific Absorption Rate
SMA	Subminiature version A

SMD	Surface Mounted Devices
SPEAG	Schmid & Partner Engineering AG
UB	University of Barcelona
UHF	Ultra-High Frequency
WBAN	Wireless Body Area Networks

1. Introduction

The impact of radiofrequency (RF) and microwave applications in the field of medicine has increased steadily in recent years. RF is now widely used in the prevention, diagnosis and treatment of a variety of diseases, and plays a major role in imaging, thermal therapies, drug delivery and microwave-based sensors, to name only a few of its applications [1], [2]. In particular, wireless biotelemetry allows minimally invasive monitoring of physiological parameters, improving the patient's comfort and care, and drastically reducing hospital costs [3]. These advantages will be particularly welcome in the future healthcare scenarios based on P4 medicine, especially in view of the current demographic shifts towards more elderly populations and the economic impact that this development is bound to have [4].

P4 medicine (the four "p"s stand for "Predictive, Preventive, Personalized and Participatory") has evolved rapidly over the last decade and represents a revolutionary new medical paradigm which places the individual patient at the center of healthcare [5]. P4 medicine has emerged at the intersection of three main trends in the transformation of the healthcare system [6]:

1. The computational and mathematical modeling of biological and medical systems, used as a tool to understand the biological complexity of disease.
2. The growing concern of the population with healthy lifestyles, and the increased demand for access to personal information in order to improve personal health management.
3. The digital revolution, which allows the gathering of huge amounts of data through diagnostic tests, e-health apps and other tools, which can be stored, analysed and communicated in an efficient way.

As these trends advance, medical devices that provide individualized and long-term physiological data to the patients, consumers or physicians are destined to become a fundamental part in the healthcare system. Thousands of medical devices with wireless biotelemetry are likely to enter our daily lives in the near future.

In this scenario, researchers are seeking to overcome the current limitations found in wireless biotelemetry and RF biomedical devices. One of the most challenging issues is antenna design, especially when working inside or close to the body. This PhD thesis presents an analysis of the interactions between biological tissues and microwave radiation in order to describe the design and characterization of antennas for two main applications: wireless biotelemetry and microwave hyperthermia for cancer treatments.

1.1. Wireless Biotelemetry

In the new era of the Internet of Things (IoT), the smart objects surrounding us are wirelessly interconnected in different ways. Sensor network technologies and Radio Frequency Identification (RFID) play a leading role in this paradigm, in which information and communication systems are evolving into devices embedded in the environment [7].

Wireless Body Area Networks (WBANs) encourage the integration of the healthcare system in the IoT. In recent years, medical devices with biotelemetry capabilities have become extremely popular in the scientific community and now have a large number of applications [2], [8]–[13]. Usually, the deployment of these devices in a WBAN allows the collection and communication of physiological data from an in-body or on-body device to an external base station. Then, this medical information can be presented directly to the patient or sent to the cloud to be transferred to a healthcare unit, saving time and resources. The main elements involved in this process are shown in Figure 1.

The principal aspects of a wireless implantable system for biotelemetry are presented in [14] and identified from the antenna engineer's point of view. Applying this idea not just to implantable but also to wearable devices, the main parts of a wireless biotelemetry system that an antenna engineer has to deal with are the following:

Base station: The base station acts as the intermediary between the sensor node and the cloud. It can be embedded in the sensor device or in an external system (especially in in-body devices). Some important aspects regarding the sensitivity of the receiver and the antenna performance determine the quality of the communication link.

Channel propagation: The propagation of the electromagnetic (EM) waves from the medical device to the base station in a real scenario is sensitive to the environment. Thus, multi-path propagation and the scattering appearing due to nearby objects and walls must be considered in order to improve the performance of the system.

Human body: In terms of electrical properties, the human body acts as a heterogeneous, complex, time-dependent, lossy and dispersive medium. Apart from allowing smaller designs due to the high permittivity of the biological tissues, designing antennas in such hostile conditions represents a real challenge. Moreover, safety regulations limit the power budget for wireless transmission, making the engineer's task even harder.

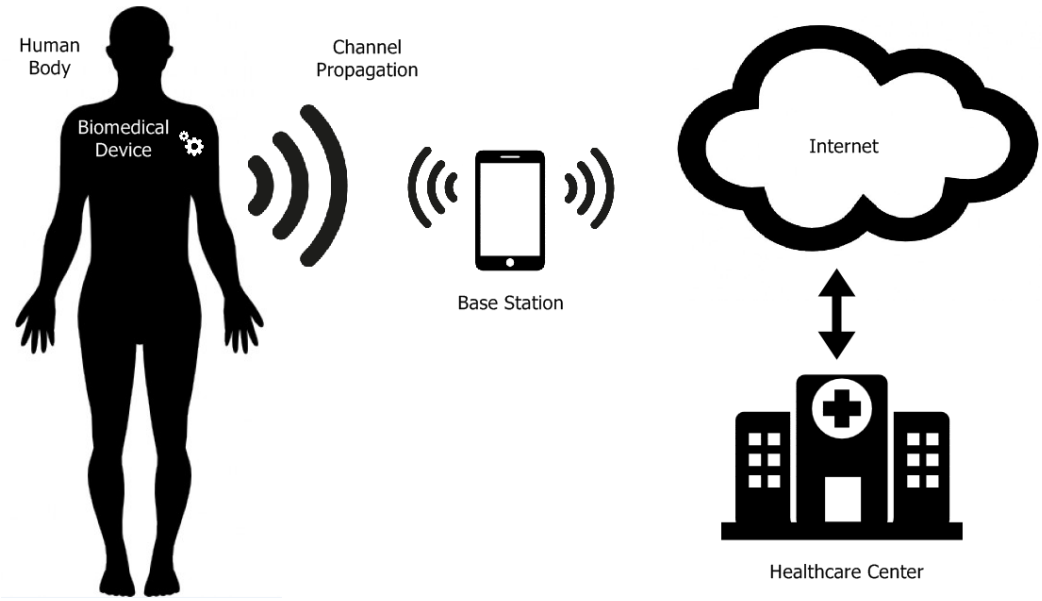

Figure 1. The main elements involved in the remote monitoring system of physiological data from an in-body or on-body biomedical device.

Insulation and packaging: The packaging of the device is a crucial aspect in the antenna design. The near-field of the EM radiation interacts directly with the materials used in the substrate and superstrate of the antenna, modifying its behavior. For in-body devices, the biocompatibility of these materials is also an indispensable requisite to avoid harmful effects in the biological tissues.

Antenna: The choice of the antenna type and the shape of the radiator are the key points for providing a medical device with wireless capabilities. The goal of an antenna engineer is to provide a suitable design in terms of efficiency, operating frequency, bandwidth and radiation pattern. Other aspects such as the available volume, the interaction of the EM radiation with the insulation and the human body, as well as the influence of other electronic components in the device will have a key role in the performance of the antenna.

Electronics and power supply: The total volume occupied by the biomedical device depends not only on the antenna but also on the electronic components and the power supply. The electronic components make the device work properly, and integrate the communication and processing modules. The goal of the power supply is to provide the required power defined by these modules and components. New approaches for replacing internal batteries are appearing in order to reduce device size, a particularly important issue in implantable devices. These approaches include energy harvesting or wireless power transfer.

Biosensors and bioactuators: Another important aspect in the packaging of the device is the placement of biosensors or bioactuators. Usually, they need to be in contact with some part of the human body and are defined by the application.

Manufacturing process: The manufacturing process is a crucial step in transferring the simulated results to real life situations. An accurate, reliable and repeatable fabrication process is important to achieve successful performance.

Characterization and Experiments: All the parts involved in the development of the system have to be validated and characterized through experiments. The results obtained must confirm the correct functioning of the system and the safety requirements. An adequate measurement setup is mandatory in order to obtain credible and accurate results and avoid interferences with the lab equipment.

As previously noted, biomedical devices can be classified as on-body or in-body depending on their location. The choice of one or other type of device may depend on economic aspects, social evolution, research development and technological challenges.

On-body or wearable devices are already present in our everyday life. Smart watches and wristbands with sensing capabilities, for instance, are a reality today. New trends in wearable devices will lead to the blossoming of other types of product, such as headwear or eyewear devices for virtual or augmented reality, smart footwear and bodywear for sport and fitness, neckwear and jewelry for fashion purposes, and so on. According to [15] by 2026 the market for these smart wearable products will move over $150 billion annually. In the healthcare system, wireless on-body devices are being introduced, as they enable noninvasive monitoring of vital signs. However, certain challenges remain unresolved, among them miniaturization, security, standardization, energy efficiency, robustness and unobtrusiveness [10].

Most in-body devices are still in development and require a specific medical prescription in order to be used. These devices first appeared in 1958, when *Rune Elmgvist et al.* succeeded in implanting the first pacemaker in a human body [16]. Since then, in-body devices, commonly known as Implantable Medical Devices (IMD), have covered a niche area when physiological parameters are only accessible from inside the human body or when wearable devices were not sufficiently powerful. Nevertheless, apart from implanted pacemakers and some ingestible endoscopic capsules with biotelemetry capabilities, not many in-body medical devices are available on the market; most of them are still in development, at testing or prototyping stage [17]–[19].

In the review in [19], in-body wireless devices are classified in implantable, ingestible or injectable depending on their method of insertion into the human

body. These devices open up a promising spectrum of new healthcare applications, but the list of challenges to overcome is still longer and more demanding than in the case of wearables: a greater level of miniaturization, biocompatibility, safety considerations, powering, and so on.

In this context, several technologies have been proposed as possible solutions for a wireless biotelemetry system for either in-body or on-body devices. Among them, RFID technology is an already existing low-cost and low-power solution to overcome some of the limitations mentioned [20], [21]. RFID systems provide standardized communication protocols and integrated commercial chips that facilitate the development of the medical device with wireless biotelemetry. In addition, some RFID chips with sensing capabilities have recently been developed [22], enabling this technology to perform new functions. For all these reasons, although still in early stages of deployment [21], RFID-based systems are expanding from the industrial sector to the healthcare system [23]–[25], especially for the identification and tracking of patients [26]–[29]. The main elements involved in the RFID systems differ slightly from the classical remote monitoring system, as Figure 2 illustrates.

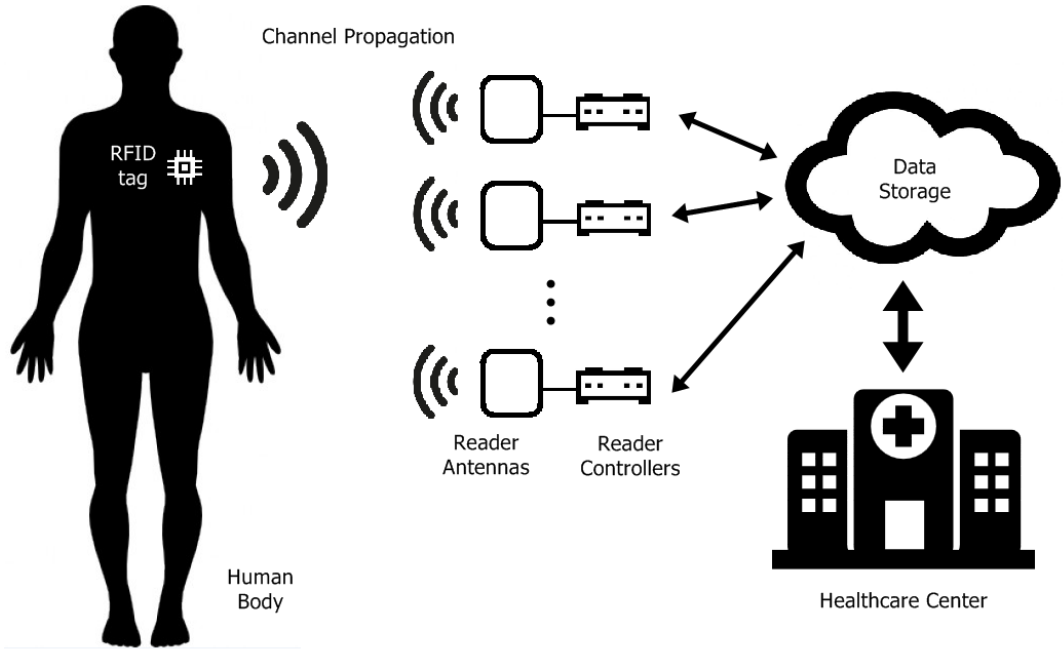

Figure 2. The main elements involved in a RFID-based tracking system implemented in a healthcare center.

1.2. Microwave Thermal Therapies for Cancer Treatments

Besides transmitting information, microwaves have other functions in biomedicine. The thermal increase produced by the microwaves when passing through biological tissues is applied in the treatment of certain cancers, among them breast, cervix, head and neck, rectum, bladder, esophagus, lung, and superficial tumors [30]–[34]. It is well demonstrated that hyperthermia, a form of moderate tumor heating ranging between 39 and 45 °C, enhances the effectiveness of radiotherapies and chemotherapies. Temperatures higher than this level belong to thermal ablation. The biological reasons for the use of hyperthermia as a thermal sensitizer for radiotherapy and chemotherapy are summarized in [35]. Although the use of microwave hyperthermia is spreading in the cancer treatments, some aspects still need improvement. One of the major concerns when applying microwave hyperthermia is heating selectivity. To do that, focusing algorithms [36] and nanoparticles with thermal sensitivity [37] are under development.

1.3. Thesis Overview

This thesis focuses on the design and characterization of on-body and in-body antennas for various biomedical applications. Although the initial main area of research was the biotelemetry of implantable biomedical devices, new opportunities and collaborations arose over the first few years. By the end, the scope of the thesis broadened to include RFID systems and on-body microwave hyperthermia treatments for breast cancer, all of them approached from the point of view of antenna engineering. Thus, the points discussed in the thesis are related to:

- The antenna design
- The packaging
- The manufacturing process
- The characterization and experimental validation
- The effects on the human body
- The implementation of three antenna demonstrators covering different applications

1.3.1. Objectives

The main goals of the thesis are:

- To present a state-of-the-art of the main challenges in in-body antennas.
- To analyze the design of different in-body antenna miniaturization methods in order to increase the radiation efficiency.
- To assess the influence of the human body on antenna performance in greater detail.
- To explore the feasibility of Low Temperature Co-fired Ceramic (LTCC) technology for manufacturing in-body antennas.
- To experimentally characterize these in-body antennas and to propose new measurement techniques to overcome the limitations of the current setups.
- To present a new implantable broadband Planar Inverted-F Antenna (PIFA) design based on LTCC technology for biotelemetry.
- To propose novel in-body Ultra High Frequency (UHF) RFID tag designs.
- To present a configurable compact on-body microwave applicator for the treatment of breast cancer through hyperthermia.

1.3.2. Background and Framework

The main research activities performed in this thesis were carried out at the laboratory of the Radiofrequency Group (GRAF) at the Department of Electronics and Biomedical Engineering of the University of Barcelona (UB). Certain tasks were performed elsewhere, as shown in the list below:

- **GRAF Laboratory**

Most of the work for the thesis was carried out at this laboratory. RF design, EM simulations, characterization and experiments were conducted here.

- **Francisco Albero SAU (FAE) facilities**

This company provided the installations, equipment, materials, knowledge and resources needed to manufacture most of the antenna prototypes.

- **Biomedical Computing and Devices Laboratory (Kansas State University)**

The microwave hyperthermia system for breast cancer treatment project was created during a stay at this center.

This thesis was supported by the following projects:

- Spanish Ministry of Science and Innovation, project TEC2010-21484

- Spanish Ministry of Economy and Competitiveness, project TEC2013-40430-R
- National Science Foundation, USA, under grant CBET 1337438

1.3.3. Outline and Original Contributions

The thesis is divided into two parts. The first part presents the theoretical framework and outlines the development of the research into implantable antennas, from the first design steps to the prototyping and experimental characterization. The second part focuses on the final biomedical applications – an implantable antenna, an implantable RFID and an on-body hyperthermia device.

A summary of each chapter is presented below.

PART 1. FRAMEWORK AND DEVELOPMENT

Chapter 2. Antennas in the Presence of a Human Body
This chapter presents an overview of the main aspects involving the design of antennas for biomedical applications, placing particular emphasis on implantable antennas. Special attention is given to understanding the challenges and strategies in the design of these antennas. Other elements involved in the design process, such as electromagnetic computational tools or human body phantoms, are also described.

Most of this chapter is based on concepts that are already known, while some parts can contribute to a better comprehension of important issues concerning the design process of implantable antennas. The state-of-the-art presented also sheds light on the current trends in design strategies for implantable antennas.

Chapter 3. Analysis of In-body Antenna Miniaturization
This chapter focuses on the miniaturization strategies of implantable electrically small antennas (ESA). The main goal here is to identify the most efficient miniaturization method for in-body multilayer square PIFAs in terms of efficiency. Antenna parameterization and several radiator structures are presented.

This chapter offers important advice regarding the miniaturization process of implantable antennas. On the basis of the results, a final prototype is presented for implementation in LTCC technology.

Chapter 4. Influence of Phantoms on In-body Antenna Performance
This chapter studies the interaction between phantoms and EM radiation in depth. Variations in antenna performance due to several phantom parameters, such as geometry, volume, implant depth and frequency, are quantified and analysed. The antenna orientation and the use of anatomical phantoms are also assessed.

The results of this chapter provide useful clues for understanding why different phantoms lead to variations in efficiency, gain, and other antenna parameters. These variations were also found when comparing different implantable antennas available in the literature review. Therefore, in order to compare the antenna designs of different research groups, a characterization protocol for phantom dimensions and implant depth is proposed.

Chapter 5. Fabrication and Characterization of In-body Antennas Based on LTCC Technology

In this chapter the manufacturing process of multilayered antennas in LTCC technology is described and assessed. Sensitivity tests are carried out to quantify possible fluctuations in antenna performance due to the manufacturing process. In addition, three measurement techniques are presented with the aim of minimizing the coaxial effects in the implantable antenna characterization.

The aim here is to address the critical issues that appeared during the antenna manufacturing in LTCC, from the industrial point of view. Most of this chapter presents new approaches on how to improve the characterization of an implantable antenna, such as a measurement setup based on optical fiber.

PART 2. ANTENNA DEMONSTRATORS

Chapter 6. Design and Characterization of a Multilayered Broadband Antenna for Compact Embedded Implantable Medical Devices

A new compact implantable antenna design is presented to meet some of the challenges presented in previous chapters. The main features of this novel design are its miniaturized size, its structure that allows integration of electronic circuits of the implantable medical device inside the antenna, and enhanced bandwidth that mitigates possible frequency detuning caused by the heterogeneity of biological tissues. The antenna is manufactured and validated experimentally.

Chapter 7. Design and Characterization of a Miniaturized UHF RFID Tag

In this chapter, a novel miniaturized UHF RFID tag structure is presented for in-body applications. Taking into account previous designs presented in the thesis and the impedance matching of RFID chips, PIFA-based antennas with inductors are evaluated.

Chapter 8. Design and Characterization of a Phased Antenna Array for Intact Breast Hyperthermia

This chapter presents a new compact and wearable microwave antenna array for delivering hyperthermia to tumors located at different sites within the breast. Various parameters are assessed in order to optimize the configuration of the system. A focusing algorithm has been developed to maximize the selectivity and resolution of the applicator, which aims to facilitate controllable power deposition

within the intact breast. Finally, an *ex-vivo* experimental thermal validation on a preliminary prototype indicates the practical feasibility of the system.

Chapter 9. General Discussion, Conclusions and Future Work
A summary of all the work performed in the thesis is presented, together with a general assessment of the most salient issues. Some recommendations and possible future contributions are also discussed.

Appendix A. Characterization of LTCC In-body Antennas
This appendix shows characterizations of the whole range of antenna designs manufactured in LTCC technology and presented in Chapter 5.

Appendix B. Scientific Curriculum Vitae of the Author

Part 1

FRAMEWORK AND DEVELOPMENT

2. Antennas in the Presence of a Human Body

2.1. Introduction

The human body plays a crucial role in the design and characterization of antennas for biomedical applications. Its heterogeneous, dispersive and lossy behavior significantly alters antenna performance and EM propagation. Anatomical variability between patients also increases the complexity of finding a suitable design for a desired application. Thus, several considerations have to be taken into account when designing an antenna for use inside or close to the human body.

This chapter focuses on the main aspects involved in the interaction between antennas and biological tissues. The principal goals here are:

- To better understand antenna performance in the presence of a human body.
- To present strategies to achieve the desired antenna performance.
- To introduce the modeling methods and computational tools used in the design process.
- To review existing human models and phantoms.
- To describe the current measurement issues for in-body antennas.
- To present the current state of the art for implantable antennas.

2.2. Microwaves and Biological Tissues

This section presents a theoretical approach to the particularities of the interaction between microwaves and biological tissues. Frequency ranges used in biotelemetry, and defined by international organisms (see Subsection 2.3.3), are comparable to the size of human body in terms of wavelength. This similarity in size implies some macroscopic electrical effects that are described in [38]: 1) the induction of dipolar polarization, 2) the alignment of existing dipoles and 3) the movement of free charges.

2.2.1. Tissue Dielectric Properties

The electrical permittivity ε and the electrical conductivity σ of a biological tissue define the interactions between it and an EM field that is present [38].

For a homogeneous, isotropic and linear medium, absolute permittivity and conductivity can be defined as complex quantities [14], as given by Equation 1 and Equation 2,

$$\varepsilon(\omega, T) = \varepsilon_O(\varepsilon_r' - j\varepsilon_r'') \qquad (1)$$

$$\sigma(\omega, T) = \sigma' - j\sigma'' \qquad (2)$$

where ε_O is the permittivity of the vacuum (ε_O =8.8541878176x10^{-12} F/m), ε_r the relative permittivity of the medium and σ electrical conductivity expressed in S/m. Both parameters are dependent on the frequency ω and the temperature T.

Electrical permittivity describes the phenomena of induced polarization and the alignment of existing dipoles in the presence of an applied electric field. The real part (ε') represents the lossless component of the medium, related to the polarization, while the imaginary term (ε'') describes the energy losses due to the damping of the vibrating dipole moments and the time lag responses of the medium [39]. The electrical conductivity is a measure of the capacity of a material to allow free electric charges to circulate.

Considering Equation 1 and Equation 2, the relative effective permittivity ε_e' and conductivity σ_e' can be expressed as:

$$\varepsilon_e' = \varepsilon_r' - \frac{\sigma''}{\omega\varepsilon_0} \qquad (3)$$

$$\sigma_e' = \sigma' - \omega\varepsilon_0\varepsilon_r'' \qquad (4)$$

Taking into account Maxwell's equations, the complex effective permittivity ε_e can be redefined as:

$$\varepsilon_e = \varepsilon_O(\varepsilon_e' - j\varepsilon_e'') = \varepsilon_O\left(\varepsilon_e' - j\frac{\sigma_e'}{\omega\varepsilon_0}\right) \qquad (5)$$

The loss tangent $tan\ \delta$ helps to understand the degree to which a medium can be said to be "lossy". It corresponds to the relationship between the imaginary part and the real part of the complex effective permittivity:

$$tan\ \delta = -\frac{\varepsilon_e''}{\varepsilon_e'} = \frac{\sigma_e'}{\omega\varepsilon_0\varepsilon_e'} \qquad (6)$$

The dielectric properties of biological tissues are extracted from the review work of *Gabriel et al.* [40].

The effective wavelength λ_e of a medium at angular frequency ω can be redefined as:

$$\lambda_e = \frac{2\pi}{\omega\sqrt{\varepsilon_0\mu_0}} Re\left\{\sqrt{\frac{\omega\varepsilon_0}{\omega\varepsilon_0\varepsilon_e' - j\sigma_e'}}\right\} \qquad (7)$$

It is worth noting the dependency of the effective wavelength on the effective permittivity. Given an EM field, λ_e will be smaller in a medium than in a vacuum. This is of great relevance to the miniaturization of implantable antennas.

EM propagation in biological tissues presents higher attenuation rates due to the losses the medium gives rise to. Moreover, reflected fields appear at the interfaces of tissues and at the air–body interface, increasing the complexity of predicting the EM behavior of an antenna in a realistic scenario within or close to a human body.

2.2.2. Biological Effects

The biological effects of RF radiation can be divided into thermal and non-thermal. For RF fields in the frequency range between 1 MHz and 10 GHz, EM energy is absorbed by tissues leading to a possible temperature increase. Such a thermal increment is produced due to oscillatory modification of the spatial orientation of bipolar molecules, mainly water in biological tissues. In a thermal effect, just such an increment of tissue temperature is produced, which can lead to harmful consequences because of the incapacity of the homeostatic system to thermoregulate correctly. For non-thermal effects, there is still controversy concerning the harmful consequences for biological tissues, but to date, there is no evidence of either carcinogenesis [41] or EM hyper sensibility [42].

The Specific Absorption Rate (SAR) quantifies EM radiation absorption by tissues and represents the amount of energy or power deposition per unit mass of biological tissue. The local SAR is expressed as:

$$SAR = \frac{|\boldsymbol{E}|^2 \sigma_e}{2\rho} \quad (8)$$

where $\boldsymbol{E}$ is the electric field strength (V/m), σ_e is the effective electrical conductivity (S/m) and ρ is the mass density of the tissue (kg/m^3) [43].

The body's thermal sensors are located in the skin and do not readily detect the warming of deep areas of the body. Therefore, significant amounts of RF energy can be absorbed without it being immediately noticeable. This is of specific concern in the design of in-body medical devices that use biotelemetry. Limitations established by the pertinent organisms guarantee non-harmful levels of RF radiation (see the next section).

The spatial-average SAR is computed in EM solvers and measured in RF laboratories to check that its maximum peak remains below the limits indicated in regulations. The spatial-average SAR is calculated as:

$$SAR\ (V) = \frac{1}{mass(V)} \int_V SAR(r)\ dm \quad (9)$$

where V is the finite volume that a region with a specific mass occupies. SAR assessment is also useful to determine the maximum radiation power a device is permitted.

The thermal evolution of a biological tissue is indicated for safety purposes or for thermal therapies, such as the design of microwave hyperthermia devices. It is possible to determine thermal variations in a biological tissue by means of the bioheat equation (Eq. 10) defined by Pennes [44]:

$$\rho C \frac{\partial T}{\partial t} = \nabla \cdot k \nabla T + Q - B(T - T_{bl}) + A_0 \qquad (10)$$

where ρ is the density of the material (kg/m^3), C is its specific heat capacity (J/kg°C), T is the temperature (°C) at a time t (s), k is the thermal conductivity (W/m°C), Q is the heat source or volumetric power deposition (W/m^3], B is the blood perfusion coefficient (W/m^{-3} °C), T_{bl} is the blood temperature (°C), and A_0 is the heat generated by metabolism (W/m^{-3}). The heat source in the Pennes equation is calculated from the EM fields using Equation 11:

$$Q = \boldsymbol{J} \cdot \boldsymbol{E} \qquad (11)$$

where $\boldsymbol{J}$ is the current density (A/m^2).

2.2.3. Exposure Guidelines and Regulations

In recent years, concern associated with microwave radiation has grown due to the continuous rise of wireless communications. In order to avoid harmful effects in the human body, several guidelines and regulations for EM fields have been developed based on scientific evidence. The regulation for SAR measurements and their maximum acceptable values are established by the American National Standards Institute (ANSI), the Institute of Electrical and Electronics Engineers (IEEE) [43] and the International Commission on Non-Ionizing Radiation Protection (ICNIRP) [45] (Table 1).

The precise property that appears to be responsible for the effects of EM radiation on the human body depends on its frequency. For this reason, three basic EM exposition restrictions are defined:

- Current density (1 Hz - 10 MHz)
- SAR (100 kHz – 10 GHz)
- Power density (10 GHz – 300 GHz)

Table 1. SAR levels according to IEEE and ICNIRP regulations for the general public [43], [45].

Cube mass	Whole body average SAR (W/kg)	Head and trunk localized SAR (W/kg)	Limb localized SAR (W/kg)
10 g	0.08	2	4

For the frequency range of interest in biotelemetry, SAR regulations have to be addressed. The SAR limits are calculated on the basis that a temperature rise of 1°C in a resting person due to radiation is considered to be harmful. According to the ICNIRP and IEEE standards ([43], [45]), this occurs at an average SAR value of 4 W/kg over the whole body for 30 minutes. From this experimental SAR value, regulations apply a correction factor and establish basic restrictions for reference purposes.

The regulations propose limits to both localized SAR (in a cube of 10 g of tissue) and the average SAR over the whole body (Table 1).

According to these basic restrictions, technical organisms define maximum SAR values for wireless devices:

- United States: the Federal Communications Commission (FCC) specifies a maximum SAR of 1.6 W/kg in a cube of 1 g of tissue.
- European Union: the European Committee for Electrotechnical Standardization (CENELEC) establishes a limit of 2 W/kg averaged over a 10 g cube.

The FCC standard is more restrictive than IEEE and ICNIRP standards, since a SAR value of 2 W/kg in a 10 gram cube is equivalent to a SAR value between 4 and 6 W/kg in a 1 gram cube [46].

2.3. Challenges for the Design of Antennas in the Presence of a Human Body

This section focuses on specific challenges associated with the design of devices that employ wireless biotelemetry in the presence of a human body. The state of the art of implantable antennas is also assessed from different points of view.

2.3.1. Miniaturization

Devices working in a WBAN usually require a certain degree of miniaturization to increase patient comfort and facilitate its placement, especially for devices

operating inside the body. Typical limitations of electrically small antennas (ESAs) in terms of bandwidth, quality factor and gain [47]–[50] apply to these designs. Due to the presence of a lossy medium, additional challenges have to be overcome for in-body antennas. In [14], an accurate analysis of the limitations of implantable antennas is presented using submarine radiators as an analogy. The main conclusion of that study is that the results given by *Wheeler* [51] provide valuable information for estimating the limitation of radiation efficiency as a function of the antenna size (the radius of the sphere enclosing the radiator).

The main objective of the miniaturization process is to reduce the size of the antenna at a given frequency while maintaining an adequate level of radiation efficiency. Bandwidth and radiation pattern are also sensitive to size reduction. As miniaturization for in-body devices presents more challenges than for on-body devices, only an overview of the former is presented here.

Several miniaturization strategies have been presented in the literature for the design of in-body antennas. Antenna design based on patch radiators, such as planar inverted F antennas (PIFAs), emerges as the most commonly proposed structure for implantable antennas of small volumes. Multilayer PIFA structures have also been proposed. Other radiator structures, such as monopoles, dipoles, loop antennas and 3D-structures, are also present in the literature. A summary of some representative antenna designs for implantable devices is provided in Table 2.

Lengthening the current flow path on the patch surface allows the available space to be taken advantage of to increase the miniaturization. Serpentines [52]–[57], spirals [53], [54], [57]–[61] or fractal geometries [62] have been investigated for implantable antennas. The work presented by *Best et al.* [63] studies the influence of the radiator current vector on the antenna size, reporting that nearby conductors with currents flowing in the opposite direction lead to an increase of the resonant frequency. A thinner radiator also reduces the total size of the antenna, but produces greater current concentrations in the antenna, leading to a bandwidth reduction; as described in [49].

Table 2. Antenna designs for implantable devices.

Antenna design	References
Patch	[54], [64]–[67]
One-layer PIFA	[64], [53], [68]–[79], [55], [80], [52]
Multilayer PIFA	[68], [79], [81]–[84]
Monopoles	[85]–[88]
Dipoles	[56], [59], [60], [89]–[92]
Loop	[93], [94]
3D-structures	[61], [95], [96]

Another miniaturization technique for in-body antennas is to use materials with a high dielectric permittivity (substrate and/or superstrate) or a technology focused on the compaction of the electronics with the antenna. This is the case of the LTCC technology used in this thesis, which has certain features (such as the implementation of internal pathways and cavities) that allow integrated microstructures to be embedded within the antenna. Thus, the complete structure configures a compact implantable medical device [97]–[100].

Loading techniques to improve impedance matching may help in the process of reducing antenna volume. Capacitive and inductive loadings are presented in [67] and [89], respectively.

Finally, increasing the operating frequency of the wireless biotelemetry of the device can also help in the miniaturization of the antenna, as the wavelength and the frequency are inversely proportional.

In the next chapter, a detailed analysis of a miniaturization process for implantable antennas is presented.

2.3.2. Biocompatibility

Implantable antennas must be biocompatible to ensure patient safety and prevent implant rejection. Two main techniques are used to preserve the biocompatibility of the antenna, isolating the metallic radiator from the human tissue: employing a biocompatible substrate and/or superstrate; and the insertion of a thin layer of a low-loss biocompatible coating (biocompatible encapsulation) [101].

Table 3 shows biocompatible materials used to isolate implantable antenna presented in the literature.

As I mention previously, a high permittivity allows greater miniaturization, while a low loss tangent means low losses and better antenna performance. Therefore, I chose LTCC for this thesis as a suitable substrate for implantable antennas because of the following features it exhibits:

- High permittivity
- Low loss tangent
- Multilayer technology
- Implementation of internal pathways and cavities
- Possibility of embedding integrated microstructures
- Reliability in the manufacturing process
- Durability
- Biocompatibility (with certain substrates)

Table 3. Biocompatible materials used to isolate implantable antennas.

		Dielectric properties	
Polymers	**References**	ε'_e	**tan δ**
Silastic® MDX4-4210	[101]	3	0.001
Polyether ether ketone (PEEK)	[14]	3.2	0.01
Polypropylene	[14]	2.55	0.003
Polyamide	[14]	4.3	0.004
Polydimethylsiloxane (PDMS)	[90]	2.2	0.013
Polytetrafluoroethylene (Teflon)	[54]	2.2	0.0003
Parylene-C	[80]	2.95	0.013
Ceramics			
Macor	[101]	6.03	0.0047
Alumina	[14], [101]	9.2 - 9.4	0.006 – 0.008
Zirconia	[14], [101]	29	0.002 - 0.05
LTCC	[97]	7.8	0.005

2.3.2.1. Substrate Characterization

The LTCC substrates used in this thesis are manufactured at the company Fransico Albero S.A.U. [102] following an accurate manufacturing process described in Chapter 5. In order to validate their dielectric properties, they are characterized using a rectangular waveguide cavity resonator (Figure 3) in the laboratory where my research is performed. According to the detailed explanations described in [103], one can derive Equation 12 and Equation 13 to give the effective permittivity and the loss tangent of the material for certain resonant frequencies:

$$\varepsilon'_e = 1 + \frac{(d+t)}{2t\left[\frac{w}{a}+\frac{1}{\pi}\sin\left(n\frac{w}{a}\right)\right]}\left[\left(\frac{f_0}{f_d}\right)^2 - 1\right] \qquad (12)$$

$$tan\ \delta = \frac{(d+t)}{2\varepsilon'_e t\left[\frac{w}{a}+\frac{1}{\pi}\sin\left(n\frac{w}{a}\right)\right]}\left(\frac{1}{Q_d} - \frac{1}{Q_0}\right) \qquad (13)$$

where the dimensions of the cavity and the substrate are as given in Figure 3 (a=203.2 mm, d=430.2 mm, w=70.9 mm and t=1.35 mm); f_d and f_0 are the odd resonant frequencies with and without the dielectric substrate, respectively; and Q_d and Q_0 are the quality factor with and without the dielectric substrate, respectively. Although an exhaustive analysis of the characterization by means of this method is not within the scope of this thesis, some results are given in Table 4.

An example of the resonant frequency variations produced by fluctuations in a range close to the nominal values in substrate dielectric properties is given in [104]. Results indicate only a frequency shift of 1% when changing the substrate permittivity by up to ± 0.4. However, variations in permittivity have to be considered at the modeling stage, as other designs could lead to significant frequency detuning (see Subsection 5.3.2).

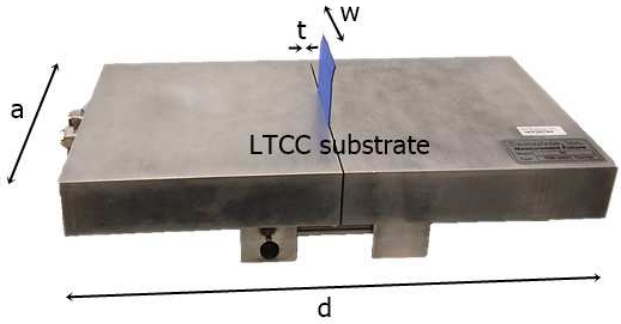

Figure 3. Set-up to measure the dielectric properties using a rectangular waveguide cavity resonator. The LTCC substrate is located in the middle.

Table 4. Main parameters of the rectangular waveguide cavity resonator with and without the dielectric substrate and the measured dielectric properties of the Heraeus 51528B LTCC substrate.

f_0 (MHz)	Q_0	f_d (MHz)	Q_d	ε'_e	$tan\ \delta$
815.5	6822	805.7	5272	7.2	0.0015
1276.5	8493	1261	6395	7.2	0.0014
1887.6	11034	1862.7	7206	7.5	0.0007
2540.5	12416	2513.8	8891	6.4	0.0023

2.3.3. Operating Frequency

Inductive couplings at frequency bands lower than 15 MHz were employed as the first method of wireless communication integrated in an IMD, such as the cardiac pacemaker presented in [105]. This consists of two inductors, one in the IMD and the other outside the body, that are able to transmit data when in close proximity. Drawbacks of this technology are related to misalignment between the inductors, slow data transfer rates and short distances of communication. Thus, RF antennas were proposed to overcome these limitations.

Table 5 classifies several frequency bands that have been used in the literature for antennas used in biotelemetry. The most commonly employed bands are the Medical Device Radio Communication Service (MedRadio) band of 401 – 406 MHz [106] and the Industrial, Scientific and Medical (ISM) bands.

The criteria by which an antenna engineer selects the operating frequency band depend on the application. While low-frequency links present lower losses through biological tissues (due to lower conductivities), high-frequency biotelemetry implies small antenna sizes and an enhancement of the communication speed.

Table 5. Antennas for biotelemetry presented in the literature classified by working frequency

Frequency band	References
401 – 406 MHz	[53]–[55], [60], [61], [64], [65], [68]–[71], [73]–[76], [78], [79], [81], [83], [85], [89], [96], [107]–[114]
433 MHz	[55], [73], [74], [94], [115]–[117]
860 – 960 MHz	[55], [77], [84], [88], [91], [92], [94], [117]–[122]
1.2 – 1.6 MHz	[59], [62], [120], [123]
2.4 – 2.5 GHz	[59], [66], [67], [70], [73]–[75], [80], [83], [89], [90], [94], [96], [98], [99], [112], [114], [117], [120], [123]–[125], [125]–[128]
More than 3 GHz	[86], [87], [117], [129]–[133]

2.3.3.1. Field Regions

Another important aspect that depends on the operating frequency selected is the space distribution of the field regions, as they substantially modify the behavior of the radiated power. The boundary between the near-field and the far-field regions in electrically small antennas ranges from 1 to 2 times the wavelength, and the reactive near-field zone finishes at a distance of $\lambda/2\pi$, as illustrated in Figure 4. This reactive region has a great impact on the behavior of the radiated power of the antenna, as reported in [86], [134]. When implanted in biological tissue, the surrounding lossy medium dramatically decreases the radiation efficiency of the antenna because of its interaction with the reactive near-field. The dimensions of these regions for the three main frequency bands studied in this thesis are comparable with the dimensions of phantoms and implant depths, as can be appreciated from Table 6. Hence, additional considerations of substrate size or implant location have to be taken into account when defining the operating frequency.

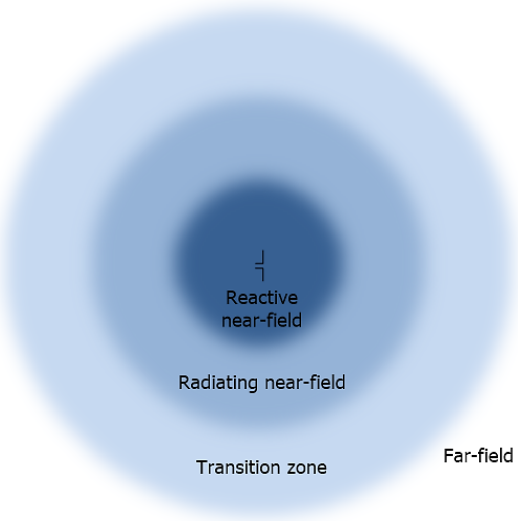

Figure 4. Field regions of an antenna.

Table 6. Field regions for antennas implanted in a skin phantom as a function of the frequency band

Regions	Distance up to (mm)	403 MHz	866 MHz	2.45 GHz
Reactive near-field	0.159 λ	17.3	8.5	3.2
Radiative near-field	λ	108.9	53.7	19.9
Transition	2 λ	217.8	107.4	39.7

2.3.3.2. Frequency Detuning

As reported in detail in [38], [111], [135], the working frequency of wireless biotelemetry systems becomes detuned, depending on the implant location, and this detuning varies for each individual. These frequency shifts are mainly due to: the mismatch of impedances between the antenna and its surroundings, which varies as a function of the body size and shape; the composition and electrical properties of tissues; the age of the individual; and the IMD placement, among others. A frequency mismatch of 70 MHz is observed between individuals for an implantable antenna operating at the MedRadio frequency of 403 MHz [111] (Figure 5). In the process of designing an implantable antenna, detuning effects have to be considered to establish a bandwidth large enough to ensure the communication link with the device in different individuals and implant locations.

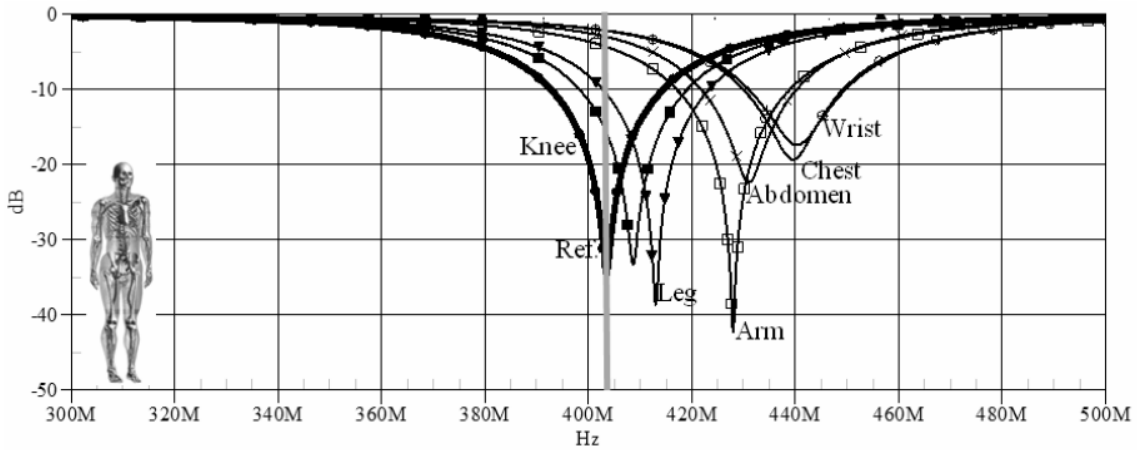

Figure 5. Example of the frequency detuning analyzed in [111]. The simulated reflection coefficient of the proposed antenna implanted subcutaneously in different locations of a male anatomical body phantom is presented.

2.3.3.3. Bandwidth

When an antenna is surrounded by lossy media, near field coupling produces strong dissipation into the environment, resulting in unusually wide band behavior [14]. This means that, although it enhances the bandwidth, the presence of the human body reduces the efficiency of the antenna.

As seen in the previous subsection, a large bandwidth is desirable in the design of implantable antennas to diminish frequency detuning effects. The effect of bandwidth enlargement due to lossy media may not be enough to fulfill this requirement. Therefore, several studies focus on the bandwidth increment of in-body antennas. Stacked implantable PIFA designs with an enlarged bandwidth are presented in [68], [71], [79], [82]. In the design presented in [79], the bandwidth is increased by embedding the hook-shaped slots at the edges of the radiating patches; while in [82], the antenna shows wideband behavior using modified ground structure. In the study reported in [56], a new resonant frequency appears in close proximity to the fundamental one, due to the introduction of a strip connected to a simple dipole. In [136], a differentially fed dual-band implantable antenna that operates at two frequencies close to the MedRadio band is presented. A single wideband is achievable by retuning the geometrical parameters of the proposed antenna.

In Chapter 6 I analyze the design of a novel multilayered implantable PIFA with broadband behavior in more depth.

2.3.4. Powering

In the presence of a human body, the maximum input power for wireless transmission is limited by radiofrequency safety regulations, as mentioned before in this chapter. SAR guidelines are intended to avoid harmful heating effects in biological tissues, but their implementation significantly reduces the delivered power. In addition, a great amount of this power is deposited in the body, reducing the radiated power and transmission range.

Conventional powering of medical devices has been via internal power supplies. However, in the case of IMD, additional issues have to be addressed, such as the periodic replacement/recharging of the battery and the increment of the total volume of the device the power supply supposes. Therefore, current research focuses on new powering methods or passive technologies to develop batteryless in-body devices [19].

2.3.4.1. Energy Harvesting

Several antennas are proposed in the literature to be used as rectennas for RF wireless power transmission [73], [137]–[139]. Inductive links are also proposed for both data and power transmission [140]. Multiband antennas allow the utilization of different frequency bands for biotelemetry, wireless power transfer and/or a wake-up signal [83], [138].

Recent studies investigate various proposals to take advantage of environmental energy sources. Examples of power harvesting include electrochemical [141], [142], thermoelectric [143], kinetic [143], [144], ultrasound [145] and photovoltaic [146], to name only a few.

2.3.4.2. Passive Technology

Passive devices do not require any power storage, as in the fully-passive in-body devices presented in [147], [148]. Passive RFID tags in the HF [149], [150] and UHF [118], [121], [151] ranges are also used. The main issue here is that an external reader in close proximity to the antenna is required.

2.3.5. Radiation Pattern

The radiation pattern of an antenna is considerably affected by the surrounding environment, especially that in the near-field region [134]. In the case of in-body antennas, the implant depth and the body model or phantom used significantly vary the spatial distribution of the EM radiation. Generally, an off-body transmission is required, meaning that the radiation pattern should substantially tend in the outwards body direction. Moreover, for on-body antennas, this directionality reduces SAR values of the tissues in close proximity to the antenna.

In Chapter 4, I present a detailed analysis of the influence of phantoms on antenna performance.

2.3.6. Efficiency

In a medical device with wireless biotelemetry, the lossy matter surrounding the antenna strongly couples with the near-field, producing an increment in lost power. This phenomenon causes a drastic radiation efficiency reduction for in-body antennas. By allocating part of the near-field to a lossless substrate instead of in lossy media, it is possible to mitigate this drawback [134]. An assessment of the radiator structure could also lead to an improvement in efficiency. Indeed, the next two chapters present a study of far-field features depending on the radiator shape, the influence of the phantom and the location of the antenna, among others.

In this thesis, the radiation efficiency is defined as the ratio between the radiated power and the power delivered to the antenna. I consider that the radiated power is in the far-field region, outside the human body.

2.3.7. Packaging

The encapsulation or packaging, including the placement of electronic components, is an important factor in the design of antennas to be used in a medical device. This is critical in IMD, where the available space is constrained by its application and its location inside the body. Due to the electromagnetic coupling between electronics and the antenna, it is advisable to take the overall design into account in simulations by integrating all the elements so that the model is as similar as possible to the real case.

In [152], a multilayer dual-band antenna integrated inside an implantable and biocompatible capsule is presented. The capsule includes a temperature sensor, a battery, a data transmitter module and a wake-up module. Examples of IMD encapsulations are also found in ingestible devices, such as endoscopic capsules, as can be seen in the work presented in [17]. In this approach, different packaging strategies are proposed in order to integrate all the necessary blocks of the IMD (antenna, transmitter, sensors and power management). Examples of antennas embedded into endoscopic capsules or other cylindrical devices can be found in [48], [72], [75], [86], [100], [117] and [144]. The main features of encapsulated antennas are their small dimensions, wide bandwidth (especially for streaming video data) and circular polarization (to favor the capture of the signal from the external receiver given the arbitrary orientation of the endoscopic capsule).

As mentioned before, LTCC technology has been already used for in-body antenna designs with packaging considerations. Actually, LTCC technology has been used for almost 20 years to produce a multilayer substrate for packing integrated circuits [154]. The fabrication method is based on processing each layer independently and then stacking and packaging them by a lamination and a firing process. This technology has shown appropriate electrical and mechanical properties and high reliability and stability, as well as allowing production of 3D-integrated microstructures [100] and passive elements [99]. LTCC technology has proven versatile for building complex multilevel channel structures, including large-volume cavities suitable for biological applications [155]. LTCC has been tested for biocompatibility and has been used in various biological applications, such as evaluation of human umbilical vein endothelial cells [156], and multi-sensor monitoring [155].

Apart from packaging purposes and to ensure biocompatibility, encapsulation is also a main element in the reduction of losses, as it isolates the near-field of the antenna from the lossy surroundings of a biological medium [134].

2.3.8. Antenna Modeling

EM simulation tools are used to predict antenna performance in a specific environment. However, in spite of having several modeling methods and an advanced level of computation, there are still some issues that compromise the simulated results. Section 2.4 indicates the modeling techniques available and their differences, as well as suggestions to reduce the burden of simulation time and computational resources in the design process. In Section 2.5, the modeling of the surrounding tissues, both in computer software and experimental validation, are discussed in detail.

2.3.9. Antenna Fabrication

Substrate features or layer misalignments derived from the inaccuracies of the manufacturing process can cause deviation from the predicted antenna performance [104]. In ESAs, imperfections at the fabrication stage are more significant because of the relatively reduced dimensions of the prototypes. In addition, for multilayered structures, the utilization of glue between layers could increase thickness and modify the effective dielectric properties of the substrate, as indicated in [14], [61], [104]. Therefore, fabrication techniques for multilayered antennas based on the integration of all the parts in a compact monolith are promising alternatives; this is the case of LTCC technology. Other factors that have to be considered during the migration from numerical models to prototyping are the thickness of metal patches and the feed method [104]. In Chapter 5, I offer a detailed description of the manufacturing process.

2.3.10. Antenna Characterization

One of the main challenges in the design process for antennas to be used in the presence of a human body is experimental validation before becoming integrated with the whole device, especially in the case of in-body antennas. Regarding the literature on in-body antennas, only a few works present *in-vitro, ex-vivo* or *in-vivo* antenna measurements in order to confirm simulated results, especially for far-field features. This is because, as discussed in [14], feeding through an unbalanced coaxial cable significantly alters antenna performance (frequency detuning up to

25% was found in that study). Thus, consideration of the effects of the cable when experimentally characterizing antenna performance is advised.

Several solutions have been developed to avoid disturbances due to the cable, such as baluns, chokes and ferrites ([61], [96] and [157]). While reflection coefficient measurements can be found in much literature, only a few studies present far-field characterization (gain, efficiency or radiation pattern). For instance, to characterize far-field antenna performance, the work in [157] determines antenna gain using the equation:

$$G\ (dBi) = G_{standard} + \left(G_{AUT} - G_{ref}\right) \qquad (14)$$

where $G_{standard}$ is the simulated gain of the reference antenna (dBi), G_{AUT} is the measured gain of the tested antenna (dB), and G_{ref} is the measured gain of the reference antenna (dB).

In Subsection 5.2.3, detailed analysis of these issues is given.

2.4. Computational Tools for EM Simulation

Modeling an antenna and its surrounding media plays a key role in the accuracy of simulation results. Several numerical techniques for EM modeling are widely adopted in the literature to predict antenna performance in the presence of a human body; the most commonly used methods are Finite-Difference Time Domain (FDTD), Finite Integration Technique (FIT) and Finite-Element Method (FEM) (see Table 7). The Method of Moments (MoM), although not generally used in biomedical applications, is commonly applied to multilayer structures.

These numerical methods can be classified according to the model of equation on which they are based (the integral equation (IE) or differential equation (DE) model), or by the domain used (time or frequency), as shown in Table 7. A detailed explanation of these four numerical techniques for modeling the interaction of EM fields with the human body can be found in the work presented in [158].

2.4.1. FDTD Method

As most of the simulations carried out in this thesis are performed using the FDTD method, a brief explanation of this modeling technique is presented here.

The FDTD method solves differential equations in partial derivatives approaching the differential operators by operators over finite differences. This allows the resolution of the Maxwell equations in the temporal domain. The way to define the finite differences is to convert the target volume into small cuboid cells with

significantly smaller dimensions than the radiation wavelength (Figure 6). Typically, the minimum spatial sampling is at intervals ranging from 10 to 20 per wavelength, thus obtaining temporal sampling that is fine enough to keep the algorithm stable.

The electric fields are defined at the center of the edges of the cubes, while the magnetic fields are taken to be at the center of the faces, as proposed by *Yee* [159] (Figure 6). Thus, cells with three electric fields and three magnetic fields can be obtained, and the Maxwell equations in finite difference equations can be solved for each cell.

Table 7. Numerical methods used in the literature for the modeling of antennas in biomedical applications.

Numerical method	Domain	Equation model	References
FDTD	Time	DE	[53]–[55], [57], [58], [76], [90], [93], [107], [111], [120], [121], [124], [128], [160]–[163]
FIT	Time	IE	[52], [67], [94], [129], [164]
MoM	Time	IE	[165]
FEM	Frequency	DE	[52], [61], [68], [69], [73], [110], [136], [157], [163], [166], [167]

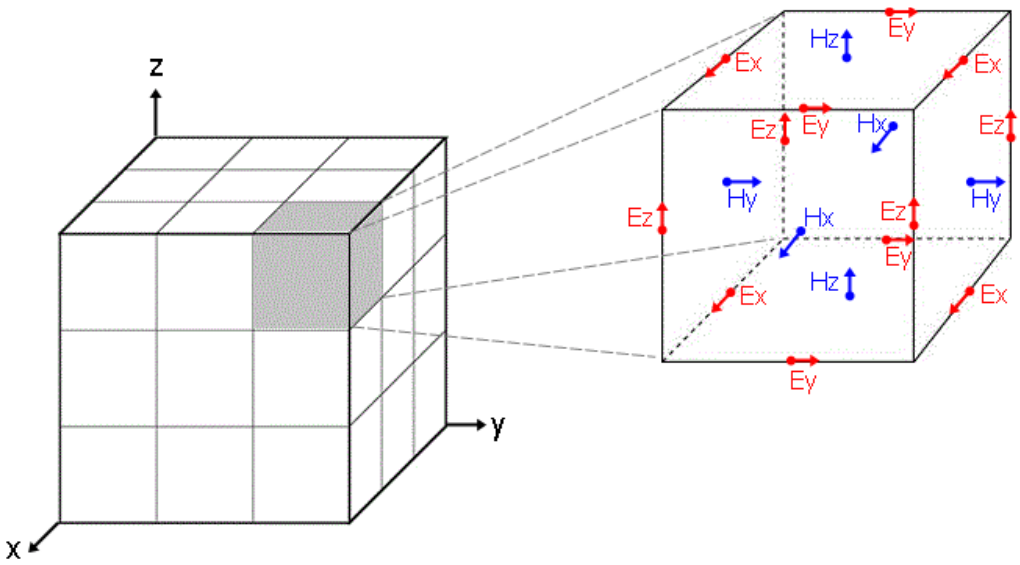

Figure 6. On the left, FDTD tissue segmentation. On the right, unit cell with electric and magnetic fields components used in the Yee FDTD algorithm [159].

FDTD resolution methods use algorithms to calculate the components of electric and magnetic fields in terms of position and time. The process is repeated iteratively until all values of the computational domain are obtained; but since the spatial domain is finite, a method of minimizing the reflection of boundaries at the end of the mesh is required. Thus, several FDTD implementations with absorbing boundary conditions have been presented, and are widely discussed in [168]. The Perfectly Matched Layer (PML), firstly introduced in [169] and widely employed nowadays, presents highly effective suppression of reflections at the boundaries using layers of materials with both magnetic and electric loss.

The FTDT method results in a powerful simulation tool as it can discretize complex 3D structures, obtaining results for the whole volume. This also facilitates the visualization of the propagated fields and the post-processing development.

2.4.2. Considerations of the Modeling Methods

The selection of one method or another depends on several factors, such as the EM software used, the computational resources available, the expertise of the antenna engineer, the kind of application and the tradeoff between accuracy and simulation speed. As shown in Table 7, FDTD is the most popular method, mainly because it can take advantage of the Graphics Processing Unit (GPU) acceleration, thus significantly reducing simulation time when dealing with complex body models.

Meanwhile, the main advantages of FEM are its high efficiency for multi-port applications as it solves all ports in only one simulation, and the highly detailed geometrical modeling, even across curved surfaces. Both FDTD and FEM solvers have the capacity to handle large, complex and arbitrary 3D structures.

The FIT method can be considered as a generalization of the FDTD method with some features of the FEM method. While FDTD has problems handling curved surfaces or highly irregular geometrically detailed boundaries (known as the “staircasing effect”), the FIT method supports advanced meshing features, such as the Perfect Boundary Approximation (PBA), which allow accurate modeling of curved boundaries.

The MoM is not commonly used in the design of antennas for use in the presence of a human body. MoM employs a surface mesh, which is not ideal for the modeling of complex 3D structures such as the human body. However, in the initial steps of the antenna design, MoM may be considered to obtain an initial frequency response, but only if the following two conditions are met: 1) the antenna follows a multilayered structure and 2) the canonical phantom is homogeneous. By evaluating the frequency response of the antenna with MoM, it is possible to save considerable time and resources at the beginning of the design process.

In this thesis, different commercial EM software packages have been used, depending on the application or the design stage: Sim4Life from Zurich MedTech AG [170], based on the FDTD method, have become the most commonly used software for biotelemetry applications in the middle and advanced design stages; Computer Simulation Technology (CST) Microwave Studio [171], based on FIT, has mainly been used for microwave hyperthermia; Advanced Design System (ADS) [172], based on MoM, has been helpfully in the initial steps of the design of multilayer antennas; and EMPro, based on FEM and integrated in ADS, has mainly been employed to verify results and as a bridge between ADS and the other platforms.

From the point of view of the antenna engineer, working with more than one simulation tool increases confidence in the results (for instance, both FEM and FDTD methods are used together in [110], [163]). In addition, in order to save time and computational resources, and depending on the problem characteristics, one method or another may be recommendable. For example, in the initial antenna design step, MoM or FEM methods can be used to obtain a first prototype in a homogeneous phantom, due to the reduced time they require. As the design and the environment become more accurate, FEM, FDTD or FIT emerge as suitable methods because of the implementation of human body phantoms and the possibility of speeding up simulations using GPU-based accelerator technology. In [52], for example, a three-layer tissue phantom is firstly evaluated in FEM and then a voxel model is tested in FIT.

In this thesis, most of the antenna designs for biotelemetry applications are firstly tested and tuned in MoM (through ADS software) and afterwards evaluated in a voxel model based on FIT or FDTD (CST or Sim4Life software, respectively). As already mentioned, the advantages of using several computer programs and numerical methods are, on the one hand, the possibility of comparing the same design through different methods and, on the other hand, the significant reduction in the time and computing resources needed for simulations.

2.5. Human Body Models

The presence of a human body in close proximity to an antenna modifies its performance because, as mentioned before, the near-field strongly couples with the surrounding lossy media. Thus, correct selection of the human model or phantom during the antenna design is crucial for the assessment of an antenna proposed for a certain application. Several models of the human body have been presented and assessed in the literature over recent decades. The work presented by *Ito* [173] summarized some of the most relevant phantoms used for wearable and implantable applications. *Merli* [14] and *Kiourti et al.* [174] present two

extensive reviews of the phantoms used in implantable applications, from simulations to experimental validations. In this section I aim to complement and update those works by presenting a non-exhaustive overview and the state of the art of several aspects that should be taken into account when dealing with human body models, especially for implantable applications.

The selection of one body model or another depends on several factors, such as the target application and the time and resources available. Generally, in the early stage of an antenna design, it is common to choose a theoretical or canonical phantom for two reasons: to save time and computational resources; and to be able to experimentally validate the results with the same model. However, at a more advanced validation stage, realistic or voxel phantoms are required. Simulations in such accurate phantoms must not be underestimated, since small fluctuations in the dielectric properties of the tissues lead to unexpected variations in antenna performance [173].

Dielectric properties of biological tissues are well established worldwide from the work of *Gabriel et al.* [40] in the nineties. They cover a wide frequency range, from 10 Hz to 100 GHz, and are easily available online at [175], [176].

It is difficult to compare antennas presented in different works, as their performance strongly depends on the phantoms used. These models differ in a large number of parameters, such as geometry, size, targeted tissues, number of tissues, accuracy of the model, operating frequency range, placement and orientation of the medical device, and temperature dependency. A review of these parameters and a discussion of their influence on antenna performance is presented below.

2.5.1. Theoretical or Canonical Phantoms

These are mostly used at the beginning of the antenna design process, although they are also utilized for analytical assessment [134], [177], for experimental validation [54], [55], [64], [96], [118] and for comparison of the performance of different antennas in the same scenario. These models can be classified according to the following parameters.

Basic shapes are commonly accepted in the literature to assess antenna performance in a human model. Rectangular cuboids are the most frequent phantom, mainly because they are easy to manufacture for validation purposes [54], [55], [64], [96], [118]. Cylindrical [121], [166], [178], [179] as well as spherical [55], [64], [134], [157], [177], [180] phantoms are widely proposed for a variety of applications, such as to represent the arm [179], the neck [121], the head [55], [64] or the eyeball [157]. For representation of the trunk, ellipsoids are

proposed in [135]. For hyperthermia treatments, semispherical phantoms attempt to simulate breast models [181], [182]. Finally, a combination of various canonical shapes entails a more accurate approach to modeling the whole human body [183]. In [184], a combination of basic shapes is used to model pregnant women.

2.5.1.2. Volume

The phantom dimensions are often selected depending on the application. There is a huge range of sizes of proposed phantoms in the literature, which makes comparison of antenna performance between prototypes very difficult. As can be seen in Table 8, phantom volumes have a wide spread of values, ranging from 37 cm^3 [180] to 14484 cm^3 [96].

Table 8. Properties of in-body antennas and phantoms in the literature.

Ref.	Freq.	Phantom Geometry	Phantom Dimensions (mm)	Phant. Vol. (cm^3)	Implant depth (mm)	Phantom Tissues
[55]	402 MHz	Cube	100x100x100	1000	~50	Skin
[55]	402 MHz	Sphere	100	2356	~50	Skin-Bone-Grey matter
[54]	402 MHz	Cuboid	50x40x20	40	7	2/3 muscle
[81]	402 MHz	Cuboid	60x50x20	60	7	2/3 muscle
[53]	402 MHz	Cuboid	50x100x100	500	1.3-3.8	Skin
[118]	868 MHz	Cuboid	40x80x160	512	5	Skin-Fat-Muscle
[178]	4 GHz	Cylinder	15x40	28.27	10	Average tissue
[179]	402 MHz	Cylinder	50x300	2356	2	Skin-Muscle-Bone
[64]	402 MHz	Sphere	90	1718	~90	6-layer
[64]	402 MHz	Cuboid	Height of 100	-	4	Skin
[94]	402 MHz-2.45 GHz	Elliptic cylinder	180x100x50	900	-	Muscle
[180]	402 MHz	Sphere	12.5	37	~5	Vitreous humor
[108]	402 MHz	Cuboid	50x100x100	500	38.1	Skin
[128]	2.45 GHz	Cuboid	152x152x20	462	8	Saline liquid-Scalp
[60]	402 MHz	Cube	150x150x150	3375	75	2/3 muscle
[185]	402 MHz	Cuboid	150x110x80	1320	15	Muscle
[80]	402 MHz – 2.45 GHz	Cube	100x100x100	1000	3	Skin
[52]	402 MHz	Cuboid	92.5x92.5x39.27	~336	18	Skin-Fat-Muscle
[84]	900 MHz	Cuboid	200x60x54	648	-	Skin-Fat-Muscle
[90]	2.45 GHz	Cuboid	180x60x60	648	4	Muscle
[96]	402 MHz – 2.45 GHz	Cuboid	355x255x160	14484	9	Skin

2.5.1.3. Implant Depth

In the case of in-body antennas, not only the volume but also the implant location is a critical parameter concerning antenna performance. The implant depth determines the amount of lossy tissue through which the EM radiation has to be propagated. The implant depth, as well as the volume of the phantom, varies across a broad range of values, depending on the application (subcutaneous or deep); from 1.3 mm [53] to 90 mm [64]. This also makes comparison between proposed prototypes harder.

2.5.1.4. Orientation of the Implanted Device

Normally, the purpose of an antenna for biotelemetry is to have its maximum gain directed outwards from the body, to improve the communication link. However, the application itself does not always allow the orientation of the antenna to be selected, leading to deterioration of the far-field parameters. In [129], the effect of antenna orientation is considered when evaluating SAR in a brain implant.

2.5.1.5. Frequency Dependence

Dielectric properties of biological tissues change with frequency, as can be seen in Table 9 for the tissues most commonly used in literature [40]. Several analytical models have been developed to match the empirical data. For instance, the well-known Cole-Cole model has been proposed to account for the frequency dependence of the complex permittivity, and can be expressed as:

$$\hat{\varepsilon}(\omega) = \varepsilon_\infty + \frac{\varepsilon_s - \varepsilon_\infty}{1+(j\omega\tau)^{1-\alpha}} + \frac{\sigma_l}{j\omega\varepsilon_0} \qquad (15)$$

where ω is the angular frequency, τ is the mean relaxation time, ε_∞ is the permittivity at field frequencies where $\omega\tau \gg 1$, ε_s is the permittivitty at $\omega\tau \ll 1$, α is a parameter related to the dispersion and σ_l is the conductivity due to ionic drift and polarization processes at lower frequencies [186].

Body phantoms together with frequency dependency should be considered in the design of multiband or wide-band in-body antennas. In [14], [75], two different in-vitro phantoms are considered for the characterization of dual-band antennas. The recent literature tends to use *ex-vivo* phantoms, which have implicit dependence on frequency (see Subsection 2.5.3.2).

Table 9. Dielectric properties of the tissues at different frequency bands [40].

	ε_r			σ (S/m)		
Frequency (MHz)	**403**	**868**	**2450**	**403**	**868**	**2450**
Skin	46.72	41.58	38.01	0.689	0.856	1.464
Fat	5.58	5.47	5.28	0.041	0.05	0.105
Muscle	57.10	55.11	52.73	0.797	0.932	1.739
2/3 muscle	38.07	36.74	35.15	0.531	0.621	1.159
Bone	13.14	12.49	11.38	0.092	0.14	0.394

2.5.1.6. Temperature and Aging Dependence

Despite not having much weight in the usual process of in-body or on-body antenna design, temperature fluctuations and the aging of tissue have a certain influence on dielectric properties. In the work presented in [187], a review of variations in tissue characteristics as a function of the temperature is presented. Meanwhile, as detailed in [188], an analytical expression for evaluating the effect of aging (mainly due to variations in the water content of biological tissues with age) on dielectric properties of tissue is developed. In biotelemetry, the dependency of dielectric tissue properties on both temperature and age are negligible. The study developed in [129] shows the evaluation of an in-body antenna design taking into account age dependency. For thermal treatments, such as microwave hyperthermia or ablation, the inclusion of temperature dependency in phantom models becomes much more relevant.

2.5.1.7. Tissues

Depending on the number of biological tissues included in a theoretical phantom, we can consider them homogeneous or multilayered phantoms. In [40] the dielectric properties of the most representative human tissues are described. For homogeneous phantoms, skin is the most used tissue in the literature [55], [56], [64], [66], [68]–[70], [74], [75], [78]–[80], [85], [89], [136], [179]. However, various works have developed implantable antennas in muscle [90], [94] or 2/3 muscle equivalent tissue [54], [60], [81], [107], [124], [189]. Other tissues have been tested, such as scalp tissue for intracranial pressure sensing [128]. In [113], rat tissue phantoms are employed to simulate the same dielectric properties as in the experimental setup.

Multilayered phantoms are usually constituted of 3 tissues (skin, fat and muscle), as can be seen in [52], [64], [75], [84], [118], [136]. In [117], a comparison between implanted bare straight dipoles in homogeneous and 3-layer tissue phantoms is presented in the ISM bands of 433, 915, 2450 and 5800 MHz. The results show that, in terms of safety requirements, the homogeneous phantom is more conservative (it tends to present more losses). To model specific body parts, other layered models have been proposed. In [135], [179], cylindrical arm models consisting of skin, muscle and bone tissues are studied. In [135], canonical models of head and trunk are also proposed, consisting of a spherical head phantom of skin, bone and grey matter, and an elliptical cylinder trunk model of skin, fat and muscle. In [64], a 6-layer (skin, fat, bone, dura, cerebrospinal fluid and brain) spherical phantom is proposed as a head model. For the modeling of breast tissues, 2-layer (skin and fibroglandular tissue) phantoms are commonly used [181]. Table 8 summarizes some representative prototypes proposed in the literature.

2.5.2. Voxel, Realistic or Anatomical Phantoms

Voxel phantoms are human models that take into account the real geometry and distribution of biological tissues. Medical imaging techniques provide detailed data for the models, which can be employed in simulation software to test antenna prototypes in a more realistic environment than canonical phantoms. One of the first available voxel human models was Hugo, from the Visible Human Project, in 1994 [190] (Figure 7 (a)). Since then, new human body models have been developed, increasing the number of tissues and the resolution. Examples of such novel models are the Japanese male and female [191], the Virtual Family [192] (Figure 7 (b)), consisting of a complete family of four members (a female and male adult, and a female and male child), the Virtual Classroom [193], that includes 2 male and 2 female children, and the CST Voxel Family [171], with 7 members (a 8-week-old female baby, a female child, 3 female adults, 1 pregnant female and 1 male). Table 10 classifies various studies that use realistic human body models.

(a) (b)

Figure 7. Available voxel human models: (a) Hugo, from the Visible Human Project [190] and (b) Duke, from the Virtual Family [192].

Table 10. Realistic human body models used in the literature.

Realistic model	References that use the model
Visible Human Project [190]	[55], [86], [121], [194]–[197]
Japanese male and female [191]	[173], [194], [198]
Virtual Family [192]	[14], [62], [76], [111], [199], [200]
CST Voxel Family [171]	[48], [63], [64], [75], [81], [159], [173], [174]
SAM phantoms	[194], [203], [204]
Realistic breast phantoms [205]	[206]–[208]

Modeling a specific part of the human body is a common practice, especially when dealing with on-body devices, such as mobile phones, microwave hyperthermia applicators or microwave imaging. For these purposes, phantoms that provide tissue information concerning the targeted part are required. For instance, Specific Anthropomorphic Mannequin (SAM) phantoms are widely utilized for SAR assessment of mobile phones [194], [203], [204]. SAM phantoms are modeled by a shell filled with a liquid mimicking the average of the dielectric properties of the head tissues. For breast cancer treatment via microwave hyperthermia, realistic voxel breast models developed by *Zastrow et al.* at the University of Wisconsin have been tested [205] (Figure 8 (a)). These models represent different types of breast classified by the American College of Radiology, from dense breasts corresponding to younger women to the fatty breasts of elder women.

Current research in this field focuses on enhancing personalized medicine by developing patient-specific body phantoms. Recent advances in commercial EM solvers provide integrated modules that allow the reconstruction of 3D human models from medical magnetic resonance imaging data (MRI) or computer tomography scans. Two examples are the Medical Image Segmentation Tool Set (iSEG) [209] available for integration with the in Sim4Life [170], and the ALBA 3DSeg module [210], developed together with CST [171]. Reconstruction of 3D human models improves patient-specific simulations in a real WBAN scenario.

Another important development in realistic phantoms is the possibility of changing their postures [171], [211], [212], as shown in Figure 8 (b). This feature permits analysis of variations in antenna performance depending on the movement, as in the work in [213], where the influence of the hand position on head SAR in mobile phones is presented.

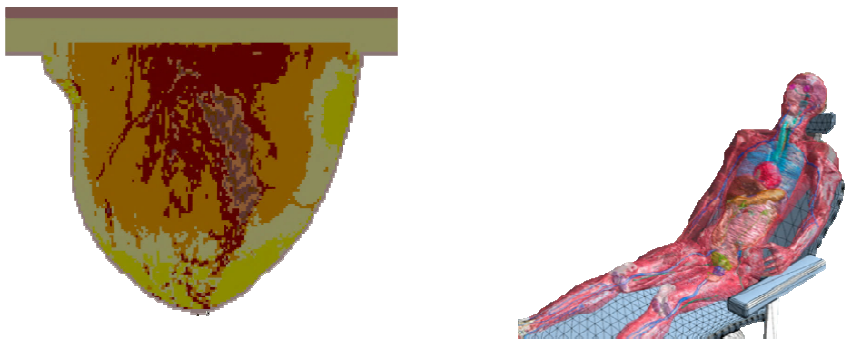

(a) (b)

Figure 8. Anatomical phantoms: (a) Voxel breast model used in microwave hyperthermia [208] and (b) POSER module from ZMT Zurich MedTech AG [211].

2.5.3. Experimental Phantoms (*In-vitro, Ex-vivo* and *In-vivo* Testing)

Experimental phantoms present a higher level of complexity than simulated phantoms due to the manufacturing or preparation process. They include both physically manufactured models and animal tissue phantoms.

2.5.3.1. *In-vitro* Testing

For experimental validation, canonical shields filled with homogeneous lossy medium are the most common phantoms in the literature, especially in implantable applications (see Figure 9). Existing solutions of canonical liquid- or gel-based phantoms are classified in Table 11.

Solid phantoms have also been proposed in several works for on-body antenna testing, such as in [173]. The Posable Phantom for Electromagnetic Systems Evaluations (POPEYE) developed by Schmid & Partner Engineering AG (SPEAG) [214] is a whole body model that allows modification of the limb positions, and covers a frequency range from 300 MHz to 6 GHz (Figure 10). These phantoms, together with other models like SAM head phantoms [215], provide practical solutions for RF dosimetry.

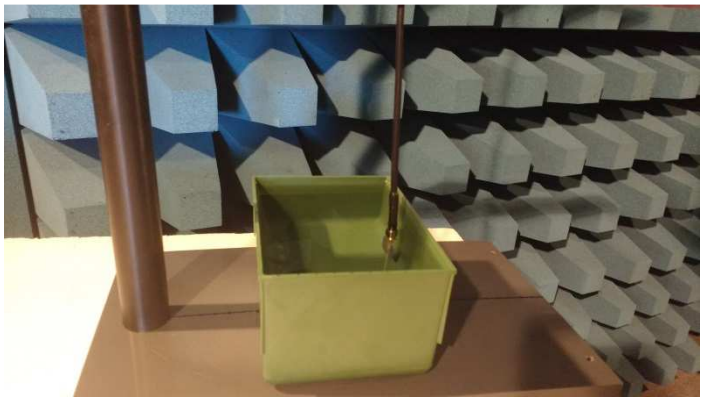

Figure 9. Liquid phantom mimicking muscle tissue.

Table 11. Typical experimental canonical phantoms found in literature.

Medium of the canonical shield	References
Liquid	[53]–[55], [64], [96], [108], [113], [114], [179], [185], [189], [216]
Gel	[75], [128]
Multilayer	[118], [217], [218]

(a) (b)

Figure 10. Human body models for experimental validation: (a) whole body phantom POPEYE with movable limbs developed by SPEAG [214] and (b) SAM head phantom also developed by SPEAG [215].

The major drawbacks of physically manufactured phantoms are the complexity of developing a heterogeneous model, with complex structures inside (organs or bones), and coverage of the dielectric properties of the biological tissues over a wide frequency range. Low-cost manufactured canonical and homogeneous phantoms developed in this thesis are detailed in Chapter 5. The characterization of manufactured phantoms is also addressed.

2.5.3.2. *Ex-vivo* Testing

Ex-vivo tissues have been tested in various medical applications, such as microwave hyperthermia [219] and microwave ablation [220], as well as in implantable biotelemetry [73], [80], [84], [86], [94], [98], [113], [151], [164]. A classification of animal tissues employed in the literature is presented in Table 12. An example of pork meat used in thermal ablation is illustrated in Figure 11 [207].

Table 12. Ex-vivo testing found in the literature.

Animal tissue	References
Minced meat	[151]
Minced pork	[73], [80]
Piece of pork	[94], [220]
Porcine abdominal tissues	[164]
Porcine eye	[98]
Rat skin	[84], [113]
Chicken breast	[219]

2.5.3.3. *In-vivo* Testing

Various studies have investigated the implantation of in-body antennas in living animals to achieve more realistic scenarios in their validation tests. For instance, in [221], a data telemetry biomedical experiment is reported in which temperature monitoring of living pigs is performed. In the work presented in [125], porcine test subjects are also evaluated when a cardiovascular stent with wireless biotelemetry is implanted in the pulmonary artery. Another *in-vivo* study is carried out in [126], where an intracranial pressure device is implanted in dogs. Rats are chosen in the studies presented in [104], [112], [222].

According to [104], the objective of *in-vivo* testing is to assess the factors that influence measurements in a surgical procedure: the appearance of air gaps between the implanted prototype and the surrounding tissues; the multiple tissues around the antenna and their frequency-dependent behavior; and the variability between test subjects and among surgical procedures.

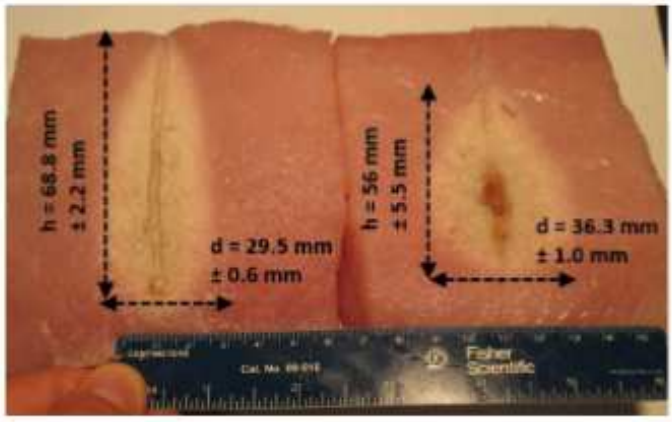

Figure 11. Implantable antenna tested for microwave ablation [220].

2.6. Conclusions

In this chapter, I have presented a detailed review of the theoretical aspects and challenges involving interaction between antennas and the human body. Changes in antenna performance in the presence of a human body have been discussed. An analysis of the current state of the art for antennas working in biotelemetry has been carried out, with special emphasis in the strategies reported in the literature to overcome the main challenges in the design of such antennas:

- *Miniaturization:* Multilayer PIFA designs are good candidates in terms of size and efficiency.

- *Biocompatibility:* Ceramic biocompatible materials like LTCC substrates show suitable dielectric properties, with high permittivity and low losses.
- *Operating frequency:* Depending on the application, different frequencies have been selected in the literature. The frequency detuning caused by the presence of biological tissues is one of the aims in the design of broadband antennas.
- *Antenna performance:* Radiation pattern and efficiencies vary significantly in proximity with biological tissues.
- *Powering:* Despite the internal power supply being the most commonly used powering method, new trends in energy harvesting or passive technologies (such as RFID) are gradually appearing.
- *Packaging:* The size of the whole device is normally increased when placing circuits or batteries in the antenna. An efficient integration between the antenna and the electronics is desirable.
- *Antenna modeling:* A tradeoff between the accuracy of results and resources required has to be taken into account when modeling the antenna and its surrounding medium. Using more than one EM software package can be considered, depending on the design stage, to increase confidence in the results.
- *Antenna fabrication:* The manufacturing process leads to inaccuracies that can severely affect antenna performance. Integration technologies, such as LTCC, allow multilayered structures in compact monoliths.
- *Antenna characterization:* Due to the presence of unwanted radiated and dissipated fields when connecting a coaxial cable with implantable antennas, some considerations have to be taken into account in the measurement setup.

Apart from these issues, I have also presented the modeling of phantoms and human bodies used in both computational tools and experimental validation. The literature shows a huge variety of dimensions, shapes, materials and realism of phantoms, which depend on several factors, like the placement of the antenna in the body, accuracy requirements or the computational tools available.

3. Analysis of In-body Antenna Miniaturization

3.1. Introduction

As mentioned in Chapter 1, the next two chapters focus on the analysis of in-body antennas for biotelemetry.

Although much work has already been done in the field of in-body antennas, there are still many open questions and technological challenges that need to be addressed (see Section 2.3). Antenna miniaturization is one of these, mainly because of the reduced space available inside the body, and with the objective of increasing patient comfort and also to facilitate the placement process. In this chapter, new in-body antennas are developed with the aim of improving the ratio between efficiency and antenna volume. Several features are analyzed to compare different in-body antennas, such as 2D and 3D-square spirals, meander antennas and fractal designs. The proposed prototypes are based on LTCC technology, which allows the integration of 3D electronics and therefore the enhancement of the miniaturization when designing an antenna.

As referred to in Subsection 2.3.1, patch designs have mainly been proposed for implantable antennas and different miniaturization techniques can be applied to them. From two reference works, [54], [64], to the present, many authors have proposed specific designs from 2D geometries to vertically stacked radiators [60], [68], [75], [78], [79], [108], [114], [223]. PIFAs and spiral-type radiators are generally used to reduce the total antenna size.

We know that miniaturization degrades gain [224]: high-gain antennas are relatively large. Moreover, these in-body antennas are designed to operate in lossy media, so the communication link is one of the major challenges [152]. Implantable antenna should provide a signal that is strong enough to be picked up by the external device, regardless of power limitations.

Previous studies have mainly focused on designing and characterizing the features of final miniaturized prototypes. In this chapter, my main goal is to compare several miniaturization techniques in terms of efficiency and gain, by decreasing the volume step by step. I analyze radiation efficiency degradation as a function of size reduction. The objective is to quantify the effect of the miniaturization process on the achievable efficiency and communication link capabilities.

To sum up, the main objectives of this chapter are:

- To present a preliminary study of in-body PIFAs based on LTCC technology.

- To assess the miniaturization process of square spiral PIFA designs in terms of efficiency.
- To propose a final suitable PIFA design in terms of size and efficiency.
- To compare the final design with other miniaturized methods and designs.

The experimental validation of the most relevant designs presented in this chapter will be addressed in Chapter 5.

3.2. Methodology

For the analysis carried out in this chapter I used Sim4Life: a commercially available EM simulator software package based on the FDTD method (see Section 2.4). The proposed antennas were embedded inside an LTCC dielectric substrate (ε_r=6.6 and σ=0.0003 S/m).

3.2.1. Preliminary Parameterization Assessment

In this section, a first antenna design is proposed, based on the work of *Kim et al.* presented in [64]. This initial 2D square spiral PIFA was chosen as the first step due to its simplicity and its potential to be miniaturized. Firstly, geometric parameters were retuned according to the different electrical parameters of the LTCC substrate and the homogenous canonical cubic phantom selected (Table 13), resulting in the design presented in Figure 12.

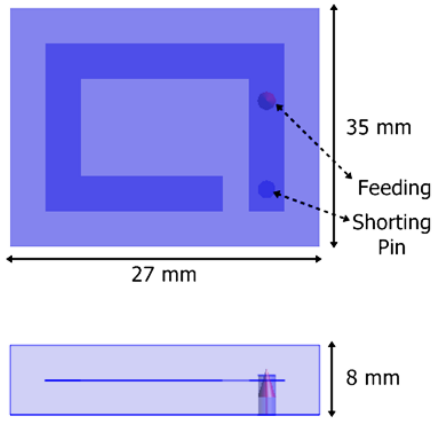

Figure 12. Antenna presented in [64] retuned according to the LTCC substrate parameters.

Table 13. Electrical parameters of the original work [64] and the design in Figure 12.

Antenna prototype		Permittivity	Conductivity
***Kim et al.* [64]**	Substrate	10.2	-
	Phantom	49.6	0.51
Retuned design (Figure 12)	Substrate	6.6	0.0003
	Phantom (skin)	46.71	0.689

In order to enhance the antenna features, a parametric study of the model was carried out. Several elements of the model, such as the phantom and substrate dielectric properties, the substrate dimensions and radiator features, were modified to assess their incidence on antenna performance and eventually to achieve a suitable and efficient miniaturized prototype. The reflection coefficient (S_{11}) and the radiation efficiency (in %) were identified as the main features to be optimized. In certain cases, bandwidth was also assessed.

3.2.2. Miniaturization Process

Antenna efficiency degradation was analyzed as a function of design and size. The antenna design from Figure 12 was taken as the starting point for the miniaturization study. In order to take advantage of the technology used and also to enhance the available space for other electronic components, the radiator width was changed from 4 mm to 1 mm, resulting in the design presented in Figure 13 (a). This antenna was named the "Reference Antenna" (RA). The bottom layer is the ground plane. The main radiator is located in the middle of the substrate. From this RA design, 2D and 3D miniaturization techniques were applied to obtain more compact antenna prototypes (Figure 13 (b) and (c)). At the same time, I evaluated the degradation of antenna efficiency.

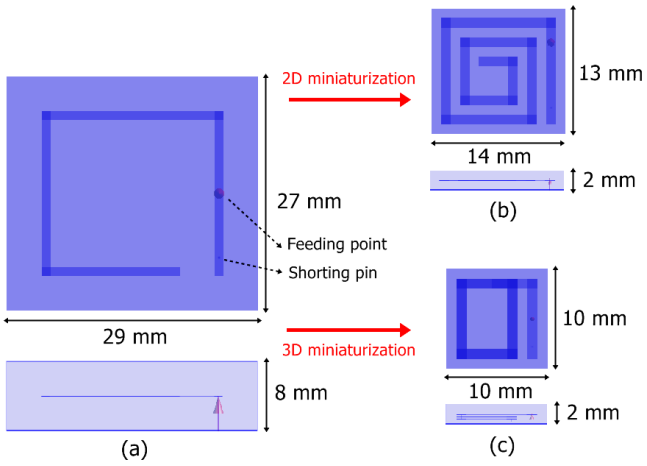

Figure 13. Top and side profile views of the PIFA prototypes: (a) reference antenna (RA), (b) final shape of the 2D miniaturization (2D-square spiral) and (c) final shape of the 3D miniaturization (3D-square spiral).

The design constraints selected to define the size of the miniaturized final prototypes were a tradeoff between the feasibility, reproducibility and manufacturing capabilities of the available technology. The manufacturing limitations led to a distance of 1 mm between metal lines in the same layer, and a substrate thickness of 2 mm; whereas metal layers in 3D designs are separated by at least 0.2 mm.

The antenna prototypes were tested located in the middle of a cubic skin phantom with edges of 100 mm. This phantom size was chosen for comparison purposes, in accordance with previous studies [174]. The dielectric properties of the phantom are provided by Sim4Life and are based on previous data reported in the literature by *Gabriel et al.* [40]. In the next chapter, several considerations concerning the use of different phantoms and implant depths will be treated in detail. The proposed implantable antennas and an external half-wavelength dipole antenna at a distance of 50 cm were used to build the communication link.

3.3. Results and Discussion

In this section, I present and discuss the results of the preliminary study and the miniaturization processes. Then, I compare the 2D and 3D miniaturization approaches in terms of efficiency and size, to eventually present the most suitable prototype.

3.3.1. Preliminary Study

The reflection coefficient of the retuned antenna presented in Figure 12 is plotted in Figure 14, showing an operating frequency in the MedRadio band (402 MHz) and a bandwidth of 19.8 MHz. The width and height of the radiator from the ground plane are both 4 mm, and this is also the distance between the radiator and the edges of the substrate.

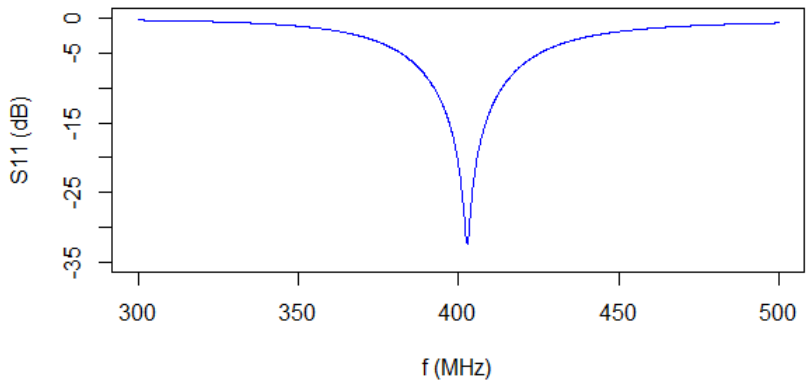

Figure 14. Reflection coefficient of retuned antenna (Figure 12).

3.3.1.1. Parameterization of the Dielectric Properties of the Phantom

To assess the radiation properties of the model in a realistic environment, a mimicking phantom has to be selected according to the application. However, it has to be taken into account that variations in the dielectric properties of the phantom lead to variations in the antenna features. A 100 mm cubic and homogeneous phantom was selected in this first approach. This is a usual first step in the process of implantable antenna design, as can be observed in the literature (see Subsection 2.4.1).

Figure 15 and Figure 16 show the modifications of the reflection coefficient and the efficiency when the relative electrical permittivity is changed (from 30 to 70) and so is the conductivity (from 0.1 to 2 S/m) of the phantom, respectively. As expected, increasing the permittivity leads to a slight shift to lower frequencies (a difference of up to 14 MHz between ε_r=30 and ε_r=70), while the efficiency increases linearly with a slop of 0.0035. There are no significant changes in the bandwidth. Incrementing the conductivity produces small variations to lower frequencies, while the bandwidth is considerably expanded from 0 to 23 MHz (Figure 17). As introduced in detail in [134], the enlargement of the bandwidth is more closely related to the losses in the surrounding medium than to profitable power radiated out of the cubic phantom. Thus, the efficiency decreases exponentially with the rise of the conductivity (from 0.3% at σ=0.5 S/m to 0.05% at σ=2 S/m), as shown in Figure 16 (b).

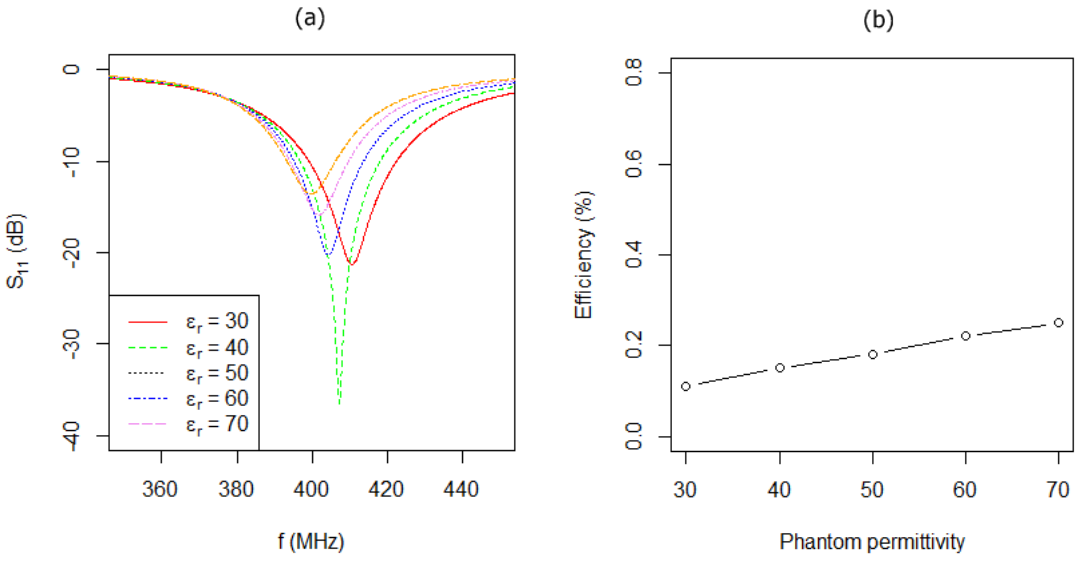

Figure 15. Phantom permittivity parameterization: (a) S11 and (b) efficiency.

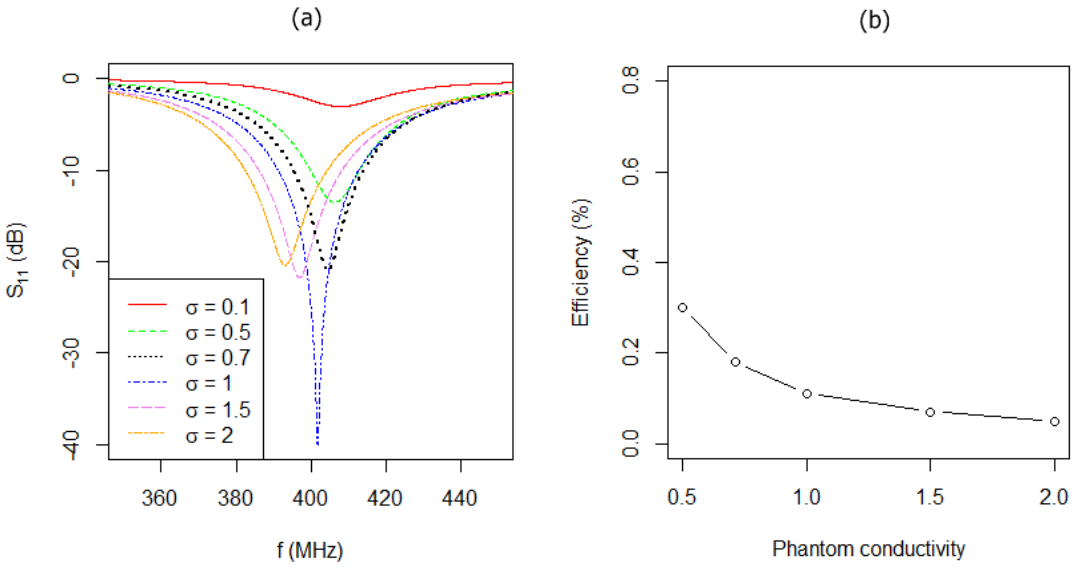

Figure 16. Phantom conductivity parameterization: (a) S11 and (b) efficiency.

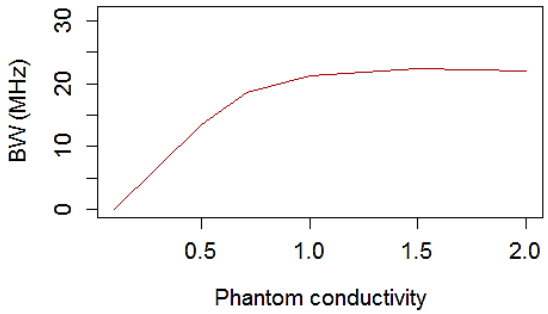

Figure 17. Bandwidth enhancement due to the increase in phantom losses.

3.3.1.2. Substrate Parameterization

The influence of the electrical properties and the substrate dimensions on the antenna features is presented here.

Substrate Dimensions

I analyzed the efficiency enhancement as a function of the substrate dimensions. First, the substrate size was augmented in all directions. Taking the initial values for the parameters defined in Figure 18 (x=35 mm, y=8 mm, $y1$=$y2$=4 mm, z=27 mm), a gradual increment of d=2 mm (from 0 to 6 mm) for x, y and z was applied. As expected, the results shown in Figure 19 indicate a rise in efficiency (up to an increment of 0.2%). The main reason for this behavior is the substitution of a certain volume of lossy phantom medium with substrate material, with lower permittivity and conductivity.

The influence of the relative position of the radiator with regard to the ground plane was also evaluated by changing *y1* and *y2* separately (*dy1* and *dy2* respectively) (Figure 18 (b)). The results shown in Figure 20 indicate that increasing only *y2* tends to increase the efficiency (up to an increment of 0.4%).

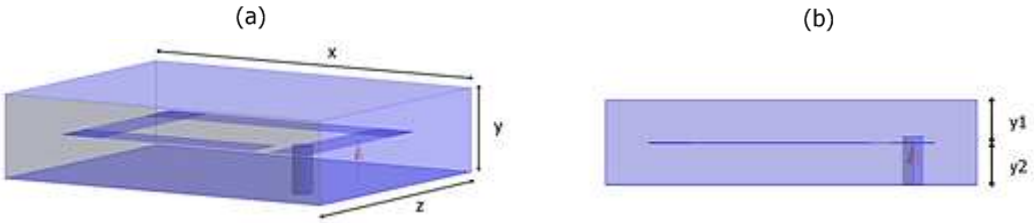

Figure 18. Substrate parameterization: (a) 3D dimensions and (b) substrate height.

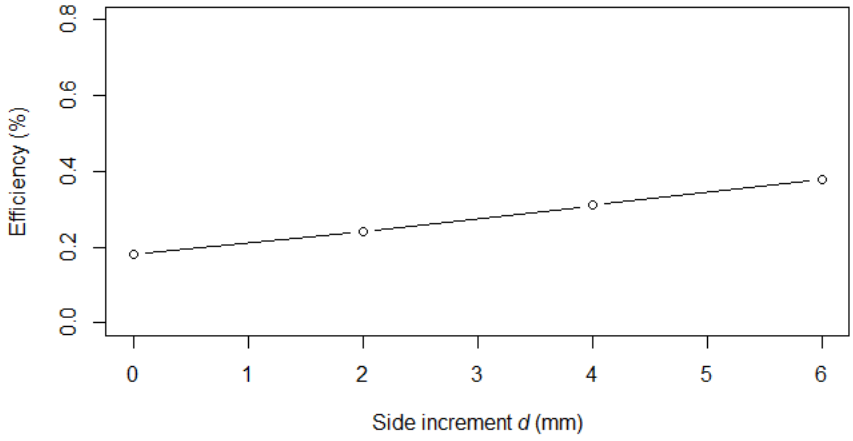

Figure 19. Efficiency as a function of the substrate size increment.

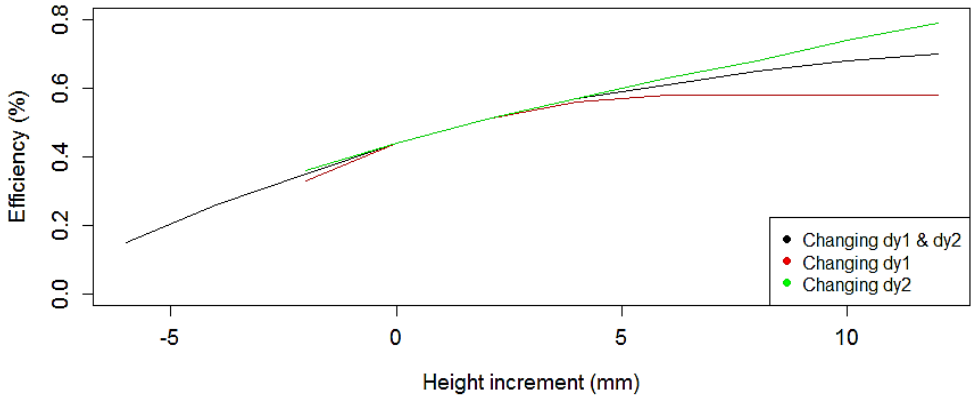

Figure 20. Efficiency as a function of the substrate height increment.

In Subsection 3.3.3, the idea of increasing the efficiency by separating the radiator from the ground plane is treated in more detail, to achieve suitable 3D miniaturization techniques.

Substrate Dielectric Properties

Figure 21 shows the variation in the reflection coefficient when the electrical properties of the substrate are changed in a range close to the nominal values. The working frequency shifted to higher values with lower substrate permittivities (a variation of 33 MHz, as seen in Figure 21 (a)), while the efficiency variations were not significant. In contrast, increments in substrate losses led to slightly wider bandwidths (Figure 21 (b)) but lower efficiencies.

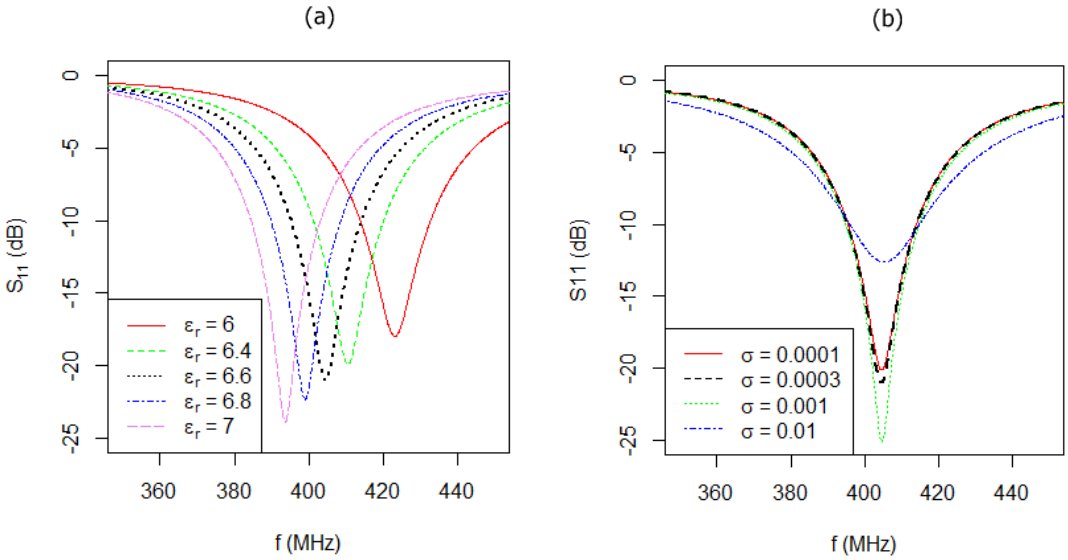

Figure 21. Parameterization of (a) substrate permittivity and (b) substrate conductivity.

3.3.1.3. Radiator Parameterization

Several radiator parameters were modified to obtain in-depth understanding of the EM behavior of the antenna. The main objective here was to take advantage of the possibilities offered by the multilayer LTCC technology and find the most efficient profile. In this subsection, only the most effective parameterizations performed are discussed

Radiator Width

The initial prototype had a radiator width of 4 mm, as noted in Figure 22 (a). Reducing the total radiator surface provides more space in the substrate to integrate additional components, as illustrated in Figure 22 (d). However, a thinner radiator produces greater current concentrations in the antenna, which leads to a bandwidth reduction, as described in [49]. So, in the model with the thinner radiator, the bandwidth was reduced from 19.8 to 12.1 MHz. Moreover, in order to match the operating frequency in the MedRadio band, the radiator length was shorter, keeping the efficiency at 0.45 (with the antenna implanted in the middle of a 100 mm cubic phantom) (Table 14).

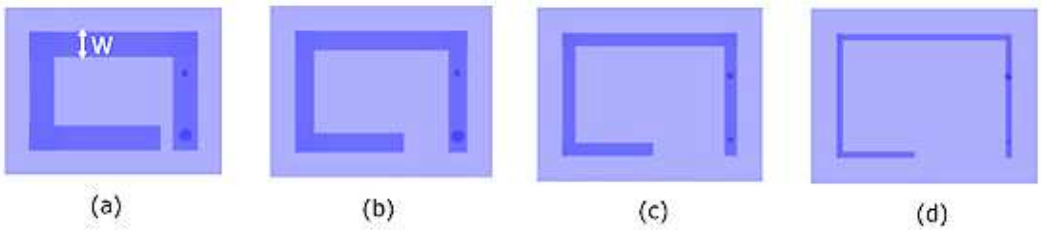

Figure 22. Radiator width W parameterization: (a) 4mm, (b) 3mm, (c) 2mm and (d) 1mm.

Table 14. Antenna characteristics of prototypes with different radiator width W.

Rad. width W	Rad. surface (mm^2)	BW (MHz)	Efficiency (%)
4 mm (Figure 22 (a))	344	19.8	0.45
1 mm (Figure 22 (d))	77 (-77.6%)	12.1 (-38.9%)	0.45

3D Spiral

Another way to take advantage of the LTCC properties is to convert the surface radiator into a 3D spiral radiator, thus reducing the antenna volume while maintaining the operating frequency at the MedRadio band. Nevertheless, the efficiency will inevitably worsen due to the reduction of the total effective volume of the antenna, from 7650 to 2584 mm^3. Figure 23 illustrates the profile of this new shape, showing three radiator layers from the top of the antenna to the ground plane. In Table 15, the distance between these layers is analyzed, and it presents similar efficiencies in all cases. Compared to the original prototype, this configuration has approximately half of the initial efficiency because of the size reduction.

Figure 23. Parameterization of the distance between metallic layers.

Table 15. Efficiency of the variations in distance D between layers.

d1 (mm)	d2 (mm)	d3 (mm)	Efficiency (%)
1	1	2	0.21
1.3	1.3	1.3	0.2
2	1	1	0.22

Radiator Ending

As the last strip of the radiator stores a great amount of electric charge (Figure 24), its relative position could have an impact in the EM behavior of the model. Figure 26 shows the efficiency as a function of the distance between the last strip and the feed, as depicted in Figure 25. Despite lower variations being obtained, the most efficient model was that illustrated in Figure 26 (b), where the last strip is located inside the spiral at a distance of 1 mm from the feed strip.

According to the idea that the position of the last strip of the radiator influences the radiation features, four different endings were proposed, as shown in Figure 27, to establish the best location for the last strip. Although there were no significant differences, the results shown in Figure 28 indicate that the 3D square spiral has the best efficiency when the radiator finishes at the top-left corner of the substrate (Figure 27 (d)).

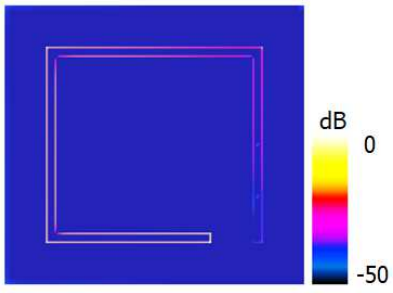

Figure 24. Electric charge distribution in the radiator of the RA prototype. Electric charge is concentrated at the end of the radiator.

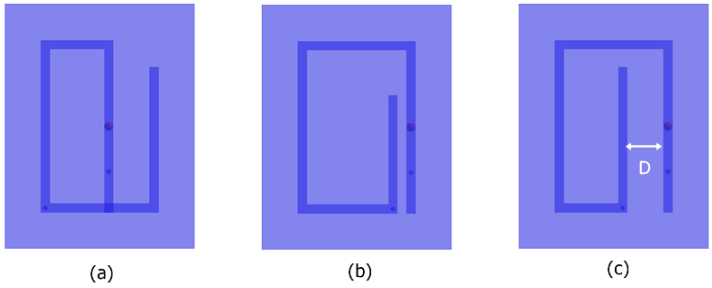

Figure 25. Parameterization of the distance D between the feed strip and the last radiator strip: (a) -4mm, (b) 1mm and (c) 4mm.

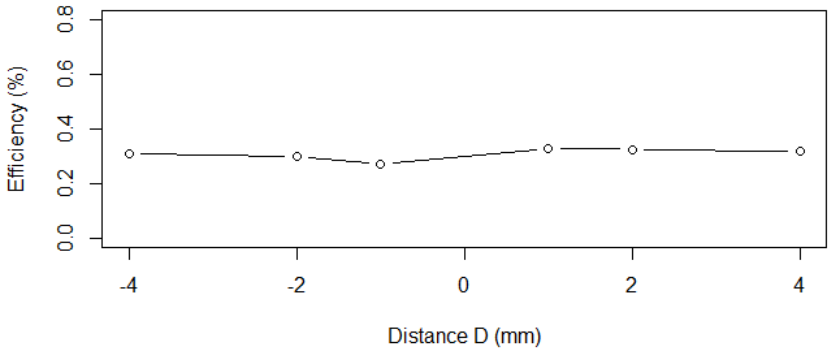

Figure 26. Efficiency as a function of the distance D between the feed and the last strip.

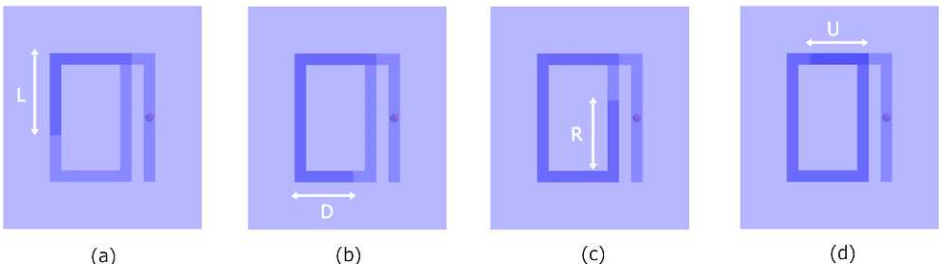

Figure 27. Parameterization of the location and the length of the last strip.

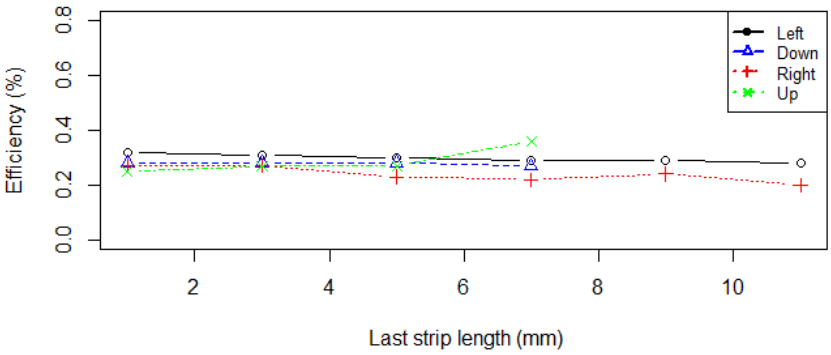

Figure 28. Efficiency as a function of the last strip length and location.

3.3.2. Analysis of the Miniaturization Process

3.3.2.1. The 2D Miniaturization

In the 2D miniaturization case, the RA was miniaturized by folding the radiator into a square spiral, a square meander and a fractal structure. In order to illustrate the steps in the 2D square spiral miniaturization process, 8 antenna designs were selected. Their planar geometries and cross-sections are shown in Figure 29. The first antenna (a) was the RA. The length, width and thickness were then gradually decreased. The nomenclature used is "2D_thickness_case", so 2D8a stands for a 2D miniaturized antenna that is 8 mm thick, with a specific length and width.

Table 16 details the dimensions and the efficiency results for each step in the antenna design. In this case, the implants were placed in the middle of a cubic phantom with edges of 100 m. There was a nearly linear relation between volume and efficiency, regardless of which geometrical dimension (L, W or H) was varied. The smallest prototype using this 2D miniaturization has a volume of 364 mm^3, achieving a size reduction of 94.2% with respect to the reference antenna.

To corroborate this nearly linear relationship between antenna efficiency and antenna volume, the relative efficiency of the antennas (in % of RA efficiency) are plotted in Figure 30. It can be observed that the efficiency decreases by a factor of about 10 when the volume decreases by a factor of about 20.

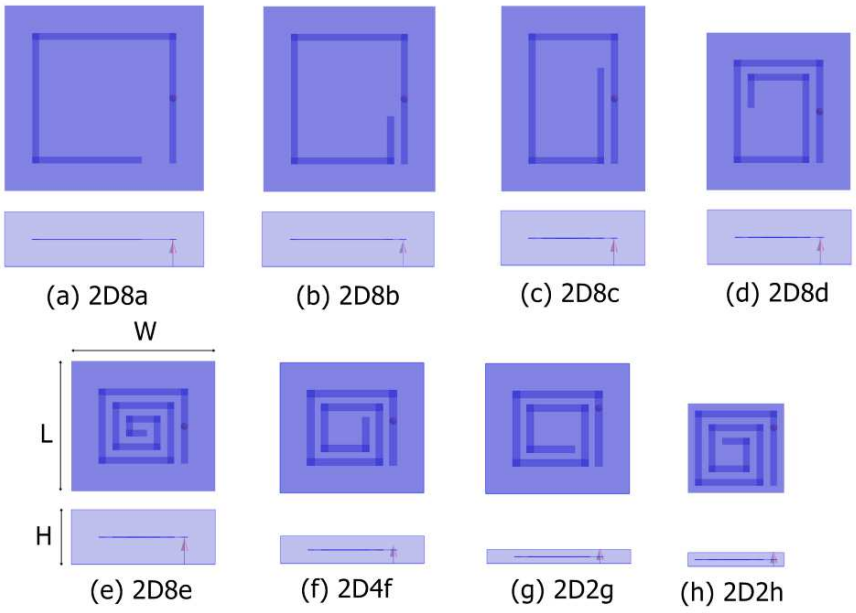

Figure 29. 2D miniaturizing process for the square spiral prototype.

Table 16. Dimensions and efficiency of the antenna prototypes shown in Figure 29.

Antenna prototype	Length (mm)	Width (mm)	Height (mm)	Volume (mm^3)	Efficiency (%)
2D8a (RA)	27	29	8	6264	0.39
2D8b	27	25	8	5400	0.36
2D8c	27	21	8	4536	0.31
2D8d	23	21	8	3864	0.27
2D8e	19	21	8	3192	0.21
2D4f	19	21	4	1596	0.10
2D2g	19	21	2	798	0.059
2D2h (2D-square spiral)	13	14	2	364	0.045

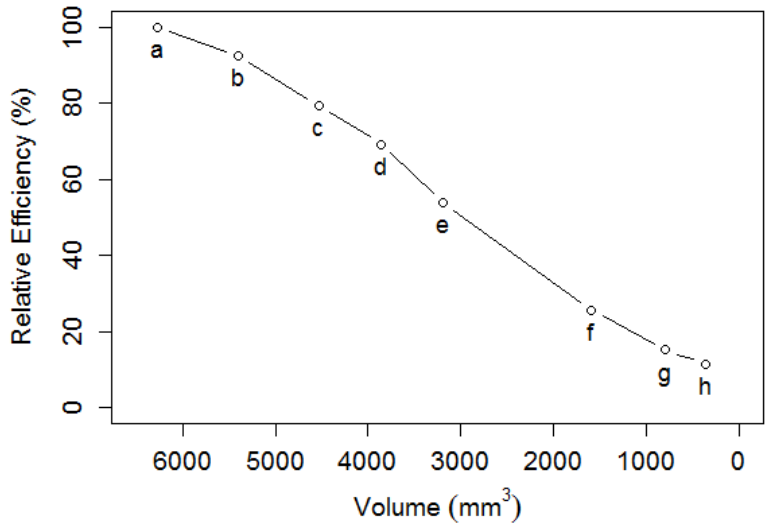

Figure 30. Relative efficiency of 2D miniaturized prototypes from Figure 29 as a function of volume.

The behavior of meander PIFAs was studied in [53], [57]. The main conclusion of those studies were that nearby conductors with currents flowing in the opposite direction lead to an increase in the resonant frequency, requiring an increment in antenna size to retune it to the desired frequency band. Consequently, the efficiency of the antenna also drops, due to the need for additional miniaturization. Figure 31 shows the vector direction of the electric current density in the meander and 2D2h prototypes. While in the 2D-square spiral antenna (2D2h) the parallel and nearby conductors have the same vector direction, in the meander antenna the vectors are sometimes in opposing directions. Moreover, although the resonant frequency is the same, the radiator lengths vary from 73 mm for the 2D-square spiral to 82 mm for the meander antenna.

Table 17 summarizes the variation of volume and efficiency for the meander and 2D2h designs, with respect to the reference antenna (RA).

Fractal geometries have also been proposed in the literature for miniaturization purposes [225] and for IMD [226]. Studies indicate that fractals present lower efficiencies due to the antiparallel vector currents of some of their sections. In my study, several fractal-based PIFAs were developed in LTCC technology for comparison purposes (Figure 32). The dimensions are given in Table 18.

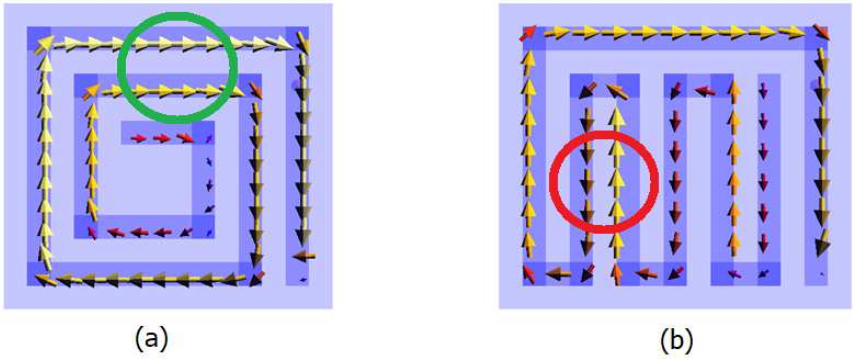

Figure 31. Vector direction of the electric current density of 2D miniaturized prototypes: (a) spiral (2D2h antenna) and (b) meander or serpentine antenna. Circled in green, parallel currents; circled in red, anti-parallel currents.

Table 17. Far-field features of the 2D miniaturized designs compared with RA.

Antenna prototype	**Volume (mm^3)**	**Efficiency (%)**
2D8a (RA)	6264	0.39
Meander	390	0.043
Variation	*-93.8%*	*-89%*
2D2h (square spiral)	364	0.045
Variation	*-94.2%*	*-88.5%*

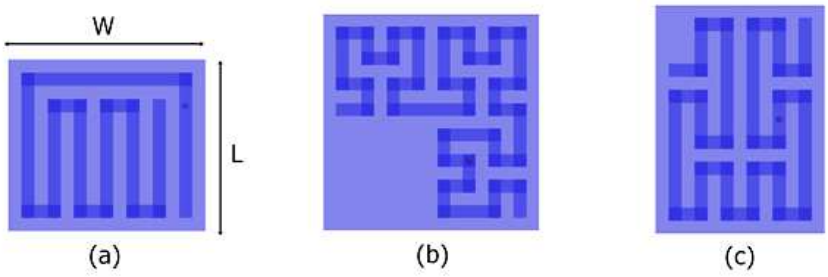

Figure 32. 2D miniaturized designs: (a) meander, (b) Hilbert fractal and (c) Peano fractal.

Table 18. Dimensions of the proposed 2D miniaturized prototypes.

	RA	2D-meander	2D-Hilbert	2D-Peano	2D-square spiral
Volume (mm^3)	6264	390	578	455	364
L×W×H (mm)	27×29×8	13×15×2	17×17×2	17.5×13×2	13×14×2

3.3.2.2. 3D Miniaturization

Many similar antennas with small variations were designed in this study to analyze and quantify the 3D miniaturization process. The starting point was the 2D PIFA called RA. The length, width and thickness were gradually decreased, and the radiator was folded into a 3D spiral. Two main 3D spiral miniaturization approaches were studied, as shown in Figure 33. In the first, the radiator was folded towards the ground plane (3D-down). In the second, the radiator was folded in the opposite direction (3D-up). The main goal of folding the radiator in a 3D structure was to further increase the degree of miniaturization given by the 2D procedure, while maintaining good far-field features.

In the 3D-down approach, the radiator is further away from the lossy medium. Accordingly, most of the near field is located in the almost lossless substrate, instead of the lossy medium. This procedure leads to an increase in the radiation power [134]. In turn, the 3D-up approach provides more internal space for future embedding of integrated electronic circuits, which opens up the opportunity of more compact modules. The selection of one or other approach depends on the application.

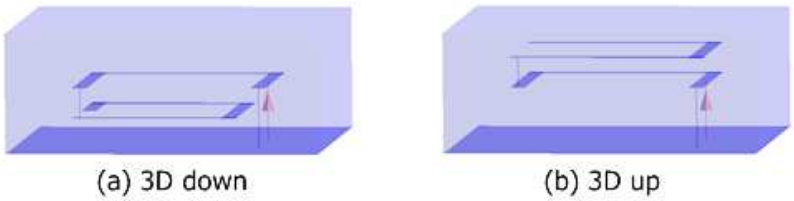

Figure 33. Two 3D miniaturization methods: towards the ground plane ((a) 3D-down) and in the opposite direction ((b) 3D-up).

In accordance with the previous discussion, 4 different 3D cases were considered (down1, down2, up1 and up2) as shown in Figure 34. In 3D-down1 and 3D-up2, the end of the radiator is located in the middle of the substrate. Consequently, the gap between the radiator and the phantom is always constant. In contrast, in 3D-down2 and 3D-up1, the gap between the radiator end and the ground plane is kept constant. The position of the gap could be relevant in terms of efficiency and when inserting electronic components.

Following the method used for the 2D miniaturization, different designs for each case were selected to illustrate the 3D miniaturization process. As an example, designs of the 3D-down1 case are depicted in Figure 35. Table 19 shows the corresponding efficiency results for these cases together with the dimensions.

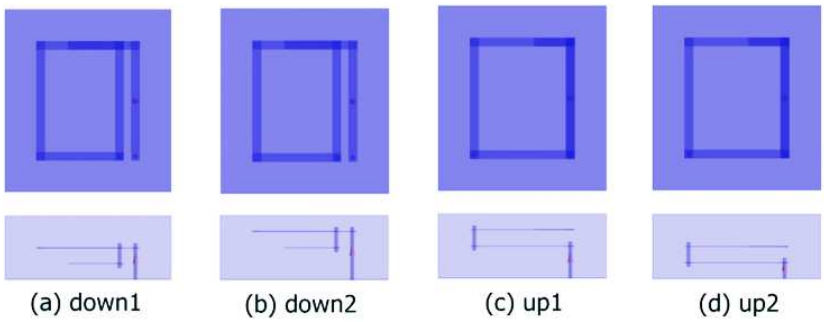

Figure 34. Two spiral miniaturization methods: towards the ground plane ((a) 3D-down1 and (b) 3D-down2), and in the opposite direction ((c) 3D-up1 and (d) 3D-up2).

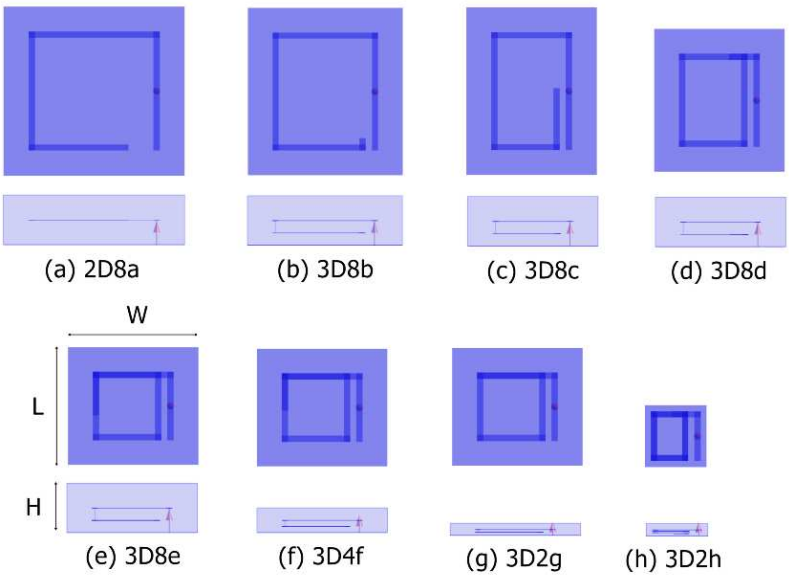

Figure 35. Example of the planar geometry and cross section of the selected antennas for the 3D-down1 configuration.

Table 19. Dimensions of the antenna prototypes shown in Figure 35.

Antenna prototype	Length (mm)	Width (mm)	Height (mm)	Volume (mm^3)	Efficiency down1 (%)
2D8a (RA)	27	29	8	6264	0.39
3D8b	27	25	8	5400	0.37
3D8c	27	21	8	4536	0.33
3D8d	23	21	8	3864	0.3
3D8e	19	21	8	3192	0.26
3D4f	19	21	4	1596	0.12
3D2g	19	21	2	798	0.07
3D2h	10	10	2	200	0.05

A detailed view of the layer-by-layer configuration of the smallest prototype (3D2h) is displayed in Figure 36. Since it is a PIFA, a shorting pin can be observed between the ground plane and the top layer. The radiator starts from the middle of the substrate, in the top layer, and is folded towards the ground plane using 4 layers connected by vias.

The efficiency results for the 4 configurations (down1, down2, up1 and up2) with 4 different antenna prototypes per configuration are shown in Figure 37. For comparison purposes, the results of the 2D miniaturization are also plotted in the same figure. As expected, in all cases, the efficiency monotonically decreased as the volume was reduced. However, one configuration outperformed all the others. By comparing the results, I can conclude that 3D-down1 is the most suitable configuration in terms of efficiency. As previously mentioned, in this configuration the near field is concentrated inside the lossless substrate, which minimizes energy dissipation in the surrounding lossy medium. This results in the better efficiency of this configuration. The same behavior can be seen in the 3D-up miniaturization, where the prototype with the gap above was slightly better than the one with the gap between the radiator and the ground plane. In the following sections, when I talk about 3D antennas, I refer to the 3D-down1 antenna configuration.

Finally, when I compare the relative efficiency of the 2D and 3D designs, I find that the 3D antennas provide better efficiency (about a 5%-15% improvement) for the same antenna volume. Consequently, I can conclude that the 3D miniaturization process leads to greater efficiency for smaller volumes, provided the proper configuration is used (i.e., 3D-down1).

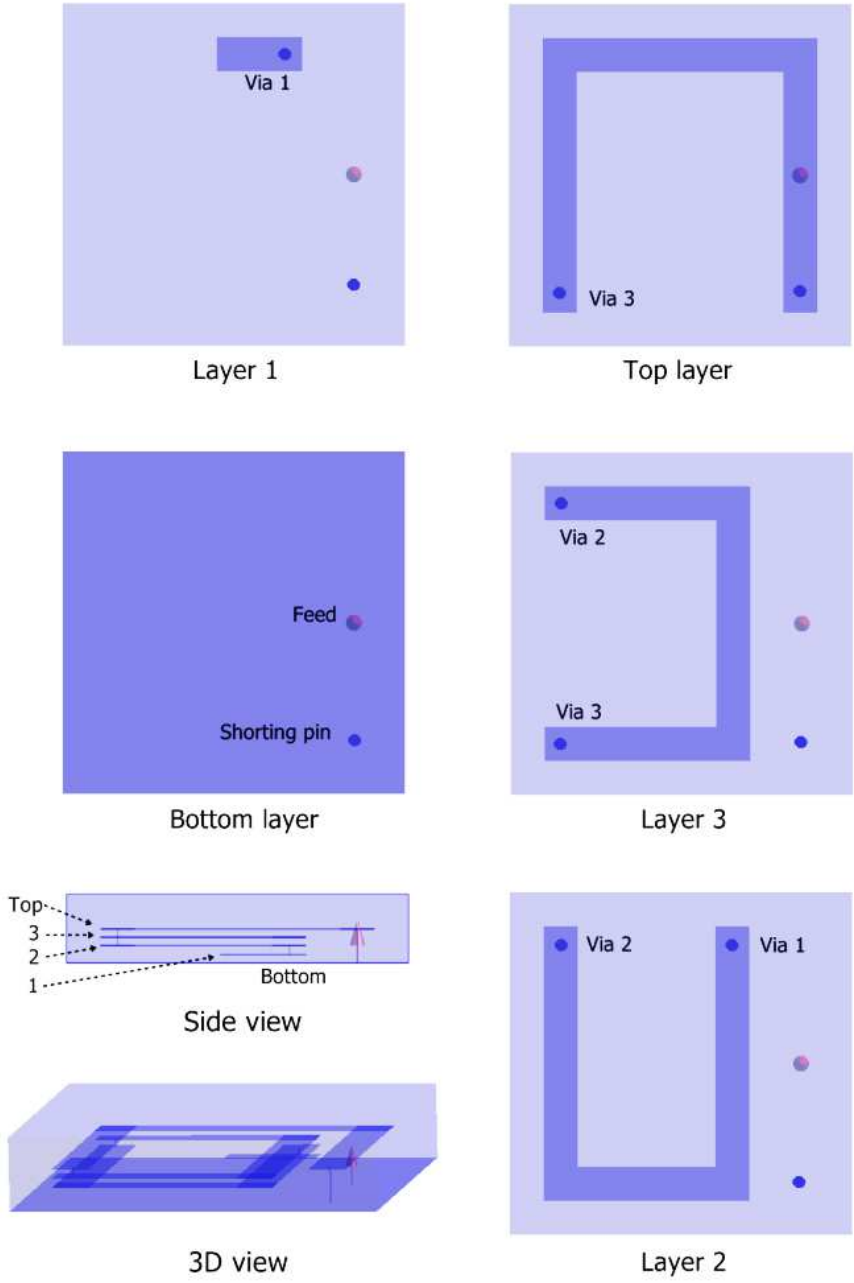

Figure 36. Geometry of the proposed 3D-square spiral antenna (case 3D2h): top view, side view and 3D view of metal and substrate. The layers are separated by 0.2 mm. The bottom layer corresponds to the ground plane.

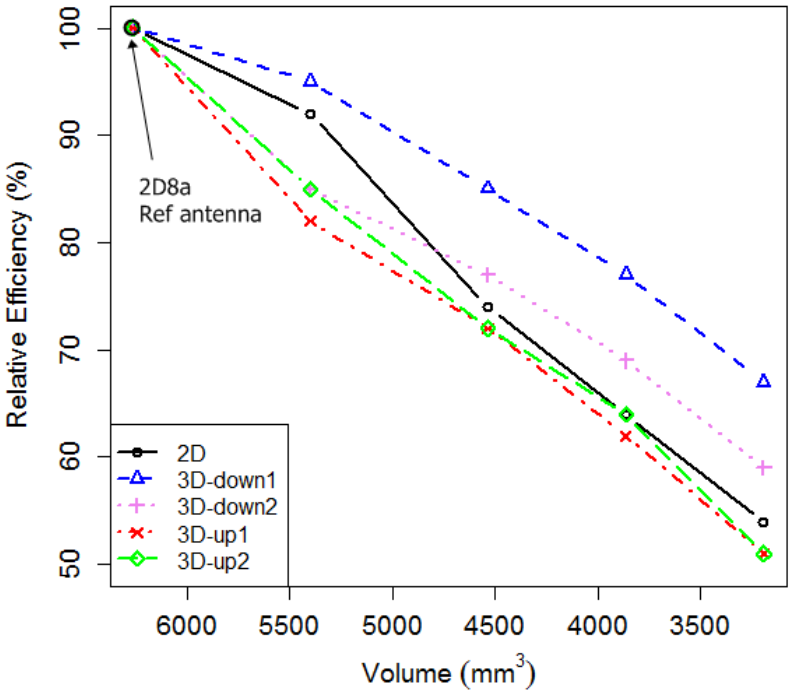

Figure 37. Relative efficiency of 3D miniaturized prototypes as a function of volume.

3.3.3. Global Discussion

Here I offer a general analysis of the antennas presented above. Table 20 summarizes the main characteristics and performance of a subset of representative antennas. Concerning directivity, it should be noted that the smaller the antenna, the more omnidirectional; as expected. A comparison of the gain for the 2D and 3D prototypes shows that the 3D antennas have higher gains than the 2D antennas for the same volume. A difference of up to 3 dB can be observed in some cases. In addition, when comparing the ratio between efficiency and volume as a merit figure, 3D antennas show better performance, especially for the smallest antenna.

The same behavior was found when I analyzed the communication link through the transmission coefficient. A 403 MHz half-wavelength dipole was placed at a distance of 50 cm from the face of the cubic phantom, close to the antenna. The transmission scattering parameter, S_{12}, was then calculated. The results for the 2D and 3D prototypes of the selected subset of antennas are shown in Figure 38. For the same volume, 3D prototypes showed approximately 6 dB better communication link performance than 2D prototypes. The greatest differences between 2D and 3D prototypes in terms of the S_{12} parameter are mainly related to near-field and polarization effects, which are not taken into account in comparisons of the gain.

Table 20. Results for the selected antennas implanted at the middle of a 100 mm cubic phantom.

Antenna prototype	Volume (mm^3)	Efficiency (%)	Merit Figure (Effi./Volume) ($x10^{-5}$)	Relative Efficiency (%)	Gain (dBi)	Direct. (dBi)
RA	6264	0.39	6.23	100	-21.1	3
2D8e	3192	0.21	6.58	53.9	-23.7	3.1
2D4f	1596	0.1	6.27	25.6	-27	2.9
2D2g	798	0.059	7.39	15.1	-29.7	2.6
2D2h (2D)	**364**	**0.045**	**12.6**	**11.5**	**-31.3**	**2.2**
3D8e	3192	0.26	8.15	66.6	-21.9	3.8
3D4f	1596	0.12	7.52	30.8	-25.4	3.7
3D2g	798	0.07	8.77	17.9	-28.3	3.3
3D2h (3D)	**200**	**0.05**	**25**	**12.8**	**-30.8**	**2.5**

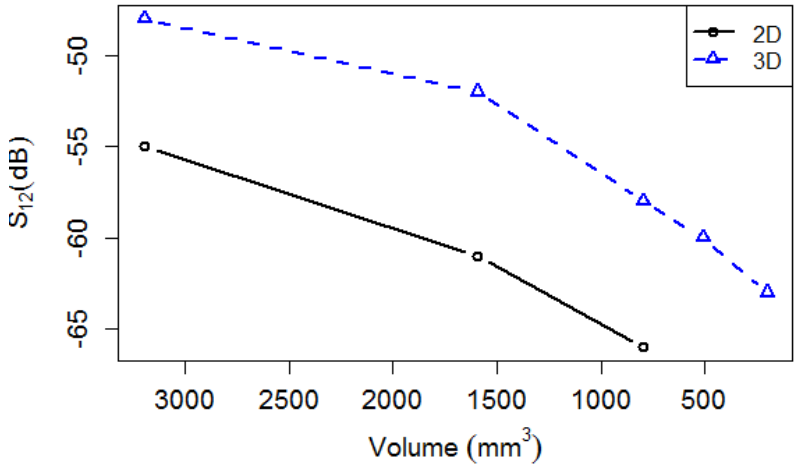

Figure 38. Transmission coefficient (S_{12}) of 2D-square and 3D-square antennas as a function of volume.

Figure 39 illustrates a comparison of all the prototypes studied in the miniaturization process. The plotted lines represent the three miniaturization methods, while the symbols represent the final prototypes. It can be seen that fractals and meander antennas are less efficient than square spirals, and that the 3D-square spiral is both the most efficient and the smallest antenna.

In Chapter 5, some of the most representatives 2D and 3D prototypes discussed in this chapter are fabricated and experimentally characterized, showing good agreement between simulations and measurements.

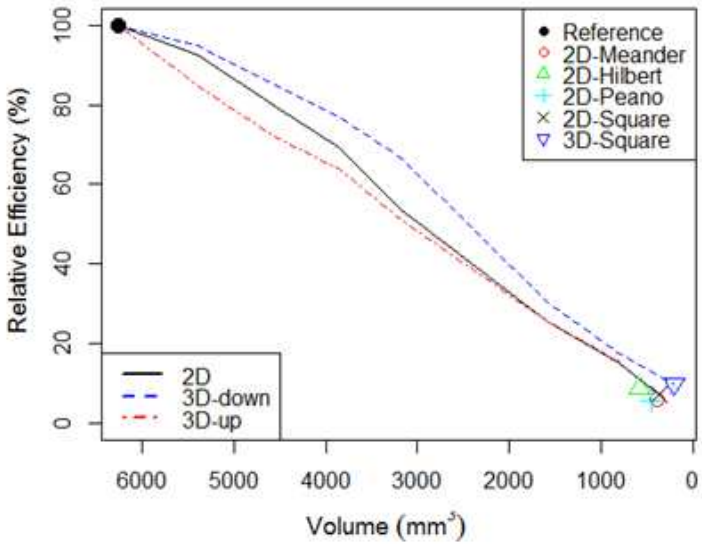

Figure 39. Efficiency (relative to RA) as a function of the volume of the antennas studied during the miniaturization process (lines) and the final prototypes (symbols).

3.4. Conclusions

In this study, 2D and 3D techniques for the miniaturization of LTCC antennas intended to work in the MedRadio frequency band were considered in detail. From my analysis, I concluded that generally speaking, 3D miniaturization techniques achieve better results than 2D miniaturization. The 3D antenna prototypes showed higher gain and efficiency than their 2D counterparts with the same volume.

Folding down the main radiator of the antenna, and separating the radiator end as much as possible from the tissue, is the best procedure to optimize gain for a given antenna volume. For the 2D prototypes, I also conclude that the square spiral PIFA is the most efficient structure, as expected; it is more efficient than the meander and fractal antennas, mainly due to the parallel currents that appear in close proximity in the radiator.

The influence of the surrounding environment on antenna performance will be studied and analyzed in the following chapter.

4. Influence of Phantoms on In-body Antenna Performance

4.1. Introduction

As previously mentioned in Section 2.4, an important aspect to take into account when designing in-body antennas is the modeling of the antenna environment. From cubic phantoms of different sizes, to highly detailed anatomical phantoms, a large number of phantoms are used in the literature to test antenna performance inside the human body. Canonical homogeneous phantoms are used instead of anatomical models to decrease the simulation time, to lighten the computational load and to allow further experimental validation in the laboratory. Moreover, the smaller the phantom is, the faster the results are obtained. Nevertheless, important differences may be observed depending on the patient's anatomy, the antenna location and the application requirements. The objective of this chapter is to go into greater depth in the effect of phantoms on the antenna's far-field characteristics and to assess their influence on the performance of various square spiral PIFA prototypes presented in the previous chapter.

The current literature demonstrates that changing the phantom size does not lead to substantial modifications in the reflection coefficient, provided that the depth of the implant is the same and the phantom is homogeneous [174]. However, phantom dimensions have a considerable influence on other parameters, such as efficiency or the radiation pattern. In this chapter, this influence is quantified and analyzed.

Meanwhile, depending on the implant location and the application requirements (such as the bit rate), frequency bands other than MedRadio could be a better choice. Thus, apart from antennas operating at a frequency of 403 MHz, I analyze antennas working at 866 MHz and 2.45 GHz. The use of these higher frequencies will allow further miniaturization of the implanted devices. However, this may produce additional degradation of efficiency. The quantification of these changes in radiation efficiency is another of the goals of this study. It would be of great interest to know, for a specific application and location, what the best choice would be in terms of body phantom, antenna design, frequency band and communication performance.

The main goals of this chapter can be summarized as follows:

- To provide a better understanding of how the surrounding lossy medium affects antenna performance.

- To evaluate the features of certain PIFAs presented in the previous chapter, such as the RA, the 2D and 3D square spirals.
- To retune the previous designs to operate at higher frequencies and assess them in various scenarios.
- To analyze the communication link, depending on the phantom and the operating frequency of the antenna.
- To provide initial insight into a characterization protocol in order to compare antennas from different research groups.

Some of the antennas presented in this chapter will be manufactured and experimentally characterized in Chapter 5.

4.2. Methodology

EM simulations were performed by using the FDTD method in the commercially available electromagnetic software SEMCAD. The antenna radiators were embedded inside an LTCC dielectric substrate (ε_r=6.6 and σ=0.0003 S/m).

The square spiral PIFA prototypes presented in the previous chapter and working in the MedRadio frequency band of 403 MHz were first tested when located in the middle of a cubic phantom with 100 mm edges. This phantom size was chosen for comparison purposes, in accordance with previous studies [174]. The antennas were also tested when placed inside the tissue at 10 mm from the tissue–air interface (Figure 40 (a)). A similar test of the antenna prototypes was carried out using a cubic phantom with 300 mm edges.

Apart from the implant depth and the phantom size, the phantom geometry is also analyzed to establish its role in the far-field features. The selected geometries are among the most commonly used by in-body antenna designers (see Subsection 2.4.1.1), such as cylinders, spheres and cubes (Figure 41).

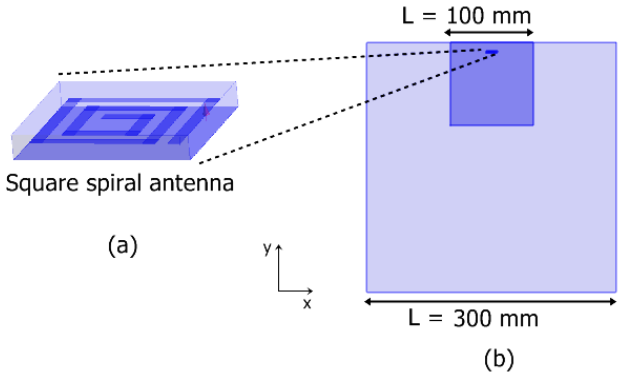

Figure 40. View of the (a) square spiral PIFA at 403 MHz implanted in (b) two cubic phantoms (100 and 300 mm)at a depth of 10 mm.

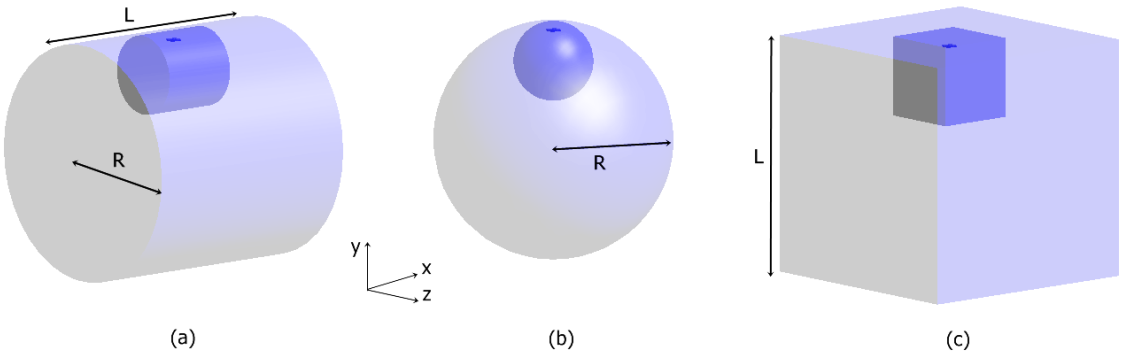

Figure 41. Phantom geometries used in simulations: (a) cylinder, (b) sphere and (c) cube. Two phantom sizes are represented for each case.

To optimize the gain and obtain the best transmission level in the desired direction of propagation (positive *y*-axis), the antenna should be oriented with the maximum of radiation in the same direction as the implant depth. Thus, vertical orientation is also analyzed in this study, as presented in Figure 42.

To compare the results in other typical frequency bands used in biotelemetry, two more square spiral prototypes were set up to operate at 866 and 2450 MHz when located inside the cubic phantom (Figure 43). The 2D and 3D miniaturization processes presented in the last chapter were applied in those prototypes. The skin frequency-dependent dielectric parameters of the cubic phantoms were provided by SEMCAD, and extracted from [40], as shown in Table 21.

Finally, the antennas were also tested in a highly detailed male anatomical model extracted from the Virtual Family dataset [192], to confirm the results in a more realistic environment. In this case, the antennas were implanted in the abdomen area (Figure 44 (b)) to simulate one of the worst cases in terms of the amount of surrounding lossy tissue. The performance and communication capabilities of the antennas were analyzed in all the cases. The latter is characterized by placing a receiver half-wave dipole at a distance of 50 cm from the edge of the phantom closest to the antenna.

Table 21. Skin dielectric parameters at different frequencies.

Frequency	Permittivity	Conductivity(S/m)
403 MHz	46.7	0.69
866 MHz	41.6	0.86
2.45 GHz	38	1.47

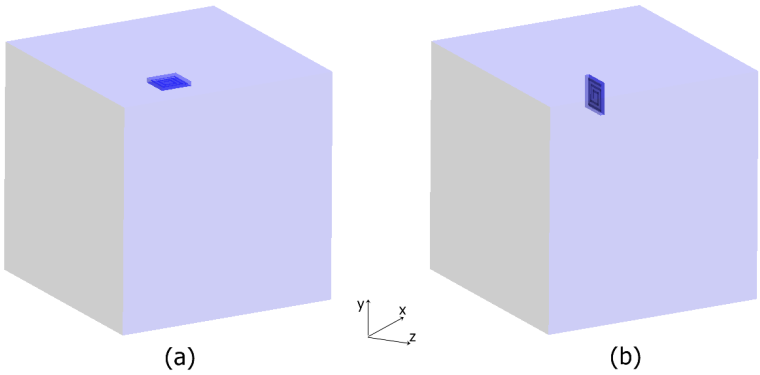

Figure 42. Modelling of the (a) horizontal or parallel and (b) vertical or perpendicular antenna orientation at an implant depth of 10 mm for a 100 mm cubic phantom.

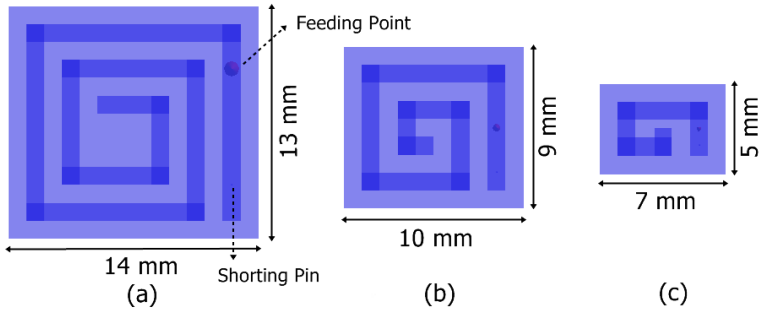

Figure 43. 2D-square spiral PIFA prototypes at different frequencies: (a) 403 MHz, (b) 866 MHz and (c) 2.45 GHz.

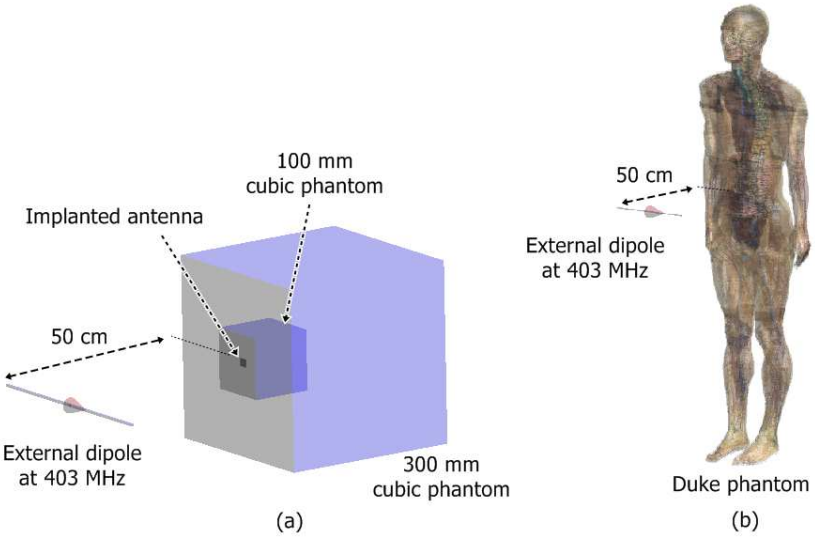

Figure 44. 3D-perspective of the setups to assess the communication link between the implantable antenna and an external dipole at 50 cm: (a) 100 mm and 300 mm cubic phantoms and (b) anatomical model.

Table 22. Outline of the overall analysis

Frequency	Miniaturization	Phantoms	Location
403 MHz	2D and 3D	100 mm edge	Centered
			10 mm deep
		300 mm edge	Centered
			10 mm deep
		Anatomical	Abdomen, 10 mm deep
866 MHz	2D and 3D	100 mm edge	Centered
			10 mm deep
		300 mm edge	10 mm deep
2.45 GHz	2D and 3D	100 mm edge	Centered
			10 mm deep
		300 mm edge	10 mm deep

Table 22 summarizes the test conditions for the different frequencies of interest, including the miniaturization process used, the phantom dimensions and type, and the antenna location. These antenna prototypes have been manufactured and characterized, and I give the most significant results in Chapter 5.

4.3. Results and Discussion

Table 23 shows the gain of the initial antenna and final 2D and 3D square spiral PIFAs presented in the previous chapter (RA, 2D2h and 3D2h, respectively, and highlighted in the table) as well as other antenna designs reported in the literature [14], [53]–[55], [64], [68], [79], [108], [157], [180] for comparison purposes. All of them operate in the MedRadio band, and were designed following a PIFA structure. It can be seen that the gain values are usually in the range of -40 dBi to -24 dBi. However, the results reveal a high level of diversity, which depends on several factors:

- Antenna volume
- Miniaturization method, how the effective current flow path has been increased (stacking multiple radiating patches, meandering or spiraling the radiator, among others)
- Technology used to manufacture the prototype (electrical properties of the substrate and design constraints)
- Electrical properties of the selected phantom and its homogeneity
- Phantom shape and dimensions, which determine the amount of lossy medium surrounding the antenna
- Implant depth, which indicates whether the air-tissue interface is in the near-field or the far-field region

Table 23. Comparison of the gain of implantable PIFA prototypes reported in the literature.

Ref.	Volume (mm^3)	Phantom size (mm)	Implant Depth (mm)	Gain (dBi)	Efficiency (%)
[54]	6480	60×50×20	7	N/A	N/A
[53]	6384	50×40×20	5	-30.6	N/A
RA	**6264**	**100×100×100**	**10**	**-25.1**	**0.18**
[64]	6144	N/A	4	N/A	0.25
[14]	5202	80×100*	20	-28.5	0.068
2D2h	**364**	**100×100x100**	**10**	**-37**	**0.013**
[68]	335.8	50×49.9	4	-26	0.31
[180]	273.6	25**	5	-24.31	8.72
[157]	254	25**	N/A	-40.35	0.38
[55]	203.6	100×100×100	48.2	-33	N/A
3D2h	**200**	**100×100×100**	**10**	**-34.6**	**0.018**
[108]	190	100×100×50	38.1	-26	1.3
[79]	121.6	N/A	N/A	-38	0.55

*Cylindrical phantom (diameter × height) **Spherical phantom (diameter)

For similar antenna sizes, miniaturization methods and electrical properties, the discrepancies between results are significant. They are due, to a great extent, to the different phantom dimensions and the implant depth used in the simulations. The results in this section provide a better understanding of such discrepancies between prototypes.

4.3.1. Cubic Phantom Dimensions

In this subsection the influence on antenna performance of the size of homogeneous cubic phantoms is assessed. The reflection coefficient of the 2D spiral square PIFA is obtained in cubic phantoms of different edge lengths L (see Figure 41 (c)), ranging from 25 to 300 mm. According to [174] , variations in the cubic phantom size do not lead to significant reflection coefficient detuning.

However, as the surrounding lossy tissue directly affects the propagation features of the antenna, the total radiated efficiency and the maximum gain are not constant. In Figure 45, it is possible to appreciate the efficiency variations depending on the size of the cubic phantom. The interest here is that the efficiency reaches its maximum at a cubic phantom close to 80 mm instead of the smallest one. The interaction of the near-field radiated by the antenna with the air–phantom boundary substantially modifies the EM propagation. Efficiency reaches its maximum when the antenna is placed in a phantom of dimensions comparable to the wavelength (108.9 mm in the 403 MHz prototype implanted into the skin phantom).

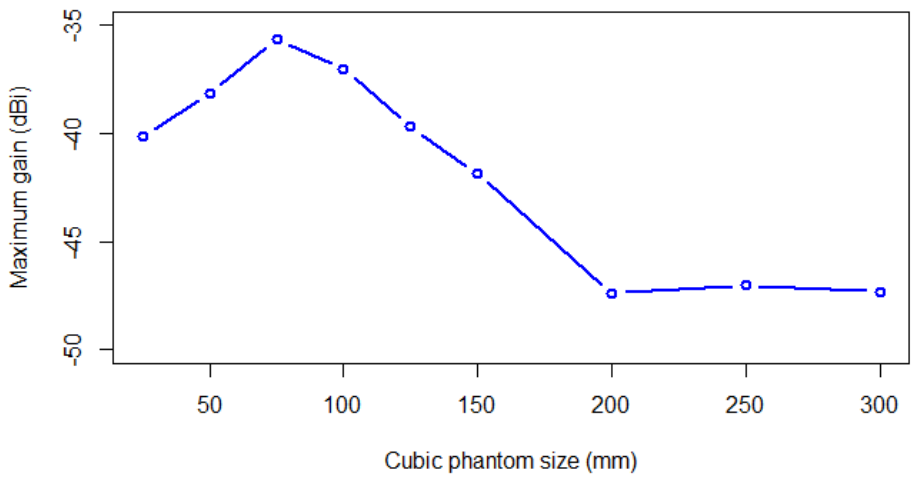

Figure 45. Maximum gain (dBi) of the 2D square spiral PIFA at an implant depth of 10 mm as a function of the edge length of the cubic phantom (L in Figure 41 (c)).

Figure 46 shows the radiation pattern of the 2D square spiral in the XY plane for three different cubic phantom sizes. The local gain along the positive *y*-axis is similar for all the cubic phantoms because the implant depth is the same in all the cases (black dot in Figure 46). Thus, if we place a dipole 50 cm from the air–phantom boundary in the positive y-direction, the values of the transmission level are also comparable, with a maximum difference of 3.4 dB, as seen in Table 24. However, the maximum gain and the radiation efficiency of the antenna depend on the whole environment; propagation in the other directions is also important.

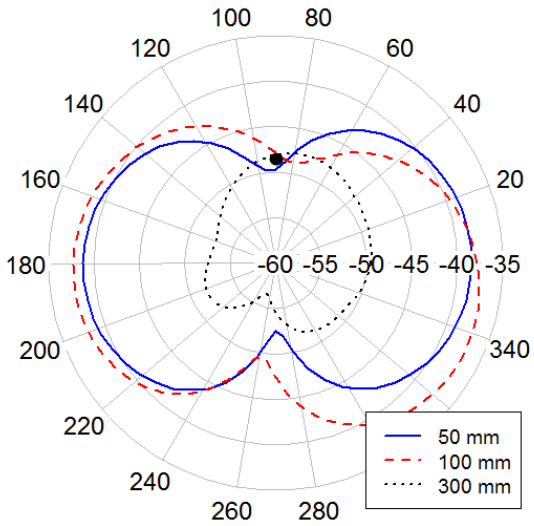

Figure 46. XY gain (dBi) radiation pattern of the 2D square spiral at an implant depth of 10 mm as a function of cubic phantom size (L).

Table 24. Transmission level at 50 cm from the air–phantom boundary for the 2D square spiral PIFA at an implant depth of 10 mm as a function of cubic phantom size (L).

Cubic phantom size L (mm)	**40**	**50**	**70**	**80**	**90**	**100**	**300**
S_{12} (dB)	-69.2	-67.6	-65.8	-66.6	-68.3	-68.2	-65.9

Table 25. Far-field results as a function of phantom type at an implant depth of 10 mm.

Antenna prototype	**Effi. (%)**	**Gain (dBi)**	**Dir. (dBi)**	**Effi. (%)**	**Gain (dBi)**	**Dir. (dBi)**
	100 mm Phantom			**300 mm Phantom**		
RA	0.18	-25.1	2.3	0.034	-30.8	3.9
2D2h (2D)	0.013	-37.0	2	0.0015	-47.3	2.7
3D2h (3D)	0.018	-34.6	2.8	0.0025	-44.7	1.3

Results of far-field features of three representative antennas presented in the previous chapter (RA, and 2D and 3D square spiral PIFAs) are shown in Table 25 for two different cubic phantom sizes: L=100 mm and L=300 mm. In order to make comparisons with most of the designs presented in the literature, here the antennas were placed at an implant depth of 10 mm. Depending on the phantom dimensions, a significant discrepancy in efficiency and gain is observed. In the case of the RA, using the 300 mm cubic phantom instead of the 100 mm cubic phantom led to a reduction in gain of 5.7 dB. The reduction for 2D and 3D miniaturized antennas is even greater: 10.3 dB and 10.1 dB respectively. Considering that the distance between the antenna and the air–tissue interface is always the same, the observed results can only be explained by taking into account reflections at the side and rear faces of the phantom, and interference phenomena. Consequently, the phantom dimensions strongly affect the antenna parameters obtained. Phantom standardization is needed to compare results of antennas manufactured with different technologies and miniaturization procedures satisfactorily.

4.3.2. Implant Depth

I varied the implant depth from 0 to 10 mm to assess its influence on antenna performance. In Figure 47 (a), the reflection coefficient of the 2D squire spiral presents a detuning of 11.7 MHz between 2 mm and 10 mm depth. The red line corresponds to an implant depth of 0 mm (i.e., an on-body scenario) and shows the return loss of the square spiral antenna inside the phantom but directly in contact with the air. The operating frequency in this case is different from in the others, due to the lack of biologic tissue on one side of the prototype, which greatly modifies its radiation features. The results are consistent with the literature. As

described in [111], increments in the implant depth of an antenna produce slight detuning at operating frequencies.

In Figure 47 (b), it is appreciable that the efficiency of the 2D square spiral antenna increases with the implant depth for a 100 mm cubic phantom. However, for a larger phantom such as a 300 mm cube, the behavior is the opposite (Figure 48). Again, the interaction between the near-field region (determined by the wavelength) and the air–phantom boundary has a crucial impact on far-field features. As shown in Figure 49, the radiation patterns of the two cubic phantoms evolve in the opposite way as a function of the implant depth.

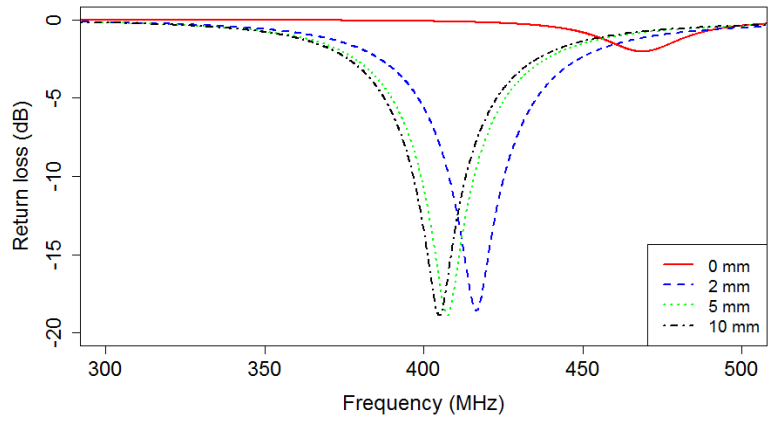

(a)

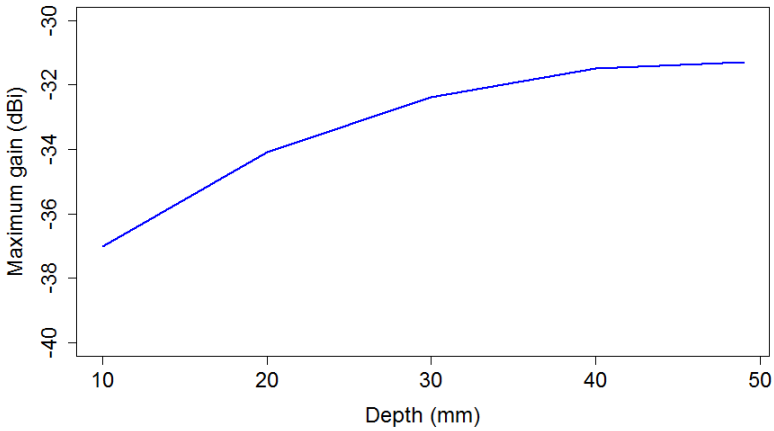

(b)

Figure 47. (a) Reflection coefficient and (b) maximum gain of the 2D square spiral in a 100 mm cubic phantom as a function of the implant depth

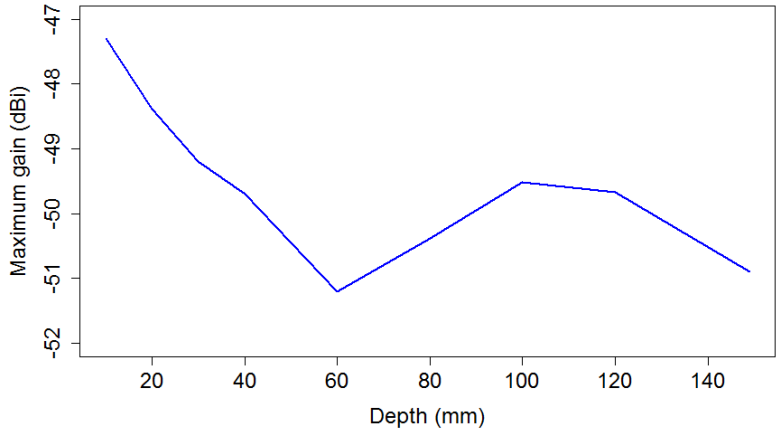

Figure 48. Maximum gain of the 2D square spiral in a 300 mm cubic phantom as a function of the implant depth.

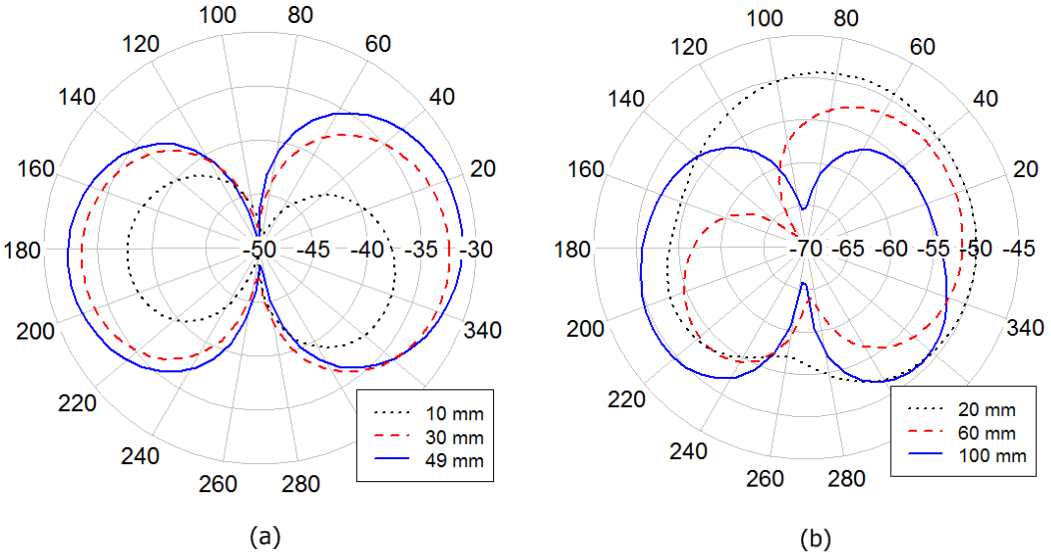

Figure 49. XY gain radiation pattern of the 2D square spiral as a function of the implant depth in a (a) 100 mm and (b) 300 mm cubic phantom.

In order to appreciate better the influence of both parameters together, Figure 50 illustrates the maximum gain of the 2D square spiral prototype as a function of cubic phantom size for different implant depths. The maximum gain in each case is depicted by a vertical dashed line. It can be observed that, the deeper the implant is, the greater the maximum gain, in the appropriate phantom. While for an implant depth of 4 mm the maximum gain corresponds to a cubic phantom with an edge length of 80 mm, for an implant depth of 24 mm the maximum gain corresponds to a cubic phantom with an edge length of 110 mm. The difference between the maximum gain in the two cases is about 7.5 dB. It is worth noting that from a phantom size of 200 mm the maximum gain stabilizes significantly for the three cases.

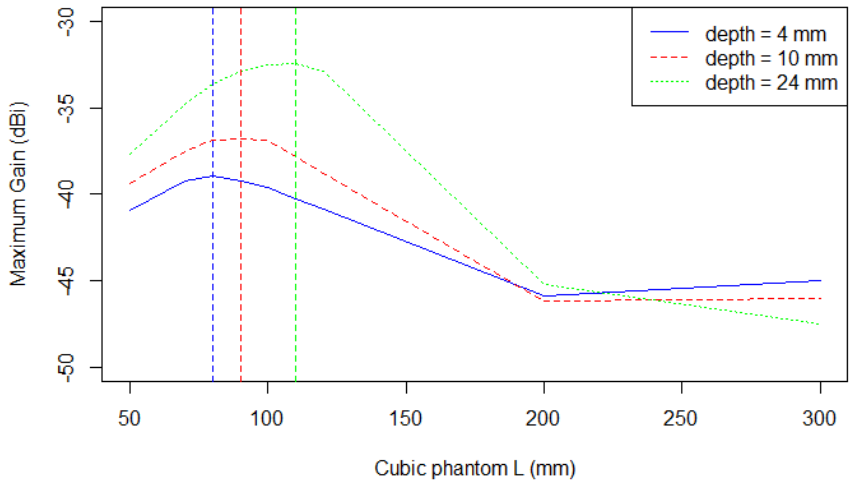

Figure 50. Maximum gain as a function of implant depth and cubic phantom size for the 2D square spiral. Vertical dashed lines show the cubic phantom size that gives the greatest maximum gain for a certain implant depth.

4.3.3. Phantom Shape

The square spiral antenna was also characterized using other phantom shapes, such as cylinder or sphere (see Figure 41 in the previous section). Far-field features of the 2D squire spiral PIFA implanted at a depth of 10 mm are presented in Table 26 (L=length and R=radius).

Based on the results in Table 26, we can see that the shape and the dimensions of the selected phantom significantly influence the radiation efficiency and the maximum gain, even despite the homogeneity and implant depth being the same. There is certainly a relationship between phantom volume and efficiency, as expected. Smaller phantoms present similar values for efficiency and gain, and the same occurred for larger ones. However, variations are greater in the large phantoms.

Table 26. Far-field features of the 2D square spiral antenna at an implant depth of 10 mm for different phantom shapes.

	Cyl 1	**Sph 1**	**Cube 1**	**Cyl 2**	**Sph 2**	**Cube 2**
Dimensions (cm)	R=5 L=10	R=5	L=10	R=15 L=30	R=15	L=30
Phantom volume (cm^3)	785	524	1000	21206	14137	27000
Efficiency (%)	0.011	0.011	0.013	0.0021	0.0025	0.0015
Maximum Gain (dBi)	-37.4	-37.3	-37	-45	-44	-47.3

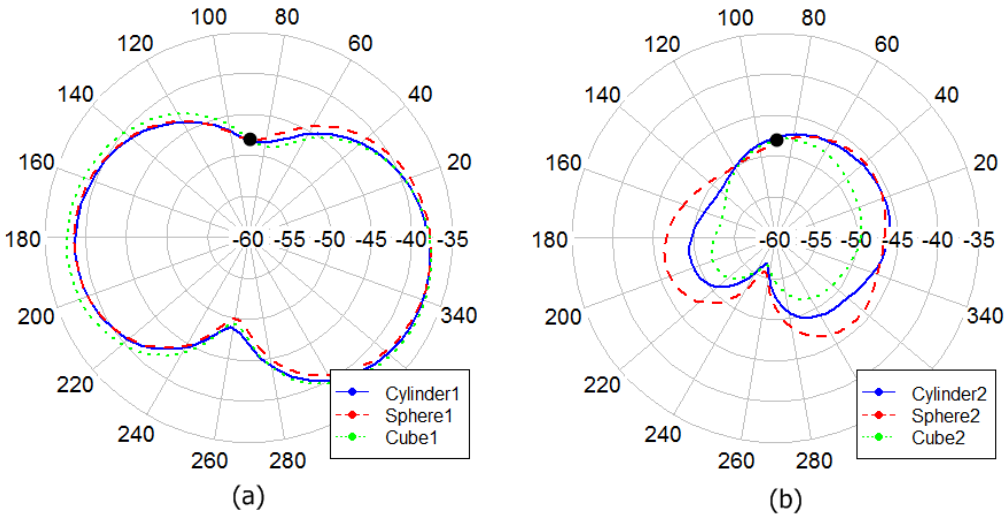

Figure 51. XY gain radiation pattern (in dBi) of the square spiral prototype in different phantoms: (a) small (R=5cm, L=10cm) and (b) big (R=15cm, L=30cm).

Figure 51 shows differences in the XY gain radiation patterns for each phantom shape. Whereas the radiation pattern varies with the phantom size, the gain in the main direction of propagation (positive *y*-axis, indicated by the black dot in the plot) is similar for all the phantoms (around -47 dB) because the implant depth is always 10 mm in that direction. The gain in the other directions are more varied due to differences between the amounts of tissue the radiated power has to cross depending on the phantom size, especially in the large phantoms (Figure 51 (b)).

Therefore, as has been reported, obtaining the maximum gain can lead to different results depending on the phantom used. In addition, the maximum gain is not necessarily in the desired direction of propagation (in this case, the positive *y*-axis). In fact, as can be observed in Figure 51, the maximum gain is close to the positive *x*-axis. Thus, when comparing in-body antennas or when trying to optimize the effective radiated power of an in-body antenna, the gain radiation pattern has to be taken into account. Sometimes, only by changing the orientation of the antenna, better results could be achieved.

4.3.4. Antenna Orientation

In order to optimize the far-field features of the 2D square spiral, the antenna was oriented perpendicular to the air–phantom boundary, as can be seen in Figure 42 (b) of the previous section. In that perpendicular orientation, the maximum radiation was in the same direction as the implant depth (positive *y*-axis), where

the transmission should be carried out. Thus, an increment of the maximum gain is expected.

In Figure 52, important differences can be observed in the maximum gain as a function of the implant depth, the phantom shape and the phantom size, between both parallel and perpendicular orientations. The perpendicular orientation shows greater values of gain in practically all the cases, especially for small implant depths, where differences from 5 to more than 10 dB are achieved. It is also appreciable that when the antennas were located close to the center of the phantoms, the results were more similar between orientations. Thus, as seen in previous subsections, the effect of the interaction between air–phantom boundaries and the near-field is observable, especially for the parallel orientation. In the perpendicular orientation, however, it seems that this unwanted near-field effect is reduced. This situation is clear in the large phantoms, where the maximum gain values for both orientations are almost the same for an implant depth of 100 mm or more (more or less the size of the wavelength) because the air–phantom boundary is located far from the near-field.

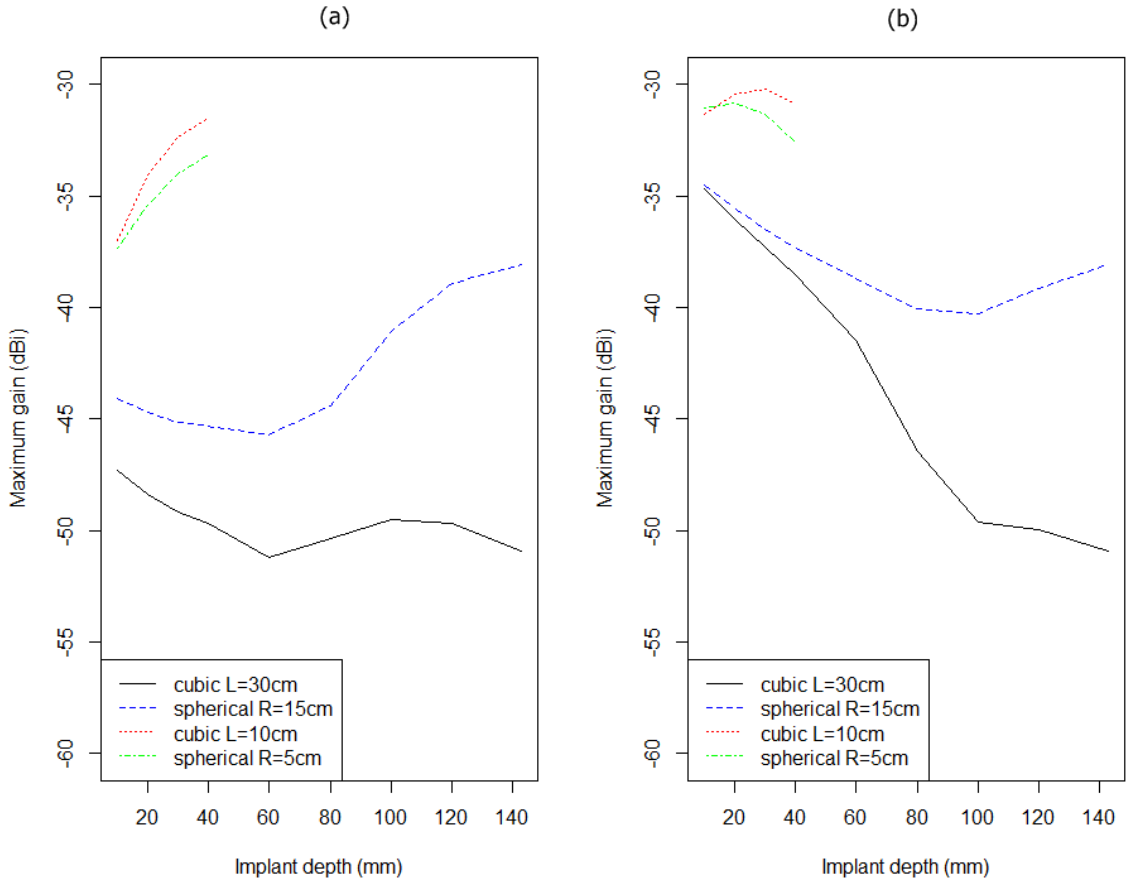

Figure 52. Maximun gain (dBi) as a function of implant depth for different phantoms: (a) horizontal and (b) vertical orientation.

In Figure 53, the XY gain radiation patterns of both configurations are compared for different depths and phantoms. The perpendicular orientation (Figure 53 (b) and (d)) leads to more radiated power for all the cases. While differences between small cubic and spherical phantoms at a depth of 10 mm (Figure 53 (a) and (b)) are not significant, these differences are notable in large phantoms at deeper implant depths (Figure 53 (c) and (d)). In large phantoms, the spherical shape presents more than 15 dB of improvement over the cube for vertical orientation.

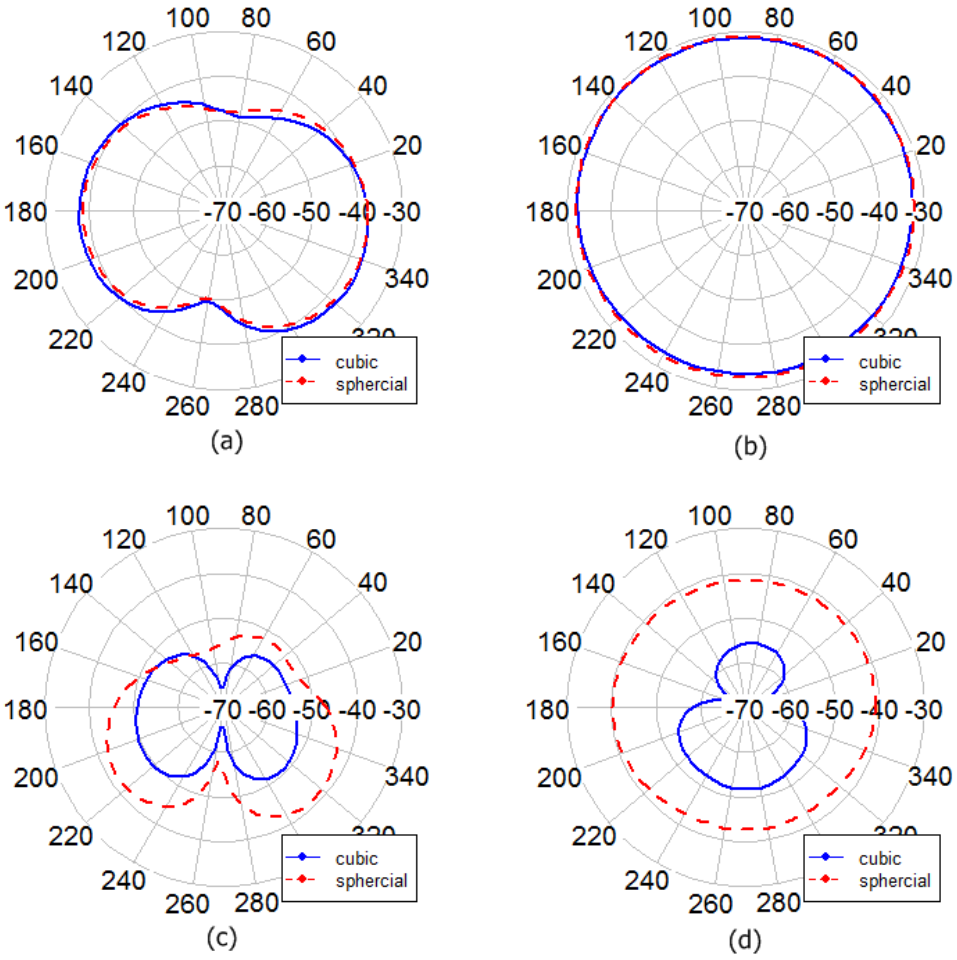

Figure 53. XY gain radiation pattern (in dBi) of the 2D square spiral PIFA in different phantoms, depths and orientations: (a) implant depth of 10 mm, small phantoms (R=5 cm, L=10 cm) and horizontal orientation, (b) implant depth of 10 mm, small phantoms (R=5 cm, L=10 cm) and vertical orientation, (c) implant depth of 100 mm, large phantoms (R=15 cm, L=30 cm) and horizontal orientation, and (d) implant depth of 100 mm, large phantoms (R=15 cm, L=30 cm) and vertical orientation.

4.3.5. Frequency Band

In this Subsection, I consider the behavior of in-body antennas in other frequency bands. I am particularly interested in the 866.35 MHz UHF band (used in RFID systems), and the 2.45 GHz ISM band. The final 2D and 3D square spiral PIFAs developed in the previous chapter to work in the MedRadio band were resized here to tune into the new frequency bands. The resulting dimensions are shown in Table 27. The antennas were tested at two locations inside the 300 mm cubic phantom: first, 10 mm from the mean body tissue–air interface; and second, in a central location.

The gain and directivity results are shown in Table 28. As expected, at the central location, the gain decreased as the frequency increased, due to higher absorption. A variation of around 20 dB was observed between the 403 MHz and the 2.45 GHz frequency bands. For this scenario (deeply implanted antennas), moving to higher frequencies would have a strong impact on communication capabilities. However, when the antenna was located 10 mm from the interface, the opposite behavior was observed (the higher the frequency, the higher the gain). Thus, at a frequency of 2.45 GHz the gain had increased as much as 12 dB for the 3D prototype, in comparison with the 3D 403 MHz antenna. This behavior is mainly due to the strong interaction between the radiated near-field and the air–tissue interface via reflections and interferences. When increasing the frequency, the boundaries between field regions decrease, as shown in Table 29. The dimensions of these regions obtained for the frequency bands used and the human body tissues are comparable with the dimensions of phantoms and implant depths.

In the study presented in [227], the gain was also found to be greater for higher frequencies. These results were attributed to the relatively enhanced patch surface area of the antenna at higher frequencies. In my study, the radiator width was always 1 mm due to fabrication constraints, so the surface area was relatively large for higher frequencies in terms of wavelength. Although this effect was noticed for shallow implants, it was negligible in the central locations, mainly due to the higher attenuation found in lossy media for higher frequencies. Taking into account these considerations, this difference in gain is large enough to consider ISM bands instead of the MedRadio band for shallow implant locations.

Regarding the effectiveness of 2D or 3D miniaturization, in Table 28 some substantial differences can be found between low and high frequencies. The 2.45 GHz prototype only presented a variation of 0.4 dB between the two methods. However, at lower frequencies, this difference rose to 4 dB. This discrepancy could be explained by looking at the radiator lengths. At 2.45 GHz, the radiator is practically not large enough to be folded in 3D (there is only 14% variation in size). In contrast, the radiators at lower frequencies are larger, which significantly

increases the 3D folding capacity (there is a reduction in size of 45% at 403 MHz and 53% at 866 MHz).

For antennas implanted at a central location in a cubic phantom of 300 mm^3, 2D miniaturization shows similar or even greater gain values than the 3D method for 403 and 866 MHz. However, 2D prototypes are bigger than 3D ones, so it seems that for such deep locations (the middle of a 300 mm cubic phantom) tissue absorption is so great that it cancels the improvement from the 3D miniaturization method.

Table 27. Dimensions and far-field features of the antenna prototypes.

Frequency	Antenna prototype	Vol. (mm^3)	Length (mm)	Width (mm)	Height (mm)
403 MHz	2D	364	13	14	2
	3D	200	10	10	2
866 MHz	2D	180	9	10	2
	3D	84	6	7	2
2.45 GHz	2D	70	5	7	2
	3D	60	5	6	2

Table 28. Gain and directivity results for the 2D and 3D prototypes selected.

Frequency	Antenna prototype	Phantom 300 mm Antenna at 10 mm		Phantom 300 mm Antenna centered	
		Gain (dBi)	Dir. (dBi)	Gain (dBi)	Dir. (dBi)
403 MHz	2D	-47.3	2.7	-50.9	2.1
	3D	-44.7	1.3	-52.3	2.1
866 MHz	2D	-37.6	5.1	-53.8	4.1
	3D	-33.6	5.5	-54.2	4.9
2.45 GHz	2D	-26.3	5.6	-72.2	6
	3D	-26.7	5.5	-72.2	6.2

Table 29. Field regions (in mm) for electrically small antennas depending on frequency band and implanted in a skin phantom (ε_r=46.7).

Regions	Distance	403 MHz	866 MHz	2.45 GHz
Reactive near-field (mm)	0.159 λ	17.3	8.5	3.2
Radiative near-field (mm)	λ	108.9	53.7	19.9
Transition (mm)	2 λ	217.8	107.4	39.7

Table 30 shows the gain, efficiency and transmission coefficient values of the antennas at an implant depth of 10 mm for the 100 mm and 300 mm cubic phantoms. Here, the variations between the phantoms were also significant. The multipath radiation in the 300 mm phantom suffered more attenuation, mainly caused by the surrounding tissue. Indeed, far-field parameters are highly affected by the amount of tissue crossed. The frequency most affected for the phantom size is the lowest one, obtaining a reduction of 88% for the efficiency and 10.3 dB for the gain. Meanwhile, the 2.45 GHz prototype presents more robustness against phantom size variation, with the efficiency decreasing slightly, by 10%, and the gain 1.8 dB.

As can be observed in the last column of Table 30, the transmission coefficient is less significant between phantoms, since the radiation in the positive y-direction crosses 10 mm of tissue in all the cases. Nevertheless, if the implant depth is increased, the transmission coefficient decreases. This effect can be seen in the radiation pattern when changing the implant depth from 10 mm to centered inside the cubic phantom of L=300 mm (Figure 54).

The variations in the 403 MHz band are less significant than in the 2.45 GHz prototype when increasing the implant depth. Indeed, as seen in Figure 54, the higher the frequency is, the greater the impact of the implant depth on the radiated power. Higher frequencies attenuate faster, especially in biological tissues, where the wavelength becomes smaller than in air. In addition, whereas the behavior of the 403 MHz tends to be dipolar, higher frequencies present a multi-beam radiation pattern, as seen for the 2.45 GHz prototype implanted at the center of the 300 mm cubic phantom.

Table 30. Comparison of far-field features between the two phantoms for the three prototypes at a depth of 10 mm.

Frequency	Phantom (mm)	Efficiency (%)	Gain (dBi)	S_{12} (dB)
403 MHz	L=100	0.013	-37	-68.2
	L=300	0.0015	-47.3	-66
Variation		*-88%*	*-10.3 dB*	*-2.2 dB*
866 MHz	L=100	0.018	-34	-65.4
	L=300	0.0053	-37.6	-64.2
Variation		*-70.5%*	*-3.6 dB*	*-1.2 dB*
2.45 GHz	L=100	0.07	-24.5	-57.7
	L=300	0.063	-26.3	-59.2
Variation		*-10%*	*-1.8 dB*	*-1.5 dB*

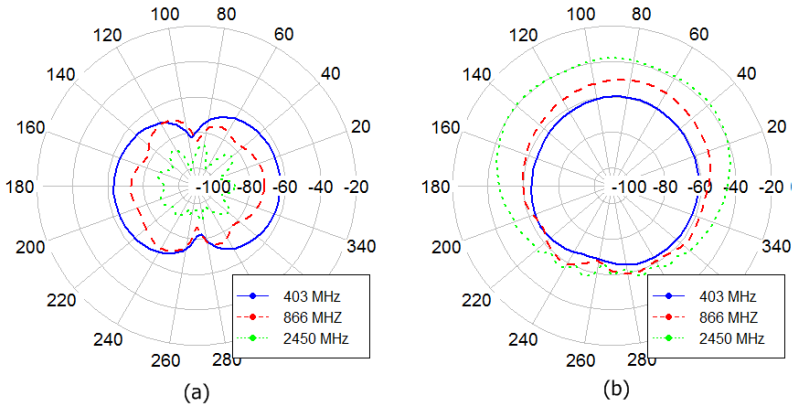

Figure 54. XY E-field radiation pattern of the 2D square spiral antenna in the three frequency bands implanted in the 300 mm cubic phantom (a) at a the center and (b) at a depth of 10 mm.

Concerning the gain in the desired direction (positive *y*-axis), the most suitable prototype at deeper locations is the 403 MHz antenna, and the worst is the antenna operating at 2.45 GHz (Figure 54 (a)). Conversely, in implants placed close to the surface (Figure 54 (b)), the behavior is reversed: the 2.45 GHz prototype radiates more power in the main propagation direction. Again, the air–phantom boundary in the radiative near-field region decreases the amount of power radiated in this direction.

The radiation patterns of Figure 55 represent the propagation of the three prototypes implanted in a 100 mm cubic phantom. There are substantial differences from the case of the 300 mm cubic phantom. On the one hand, at the center of the phantom, the depth is 49 mm instead of 149 mm, thus the air–phantom boundary is more relevant for the near-field region. The highest gain here is for the 866 MHz prototype, not that at 403 MHz. Both radiate in a dipolar way, while the 2.45 GHz antenna produces more radiation beams.

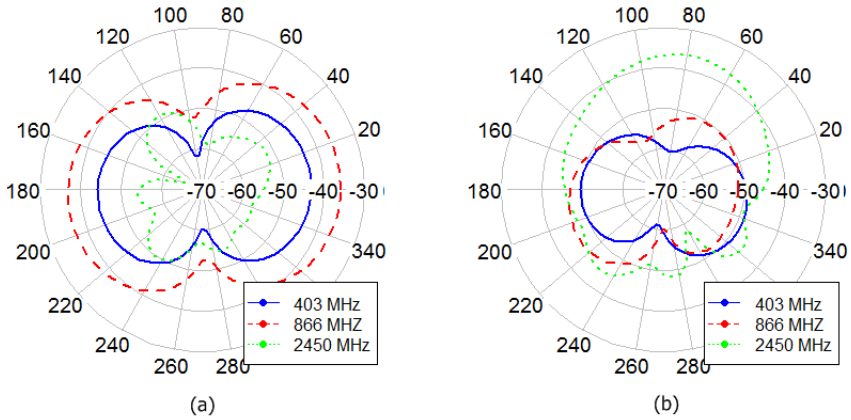

Figure 55. XY E-field radiation pattern of the square spiral antenna in the three frequency bands implanted in the 100 mm cubic phantom at a depth of (a) 49 mm and (b) 10 mm.

On the other hand, at a depth of 10 mm, the gain is lower for the lower frequency antennas, in comparison with the implants at the center; whereas the gain of the 2.45 GHz prototype is higher. The location of the phantom surface means it interacts with the near-field of the 403 MHz and the 866 MHz prototypes to a greater extent than that of the 2.45 GHz antenna.

In order to determine the ideal phantom size to optimize the gain, some simulations were performed varying the depth and the size of the phantom. Figure 56 represents the maximum gain of the 866 MHz and the 2.45 GHz prototypes as a function of the cubic phantom size for three different implant depths. It is possible to establish a phantom size where the gain reaches its maximum for the other two frequencies. For the 866 MHz antenna, as for the 403 MHz one, this maximum is near the boundary between the near and the far field (one wavelength). For the 2.45 GHz case, this size is not well determined.

Regarding the effect of antenna orientation, Figure 57 presents the *XY* gain radiation pattern for the three frequencies in a vertical orientation at a depth of 10 mm for different cubic phantom sizes. Greater differences are observed in the small phantom between frequencies than in the large one. It is also interesting to note that the gain in the positive y-direction is greater in the larger phantom, especially for the 403 MHz prototype. This is because the main radiation lobe is not in the expected positive y-direction.

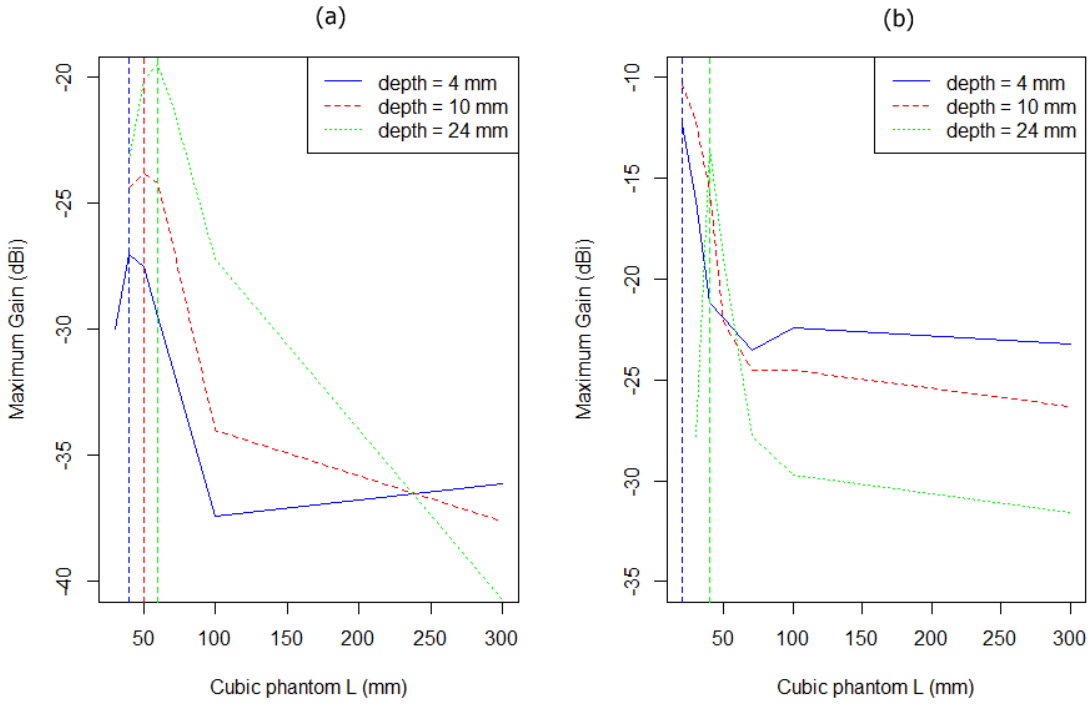

Figure 56. Maximum gain as a function of implant depth and cubic phantom size for (a) 866 MHz and (b) 2.45 GHz prototypes.

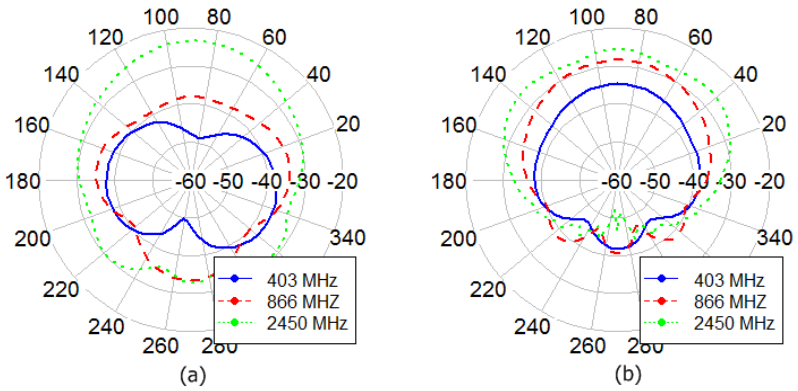

Figure 57. XY gain radiation pattern (in dBi) of the square spiral antenna in the three frequency bands implanted vertically at a depth of 10 mm in different phantoms: (a) 100 mm cubic phantom and (b) 300 mm cubic phantom.

4.3.6. Anatomical Model

I compared the results for the 100 mm and 300 mm cubic phantoms with those obtained using the highly detailed anatomical model. Figure 58 illustrates the XY and YZ gain radiation patterns of the RA prototype implanted inside the three phantoms tested. The results show good agreement between the radiation parameters using the Duke phantom (abdominal implant) and the 300 mm cubic phantom. This concordance is due to the comparable dimensions of the phantoms; whereas the 100 mm cubic phantom is relatively small. Therefore, this similarity is expected to vary depending on the implant location. Consequently, knowledge of the final placement required for the biomedical application is fundamental to determine the most accurate cubic phantom for each case, when calculating the far-field features of an implantable antenna and validating the simulation results.

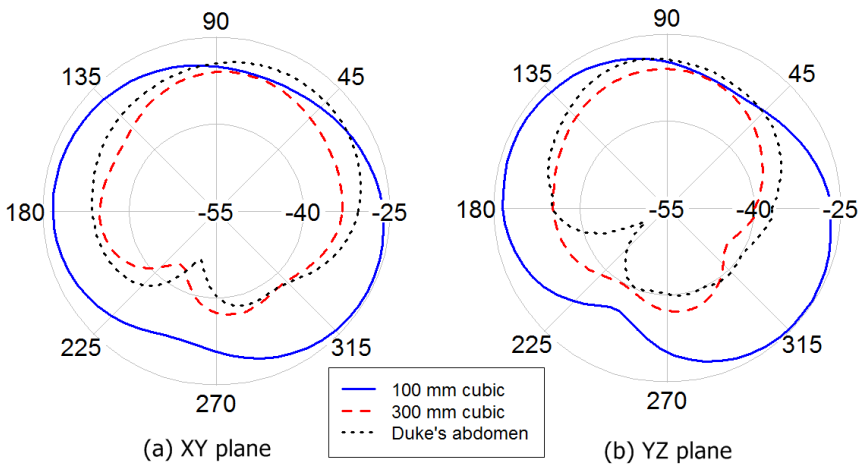

Figure 58. XY gain radiation pattern (dB) of the RA in the three phantoms at an implant depth of 10 mm.

4.3.7. Characterization Protocol

Considering all the previous results, I suggest to further explore a characterization protocol for in-body antennas.

It could be said that there are two different ways to approach the design of an in-body antenna, depending on the purpose:

- To design an in-body antenna for a specific application, knowing in advance the average dimensions of the phantom and the implant depth (so it should be characterized under these conditions).
- To design an antenna that efficiently operates inside the body, without knowing in advance the specific application (actually, a frequent situation in the literature).

For the second case, the standardization of the phantom dimensions and the implant depth when characterizing an in-body antenna could help antenna designers. By evaluating the antenna performance under these conditions, it could be possible to obtain an idea of the suitability of an antenna working in a general in-body scenario. Moreover, thanks to this protocol, the comparison of the performance of different in-body antennas would be more accurate and direct. Thus, from the point of view of the antenna engineer, the selection of one design or another for a specific application would be easier and faster.

For example, for in-body applications operating in the MedRadio band, a good solution for modeling the antenna and its surrounding tissue could be the location of the antenna in the center of a 100 mm or 200 mm homogeneous cubic phantom. This selection is based on the following considerations:

- The *reactive* near-field region in skin (ε_r=46.7) is 17.3 mm (see Table 29). A cube with an edge length of 100 mm ensures that, if the antenna is placed in the center, the air–phantom boundaries are outside this region.
- The *radiative* near-field region in skin (ε_r=46.7) is 108.9 mm (see Table 29). A cube with an edge length of 200 mm ensures that, if the antenna is placed in the center, the air–phantom boundaries are outside this region.
- Locating the antenna in the center of the phantom avoids variations in the far-field region due to antenna orientation.
- Cubic phantoms with an edge length of 100 mm are already used in the literature (see Table 8 in the Section 2.5).
- Cubic phantoms are easier to manufacture.

However, knowing the important influence of air–phantom boundaries on antenna performance, optimal phantom dimensions could be determined in advance for the near-field regions. This would reduce simulation time and computational load.

4.4. Conclusions

The influence of the phantom on antenna performance was assessed in this chapter. First, strong differences were observed in terms of antenna gain and efficiency depending on the phantom size. Using a 300 mm cubic phantom instead of a 100 mm cubic phantom resulted in a reduction in gain of up to 10 dB. Moreover, when using the anatomical model with an antenna implanted 10 mm underneath the abdominal skin, good agreement was obtained with the 300 mm cubic phantom. The results indicate that other parameters such as the implant depth and the orientation of the antenna also lead to significant variations in antenna performance. For shallow implants, the antenna should be perpendicularly oriented to achieve greater values of gain; whereas deep implants are less sensitive to orientation. Three different canonical shapes were employed, giving rise to considerable variations in antenna features, especially as the phantoms become larger.

The square spiral PIFA prototypes from the previous chapter were resized to operate in the ISM band of 866.35 MHz and 2.45 GHz. The results indicate that the interaction between radiated field regions and the air–tissue interface is critical in terms of antenna performance. Indeed, for shallow implants, antennas working at higher frequencies can achieve better performance due to the fact that they have a smaller near-field region. In addition, the relative larger size of antennas at 2.45 GHz also improves their efficiency. Both points compensate the increase of the radiation absorption in high frequencies.

Finally, considering these results, I suggest the development of a characterization protocol for in-body antennas. Even though this is not the objective of this thesis, the development of such standardization could help antenna engineers. This protocol recommends placing the antenna in the center of a cubic phantom. The dimensions of this phantom have to be set according the operating frequency with the aim of reducing the interaction between the air-tissue interface and the near-field region. The development of such a protocol could assist in determining the most suitable prototype for an in-body application from all the designs and proposals provided by researchers and companies.

5. Fabrication and Characterization of In-body Antennas Based on LTCC Technology

5.1. Introduction

The previous two chapters focused mainly on specific issues related to the design of in-body antennas. In the development of IMDs, however, the design stage is only the first step in the process. Once the prototype is created through computational modeling and simulations, it must then be manufactured and experimentally validated. In this chapter, a detailed description and an analysis of the fabrication process is presented, as well as some relevant topics regarding the characterization of in-body prototypes.

As previously introduced in Subsection 2.3.2, LTCC technology provides several advantages for the fabrication of in-body antennas and the packaging of the whole IMD: lossless substrate, high resolution, multilayer compact structures, integration with electronics, implementation of internal cavities and vias, durability, biocompatibility, etc. Nevertheless, the LTCC manufacturing process comprises complex physical and chemical procedures that introduce tolerances in the initial design, leading to slight variations in the dimensions or in the electrical properties of the substrate. If these alterations are sufficiently large, they may even compromise the antenna performance. Thus, the antenna designer must to have a good knowledge of all the manufacturing steps in order to avoid (or at least control) these tolerances.

Once the in-body antennas are manufactured, another source of error in their characterization is the measurement setup itself, as described in Subsection 2.3.10. The feeding of the antenna or the presence of unbalanced currents along the coaxial cable may alter the measurement of the antenna performance, such as the reflection coefficient, the radiation pattern or the efficiency [83], [228]. In this chapter several measurement techniques for avoiding these effects will be discussed:

- Feeding method: coplanar launcher or direct feeding.
- Reflection coefficient characterization: direct coaxial or coaxial with splitter.
- Radiation pattern characterization: standard configuration or fiber optics.

So the principal objectives of this chapter are:

- To describe the manufacturing process of in-body antennas in LTCC technology.
- To identify the main issues related to the manufacturing process.
- To quantify the sensitivity tests of the manufacturing process in the antenna performance.
- To present the experimental validation of some of the in-body prototypes proposed in the previous two chapters.
- To highlight the main problems related to the characterization of in-body antennas.
- To propose solutions for certain measurement issues.

5.2. Methodology

The proposed antenna designs assessed in this chapter are taken from the previous two chapters, in which computational models and simulated results were presented. Here, experimental validation is performed through LTCC antenna fabrication, manufactured phantoms and in-vitro measurements.

5.2.1. Fabrication in LTCC Technology

The LTCC technology is based on multilayer ceramic technology, which includes all the processes and materials used to obtain devices composed of several ceramic layers with printed circuits. After a final consolidation process of all these materials, a multilayer hermetic structure is obtained as a single block. Unlike thick film technology in which the final device is not a monolithic structure, the LTCC technology allows the inclusion of opened and closed cavities as well as the interconnection of components from the surface to the inner layers like, for example, Surface Mounted Devices (SMD) [229]. For the antenna designer these features are particularly valuable since they allow the inclusion of other electronic components such as the sensoring, harvesting or a RFID chip.

The LTCC fabrication process is divided into several steps (Figure 59) that will be detailed below. All were carried out at the facilities of the Francisco Albero S.A.U. company.

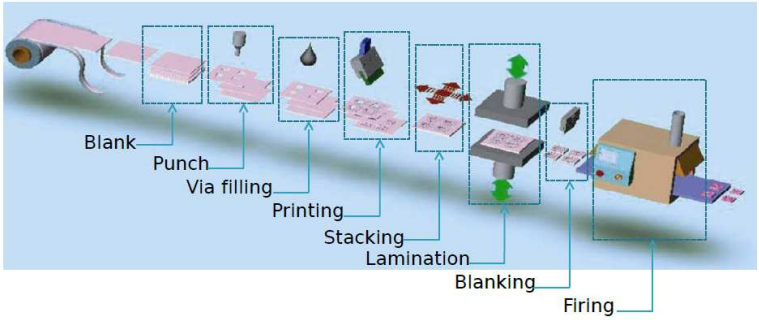

Figure 59. Manufacturing process of the LTCC technology.

5.2.1.1. Mask Design

Before initiating the fabrication process, the designs of the prototypes are placed together in the same virtual mask according to the size of the green tape sheets. Several masks were designed: one mask for each layer with metallic paths (Figure 60) and another one for each layer with cavities and vias. It can be seen that in a manufacturing lot it is possible to print various prototypes depending on their size and on the ability of the designer. Apart from the vias, cavities and metallic parts, other elements are defined in the masks, such as the registers (or tape limits), the fiducials (which will help in the alignment between sheets), the cut marks and the identification of the lot (indicated in Figure 60).

The ceramic substrate tends to shrink in the horizontal plane due to thermal treatments (by a factor of 0.88 for each substrate used). Two methods can be applied to remedy this problem. The first is the zero-shrinkage technique, which involves the application of a green layer of a specific material, such as alumina, which sinters at much higher temperature than LTCC substrate, on the top and the bottom of the multilayer structure. Those materials can be eliminated after the firing step. As the alumina layers do not co-fire, they maintain their dimensions and avoid the shrinkage of the LTCC substrate in contact with it, and hinder the horizontal shrinkage of the whole structure. However, for structures thick enough, a significant shrinkage and deformation can appear in the middle layers. The second method is free-sintering, which consists in scaling the designed mask by the shrinkage factor. Here, the problem appears in the accuracy of the shrinkage and in the cavity deformations.

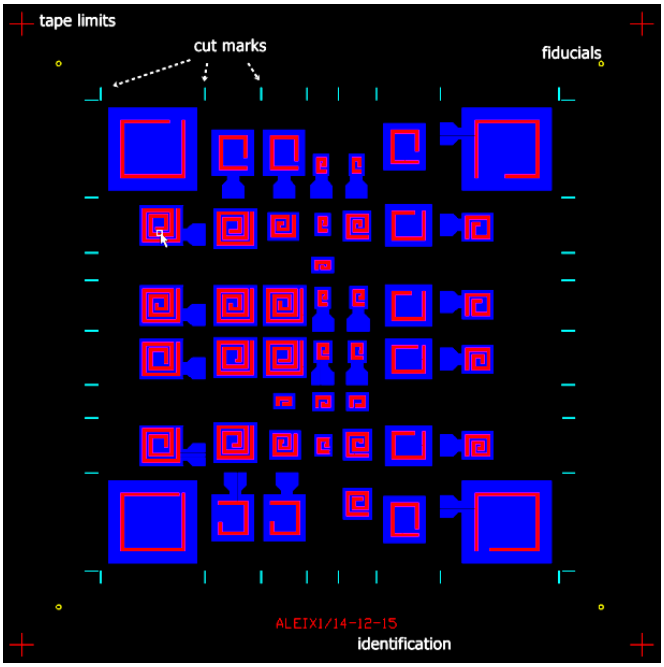

Figure 60. Mask design of a LTCC lot with several prototypes at different frequencies. In purple, the radiator paths. In blue, the groundplane. Cut marks, fiducials, tape limits and the lot identification are also indicated.

5.2.1.2. Tape Blanking

The first step in LTCC manufacturing is called tape blanking and involves cutting the green tapes with a guillotine according to the desired size (202 x 202 mm). This size is determined by the equipment available, the features of the device and the productivity desired [229]. Heraeus powder 51528B was used for the ceramic slurry formulation suitable for the casting process at FAE company. The thickness of the green tape depends on the parameters in its fabrication process, and can range from about 100 μm to 300 μm.

5.2.1.3. Punching

The function of the punching process is to drill the green tape to form the vias and the cavities in the coordinates specified by the corresponding mask (Figure 60). Dies with different shapes and sizes are available for the small holes such as vias, registers and fiducials, while for bigger cavities a method known as "nibbling" is used. This technique consists in the sequential drilling of smaller dies until the desired shape and size are achieved.

The diameter sizes used in the prototypes are 0.3 mm for the vias, 1 mm for the cavity of the Subminiature Version A (SMA) connector and the fiducials, and 3 mm for the registers.

5.1.2.4. Via Filling

The via filling is carried out with a metal paste to allow electrical connectivity between layers. The equipment used depends on the rheology of the paste, the size of the vias and the thickness of the sheet [229]. The silver paste from Heraeus (TC7304), with high viscosity, was used. To make sure that the metal paste fills the whole via, the green tape is placed on a porous base with vacuum. With the help of a plastic mask and a spatula, the paste is introduced in the vias, as shown in Figure 61. The vacuum helps the paste flow through the vias, and fills them. In addition, a light in the porous base provides a visual check of the process.

(a) (b)

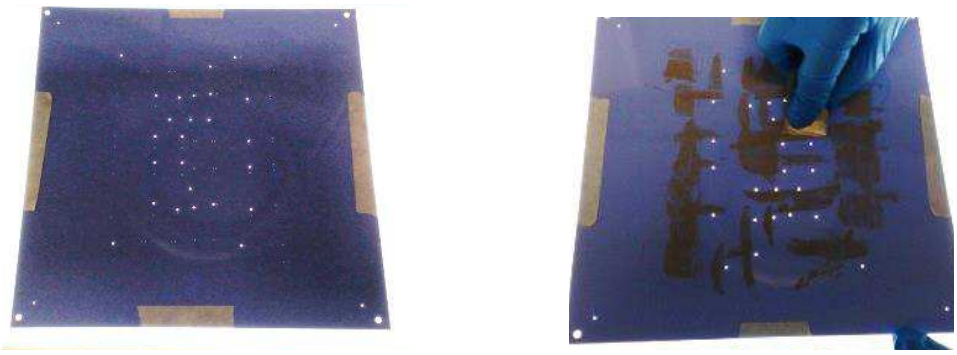

Figure 61. Example of a green tape after the punching process (a) and during the via filling process (b).

5.1.2.5. Printing

After filling all the vias with the conductive paste, the next step is to print the metallic paths in each substrate layer. The printing process and its features and challenges are clearly explained in [229]. Basically, the printing process consists in a squeegee impregnated with the metal paste that moves a screen forward with a certain pressure. The metal paste used in this study was a silver paste from Heraeus (TC7303). A negative pattern of the design is contained in the screen, allowing the metal paste to flow through a textile mesh and to be deposited on the substrate, as can be seen in Figure 62.

In multilayer ceramic technology this process requires high accuracy to ensure enough resolution and repeatability. Although the available equipment in FAE could provide a resolution of about 150 µm, the path width of the selected prototypes was raised from 300 µm to 1000 µm because of the complexity of the process. An example of the equipment used and the final result is shown in Figure 63.

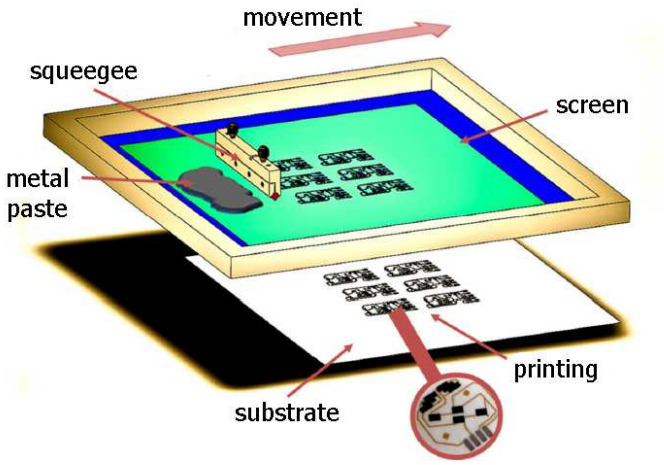

Figure 62. Sketch of the printing procedure [229].

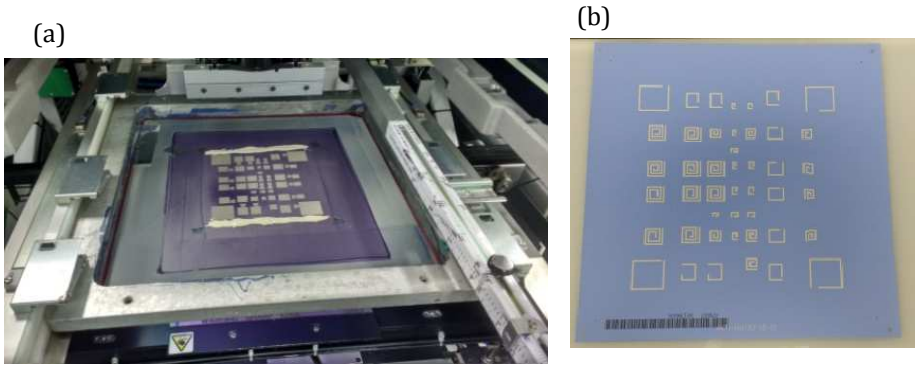

Figure 63. Equipment for the printing process (a) and result of the green tape after the printing process.

It should be borne in mind that the bottom or top layer has to include the cut marks for the posterior blanking of the individual parts.

5.1.2.6. Stacking

The stacking of the layers is carried out with a slight increase in the temperature and the pressure. Apart from putting one layer on top of the other, the stacking process has the function of properly aligning the designs, with only a few micras of error, thanks to the artificial vision and the fiducials of each layer (Figure 64).

Figure 65 shows an example of the desired final stacking profile. Yellow paths stand for metallic parts: "cond2" layer corresponds to the groundplane, "pcX" layers are the paths that conform the radiator and "pcviaX" layers are the vias. The blue layers correspond to the LTCC substrate layers.

Figure 64. Equipment of the stacking process.

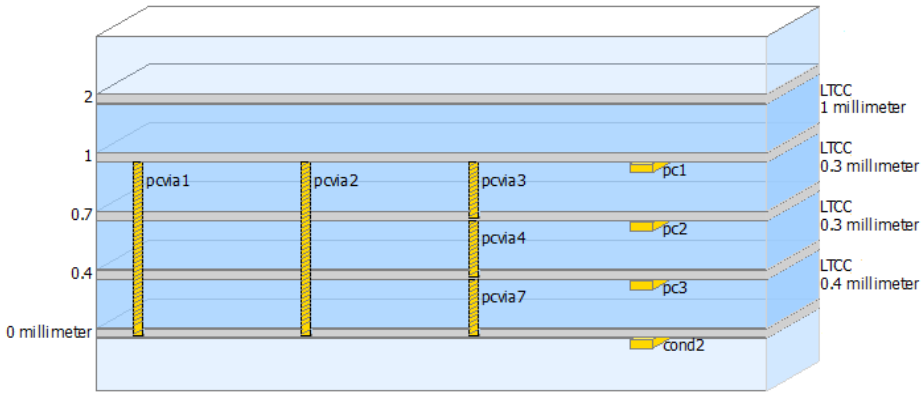

Figure 65. Profile example of a prototype with three metallic layers for the radiator ("pcX") and a metallic layer for the groundplane ("cond2"). Metallic vias are depicted with "pcviaX". The distance between layers are also expressed.

For the zero-shrinkage method, alumina layers are required on the top and the bottom of the structure.

5.1.2.7. Lamination

The lamination process performs a pressing of the whole structure at a temperature around 70 °C during 30 minutes to conform a monolithic structure. This process is critical, since after this point it is not possible to separate the layers without compromising the whole structure.

The main challenge here is to avoid deformations of cavities due to the pressing, especially in the free-sintering method. During the stacking process, the cavities can be filled with a paste made of a sacrificial material (which burns out completely before the ceramics sintering, at about 450 °C) to prevent shrinkage and deformation.

5.1.2.8. Blanking

The blanking step consists in cutting the structure in the individualized devices. This process can be done automatically or manually, depending on the accuracy required. The visible cut marks on the top layer will guide in this process, as shown in Figure 66, where alignment cameras are used in an automatic device.

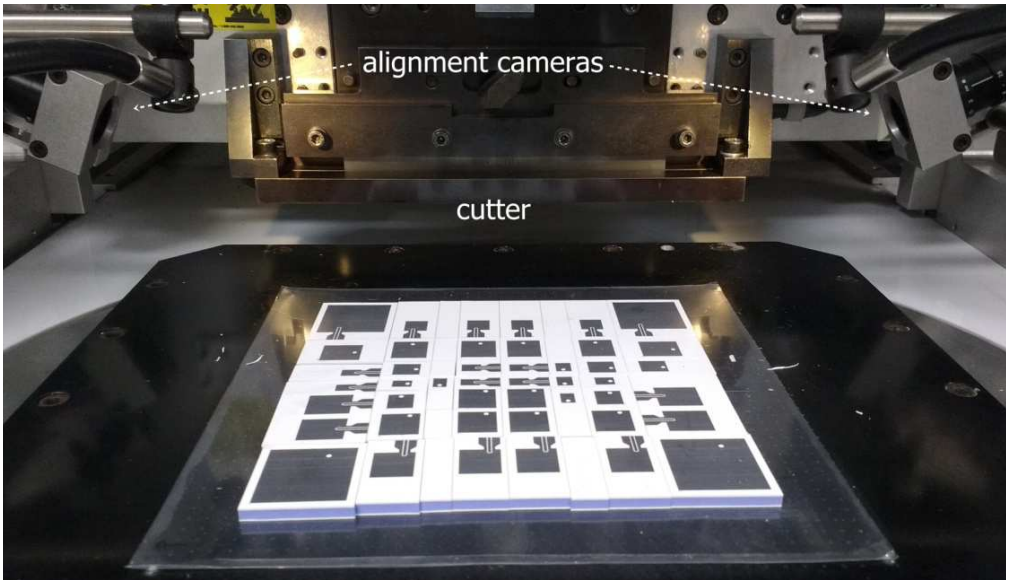

Figure 66. Blanking equipment.

5.1.2.9. Firing or Sintering

The firing or sintering is the last process before the final device is obtained. Here, the individual blocks are submitted to a complex thermal procedure inside a furnace (Figure 67), explained in detail in [229]. The first thermal cycle consists in the removal of the organic additives such as the sacrificial paste of the cavities. The

second cycle aims to sinter all the materials in a perfect hermetic monolithic structure.

The indicated thermal process for the presented prototypes was previously optimized in FAE. The first cycle consists in a temperature increase of 2 °C/min until reaching 860 °C, while the second cycle corresponds to 2 hours at 860 °C.

Examples of some of the final prototypes obtained are shown in Figure 68. Zero-shrinkage method and automatic cutting are shown in Figure 68 (a) and free-sintering and manual cutting in Figure 68 (b). For the zero-shrinkage method, the removal of the alumina layers and the cleaning of the resulting devices with ultrasounds are required.

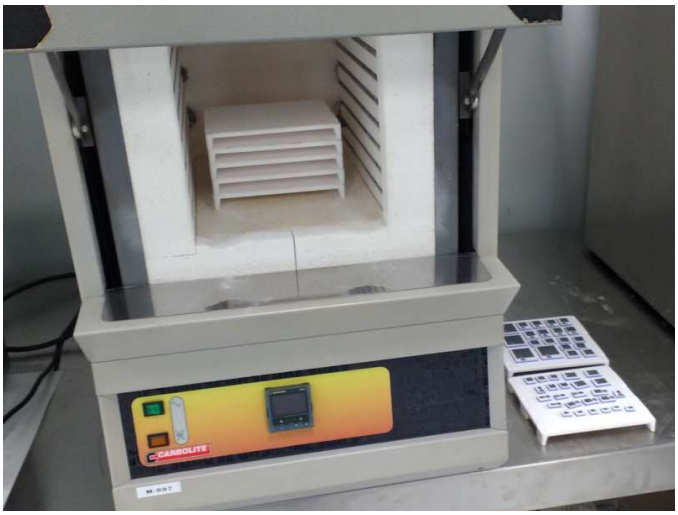

Figure 67. Furnace equipment for the sintering process.

(a) (b)

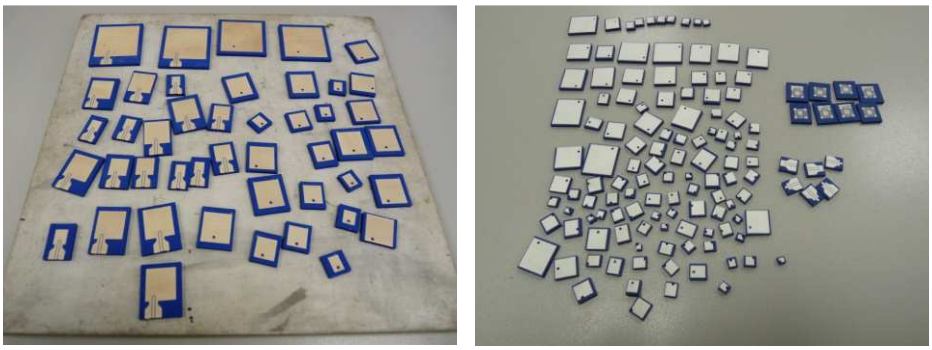

Figure 68. Final manufactured prototypes following the zero-shrinkage method (a) and the free-sintering method (b).

5.1.2.10. Assessment of the LTCC Fabrication Process

The prototypes chosen for the experimental characterization correspond to the 2D and 3D square spirals at 403 MHz presented in the previous chapters ("2d2h" and "3d2h" respectively, henceforth called "2d403" and "3d403" respectively). Their counterparts at the resonant frequencies of 866 MHz and 2.45 GHz have also been selected for measurements ("2d866", "3d866", "2d2450" and "3d2450" respectively). 2D antennas at the three frequencies of study with a radiator width of 0.3 mm have also been assessed, as shown in Figure 69, as proof of feasibility of manufacturing smaller designs (prototypes "2d403t", "2d866t" and "2d2450t"). Table 31 summarizes the prototypes presented and their dimensions. Skin cubic phantoms of 10 mm are used to mimic the body tissue properties, prepared as indicated in Subsection 2.4.3.

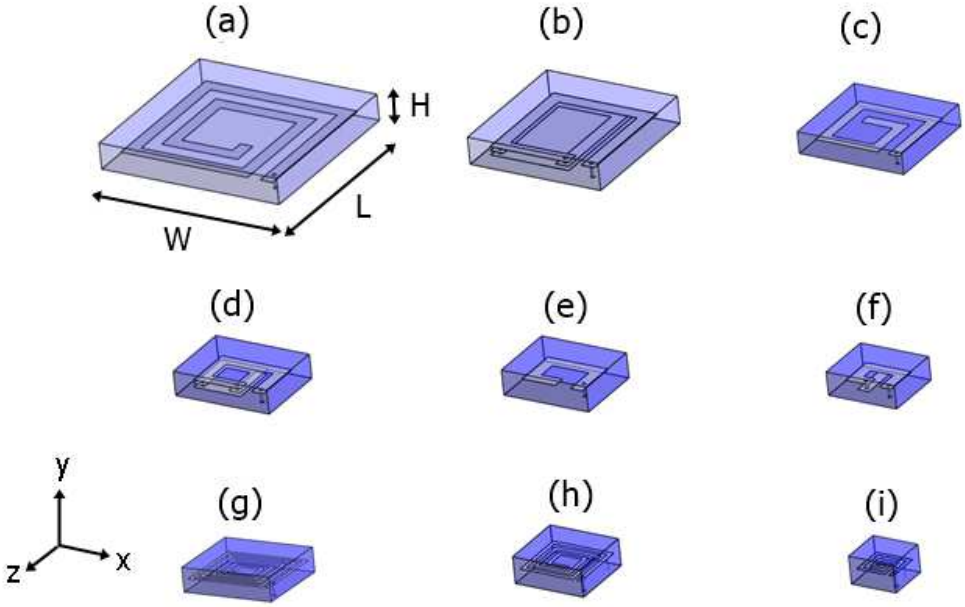

Figure 69. Selected final prototypes: (a) 2d403, (b) 2d866, (c) 2d2450, (d) 3d403, (e) 3d866, (f) 2d2450, (g) 2d403t, (h) 2d866t, (i) 2d2450t.

Table 31. Dimensions of the selected antennas.

Prototype	Config.	Frequency	Volume (mm^3)	W (mm)	L (mm)	T (mm)
2d403	2D	403 MHz	364	14	13	2
3d403	3D	403 MHz	200	10	10	2
2d403t	2D	403 MHz	100.32	7.6	6.6	2
2d866	2D	866 MHz	180	10	9	2
3d866	3D	866 MHz	96	8	6	2
2d866t	2D	866 MHz	53.76	5.6	4.8	2
2d2450	2D	2.45 GHz	77	7	5.5	2
3d2450	3D	2.45 GHz	60	6	5	2
2d2450t	2D	2.45 GHz	19.8	3.3	3	2

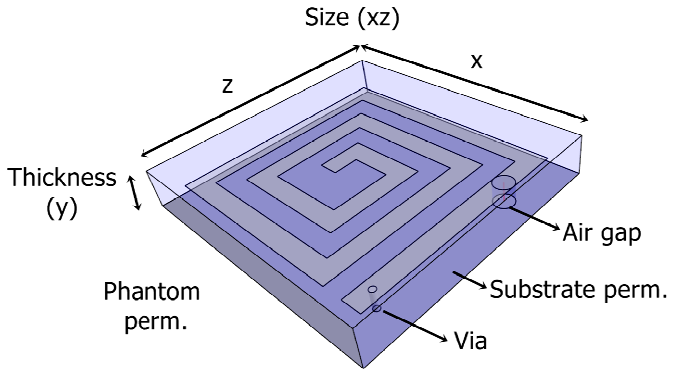

Figure 70. 3D perspective of the sensitivity test parameters.

In order to quantify possible errors in the antenna performance due to the fabrication processes, sensitivity tests of several relevant parameters are performed. In [104] various sensitivity tests were carried out to identify and quantify sources of potential experimental uncertainties, such as the gluing effect, the antenna radius, the patch alignment, the substrate permittivity, the electrical properties of the phantom or the relative location of the antenna in the phantom. In our case, simulations of relative frequency detuning as a function of small variations in antenna parameters and the surrounding permittivity are assessed in the three frequencies and the 2D configurations (Figure 70).

5.2.2. Phantom Realization and Characterization

In accordance with the characterization protocol suggested in Subsection 4.3.7, 100 mm cubic and homogeneous phantoms have been used in the laboratory. The low-cost recipes have been taken from [230] and are available online at [231]. These recipes are based on salt, sugar and deionized (or distilled) water. As the relative permittivity of the distilled water is about 80, the addition of sugar allows its reduction up to nominal values of biological tissues. The conductivity is basically increased by adding salt, which also raises the permittivity slightly [75].

The manufactured phantom liquids are characterized with the commercial complex permittivity measurement system Agilent Technologies 85071E, together with the HP8720C network analyzer and the software provided by the company. A coaxial open-ended probe is inserted in a cuboid shell filled with the liquid, as shown in Figure 71. The calibration process is based on the measurement of open, short and water at 20° C (water properties are closer to liquid phantom properties).

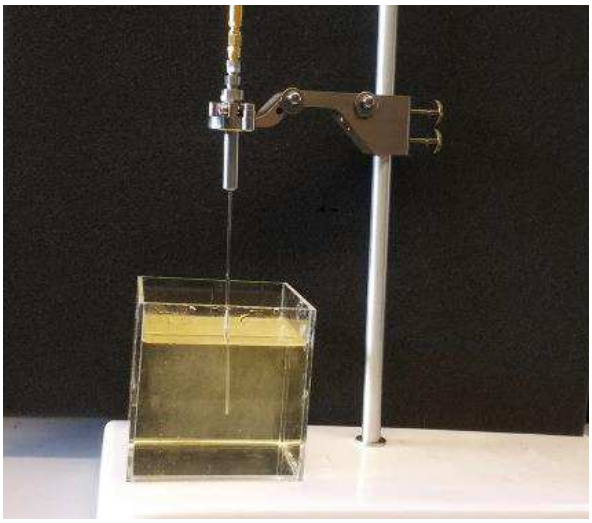

Figure 71. Characterization set up of the dielectric properties of liquid phantoms.

5.2.3. Antenna Characterization

The experimental measurements of in-body antennas are carried out using the typical configuration for this purpose: a coaxial cable and a direct connection through a SMA connector. Antennas are implanted in the center of a 100 mm cubic, homogeneous and liquid phantom.

The most relevant prototypes, presented in Table 31, are experimentally characterized through the reflection coefficient.

A modification of the Equation 14 presented in Subsection 2.3.9 is used to estimate the measured gain from the received power, defined as:

$$G_{AUT}\ (dBi) = G_{ref} + \left(P_{AUT} - P_{ref}\right) \qquad (16)$$

where G_{AUT} is the estimated gain of the tested antenna (dBi), G_{ref} is the simulated gain of a reference antenna (dB), P_{AUT} is the measured received power of the tested antenna (dB) and P_{ref} is the measured received power of the reference antenna (dB). Both antennas have to be fed by the same power and have to resonate at the same frequency.

A detailed analysis of the issues found when measuring in-body antennas is presented with the aim of understanding and minimizing differences between experimental results and simulations. Several solutions for overcoming these mismatches in the results are proposed. Moreover, the addition of a coplanar launcher in the antenna connection is also presented in order to facilitate the manufacturing.

5.3. Results and Discussion

In this Subsection I discuss the most relevant issues related to the fabrication of the LTCC prototypes. A range of frequency detuning tolerance is assessed from the results obtained in the sensitivity tests. The results of the aforementioned characterization methods for eliminating the coaxial cable effects are also presented and discussed. Reflection coefficient characterization through a coplanar launcher and a splitter are compared to direct coaxial feeding. A first approach of the radiation pattern and gain measurements by means of an optical fiber link is also presented.

5.3.1. Prototyping in LTCC Technology

Although many fabrication lots have been developed in this thesis, only the most relevant manufactured antenna prototypes and the most important results in their fabrication process will be shown here.

In Figure 72 (a) fabricated antennas with the free-sintering method and resonating at 403 MHz (left side), 866 MHz (middle) and 2.45 GHz (right side) are presented. The difference in size depending on the operating frequency is observable immediately. For the smaller prototypes, the SMA connector soldering is a challenge. The manual cutting used in this case allows removal of the substrate behind the limit marked by the groundplane. Figure 72 (b) shows antennas fabricated with the zero-shrinkage method and automatic cutting, which maintains undesired substrate behind the groundplane (shown in blue). In practical terms, this is equivalent to considering a decrease in the effective electrical permittivity surrounding the antenna.

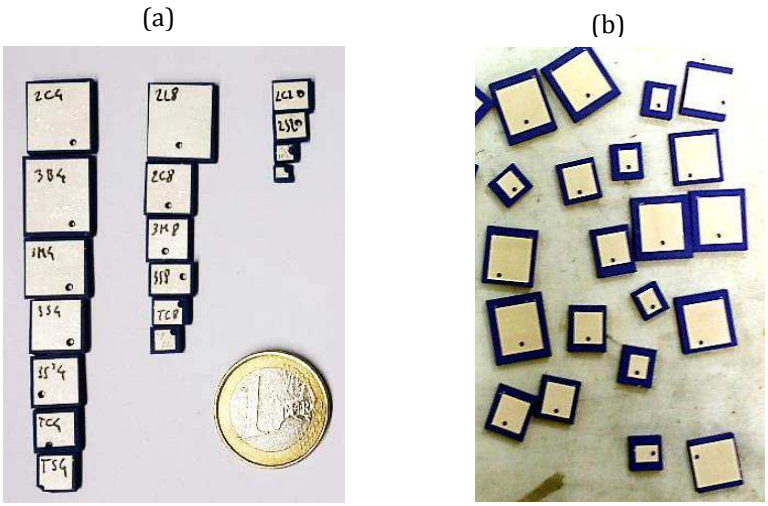

Figure 72. Example of manufactured antennas in LTCC technology: (a) with the free-sintering method and manual cutting and (b) with the zero-shrinkage method and automatic blanking.

Certain parameters of the physical properties of the manufactured antennas have been studied. Figure 73 presents a detailed view of the air gap or cavity where the inner conductor of the connector is placed. Notice the significant misalignment between the punching of the hole and the printing of the serigraphy, especially in Figure 73 (a). If this misalignment were more accentuated, a short circuit between the groundplane and the inner conductor of the connector might cause complete antenna malfunction. On the other hand, whereas the diameter of the cavity shown in Figure 73 (a) is equal to 0.934 cm, in Figure 73 (b) it measures 0.834 mm. Such differences can lead to a frequency detuning because of a sudden change in the electrical properties of the medium in such close proximity from the feeding point.

Differences in the color of both the LTCC substrate and metallization in the two prototypes of Figure 73 are due to the fact that Figure 73 (a) applied the zero-shrinkage method while Figure 73 (b) was manufactured via free-sintering. In the zero-shrinkage method, part of the alumina remains attached to the silver, darkening its color. Apart from the color, other changes arise in the profile of an antenna with zero-shrinkage firing, as in Figure 74; it can be seen that there is absence of contraction only in the superficial layers, but in the middle layers there is shrinkage of about 0.175 mm, thus altering the real size of the radiator and therefore the antenna performance. In the same picture, the thickness of the substrate measures 2.078 mm, but this depends on several factors such as (among others) the position of the antenna in the mask, or the choice of the sheets conforming the substrate.

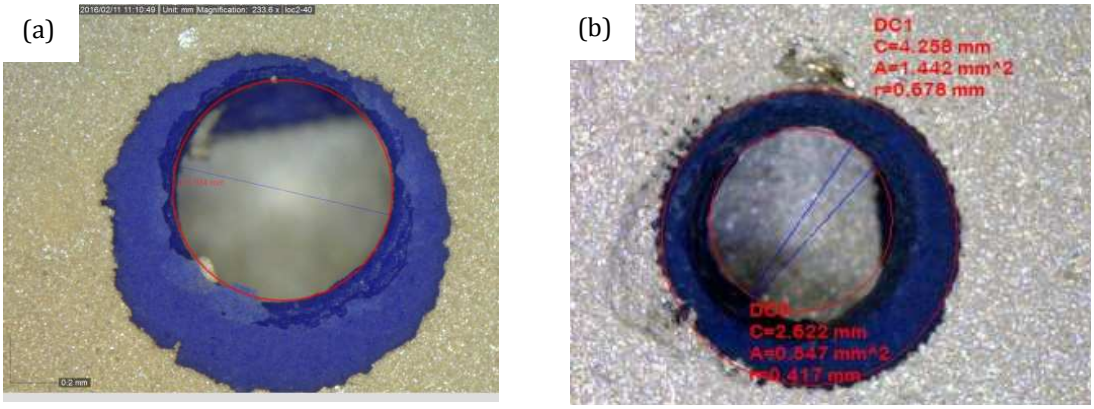

Figure 73. Detailed views of the cavity for the SMA connector in the direct connection feeding. Antenna in (a) used the zero-shrinkage method while antenna in (b) used free-sintering.

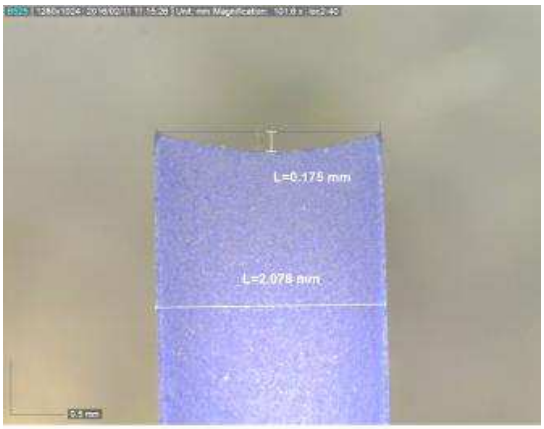

Figure 74. Profile detail of an antenna manufactured with the zero-shrinkage technique. A significant shrinkage can be appreciated in the center of the substrate.

Another source of error is the diameter of the vias due to layer misalignment and the fact that the sacrificial paste in the cavity is not perfect. Thus, the resulting via is not a perfect cylinder, contrary to the assumptions in simulations. The X-ray images allow us to see inside the prototypes (Figure 75). The irregular shape of the via is noticeable in the profile view (Figure 75 (b)).

Although most of the prototypes have been designed with a radiator width of 1 mm due to the complexity of the fabrication process, some antennas with radiators of 0.3 mm-width have also been manufactured. To avoid short circuiting in the radiator, the cavity for the SMA connector had to be shifted towards the external part of the substrate, as seen in Figure 76. The problem then appeared when trying to connect the SMA connector in such a small part of the radiator, causing malfunctioning in many of the prototypes. Another issue related to the cavity for the connector is that its placement is so close to the edge that this may lead to the rupture of the substrate, as can be seen in Figure 76 (b).

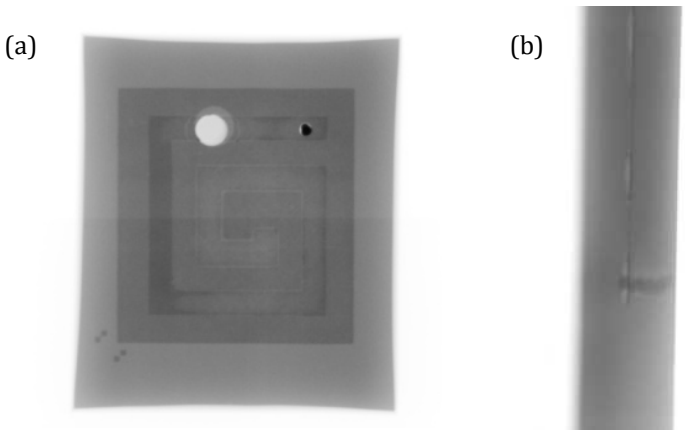

Figure 75. X-ray images of a manufactured antenna: (a) frontal view and (b) lateral view. The metallic via shows an irregular shape.

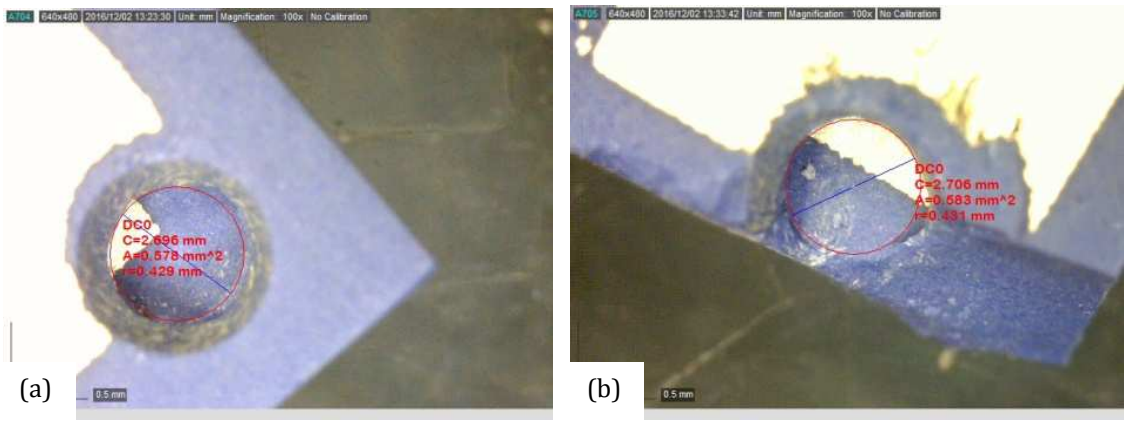

Figure 76. Detailed views of the air cavity in thinner prototypes.

5.3.2. Sensitivity Tests

Because of the aforementioned physical issues concerning the fabrication of LTCC antennas, sensitivity tests of some of the parameters in Figure 70 were carried out. Results of the relative frequency detuning for prototypes operating at the three frequencies of interest are shown in Figure 77.

The results in Figure 77 show that the most relevant parameters in terms of frequency detuning are the substrate permittivity and the horizontal size (Figure 77 (b) and (c), respectively), leading to variations of up to ± 10% for the range of study selected. In the case of the substrate permittivity, it should be borne in mind that every time a new lot of the green tape is created, slight variations in the material composition may lead to changes in the electrical parameters of the substrate. In addition, the whole fabrication process itself has to be controlled to a sufficient degree to guarantee a minimum error in the electrical properties of the substrate. Therefore, it is strongly advisable to accurately characterize the substrate permittivity and conductivity before manufacturing a new lot. For its part, the scale factor is determined by the sintering method used: either zero-shrinkage or free-sintering. The former ensures a null scale factor in the superficial layers but not in the middle, as seen in Figure 74; the latter presents a constant horizontal scale factor of 0.88 for all the substrate, and is thus the more reliable method.

The influence of the other parameters studied is less relevant, as seen in Figure 77 (a), (d), (e) and (f), where in most cases the frequency detuning is less than 0.6%. Hence, in the frequency characterization of the antennas, the phantom permittivity may have small variations without compromising the frequency detuning (Figure 77 (a)). Phantom recipes of salt, sugar and distilled water are therefore indicated for this purpose. The substrate thickness does not exceed 100 μm in any case (scale from 0.95 to 1.05), resulting in a frequency detuning of less than 0.4% (Figure 77 (d)).

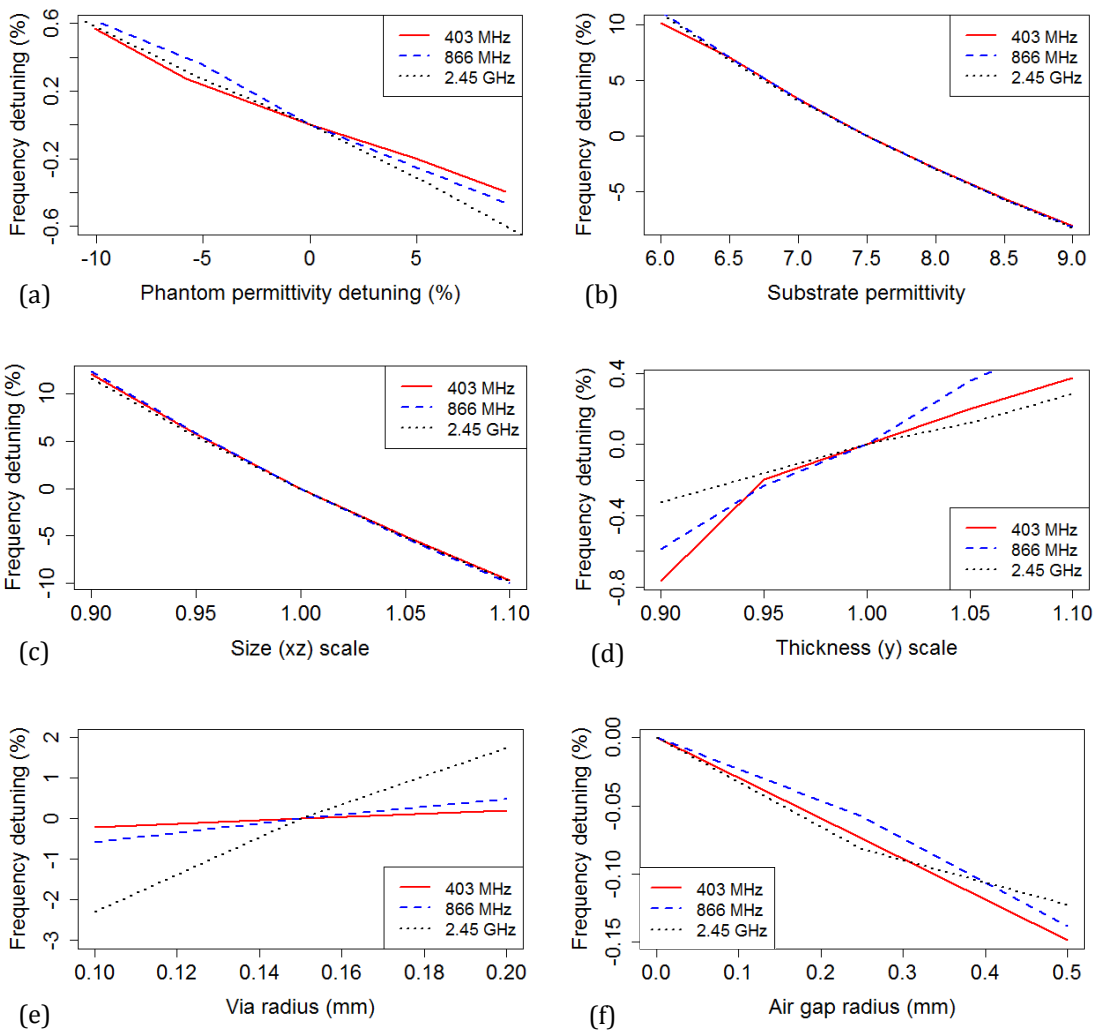

Figure 77. Sensitivity test results for the selected parameters: (a) phantom permittivity detuning, (b) substrate permittivity, (c) horizontal size scale, (d) thickness scale, (e) via radius and (f) air gap radius.

Whereas the size of the vias is not significant for the lower frequencies, as can be seen in Figure 77 (e), it can be critical for the antennas operating at 2.45 GHz. This can be controlled by improving the alignment of the layers and by determining the scale factor of the cavity (in spite of the sacrificial paste). The cavity for the placement of the inner conductor of the SMA connector was found to be almost negligible for the frequency detuning (Figure 77 (f)).

Taking all these considerations into account, a tolerance error of the frequency shift of around 2% due to the fabrication process will be tolerated.

5.3.3. Dielectric Properties of Manufactured Phantoms

Dielectric properties of the manufactured skin-based 100 mm cubic phantoms at the three selected frequencies are shown in Table 32. It can be observed that the higher the frequency, the greater the differences between theoretical and measured results. It is also noticeable that conductivity values in the frequency band of 2.45 GHz were not achievable with these recipes because the targeted value was outside the feasible range. Thus, a larger bandwidth is expected in that frequency, due to the increase in losses.

Table 32. Recipes, targeted and measured dielectric properties of liquid skin phantoms at a temperature of 20 °C.

	Recipe (g)			**Targeted values**		**Measured values**	
Frequency	**Water**	**Sugar**	**Salt**	**ε_r**	**σ (S/m)**	**ε_r**	**σ (S/m)**
403 MHz	500	736.4	31.5	46.7	0.69	47.5	0.6
868 MHz	500	721.9	11.7	41.6	0.86	40	0.76
2.45 GHz	500	517.6	18.9	38	2.8*	33.6	2.49

*The targeted value should be 1.46, but it is not achievable with these recipes.

5.3.4. Experimental Characterization of In-body Antennas

The preliminary characterization of the in-body antennas proposed in the previous two chapters, and summarized in Table 31, is presented here. Figure 78 shows the measured and simulated reflection coefficients of the selected prototypes. For the antennas operating at 403 MHz (Figure 78 (a) and (b)), we can observe a frequency detuning of 2 MHz and 8.3 MHz for the 2D and 3D prototypes, respectively (i.e., a relative frequency detuning of 0.5 % and 2.1 %, respectively). Differences in the S_{11} level between simulations and measurements are more relevant (12 dB and 6.4 dB for the 2D and 3D prototypes, respectively). For the antennas operating at 866 MHz (Figure 78 (c) and (d)), the relative frequency detuning is 1.2 % in the 2D design and 1.6 % in the 3D design, while S_{11} levels vary from 2.1 dB in the 2D antenna to 11.5 dB in the 3D prototype. Regarding the antennas operating at 2.45 GHz (Figure 78 (e) and (f)), the relative frequency detuning increases up to a 2.9 % for the 2D model and 0.8 % for the 3D antenna. The S_{11} levels between simulations and measurements change less than 1 dB in the 2D model but 12.6 dB in the 3D one.

Figure 78 (g) and (h) depict the reflection coefficient of the prototypes 2d403t and 2d866t, which show similar behaviors to their counterparts at the same frequency. The manufacturing of antennas of this kind with thinner radiators in LTCC technology presents promising results.

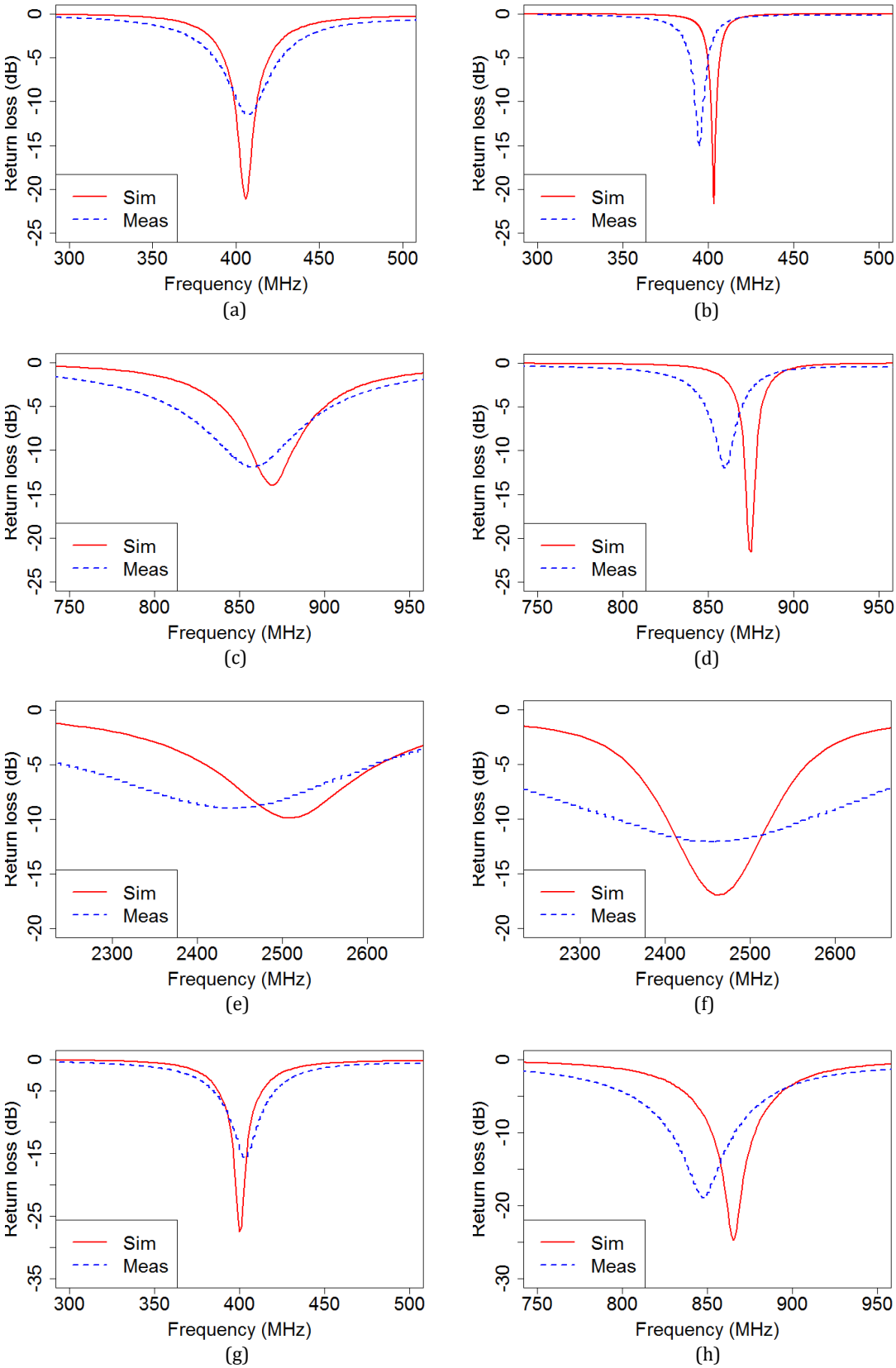

Figure 78. Preliminary reflection coefficient measurements and simulations of the prototypes presented in Table 31: (a) 2d403, (b) 3d403, (c) 2d866, (d) 3d866, (e) 2d2450, (f) 3d2450, (g) 2d403t and (h) 2d866t

As mentioned in the previous Subsection 5.3.2, a relative frequency detuning of up to 2% is tolerated due to the inaccuracies in the manufacturing process. The results indicate that the frequency detuning is, in general, within that range. However, in certain cases this 2% of tolerance is exceeded, suggesting that the measurement setup is also a source of errors. In addition, differences in the S_{11} levels are significant in most cases. In the next section, improvements in the measurement setup to suppress the coaxial cable influence on the measurements are proposed.

Another issue regarding the measurement setup is the fragility of the SMA welding in the groundplane. Indeed, the metallic layer of the groundplane of several prototypes broke during the measurement process. Therefore, a solution for improving the robustness of the SMA connection by means of a coplanar launcher is considered.

The characterization of the far-field features of the proposed antennas will be assessed according to these measurement improvements.

5.4. Improvements in the Measurement Setup

In view of the results presented in the previous Section, and in order to understand the influence of the measurement setup on the measures, a revision of the theoretical aspects involving in-body antenna measurements is presented here.

As already explained in Subsection 2.3.10, several measurement challenges arise when dealing with ESAs located in an in-body scenario. In general, the measurement of in-body antennas is performed by a coaxial cable, as this avoids complex and costly system measurements. However, antennas surrounded by biological tissues become inefficient and the effect of the coaxial cable in radiation parameters cannot be treated as negligible.

In [14] a theoretical statement of the problem is presented (Figure 79). On the one hand, unbalanced feeding (such as coaxial cables) interacts with ESA, significantly modifying the antenna performance. As illustrated in Figure 79 (a) [14], the current distributions of the back side of the groundplane flow to the outer conductor of the cable, generating new radiated fields and altering the measurements in free space. On the other side, when implanting an ESA into a lossy medium (Figure 79 (b) [14]), the currents on the coaxial cable couple with the lossy medium leading to a dissipated field that also affects the antenna characterization.

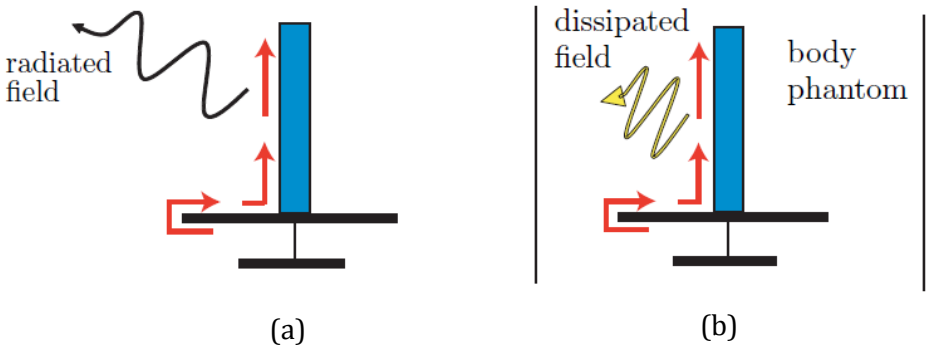

Figure 79. Illustrations of the current distribution (red arrows) due to the presence of a coaxial cable to feed an ESA, shown in [14]: (a) the currents on the cable contribute to the radiated field (black arrow) in free space, while in (b), when a body phantom surrounds the antenna, these currents dissipate in the biological tissue (yellow arrow).

The consequences of the radiated and dissipated fields that appear due to the unbalanced feeding and the body phantom are resonant frequency shifts and variations in the radiation parameters. Indeed, if the antenna radiation efficiency is low enough, fields radiated due to the coaxial cable may be the main contribution in radiation measurements. Therefore, discrepancies between radiation patterns found in simulations and in measurements are difficult to prevent, as seen in [232], where significant differences appear between simulated and measured radiation patterns.

Several solutions have been proposed in the literature to address these issues. Most classical solutions involve the addition of baluns, chokes or ferrites to reduce the current flow in the coaxial cable, as described in [61], [96], [161] and [157]. To measure the reflection coefficient, the work presented in [61] uses a choke, whereas magnetic beads inside a plastic tube are picked up in the antenna proposed in [96]. In addition, in [96], the feeding and measurement cables are carefully positioned and foam absorbers are used to enclose the cables in the measurement setup and to measure gain radiation patterns. In [157], a ferrite-core material along the coaxial cable provides a measured radiation pattern in good agreement with simulations. A quarter-wavelength balun is used in [161] to ensure maximum transmission efficiency.

In the antenna prototype proposed in [83] the presence of a coaxial cable surrounded by a vacuum shell and a reduced implant depth in the body phantom in order to mitigate the effect of the coaxial cable are both discussed. The authors point out the difficulty of measuring the radiation pattern due to the exact location of the antenna in the phantom, the feeding coaxial cable and the liquid phantom itself. Thus, only measurements of the horizontal radiation pattern are carried out. Transmission levels of the same antenna are evaluated further in [14] when the

antenna is already integrated with the whole IMD, therefore avoiding the cable effects. Fiber optics has been proposed as a promising technology to measure radiation features without cable interferences. In another study presented by the same group, in [228], it is demonstrated that the effect of the coaxial cable is reduced when the groundplane is in direct contact with the phantom. In that situation, the current distributions flowing in the back side of the groundplane are attenuated by the high losses of the phantom, preventing them from flowing to the outer conductor of the coaxial cable.

According to these considerations and also other manufacturing issues, I present three methods to improve the measurements of in-body antennas:

- A coplanar launcher as a feeding method to facilitate the soldering of the SMA connector.
- A splitter as a balun to reduce the currents flowing back to the coaxial.
- A radiation pattern measurement setup based on a fiber optics link as a first approach to reduce the effect of metallic interferences in radiation.

The main goal of the first method is to facilitate the manufacturing process, while the second one aims to enhance the reflection coefficient characterization. The aim of the development of the fiber optics link is basically to improve the radiation pattern measurement.

5.4.1. Feeding Connection

A critical point when experimentally characterizing in-body antennas is the connection between the radiator and the coaxial cable, especially when the antenna radiator, which has to be connected to the inner coaxial conductor, is surrounded by the substrate. In this case, the soldering of both parts may become a really hard task. Two methods have been explored and evaluated in terms of the reflection coefficient and radiation pattern to solve this problem (both using a SMA connector): a coplanar launcher and a direct connection.

Computational simulations of the two configurations have been carried out to determine the reflection coefficient and the radiation pattern. The results are compared to the “ideal” feeding, illustrated in Figure 80 (a). For the feeding of the coplanar launcher, a feed point to coaxial transition has been performed (Figure 80 (c)).

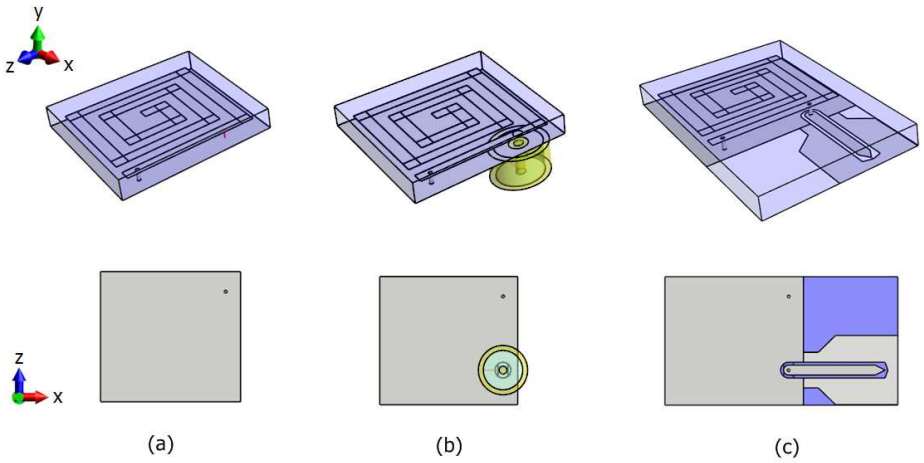

Figure 80. 3D perspective of the feedings connections: (a) "ideal" feeding, (b) direct connection and (c) coaxial launcher.

Direct Connection

This technique consists in placing the SMA connector directly in the radiator, as shown in Figure 80 (b). A 1 mm-diameter cavity allows the inner conductor of the SMA connector to pass through the first 1 mm of substrate and to reach the radiator. The difficulty lies in the welder of the inner conductor of the SMA connector, since it is not accessible. One solution consists in exerting a certain pressure between the SMA connector and the antenna and then soldering the outer conductor to the groundplane. An air gap will remain in the cavity as the SMA inner conductor has a diameter of 0.8 mm. The advantage of this configuration is that the coaxial cable is behind the groundplane, reducing its effects on the antenna performance. Direct connection was the feeding method used in Subsection 5.3.4 to perform the preliminary characterization of the antennas.

Coplanar Launcher

In this method, a coplanar launcher is used as a transition between the SMA connector and the radiator. During the LTCC manufacturing process, a via filled with metal paste is placed instead of a cavity. The groundplane is then modified according to Figure 80 (c) and is directly connected with the coplanar launcher. The advantage of this configuration is the simplicity of the SMA connector welding. However, as the coaxial is not behind the groundplane, it may significantly modify the behavior of the antenna, both in terms of frequency detuning and in terms of variations in the radiated fields.

To mitigate the frequency detuning and to suppress the resistive losses due to the coplanar launcher, a calibration of the connector is required. The calibration

process consists in determining the first-order reactive parameters (inductive and capacitive) when shortening and opening the output of the coplanar launcher connector (Figure 81 (a) and (b), respectively) and immersed in the phantom liquid. The equivalent reactive parameters are then calculated by means of the launcher impedance in each case:

$$Z = 50\frac{1+S_{11}}{1-S_{11}} \qquad (17)$$

where S_{11} is the launcher return loss in each case.

The equivalent first-order reactive component of the open circuit corresponds to parallel capacitor:

$$C_{eq} = \frac{imag(Y)}{2\pi f} \qquad (18)$$

where $imag(Y)$ is the imaginary launcher admittance in an output open circuit.

The equivalent first-order inductive parameter of the short circuit consists in a series inductor, defined in Equation 19,

$$L_{eq} = \frac{imag(Z)}{2\pi f} \qquad (19)$$

where $imag(Z)$ is the imaginary launcher impedance in an output short circuit.

The values of the reactive components are then considered directly in the network analyzer when characterizing the antennas.

Table 33 presents values for the reactive parameters of manufactured open and short circuits (Figure 81) for the three frequencies. These parameters are introduced in the Network Analyzer for calibration purposes. In addition, the resistive losses of the coplanar launcher when immersed in the phantom liquid and found in the calibration process are also introduced in the model of the Network Analyzer.

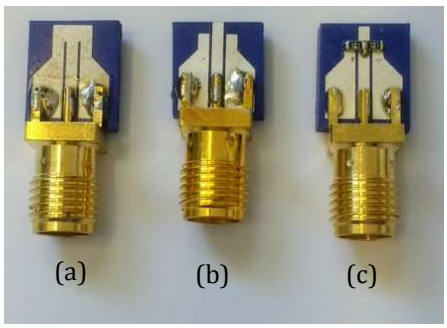

Figure 81. Manufactured coplanar launchers used for calibration purposes: (a) short circuit, (b) open circuit and (c) load of 50 Ω.

Table 33. Values of the reactive equivalent components of the coplanar launcher calibration.

Frequency	Short circuit, L_{eq} (nH)	Open circuit, C_{eq} (pF)
403 MHz	0.181	1.403
866 MHz	0.178	0.828
2.45 GHs	0.157	0.851

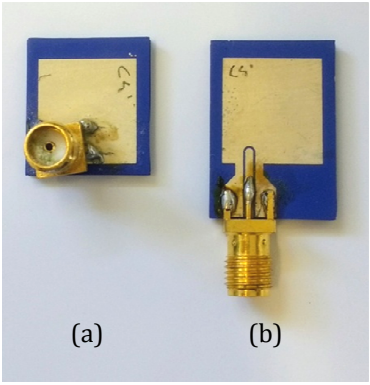

Figure 82. Manufactured prototypes working at 403 MHz (a) with direct feeding and (b) coplanar launcher feeding.

Figure 82 shows a zero-shrinkage manufactured prototype operating at 403 MHz fed by the direct connection and the coplanar launcher (Figure 82 (a) and (b) respectively).

To compare the effect of the feeding method on the frequency detuning of the antenna, simulated results of the reflection coefficient are plotted in Figure 83. In Figure 83 (a) the measurement of the direct connection feeding is compared to the simulations of the direct connection as well as the coplanar launcher feedings. There is an appreciable shift of 5 MHz between direct connection measurements and simulations, mainly due to the absence of a device preventing the currents from flowing back to the outer conductor, although they are close to the tolerance range set by the sensitivity tests. A shift of 17 MHz is observed between simulations of the two feeding methods. Simulated results of the coplanar launcher show high losses beyond the operative bandwidth as a consequence of its direct contact with the lossy phantom.

Figure 83 (b) shows the measurements of the antenna fed by the coplanar launcher before and after the calibration. While the measurement without the calibration also shows resistive behavior throughout the frequency range, in the measurements after the calibration these losses are no longer present. This is due to the compensation of the resistive losses made during the calibration process. However, a difference of 11 MHz in the resonant frequency remains with respect to the simulation of the direct connection.

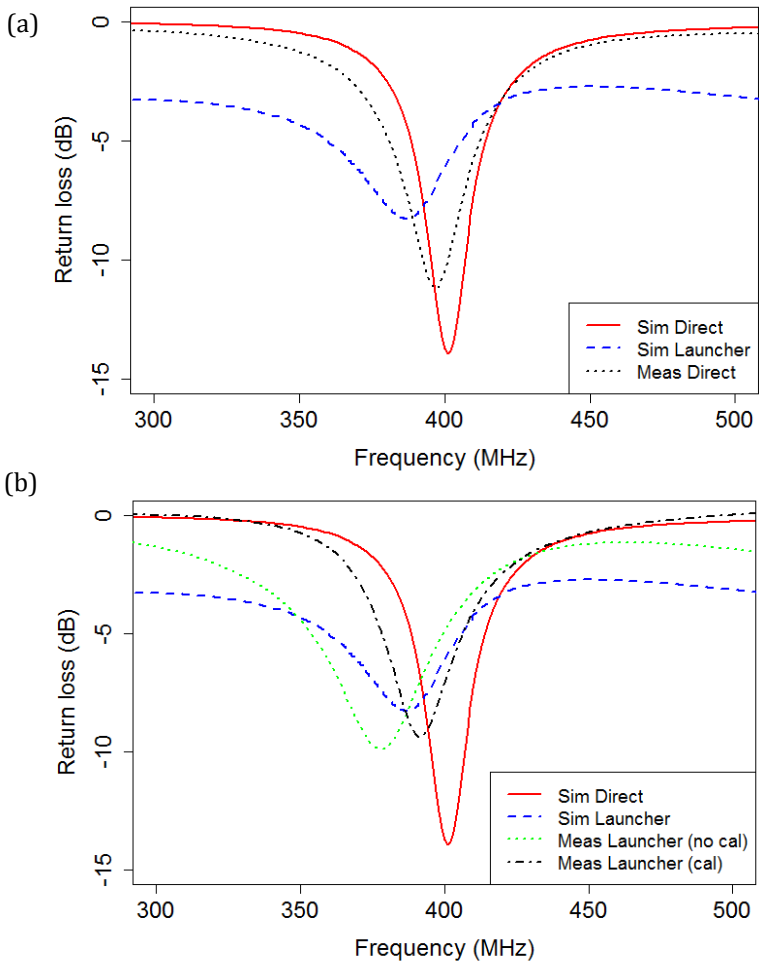

Figure 83. Reflection coefficients of manufactured prototypes working at 403 MHz with different feedings: (a) direct connection and (b) coplanar launcher.

In order to assess the influence of the feeding method on the radiation pattern, simulations of the 2d403 and the 2d866 antennas are performed for different cases. In Figure 84 the simulated radiation patterns of the 2d403 antenna in both feeding setups are compared to the ideal situation (see Figure 80) for the three planes. Results indicate that the direct connection is more similar to the ideal situation than the coplanar launcher, although few changes can be observed. However, a rise in the frequency increases these differences, as seen in Figure 85, where radiation patterns of the 2d866 antenna are depicted.

In view of the results, the coplanar launcher should only be employed when characterizing antennas at low frequencies, such as the MedRadio band, in order to facilitate the soldering process of the SMA connector. However, due to significant variations in the radiation pattern, we do not support its use for far-field characterization at higher frequencies.

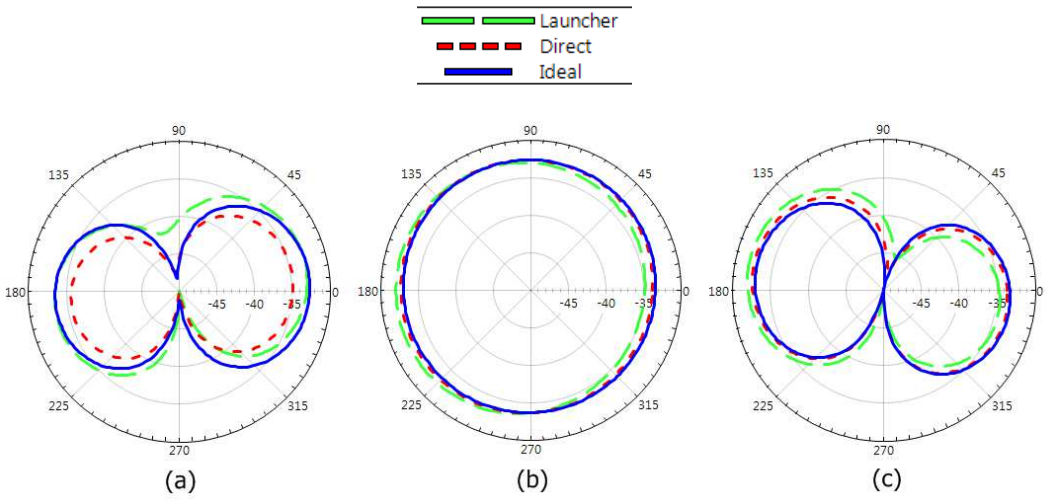

Figure 84. Gain radiation pattern at 403 MHz. (a) xy-plane, (b) xz-plane, (c) yz-plane.

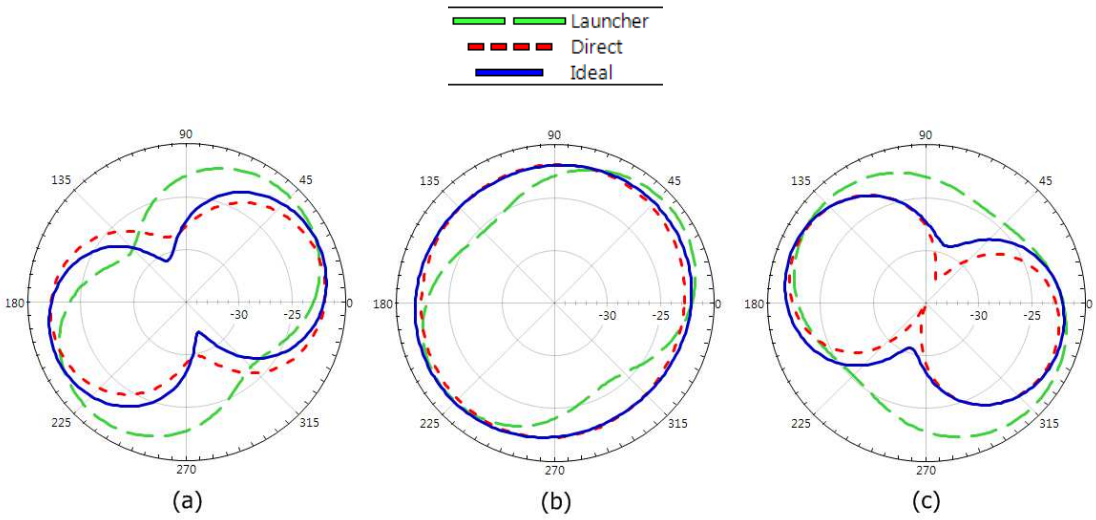

Figure 85. Gain radiation pattern at 866 MHz. (a) xy-plane, (b) xz-plane, (c) yz-plane.

5.4.2. Balancing the Feeding

PIFA antennas are generally classified as unbalanced, mainly due to the groundplane that means that most of the radiation is performed only in the radiator. However, in practice, if the groundplane is not large enough (as usually happens in ESA) it also contributes to the radiation, with the PIFA as a kind of balanced antenna and the coaxial cable a distortion element. This behavior directly affects both the resonance frequency and the far-field features. In order to minimize these unwanted effects in the reflection coefficient measurement, here I present an alternative solution involving a power splitter, used as a transition component from an unbalanced to a balanced signal. The splitter selected is the SCPJ-2-9 model from Mini Circuits [233], which works from 200 to 900 MHz. To be

used as a balun, the splitter must have a phase shift of 180 degrees. The advantage of using an splitter as a balun instead of a choke is that the choke acts as a common mode filter, whereas the balun makes a conversion from the common mode (unbalanced) to the differential mode (balanced). The remaining signal in common mode when using a balun is significantly smaller.

Figure 86 and Figure 87 display the procedure for measuring antennas with the power splitter. First, the 3-port transmission levels of the splitter are measured. Then, the 3-port splitter is converted into a 2-port component through the ADS software [172], and it is connected virtually to the measures of the antennas, as indicated in Figure 86 (b). Then, the resulting de-embedding of the circuit provides the reflection coefficient of the antenna treated as a balanced antenna, without the currents coming back through the coaxial cable. Reflection coefficient measures of the 2d403 prototype with and without the splitter are carried out and compared to the simulations.

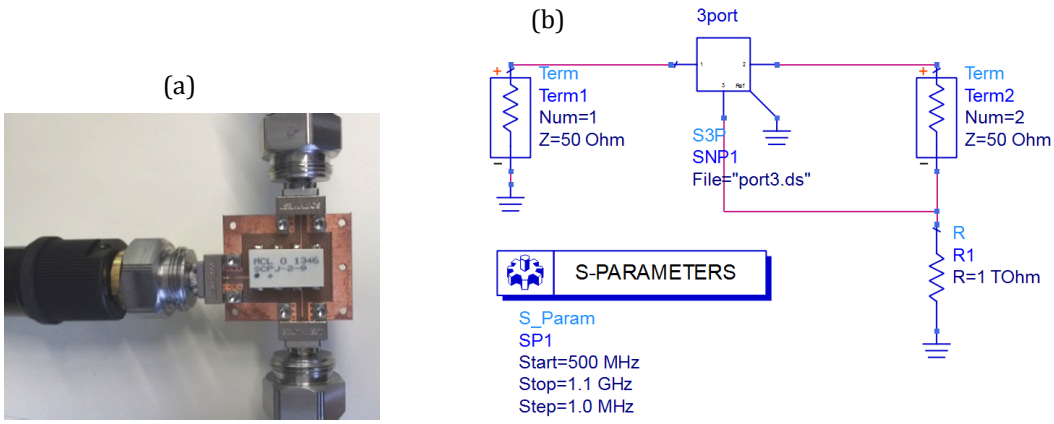

Figure 86. (a) Splitter connected as a 3-port for calibration purposes and (b) circuit used in ADS software to transform the 3-port to a 2-port.

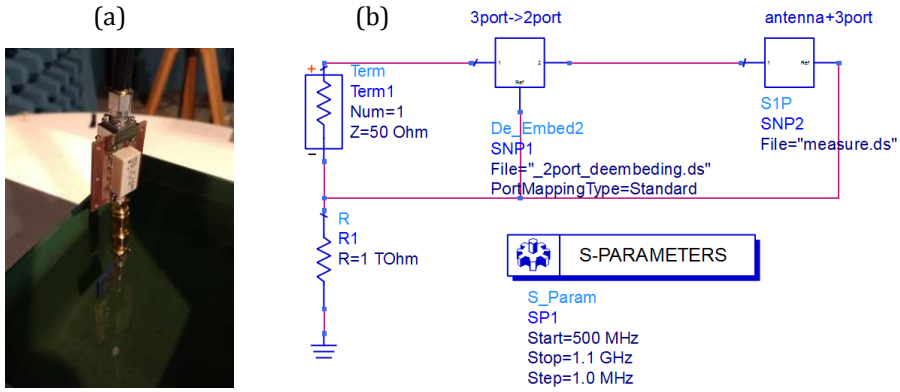

Figure 87. (a) Splitter connected to an in-body antenna for experimental validation and (b) circuit used in ADS software to obtain the reflection coefficient without the distortion of the splitter.

The use of the splitter to cancel the currents flowing back to the coaxial is analyzed. In Figure 88 the reflection coefficient of the 2d403 manufactured antenna is presented. Two measurements have been carried out: without the splitter and with the splitter (without de-embedding and with de-embedding). In this case, a difference of only 3 MHz is obtained between simulation and direct measurement, although the S_{11} level has a variation of 11 dB. When measuring the antenna with the splitter and applying the de-embedding process, the same frequency is matched and a variation of only 2 dB is obtained, showing good agreement between simulations and measurements. It should be noted that a larger bandwidth is obtained with the use of the splitter, probably due to an underestimation of the latter's resistive losses. However, in view of the results, the use of the splitter for the frequency characterization is suggested.

In Figure 89 the gain radiation pattern of the 2d403 manufactured antenna is presented and compared with simulations. The horizontal plane shows good agreement between measurements and simulations, with a maximum variation of 2.6 dB. Nevertheless, the differences for the *xy*-vertical plane are more significant, for two main reasons: the first is the addition of a 90 degree connector to place the antenna in the vertical plane and the second is the complexity of the splitter de-embedding process for the far-field measurement setup, which may introduce new distortions to the radiation. The difficulty of carrying out the far-field measurement in more than one plane has been described elsewhere in the literature [83].

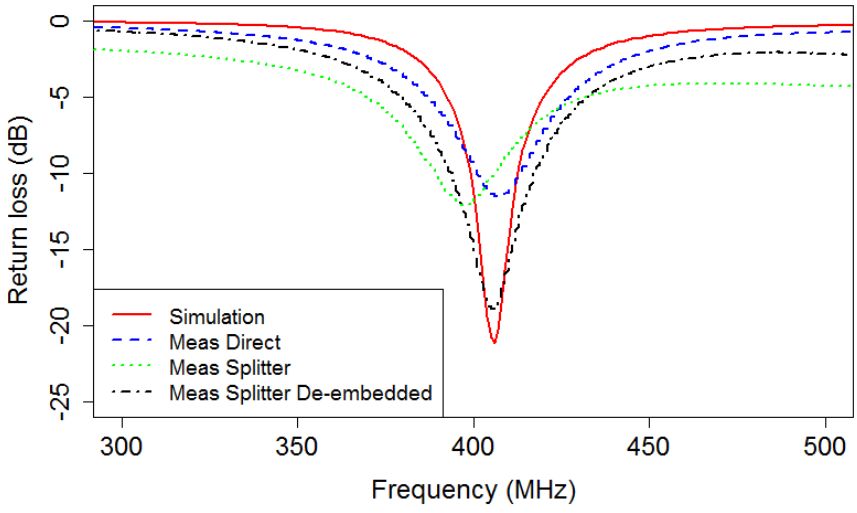

Figure 88. Reflection coefficients of the 2d403 prototype with and without the splitter.

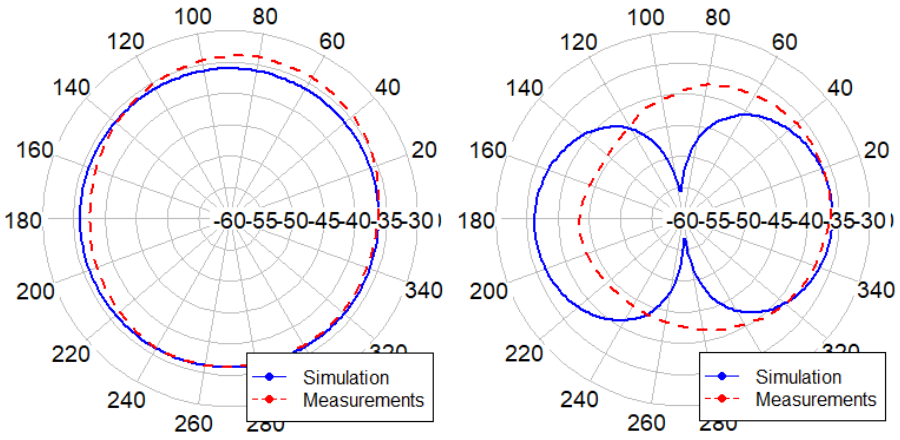

Figure 89. Simulated and measured gain radiation patterns of the 2d403 prototype in the (a) xz-plane and the (b) xy-plane.

It can be concluded that, although the horizontal radiation pattern has been successfully measured, the use of a splitter is not indicated when measuring the vertical radiation pattern. Therefore, a measurement setup based on fiber optics is considered as a more promising method to solve all of the problems associated with the distortion effects of the coaxial cable and connectors.

5.4.3. Fiber Optics Link

Fiber optics have been used to measure ESAs, as described in [234]. However, the use of fiber optics to characterize antennas in an in-body scenario is still a challenge. The main goal of using an optical fiber-based measurement setup for in-body ESAs is the same as when using a balun, choke or splitter – that is, to remove the large distortion produced by the unwanted radiation from a coaxial cable. In addition, the advantage of the optical fiber over other methods is the drastic reduction of the conductive parts that distort the radiated fields. Thus, fiber optics has emerged as a promising technique for measuring the far-field of in-body antennas.

The configuration of the proposed measurement setup is shown in Figure 90 (b). In the standard configuration the equipment used comprises a RF Signal Generator to feed the coaxial cable and a Network Analyzer with a wideband antenna to detect the transmitted radiation (Figure 90 (a)). However, in the optical fiber configuration, the transmission line consists in an optical fiber link instead of a coaxial cable. At the beginning of the fiber, the analog RF signal is modulated into an optical signal by a transceiver. At the end of the fiber, a receiver performs exactly the opposite operation, trying to obtain, as far as possible, the same original RF signal.

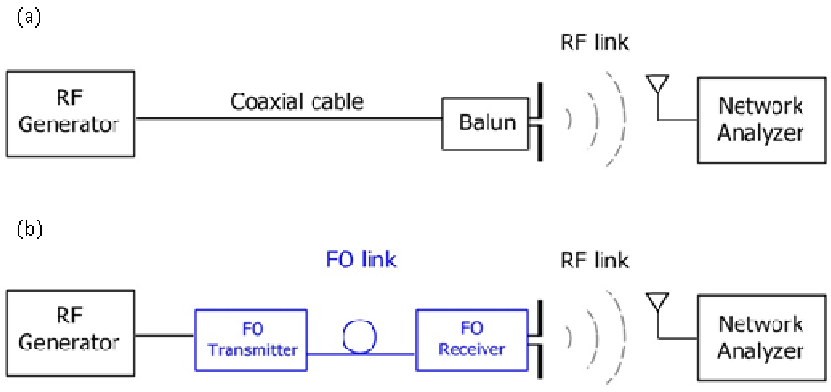

Figure 90. Measurement setups: (a) standard configuration (coaxial cable and balun) and (b) optical fiber configuration (optoelectronic modulation).

In the optical fiber configuration, there are two elements involved in the optical conversions:

- Fiber optic transmitter: Converts the RF signal into an optical modulated signal.
- Fiber optic receiver: Converts the optical modulated signal into a RF signal.

Two different transmitter devices have been used because of their features and their reduced cost. The first one is the SPINNER FO-Transceiver Module BN 528992 [235], shown in Figure 91 (a). This transceiver comes totally integrated into a tuned and tested module, and it also acts as a receiver if needed.

Figure 91 (b) shows the other transmitter, the AVAGO AFBR-1310Z [236], which requires the implementation of an external Printed Circuit Board (PCB) (Figure 92). Nevertheless, its cost is 10 times lower. Table 34 lists some of the differences between the transmitters.

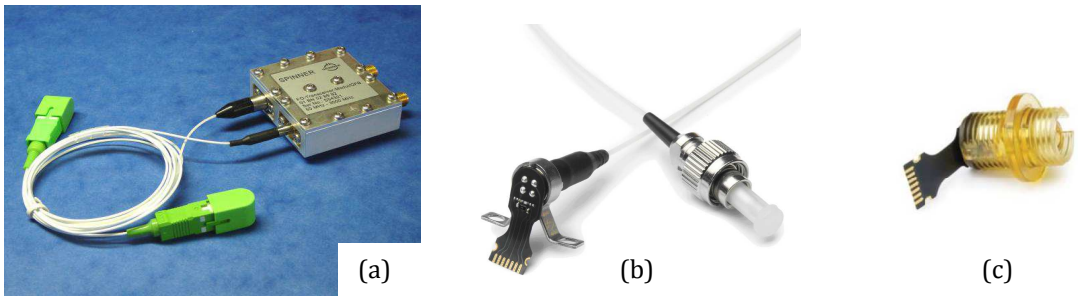

Figure 91. Fiber optic modules: (a) SPINNER transceiver/receiver [235], (b) AVAGO transceiver [236] and (c) AVAGO receiver [236].

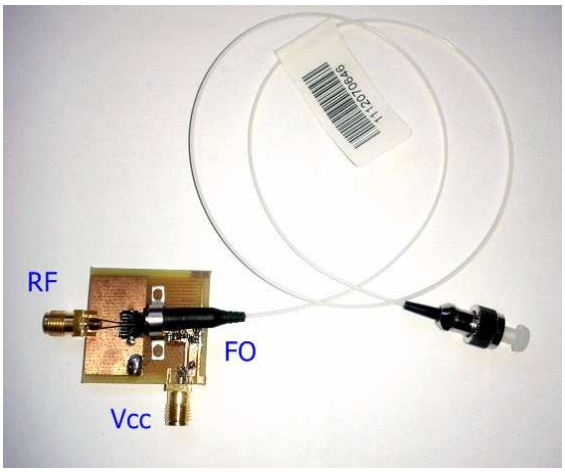

Figure 92. Implemented PCB for the transmitter module AVAGO AFBR-1310Z.

Table 34. Differences between optical transmitters.

	SPINNER transceiver	**AVAGO transmitter**
Receiver option	Yes	No
BW	50 MHz – 2.7 GHz	200MHz – 5.5 GHz
RF input power (max)	3 dBm	20 dBm
Operation Temperature	-10 °C … 45 °C	-40 °C … 85 °C
Technology	DFB Laser Diode	Fabry-Perot Laser
Integration	Yes	No, PCB required
RF supply voltage	12 V	5 V

The optical receiver has been selected to interfere as little as possible with the antenna. The AVAGO AFBR-2310Z [236] presents good features, apart from having few metalized parts (Figure 91 (c)); however, as can be seen in Figure 93, a simple external circuit is required. The receiver acts as a splitter, so the RF output is balanced. Table 35 shows the main features of the optical receiver.

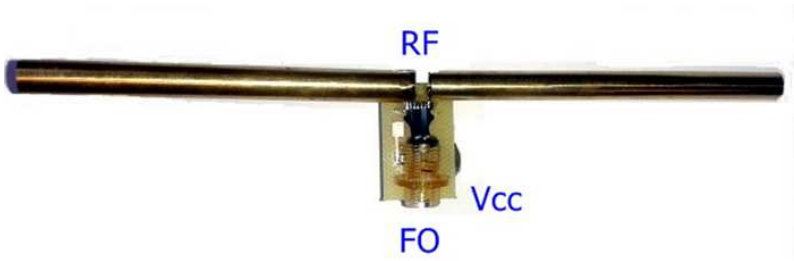

Figure 93. PCB used for the receiver module AVAGO AFBR-2310Z. The RF output is connected directly with a cylindrical dipole as a proof of concept.

Table 35. Main features of the optical receiver.

	AVAGO receiver
BW	200 MHz – 5.5 GHz
Optical input power (max)	7 dBm
Operation Temperature	-40 °C … 85 °C
Integration	No, PCB required
RF supply voltage	3.3 V

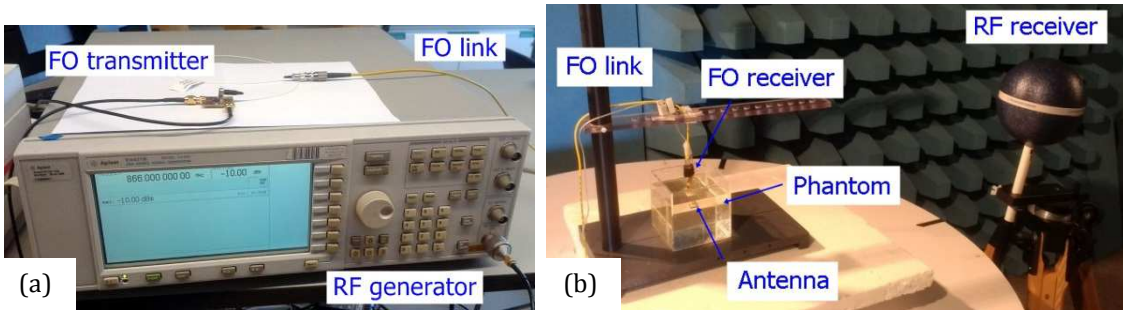

Figure 94. Optical fiber configuration: FO transmitter (a) and FO receiver (b).

Figure 94 presents the whole optical system for the measurement of antenna parameters. Note that only the RF link is placed inside the anechoic chamber in order to avoid interferences with the other elements.

The measurement setup based on fiber optics is conceived as a first approach to characterize the radiation pattern of in-body antennas. Transmission levels have been obtained in an off-body proof of concept scenario. However, further developments are required to resolve the following issues in an in-body scenario:

Fiber Optics Power

Although the system works relatively well in an off-body scenario, the maximum power available in the receiver optical module is too low for an in-body scenario. Thus, the radiated power is not high enough to compensate for the losses in the surrounded medium, resulting in an undetected signal by the external receiver antenna. This problem may be solved by increasing the available power in the receiver optical module. However, amplifiers should not be used in this part in order to avoid interferences with the radiated fields. So, it is recommendable to obtain a new optical fiber link with more available power.

Feeding of the Optical Receiver Module

The main goal of using optical fibers is the removal of metallic parts to avoid interferences. However, the receiver module has a DC feeding of 3.3 V. Initially, the feeding solution was to provide an embedded small battery, but the intensity required was insufficient to feed the whole circuit. So, an external device (Arduino UNO) was used to feed the system. The problem appeared with the cable from the Arduino to the receiver module, which introduced interferences in the radiated fields. A solution to this would be the development of a new feeding system also based on fiber optics, as in [234].

Sealing of the Receiver Module

As the receiver optical module is in close proximity to the in-body antenna, a sealed packaging should be developed to avoid its direct contact with the phantom liquid.

5.4.4. Discussion of the Measurement Improvements

The reflection coefficient and gain radiation pattern of the most relevant antennas are shown in Appendix A. Measured reflection coefficients are carried out with the addition of the power splitter for antennas working at 403 and 866 MHz. However, the splitter does not work properly at 2.45 GHz, as pointed out in the specifications. On the other hand, measurements were not performed for the 2d2450t prototype (Figure 69 (i)) because the antenna size was too small to solder the SMA connector. For the other cases, frequency detuning is below the threshold of 2%, in agreement with sensitivity tests.

Table 36 presents a summary of the resonant frequency and the S_{11} level at that frequency for simulations and experimental characterization with and without the power splitter. Note that both frequency detuning and S_{11} level variations have been significantly improved thanks to the power splitter, and that 2D prototypes present greater similarity between simulations and measurements, probably due to the increase in the variables in the manufacturing process in the 3D antennas, which accumulates more tolerances.

Regarding far-field features, measurements were carried out with the power splitter to avoid currents flowing back to the outer conductor of the coaxial cable. However, only the measurements in the horizontal plane (xz-plane) significantly matched the simulations. Improvements in the measurement setup for the other planes are required.

Table 36. Simulated and measured S_{11} levels and resonant frequencies of the presented prototypes with and without the power splitter.

	Simulated		**Meas. without splitter**		**Meas. with splitter**	
Prototype	$S_{11}@f_{res}$ (dB)	f_{res} (MHz)	Variation S_{11} (dB)	% freq. detuning	Variation S_{11} (dB)	% freq. detuning
2d403	-23.5	406	+12	0.5	+4.6	0.2
3d403	-21.6	403	+6.4	2.1	-0.5	1
2d403t	-28.6	400	+12.9	0.8	-3.3	0.7
2d866	-14	869	+11.9	1.2	+0.4	0
3d866	-23.5	874	+11.5	1.6	+9.8	0.8
2d866t	-26.6	865	+7.7	1.6	-2.2	0.8
2d2450	-10	2510	+1	2.9	-	-
3d2450	-24.7	2460	+12.6	0.8	-	-
2d2450t	-45.3	2457	-	-	-	-

Although the fiber optic link appears to be a good solution to avoid interferences in the far-field measurements, further development is required to overcome several challenges that remain.

5.5. Conclusions

In this chapter, the LTCC fabrication process for in-body antennas was analyzed. Sensitivity tests were carried out to quantify the frequency detuning due to inaccuracies in the process, and found that the substrate permittivity and the scale factor were the most relevant parameters. A limit of a relative detuning up to 2% was then considered as acceptable. In addition, the free-sintering method was considered more appropriate, since the scaling factor allows more control than the zero-shrinkage method. The radiator width of manufactured antennas was set to 1 mm in order to combine small size and technological feasibility. Nevertheless, prototypes with a 0.3 mm radiator width were successfully manufactured.

Preliminary antenna characterization showed relative frequency detuning up to 2.9% and significant differences in the S_{11} levels at the resonant frequency. In addition, direct feeding through a SMA connector presented low robustness during the manipulation of the antenna prototypes. Therefore, three measurement setups were proposed as alternatives to improve the characterization of in-body antennas:

- The coplanar launcher facilitates the soldering of the SMA connector. However, it is only suitable for antennas operating at the MedRadio band; at higher frequencies it significantly distorts the radiation pattern.
- The power splitter was found useful for suppressing the currents flowing in the coaxial outer conductor at frequencies up to 900 MHz. Reflection coefficient measurements showed a significant improvement. Gains in

radiation pattern measurements were indicated only for the horizontal plane, as too many distortions were found in the vertical one.

- A first version of a measurement setup based on fiber optics was developed and presented as a promising system to characterize the radiation pattern free of coaxial cable distortions. However, further development is needed to overcome several challenges that remain in an in-body scenario, such as the power, the receiver feeding and the sealing.

The characterization of the most relevant prototypes at 403 MHz, 866 MHz and 2.45 GHz is presented with the use of the power splitter. 2D prototypes show more agreement between simulations and measurements because of their lower technological complexity. Measurements at 2.45 GHz present more differences with simulations because of the unsuitability of the splitter at this frequency.

Finally, in view of the results and with the conclusions of the previous Chapter, we strongly recommend the establishment of a measurement protocol for in-body antennas, not only for the phantom dimensions and implant depth but also for the measurement setup itself.

Part 2

ANTENNA DEMONSTRATORS

6. Design and Characterization of a Multilayered Broadband Antenna for Compact Embedded Implantable Medical Devices

6.1. Introduction

The next three chapters will focus on novel antenna designs for specific biomedical applications; either to overcome the biotelemetry challenges presented in Chapter 2 or to improve breast cancer treatments through microwave hyperthermia.

As already mentioned in Chapter 1, antennas are an essential element of the implantable and ingestible medical devices used in a growing number of desapplications for the wireless monitoring of physiological parameters [18]. Compared to other approaches such as inductive links, implantable antennas offer the advantages of reduced invasiveness, increased transmission data rate, increased communication range, and reduced sensitivity to coils' positioning [237]. Implantable antennas have been investigated in therapeutic and diagnostic applications, including but not limited to gastrointestinal endoscopy [238], artificial hip [239] and knee [240] measurements, and monitoring of intracranial pressure [241], cardiovascular pressure [242], glaucoma [139], or blood glucose [75].

Subsection 2.3 described the current design requirements for implantable antennas, which include frequency of operation, bandwidth enlargement, size miniaturization, biocompatibility, limited power absorption in body tissue, and mechanical robustness [237]. Although size reduction is a primary design objective for practical implantable antennas, other objectives must be addressed during the design stage in order to optimize antennas for specific applications.

Some of the designs found in the literature (see Subsection 2.3) present antenna prototypes of compact volume. However, they do not consider the impact of integrating the electronics necessary for signal conditioning of sensor data (such as amplifiers, digital converters and transceivers), for power management circuitry and for the sensor itself [237]. Consequently, the final volume of the complete implantable medical device (IMD) with the antenna and necessary electronics will be increased, as in [241].

Another challenge when designing implantable antennas is the detuning observed when the device is implanted at various body locations. This study builds upon our previous work [111], in which we evaluated frequency shifts caused by the

dispersive heterogeneity of electrical properties of tissue and distinct anatomical geometries. Results showed that a bandwidth of at least 70 MHz is required for implantable antennas based on a PIFA structure operating at the MedRadio 401–406 MHz frequency band.

Finally, in order to ensure the biocompatibility of the IMD and to reduce induced currents and power absorbed by the human body, systems were generally embedded inside dielectric substrates [64].

In view of the above considerations regarding implantable antenna design, in this chapter I present a broadband PIFA for wireless biotelemetry applications. This study attempted to achieve the following:

- A suitably miniaturized design to improve versatility and applicability of the antenna.
- A structure capable of integrating an IMD into the internal cavity of the antenna.
- An operating bandwidth of at least 70 MHz to offset detuning effects caused by the heterogeneity of tissues at various locations within the human body.

The device proposed, which operates in the MedRadio 401–406 MHz frequency band [106], was based on multilayer LTCC technology, thereby guaranteeing a biocompatible substrate for the device [156] and the integration of other electronic components [185].

6.2. Materials and Methods

6.2.1. Antenna Design

The proposed antenna geometry (Figure 95 (a)) comprises four stacked layers of LTCC dielectric substrate with ε_r = 6.7 and σ = 0.0026 S/m and two embedded radiators. The main radiator, which is a folded square inverted-F structure that followed the perimeter of the antenna module (Figure 95 (b)), is located between the first and second layer and between the second and third layer of the LTCC substrate. The secondary radiator consisted of a meander inverted-F structure; this radiator was located between the third and fourth layer. The two radiators shared a common ground plane, but only the main radiator was fed the incoming signal at the feed point identified in Figure 95 (b) and Figure 95 (c) and generated the first resonance peak. Due to electromagnetic coupling, part of the energy was transferred to the secondary radiator, and it created a second radiation peak.

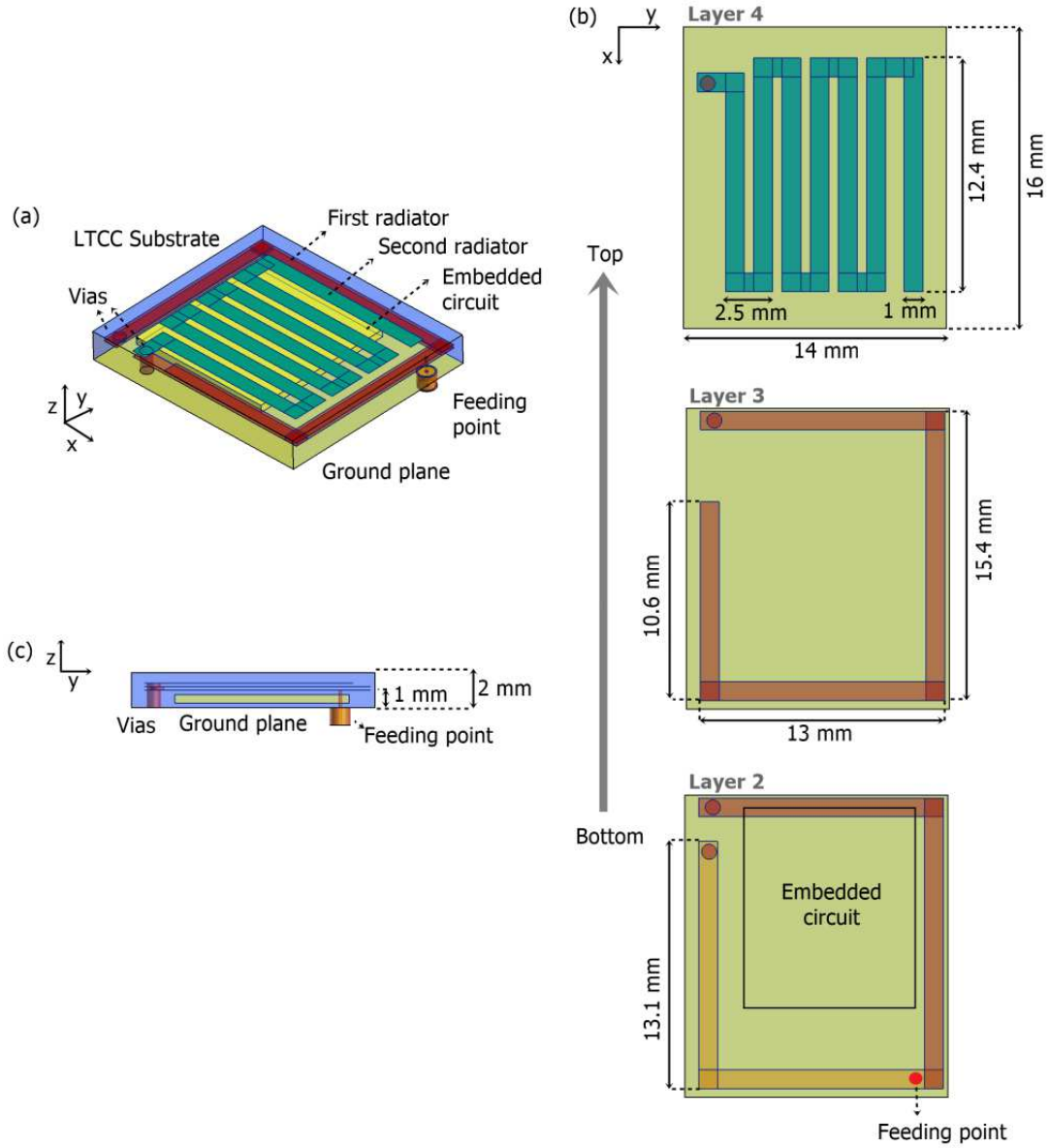

Figure 95. Geometry of the proposed antenna: (a) 3D view, (b) top view of each metallic layer, and (c) side view. The main radiator was located in the second and third layers, with two turns separated by 0.2 mm. The secondary radiator, a meander inverted-F structure, was located in the fourth layer. The light yellow area in (a), (b) bottom, and (c) shows an example location for embedding circuitry.

The combination of the two resonance peaks resulted in bandwidth broadening. The antenna design was optimized to operate at 403 MHz when being implanted inside muscle tissue (ε_r = 57.1 and σ = 0.797 S/m) [40]. The antenna has a volume of 448 mm^3, with a width of 14 mm, length of 16 mm, and thickness of 2 mm.

6.2.2. Methodology

Simulation results obtained in this study were based on electromagnetic modeling using the FDTD method, as detailed in Subsection 2.4.1. The commercially available electromagnetic simulator Sim4Life from Zurich MedTech AG [170] was used.

The antenna was centered with the rectangular section and implanted within the phantom at a depth of 15 mm from the edge as shown in Figure 96 (a). The antenna geometry, with the main radiator placed at the periphery, provided a wide internal space for future embedding of electronic circuits (light yellow area in Figure 95 (a), (b) [bottom], and (c)). Such electronic elements could lead to unexpected detuning due to electromagnetic coupling interaction. The electronic elements were approximated as a metallic box embedded in the prototype as a first approach to quantify their influence on the antenna performance. Metallic box volumes ranging from 0.5 × 0.5 × 0.5 mm^3 to 10 × 10 × 0.8 mm^3 and located at different positions were evaluated.

In order to validate the design, the antenna was manufactured and measured when being implanted within a phantom at a depth of 15 mm from the edge. The phantom contained de-ionized water, salt, sugar, and hydroxyethyl cellulose as indicated in FCC guidelines for human exposure to radiofrequency electromagnetic fields [243]. Dielectric properties measurements (ε_r = 57.2, σ = 0.8 S/m) were performed with the Agilent 85070E open-ended coaxial dielectric probe kit and the HP8720C network analyzer. In order to avoid external interferences and multipath reflections, the experimental setup was placed inside an anechoic chamber. In order to facilitate the soldering of the connector, the antenna was fed by a standard SMA connector through a coplanar wave guide launcher, as illustrated in Figure 96 (a). Experimental measurements of the reflection coefficient were also carried out with the setup shown in Figure 96 (b).

Electromagnetic simulations were employed to evaluate the proposed antenna design when being implanted at a depth of 15 mm in the arm, chest, and head of a whole-body male anatomical model to assess the detuning of antenna response caused by different body locations [111] at the same depth. The model was extracted from the Virtual Family dataset [192], which is based on high-resolution magnetic resonance images of healthy male volunteers. All tissues and organs were reconstructed as unstructured 3D-triangulated surface objects, thereby yielding high-precision images of individual body features. Antenna reflection coefficient, SAR distribution, radiation pattern and the transmission channel between the implanted antenna and an external dipole were evaluated. The quality of the transmission channel was assessed by the power received by the external dipole when being positioned at varying distances from the implanted antenna. An isotropic antenna was used to measure the received power. The effective area of

the dipole was used to compare the measured electric field with the simulated received power. The far-field radiation pattern and peak gain were computed using simulations with the antenna implanted inside the homogeneous phantom block surrounded by free-space. Measurements of the radiation pattern were also carried out using the received power of the isotropic antenna in steps of 15 degrees. Normalization of both simulated and measured radiation patterns were performed for comparison purposes.

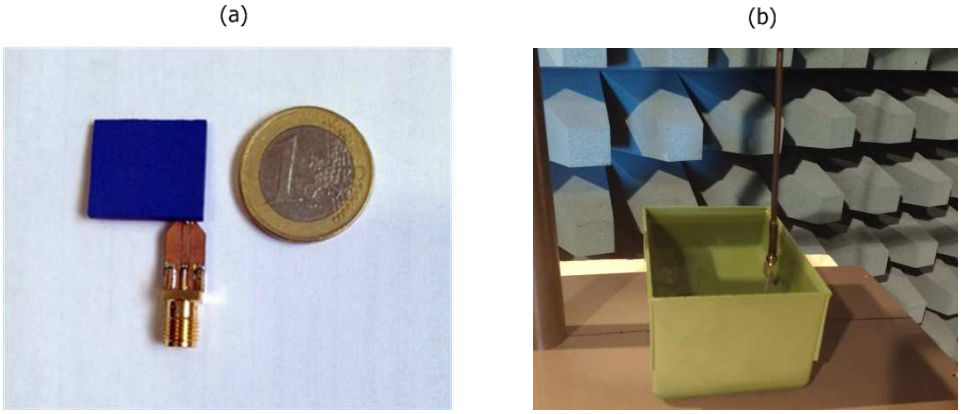

Figure 96. (a) Muscle tissue cuboid phantom used in simulations, (b) manufactured prototype in LTCC fed by a standard SMA connector through a coplanar wave guide launcher and (c) muscle tissue cuboid phantom used in the measurement setup.

6.3. Results

6.3.1. Reflection Coefficient

Figure 97 shows the simulated and measured reflection coefficients of the antenna implanted on muscle tissue cuboid phantom at 15 mm from the edge, as shown in Figure 96 (b). Two resonance peaks were combined, generating a −10 dB bandwidth of 103 MHz (358 – 461 MHz) for the simulation and 92 MHz (352 – 444 MHz) for the measurement. S11 at 403 MHz was −11.5 dB and −16 dB for simulation and measurement, respectively. Minor detuning to lower frequencies and bandwidth narrowing were observed in experimental results.

Figure 98 shows the simulated antenna reflection coefficient with the antenna implanted in the muscle tissue cuboid phantom considering four different antenna locations and sizes for the internal metallic box. Differences in antenna detuning were observed with respect to the reference antenna without the internal metallic box (trace (a) in Figure 98). For a box with dimensions 5 mm × 5 mm × 0.5 mm and located 7 mm from to the feed point (trace (b)), the −10 dB bandwidth was 92 MHz (354.8 – 446.8 MHz). For a box with dimensions 10 mm × 10 mm × 0.5 mm and

located 4.5 mm from to the feed point (trace (c)), the −10 dB bandwidth was 87 MHz (354.9 – 442.8 MHz). When the thickness of the box increased from 0.5 mm to 0.8 mm (i.e., the embedded box was at 0.2 mm from the main radiator), a strong narrowing in the bandwidth was observed. For a box with dimensions 10 × 10 × 0.8 mm (trace (d)), the −10 dB bandwidth was 67 MHz (345 – 412 MHz). Proximity of the metallic box to the feed point increased impedance mismatching. For a box with dimensions 10 mm × 10 mm × 0.5 mm and located 1 mm from to the feed point (trace (e)), a mismatch of S11 > −10 dB was observed between 373.7 and 403.6 MHz, generating a −10 dB bandwidth of 22.3 MHz (351.4 – 373.7 MHz) and 46.2 MHz (403.6 – 449.8 MHz).

Simulated reflection coefficients of the antenna, without embedded metallic boxes, when being implanted in the muscle tissue cuboid phantom and in the arm, chest, and head of the whole-body model are shown in Figure 99. A shift of the resonance peak at 370 MHz of the antenna implanted into the muscle tissue cuboid phantom towards higher frequencies was observed for the antenna implanted into the anatomical body. The second resonance peak at 435 MHz for the antenna implanted into the muscle tissue cuboid phantom shifted to higher frequency when the antenna was implanted in the arm and chest and did not change significantly for the antenna implanted in the head. A combination of the two resonance peaks produced a −10 dB bandwidth of 93 MHz (371.1 – 464.5 MHz) with a S11 of −16.1 dB at 403 MHz for the antenna implanted into the head, while the −10 dB bandwidth showed two sections 379.5 – 408.6 MHz and 436.7 – 492.3 MHz for the antenna implanted into the arm, and 375.9 – 407.8 MHz and 424.6 – 481.39 MHz for the antenna implanted into the chest.

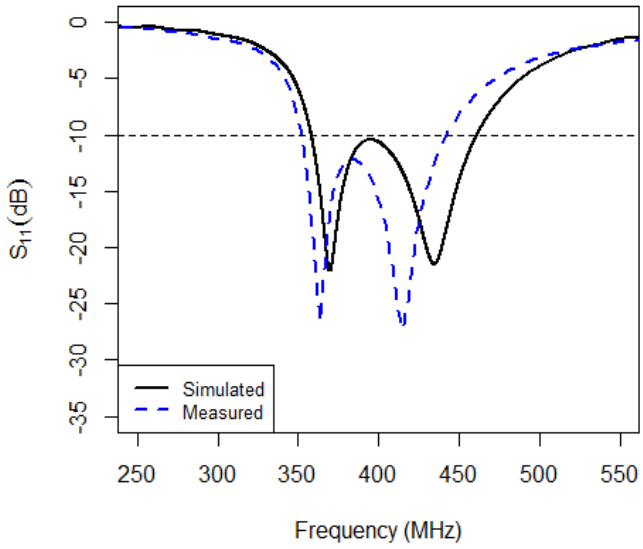

Figure 97. S_{11} of the simulated and measured antenna implanted in the muscle tissue cuboid phantom.

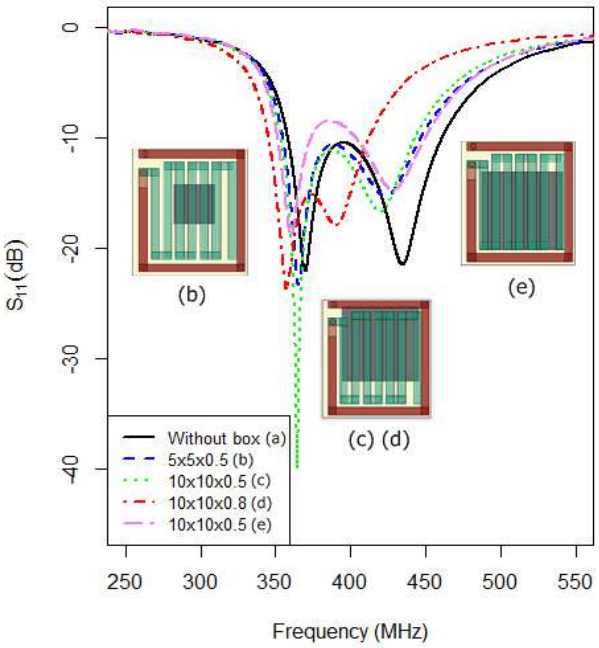

Figure 98. Simulated reflection coefficient of the antenna implanted in the muscle tissue cuboid phantom (a) without and (b)–(d) with embedded metallic boxes of varying size. The boxes' dimensions were (b) 5 × 5 × 0.5 mm, (c) 10 × 10 × 0.5 mm, (d) 10 × 10 × 0.8 mm, and (e) 10 × 10 × 0.5 mm.

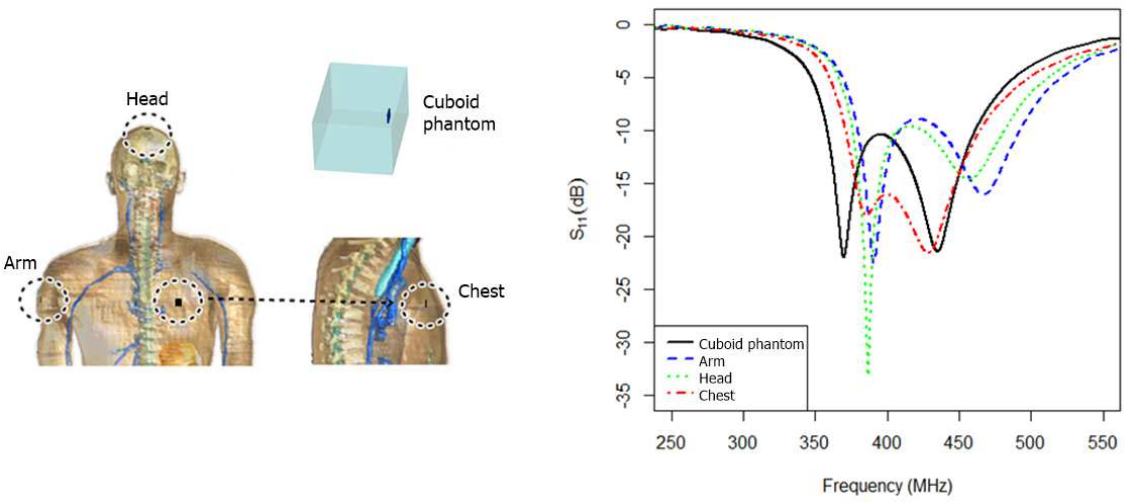

Figure 99. Simulated reflection coefficient of the antenna implanted inside the muscle tissue cuboid phantom and into the arm, chest and head of the anatomical male body model [192].

6.3.2. Specific Absorption Rate

The 3D near-field distributions were calculated, and numerical analysis of the SAR was performed at 403 MHz. The antenna, which was numerically analyzed without an embedded metallic box, was tested in a muscle tissue cuboid phantom and in

the head, chest and arm of the male anatomical model as shown in Figure 99. For comparison with previous studies, antenna input power was set to 1 W. The 1-g and 10-g averaged peak SAR results are shown in Table 37.

In order to meet basic SAR restrictions for general public exposure (i.e., IEEE C95.1-1999 [1-g averaged SAR < 1.6 W/kg] and IEEE C95.1-2005 [10-g averaged SAR < 2 W/kg] [43]), power delivered by the antenna had to be modified. If the highest SAR value obtained in the analysis (Table 37, in the arm) was considered, the delivered power had to decrease to 3.7 mW in order to satisfy the most restrictive SAR regulation (i.e., SAR < 1.6 W/kg).

Table 37. Specific absorption rate (SAR) results.

	1-g averaged		**10-g averaged**	
Antenna location	**SAR (W/kg) 1W input power**	**Max. power (mW) to meet 1-g averaged SAR restriction**	**SAR (W/kg) 1W input power**	**Max. power (mW) to meet 10-g averaged SAR restriction**
Muscle tissue cuboid	380.9	4.2	90.0	22.2
Arm	435.9	3.7	93.9	21.3
Chest	398.3	4.0	91.5	21.8
Head	323.6	4.9	89.0	22.5

Maximum power calculations based on SAR basic restrictions for general public exposure: IEEE C95.1–1999 (1–g averaged SAR < 1.6 W/kg) and IEEE C95.1–2005 (10–g averaged SAR < 2 W/kg). The setup and locations are presented in Figure 99.

6.3.3. Transmission Channel

The transmission channel between the proposed antenna and a half-wavelength dipole was evaluated in terms of received power. The proposed antenna was located at 15 mm from the edge of the muscle tissue cuboid phantom and into various locations within the anatomical model. The same study cases as in Figure 99 were considered. The simulated half-wavelength dipole antenna was positioned at distances ranging from 1 cm to 100 cm from the phantom-air and skin-air interfaces. In the experimental measurements, the isotropic antenna was positioned at distances ranging from 10 cm to 100 cm from the phantom-air interface as shown in Figure 100. On the basis of SAR results and limitations (Table 37), the transmitting antenna was assumed to have an input power of 3.7 mW (i.e., the most restrictive case). Power received at the external half-wavelength dipole was obtained by the transmission coefficient, determined by the relation between

available power at the transmitter implanted antenna and received power at the 50 Ω load that terminated the receiver antenna [128].

Results from the muscle tissue cuboid phantom and the anatomical model are illustrated in Figure 101. Received power showed a variability of ±4 dB when the half-wavelength dipole antenna was at 20 cm from phantom-air and skin-air interfaces for the various implanted antenna locations. Maximum deviations up to ±5 dB were observed when the half-wavelength dipole antenna was at 100 cm from phantom-air and skin-air interfaces. The largest received power was observed when the antenna was implanted into the arm; the lowest received power was found when the antenna was located in the chest.

Figure 100. Experimental setup to measure the received electric field by the external isotropic antenna.

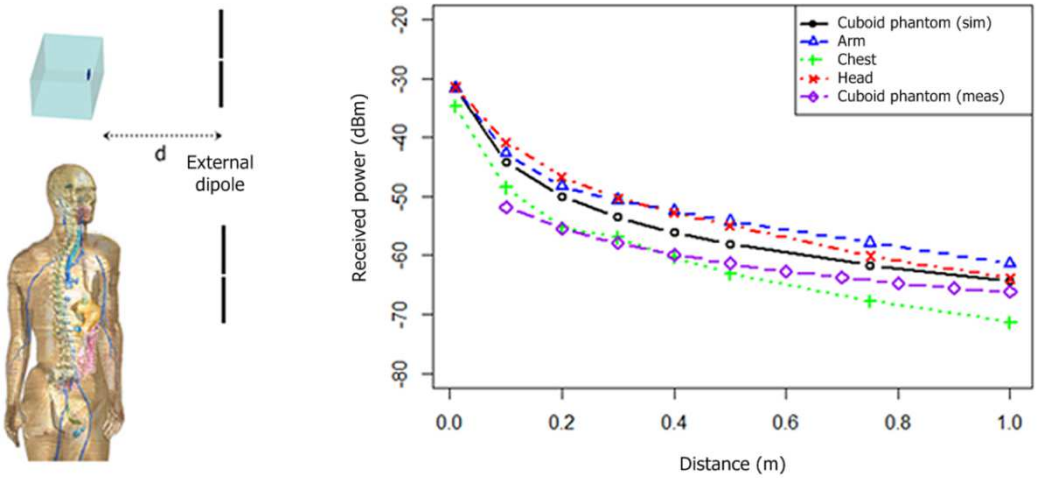

Figure 101. Power received by the external dipole as a function of distance d for the same cases as in Figure 99. Measured results of the antenna implanted in the muscle tissue cuboid phantom are also represented.

6.3.4. Radiation Pattern

Figure 102 shows the simulated and measured normalized antenna radiation patterns when being implanted in the muscle tissue cuboid phantom at 15 mm from the phantom edge for the xz-plane. The normalized received power of the isotropic external antenna in steps of 15 degrees along the xz-plane was used to perform the measured radiation pattern. The axes are detailed in Figure 95.

Table 38 shows the main parameters for the simulated and measured radiation patterns.

Table 38. Main radiation pattern parameters.

Parameter	Simulation	Measurements
Step degree	1.66°	15°
Maximum direction	85°	45°
3 dB beamwidth	147°	120°
Front-to-back ratio	3.6 dB	1.3 dB

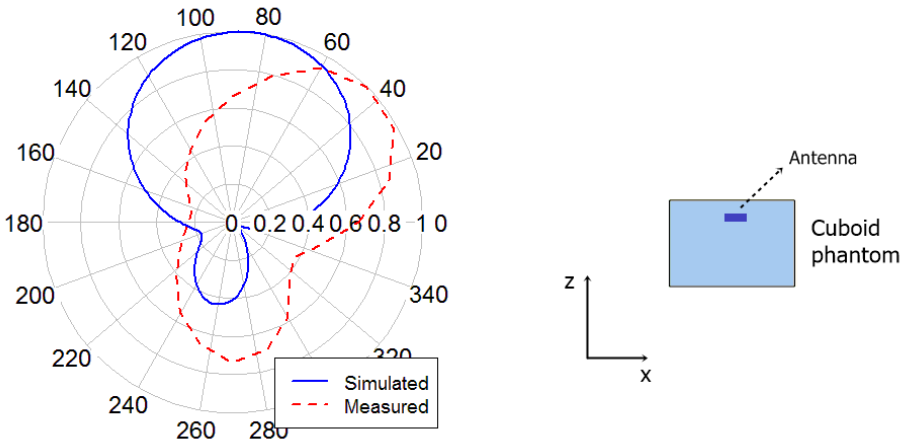

Figure 102. Simulated and measured normalized antenna radiation pattern (dBi) for the xz-plane with the antenna implanted in the muscle tissue cuboid phantom.

6.4. Discussion

This study aimed to design a miniaturized antenna for an IMD and to evaluate its feasibility. The proposed design employed LTCC technology with four stacked layers and two embedded radiators. Only the main radiators were fed the incoming power signal, and energy was coupled to the second radiator. Each independent radiator generated a resonance peak. Coupling between the two

radiators produced a combination of the two resonances and subsequent bandwidth enlargement. Simulated and measured models achieved bandwidths of 103 MHz and 93 MHz respectively. A bandwidth greater than 70MHz was achieved in both cases, fulfilling the requirements considered in previous studies [111].

The main radiator of the proposed antenna was specifically placed at the periphery of the device to allow integration of IMD electronic circuits inside the core of the antenna. The main influence of the embedded box on the antenna return loss was a slight frequency shift to lower frequencies and bandwidth narrowing. Embedded box sizes up to 10 × 10 × 0.5 mm rendered a suitable performance at the MedRadio band, with a −10 dB bandwidth reduction of 15% with respect to the design without the box. Increasing box height to 0.8mm produced a reduction in antenna bandwidth of 34.9%. When the box was located at a distance of 1mm or less from the antenna feed point, unacceptable antenna mismatching was generated in the frequency of interest.

When the antenna was implanted in various locations on the human body, a shift to higher frequencies was observed for the first resonance peak. When it was implanted in the arm and chest, the second resonance peak shifted to higher frequencies and the combination of the two resonances peaks was compromised. When implanted in the head, the second resonance peak did not shift to higher frequencies and combined with the first resonance peak, generating an improved matching at the frequency of interest.

SAR analysis was performed at 403 MHz for the muscle tissue cuboid phantom and implanted in the arm, in the head and in the chest of the male anatomical model. The antenna implanted in the arm generated the highest SAR for the cases of 1-g averaged SAR and 10-g averaged SAR. Based on SAR basic restrictions for general public exposure, the maximum delivered power of the antenna was found to be 3.7mW.

A half-wavelength dipole antenna was placed at various distances from the antenna implanted into the muscle tissue cuboid phantom and at various locations within the anatomical model. When the half-wavelength dipole was located at 1 cm from the phantom-air or skin-air interface, the power received at the dipole was similar for all antenna locations. For dipole to phantom-air or skin-air interface distances between 10 cm and 30 cm, the antennas implanted in the head and arm generated similar power, and the values were around 4 dB more than the antenna implanted in the tissue phantom and around 10 dB more than the antenna implanted in the chest. For distances greater than 40 cm, the antenna implanted into the arm generated the highest power in the receiver half-wavelength antenna. The antenna implanted in the chest generated the lowest power in the receiver dipole for all the distances evaluated. Depending on the antenna location, the surrounding tissues presented distinct dielectric properties and geometries,

leading to unique radiation patterns for each location. The amount of lossy media surrounding the antenna and the reflections caused by tissue interfaces directly impacted the transmission channel quality. The measured results for the antenna implanted in the muscle tissue cuboid phantom show a reduction of the simulated received power of around 8 dB and 1 dB at distances of 10 cm and 100 cm from the source respectively. The conversion from an isotropic antenna to a half-wavelength dipole through the effective area is not totally accurate for regions close to the near-field, while for larger distances the results converge. Another issue related to the measurements is the influence of the coaxial cable of the measurement setup in electrically small and implantable antennas, as reported in [49], [152].

A simulated peak gain of −32 dB was achieved when the antenna was implanted in the muscle tissue cuboid phantom surrounded by the free-space. The radiation pattern for both simulations and measurements (Figure 102) shows a directional performance in the positive z-axis, where the amount of lossy tissue for the microwaves to cross is lower and, therefore, the attenuation is also reduced. The measured maximum level of the normalized radiation pattern shifts 40° from the simulated results. A 27° reduction in the 3 dB beamwidth and a 2.3 dB drop in the front-to-back ratio are also observed in the measurements.

Features of other implantable antennas reported in the literature are shown in Table 39. It can be seen that the antenna presented in this paper achieved the required performance in terms of bandwidth, miniaturization, and gain. The results for received power in this study were in agreement with simulated communication links reported in previous designs of compact implantable antennas. Received power of the antenna presented by Kiourti et al. [72] was −56.2 dBm at a distance of 20 cm from the head, while the antenna presented in this study achieved −45.7 dBm. In addition, the received power obtained showed the influence of miniaturization on the transmission channel. Kim et al. [64] evaluated the communication link between a large antenna (40 mm × 32 mm × 8 mm) implanted in the human chest and an external half-wavelength dipole. When the half-wavelength dipole was located at 30 cm from the phantom-air or skin-air interface, maximum available power was −30 dBm. In the design proposed in our study (16 × 14 × 2 mm), available powers ranged from −50 dBm to −56 dBm for the same phantom-air or skin-air to half-wavelength dipole distance. This variation between prototypes was primarily due to the drastic reduction (95.6%) in antenna size.

Computational and experimental approaches were used in the design and characterization of the miniaturized antenna for an IMD. The strengths of the proposed design to resolve shortcomings of current state-of-the-art in implantable antennas include a balanced performance between a miniaturized design with general volume of 14 × 16 × 2 mm^3, integration of electronic circuits of the IMD

with volume up to 10 × 10 × 0.5 mm^3, and an enlarged bandwidth up to 103 MHz in order to consider the dielectric properties and geometry disparity of the antenna implanted within various body locations. Satisfactory agreement was found between simulations and measurements of the fabricated antenna implanted into a liquid with dielectric properties of muscle tissue cuboid phantom. Maximum antenna input power was evaluated considering SAR restrictions for 1-g averaged SAR and 10-g averaged SAR for the three body antenna locations. The transmission channel between the proposed antenna and a half-wavelength dipole showed the applicability of the antenna up to distances of 1 m, while the receptor was capable of operating with a power of −60 to −70 dBm depending on where the antenna was implanted.

This study focused on the simulated performance of the proposed antenna at three body locations and in a muscle tissue cuboid phantom at depths of 15 mm from the phantom-air and skin-air interfaces. Reflection coefficient, transmission channel and radiation pattern were measured for validation purposes in the muscle tissue cuboid phantom. Further evaluation of the antenna implanted at different body locations and variable depths, and the acquisition of communication link measurements at other distances, are now warranted. In this study, the impact of adjacent electronic circuitry on antenna performance was evaluated considering a metallic box as a first approach. Future studies for specific applications should investigate the impact of specific electronic components on the antenna performance. This study considered the antenna implanted in the adult male; further studies will evaluate the implementation of the antenna in adult females and children.

Table 39. Comparison of implantable antenna performances found in literature.

Reported design techniques/ approaches	**Volume (mm^3)**	**-10 dB BW (MHz)**	**Max Gain (dB)**	**Designed for embedded circuit**
Kim et al. [53]	10240	13	N/A	No
Kim et al. [64]	6144	32	N/A	No
Lee et al. [68]	335.8	50	-26	No
Lee et al. [82]	791	120	-27	No
Liu et al. [79]	121.6	122	-38	No
Liu et al. [71]	190	50	-26	No
Kiourti et al. [223]	1063.1	27	-30	No
Permana et al. [157]	254	10	-36.5	No
Proposed	**448**	**103**	**-32**	**Yes**

6.5. Conclusions

The design of a novel compact implantable broadband PIFA for wireless biotelemetry applications is presented in this chapter. The antenna was designed to operate in the MedRadio 401–406 MHz frequency band. Coupling between two radiators was used to enlarge the bandwidth. The design also took into account the embedding of electronic components.

The modeling analysis was based on electromagnetic calculations using the FDTD method, and the LTCC multilayer technology was used. The proposed antenna was first modeled inside fluid that mimics muscle tissue. Then, in order to test its performance in a more realistic scenario, it was simulated when being implanted into the arm, head, and chest of a high-resolution whole-body anatomical model of an adult human male.

The SAR and impedance mismatch of the antenna inside the human body were analysed, as well as the desirable bandwidth enhancement and initial tuning. Possible detuning due to the influence of an embedded electronic circuit in the prototype was also assessed. Simulated results showed a suitable operational behavior of the antenna in most of the scenarios studied. Compared to other antennas available in the literature, the presented antenna shows a satisfactory performance in terms of miniaturization, bandwidth and gain, and is designed for embedded circuits.

Finally, the antenna was manufactured and the reflection coefficient, transmission level and radiation pattern were measured. Simulated and measured results showed satisfactory agreement.

7. Design and Characterization of a miniaturized implantable UHF RFID Tag

7.1. Introduction

As seen in Chapter 1, the constant increase in hospital costs due to population aging has become a matter for concern of the scientific community and the industry in recent years. The development of new wireless communication systems for patient healthcare monitoring and the improvement of hospital resources management has become one of the main areas of research in order to address this issue [237], [244]. In this scenario, RFID-based systems represent a promising solution for the tracking of patients in hospitals and other environments, mainly due to their simplicity, reduced cost and increased safety [20], [21], [23]. In addition, the integration of sensing modules to the RFID antenna [91] and the appearance of new RFID chips with sensing capabilities [22], allows remote control of patients' physiological functions.

After its applications in the logistics sector and the textile industry, the health sector is considered the new target market of the RFID technology [23]. Actually, in the last decade, RFID systems have been gradually introduced for use in asset tracking and storage, blood management (including temperature monitoring) or pharmaceutical anti-counterfeiting, among other purposes [21]. However, approximately 26% of the RFID applications for healthcare are developed for people tracking [21] – most of them based on bracelets with inductive coupling and powered by a battery [245]. In-body RFID antennas can also be found in the literature [246], [247].

In this chapter a passive implantable UHF RFID tag for patient monitoring is presented. One of the advantages of in-body devices is that they are less likely to be lost than on-body devices such as bracelets. Furthermore, the use of RF antennas instead of inductive links increases the range of the tag to be detected. Finally, a battery-free tag allows a greater level of miniaturization and a reduction of the RF power deposited inside the tissue, which is critical in in-body scenarios. The proposed RFID tag is based on LTCC technology, which has promising features for IMD, as already mentioned in Subsection 2.3.7.

The strategy followed for the design of the RFID tag antenna comprises two parts:

- The development of a spiral PIFA to decrease the volume.
- The addition of an inductance to match the impedances between the radiator and the Integrated Circuit (IC).

The RFID tag was designed for the Alien Higgs4 IC [248]. The antenna was designed to operate at UHF band (868 MHz) instead of LF or HF bands, in order to miniaturize the device and enhance the tag range. The UHF band also enlarges the operating bandwidth, improving the privacy and security protocols for the communications, an important issue in healthcare applications [247]. In addition, as noted in Subsection 2.3.3, when wireless devices are implanted in the body, they require an enlargement of the bandwidth in order to mitigate the frequency detuning caused by the heterogeneity and the variability of the size and the electrical parameters of the surrounding biological tissues.

Therefore, the main goals of this chapter are:

- To propose a design strategy for in-body UHF RFID tags with a high bandwidth and a small volume.
- To design and characterize a passive in-body UHF RFID tag.
- To measure the main features of the manufactured prototype in order to validate the simulated results.
- To test the feasibility of developing in-body UHF RFID tags with LTCC technology.
- To present a preliminary assessment of a RFID tag with temperature monitoring.

7.2. Materials and Methods

7.2.1. Antenna Design

The antenna is designed around two different structures, as presented in the Figure 103. Firstly, the miniaturization was accomplished by designing the radiator as a spiral PIFA. Secondly, to compensate for the capacitive behavior of the IC, an inductive line was used to match the impedance. The dimensions and location of the inductive line (L line) were tuned for operation in the desired frequency range and to avoid coupling with the PIFA. Finally, two pairs of vias separated by a short distance were set up to obtain a second-order equivalent resonant circuit, considerably enlarging the bandwidth.

The ceramic substrate based on LTCC presents a dielectric parameters of ε_r = 7.5 and tan δ = 0.0008 at 866 MHz. The Alien Higgs4 IC was placed in a cavity performed in the bottom layer, below the groundplane of the PIFA. The IC cavity was then sealed to prevent the contact with the biological tissues. The dimensions of the final prototypes were 8 x 7 x 2 mm^3.

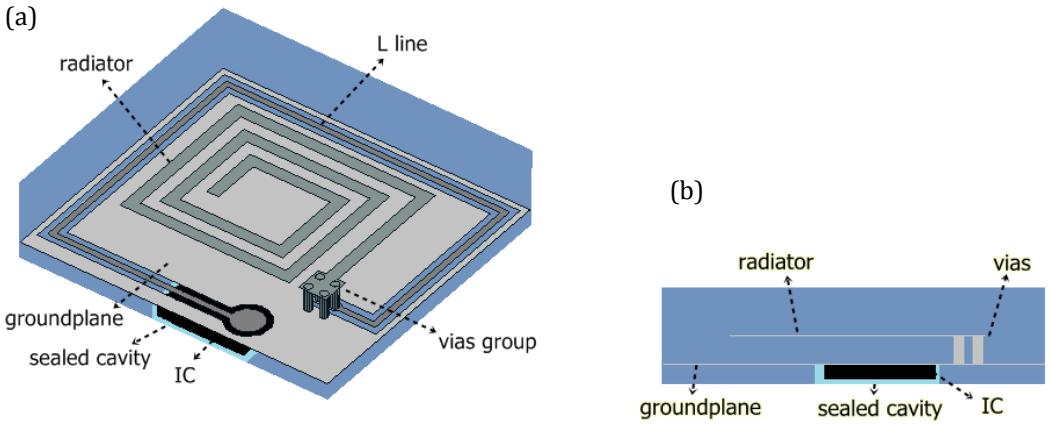

Figure 103. 3D (a) and cross-section (b) of the RFID tag with the Alien Higgs4 IC.

7.2.2. Methodology

Electromagnetic simulations were performed using ADS [172], CST Microwave Studio [171] and Sim4Life [170] software packages. ADS was used at the initial design stage as it is a faster solver for multilayer structures. CST and Sim4Life were chosen for validation purposes in a biological environment. In Section 2.4 the computational tools for EM simulation are described.

Figure 104 shows two prototypes fabricated by the company Francisco Albero SAU (FAE) [102]. The manufacture of these antennas was carried out using multilayer LTCC technology. Several layers of green ceramic already casted in the installations of FAE were stacked and laminated to form a 3D structure of low temperature sintering. Prior to the stacking, metallizations were defined by screen printing of a silver paste. The vertical connections between metal layers for the electrical feedthroughs were brought about by 300 and 200 µm punched via, which were filled with a viscous silver paste. The cavities were punched and then filled by an organic sacrificial paste, which were then burned in early stages of the sintering process to prevent its deformation during the lamination process. The sintering process was made in a furnace where the temperature was increasing slowly (2 ^{0}C/min) to burn the organics before the ceramic sintering. Then, the temperature was hold during 2 hours at 870 ^{0}C. For the used free-sintering process, none direction was constrained during the firing and sintering process. Thus, the substrate suffered from shrinkage, that in the case of the LTCC material selected in this work was 14 % in both, X and Y direction (horizontal plane). In Subsection 5.2.1 a detailed explanation of each of the stages involved in the manufacturing process is presented.

The SMA connector shown attached in Figure 104 (a) allows measurement of the reflection coefficient normalized to a coaxial cable; while in Figure 104 (b), the IC is located in the substrate cavity to check the tag range. The commercial Alien ALR-9900+ [249] was used for communication link characterization. The measurements were set up as illustrated in Figure 105. The RFID tag was implanted in the center of a 100 mm cubic skin phantom (ε_r= 41.6 and tan δ= 0.43) to mimic the biological tissues surrounding the antenna. The phantom liquid was a solution of sugar, salt and deionized water, as reported in Chapter 5.

The maximum communication distance between the implanted RFID and the external reader is determined in the far-field region by the Friis formula [246], [250], as shown in Equation 20,

$$P_R = EIRP \cdot G_R \left(\frac{\lambda}{4\pi d}\right)(1 - |\rho_R|^2) \qquad (20)$$

where *EIRP* is the equivalent isotropic radiated power, G_R is the gain of the receiver (the antenna tag), λ is the wavelength in the free-space, d is the distance between the transmitter and the receiver (the tag range) and ρ_R is the reflection coefficient of the receiver.

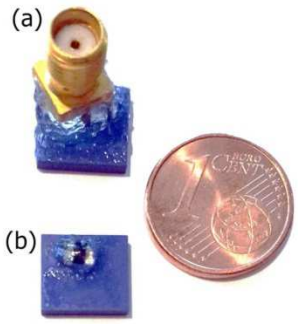

Figure 104. Manufactured prorotypes with a SMA connector (a) and the Higgs4 IC (b).

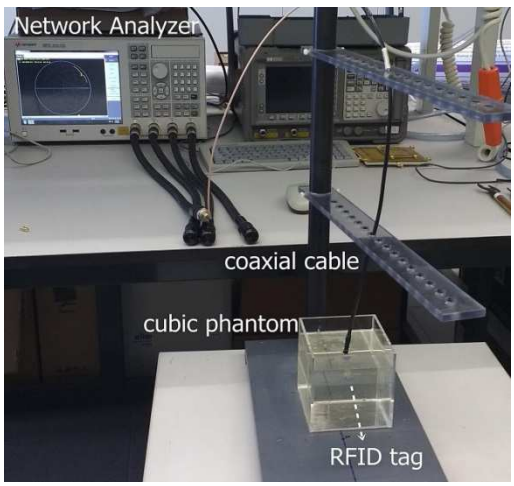

Figure 105. Set-up for reflection coefficient measurement.

7.3. Results

In the Figure 106 the measured and simulated reflection coefficients are represented. In Figure 106 (a) the reflection coefficients are normalized to the 50 Ω coaxial cable, whereas in Figure 106 (b) they are normalized to the conjugated IC impedance (see Table 40). A 6 dB bandwidth of 39 MHz was achieved in simulations; while in the measurements, the 6 dB bandwidth was 84 MHz.

To calculate the tag range, the received power is fixed to the chip power threshold sensitivity (-18 dBm), the EIRP transmitted by the external reader is 4 W and the antenna tag gain is set to -44 dBi, according to the simulations. The tag range, calculated with the Friis formula (Equation 20), is plotted in Figure 107 as a function of frequency.

A maximum tag range of 10 cm was achieved in the experimental results with the Alien's external reader. A summary of the main tag features is presented in Table 40.

Table 40. Parameters of the UHF RFID tag.

RFID tag IC	Conjugated IC impedance	Sim. 6 dB BW	Meas. 6 dB BW	Sim. Gain	Sim. Range	Meas. Range
Alien Higgs4	20.45+j190.8 Ω	39 MHz	84 MHz	-44 dBi	9 cm	10 cm

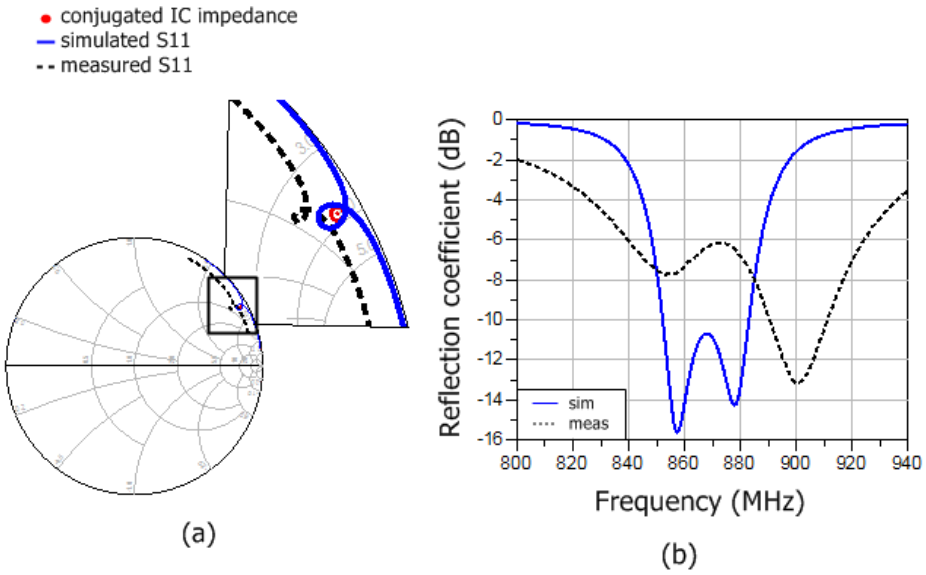

Figure 106. Reflection coefficient of the Alien Higgs4 RFID tag implanted in the cubic phantom. The Smith chart normalized to the coaxial cable is represented in (a) while the reflection coefficient level in dB normalized to the conjugated IC impedance in presented in (b).

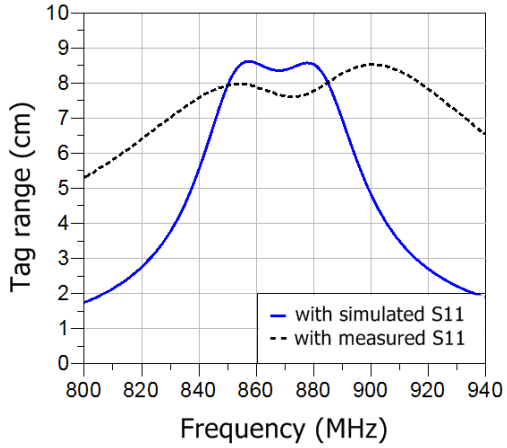

Figure 107. Tag range of the RFID implanted in the cubic phantom for the simulated and measured reflection coefficient.

7.4. Discussion

The measured reflection coefficient of the RFID tag inside the phantom was in agreement with the simulations, as seen in Figure 106. Nevertheless, a difference of 45 MHz in the 6 dB bandwidth and a slight shift of 1.72% in the central frequency between simulations and measurements were found. These deviations are mainly due to variations between simulated and real parameters, inaccuracies in the manufactured prototypes, unwanted effects of the measurement setup (see Chapter 5) and the addition of the sealing material, which was not considered in simulations. However, both results exhibit enough bandwidth to operate in the European UHF-RFID band and to mitigate the frequency detuning caused by the variability of the surrounding biological tissues.

When analyzing the Smith chart of the reflection coefficient normalized to the 50 Ω coaxial cable shown in Figure 106 (a) we can observe the capacitive behavior of the Alien Higgs4 IC. The small loop around the conjugated IC impedance is achieved thanks to the addition of the L line in the antenna, resulting in a second order resonant circuit that broadens the operating bandwidth. The measured reflection coefficient presents ohmic losses mainly due to the effect of the coaxial cable, the connectors and the currents on the phantom liquid. Moreover, the small loop in the measurements does not exactly encircle the prototype, showing a slight impedance mismatching.

The measured maximum tag range of 10 cm achieved in the experimental results was consistent with the levels calculated in the Figure 107, where the maximum tag range is almost 9 cm. This short distance is basically due to the small volume of the tag antenna, which leads to a decreased gain. Further research is now needed

to improve the efficiency, the operational bandwidth and the tag range of the antenna using optimization methods.

The present study focused on the Alien Higgs4 IC, which offers basic data for the tracking of patients and resources. However, new RFID ICs with sensing capabilities are already available on the market, such as the AMS SL900A IC [22]. Our current laboratory research is centered on the addition of physiological data in our designed RFID tags. To this end, preliminary LTCC-based prototypes with temperature monitoring have already been developed using the AMS SL900A IC.

7.5. Conclusions

In this chapter I have presented the design of a new implantable UHF-RFID tag based on multilayer LTCC technology for the remote monitoring of patients. The antenna tags were performed using a square spiral PIFA and an inductor line for impedance matching. The integration of the RFID IC in the antenna tag was considered, as well as the miniaturization of the antenna.

First, simulations were carried out to assess the impedance matching, the reflection coefficient, the gain and the operational range of the antenna. Then, the characterization of manufactured prototypes was performed when implanted inside a 10 mm cubic skin phantom. Results showed a satisfactory agreement between simulations and measurements, indicating a promising behavior of the tag for operating at the UHF-RFID band and for compensating the detuning effects of the biological tissues.

New RFID ICs with sensing capabilities are currently in development for the design of novel RFID tags with monitoring features, such as temperature.

8. Design and Characterization of a Phased Antenna Array for Intact Breast Hyperthermia

8.1. Introduction

This chapter presents the work developed in collaboration with the Biomedical Computing and Devices Laboratory group from the Kansas State University (KSU), in the US. The EM computational tools and the experimental setup used are adapted according to the KSU facilities. Unlike previous chapters, the research is not related to a biotelemetry application for in-body devices. The present study consists in the design and the *ex-vivo* validation of an on-body microwave applicator based on a phased antenna array for the treatment of breast cancer through hyperthermia. Although the applications differ according to scenario, the theoretical background between in-body and on-body propagation and between wireless biotelemetry and microwave hyperthermia is similar, as they both deal with the interaction of the RF fields with the biological tissues (see Chapter 2).

Breast cancer is the most frequent cancer among women; in 2013, it accounted for 29% of all new female cancer diagnoses in the United States [251]. Early detection is crucial in the control of the disease [252]; if the tumor is detected when it is still entirely localized within the breast, complete excision through mastectomy or lumpectomy may be curative [253]. Lumpectomy (or breast-conserving surgery) is a standard alternative to mastectomy (or total removal of a breast) for some patients with tumors of size of 4 cm or less [254], [255]. On many occasions, lumpectomy or mastectomy is preceded or followed by radiotherapy and/or chemotherapy [254]. Clinical microwave hyperthermia, moderate heating in the range of 39-44 °C for 30-90 min, has been shown clinically to be a potential adjuvant to radiotherapy and/or chemotherapy for various cancers [30]–[34]. Specifically, for superficial breast cancer and chest wall recurrence, clinical trials combining radiotherapy and hyperthermia have recorded significant improvements in complete response [256], [257]. Hyperthermia is also under investigation for thermally triggered release of cancer therapeutic agents in various targets, including the breast [258], in order to enhance the immune response [259], and combined with nanoparticles [37].

While a large proportion of tumors arise in the upper outer quadrant of the breast [260], [261], breast carcinomas can develop in any location [262]. Clinical hyperthermia applicators should have the ability to steer energy deposition to targets of varying size and shape which may be found at diverse locations within the breast. Commercially available clinical applicators for hyperthermia treatment

of superficial chest wall disease mostly employ waveguides [263]. These systems are relatively easy to use, but they are large and bulky, resulting in patient discomfort and limiting power steering. Focused ultrasound (FUS) applicators have been developed for hyperthermia and thermal ablation of deep-seated breast targets [264]. An advantage of FUS Systems is that the small acoustic wavelength (~mm) allows precise focusing of energy delivery to targets. Microwave applicators [265] offer the advantage of heating broader volumes without requiring complex control strategies, as is necessary with FUS.

Although single antenna applicators offer the advantage of simplified practical implementation and treatment delivery, their spatial control of energy deposition patterns is limited. Systems incorporating multiple antennas facilitate electronic steering of power deposition within the breast. The focusing may be achieved through simultaneous operation of multiple antenna applicators as a phased array [265]–[269], or by sequentially activating individual antennas [270]. They can be broadly classified into narrowband systems (i.e., operating at a fixed frequency) [271]–[276] or ultra-wideband systems [206], [277]–[279]. When operated as a phased array, the amplitude and relative phase of the signal supplied to each antenna can be adjusted to yield constructive interference in a desired region (target), and destructive interference elsewhere (non-target tissues).

The objective of the study presented in this chapter was to design and characterize the technical efficacy of a 915 MHz phased array applicator comprised multiple patch antennas and a shared groundplane, in order to develop a comfortable and wearable hyperthermia system and to deliver hyperthermia to tumors in varying breast locations. The patch antenna presented in [181] is proposed as the unitary element for this phased array system. To account for the diversity in breast dimensions, two 3D-hemispherical breast models with diameters of 90 mm and 150 mm were considered. We evaluated cuboid target tumors with maximum edge lengths of 10 mm (1 cm^3) and 30 mm (27 cm^3), as representative of small and large targets respectively. We investigated tumor targets centered at the midline of the breast, near the chest wall, and laterally positioned. Applicator designs were comparatively assessed by evaluating power deposited in a targeted area normalized to the total power deposited in the full breast. To validate our simulation approach, a proof-of-concept multi-antenna applicator was fabricated, and induced transient temperature profiles were measured in tissue phantoms of *ex-vivo* chicken breast.

To sum up, the main goals of the study presented in this chapter are:

- To design an on-body microwave applicator based on an antenna array operating at 915 MHz for breast cancer treatment through hyperthermia.

- To evaluate the feasibility of the applicator in different scenarios by modifying the dimension of the breast or the tumor and the location of the tumor.
- To analyze the effect of the angular spacing between antennas and the number of antennas in the array.
- To assess the implementation of a focusing algorithm that modifies the antenna phases.
- To experimentally validate the design by measuring the phantom temperature increase in a manufactured prototype.

8.2. Materials and Methods

8.2.1. Numerical Breast Phantom

Optimal configuration of a microwave hyperthermia breast applicator is a function of biophysical (perfusion and dielectric parameters) and dimensional (breast size and composition, and tumor location) parameters that may vary considerably amongst individual patients. Thus, practical systems must trade-off the optimal treatment of selected patient populations with the ability to adequately treat a wide variety of patients. To account for diversity in breast dimensions, two numerical breast phantoms have been evaluated. The phantoms are hemispheric models of outer diameter 90 mm (small breast model) and 150 mm (large breast model) and both are made of a 2 mm-thick skin layer encompassing fibroglandular tissue [181], [280]. The chest wall was modelled as a rectangular layer of 170 mm edge for the small breast model and 230mm edge for the large breast model of 15 mm-thick fat and 5 mm-thick muscle [181], [281] as shown in Figure 108. Frequency-dependent dielectric properties for water, skin, fibroglandular, fat and muscle tissue were implemented in the model, as listed in Table 41.

Cuboid target volumes of 10 mm edge length (1 cm^3) and 30 mm edge length (27 cm^3) located in the midline of the breast center and also near the chest wall were evaluated (see Figure 108). The centrally located tumor targets (Figure 108 (a, c)) were positioned with their center at 22.5 mm and 37.5 mm from the skin in the case of the small and large breast models, respectively. The tumors located near the chest wall (Figure 108 (b, d)) were positioned with their center at 15 mm from the fat layer of the chest wall.

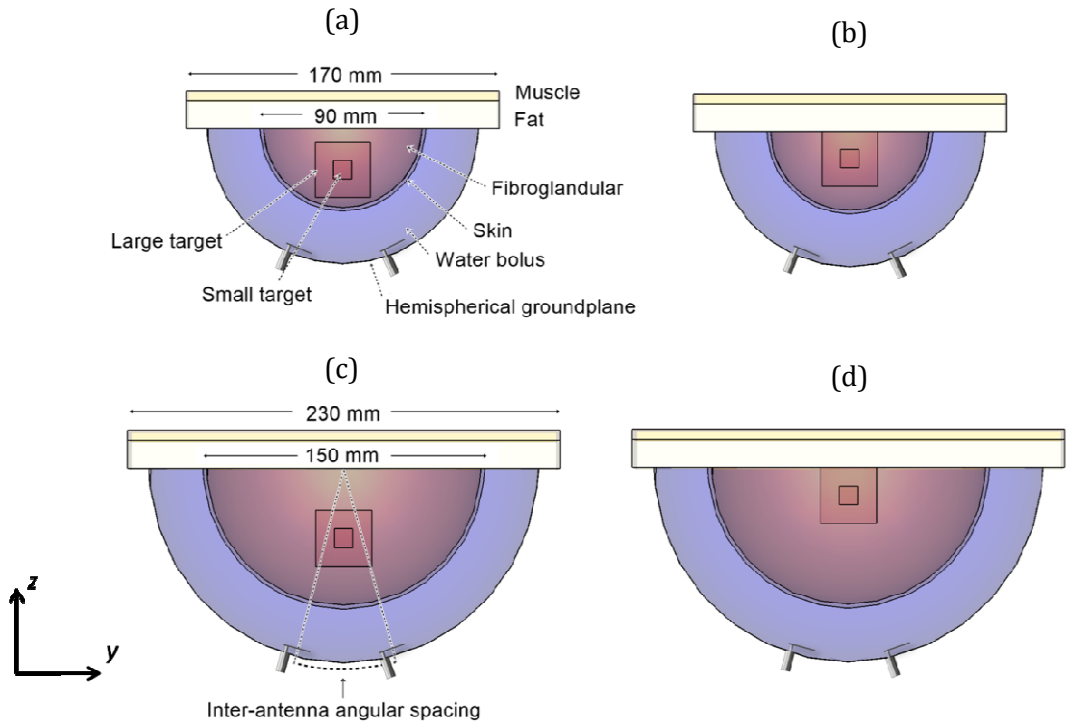

Figure 108. 2-antenna array applicator with small breast model with target located in the breast centre (a) and near the chest wall (b) and large breast model with target located in the breast centre (c) and near the chest wall (d).

Table 41. Tissue Dielectric Properties for 915 MHz.

Tissue	**Relative permittivity, ε_r**	**Conductivity, σ, S m^{-1}**	**Density, ρ, kg m^{-1}**
De-ionized water	79.9 [282]	0.20 [282]	1000 [277]
Skin	46.0 [281]	0.85 [281]	1085 [277]
Fibroglandular	41.1 [283]	0.83 [283]	1050 [279]
Fat	5.4 [281]	0.05 [281]	1069 [279]
Muscle	54.9 [281]	0.94 [281]	1041 [284]

8.2.2. Antenna Design

Array configurations with 2, 4, 8, 12, 16 and 20 patch antennas operating at 915 MHz were evaluated. All the antennas shared a hemispherical groundplane concentric to the breast target. The diameter of the hemispherical groundplane was 147 mm for array configurations for the small breast model and 207 mm for array configurations for the large breast model, which corresponds to a 25 mm

patch antenna–breast distance. The 14 mm × 3.9 mm rectangular patch antennas with groundplane to patch distance of 2.65 mm were designed following the description of the single antenna presented in [181]. The distance between the patches and the breast was fixed to 25mm for all the array configurations, since preliminary investigations showed that this value presented a compromise between power absorption (PA) as well as wearability and comfort of the applicator considering that thinner and consequently lighter water boluses will improve patient comfort [285]. The water bolus formed the cavity enclosed by the hemispherical groundplane, breast and chest wall. Deionized water, completely filling the water bolus, was used to improve impedance matching, reduce the size of the applicator and cool both the antenna and surface of the skin [181].

The antennas were positioned on the applicator circumference along orthogonal arcs (the x-axis and the y-axis) and located in the diagonal between the x-axis and y-axis as depicted in Figure 109. Antenna distribution along the orthogonal arcs was previously proposed by Bahramiabarghouei *et al.* [286]. All patch antennas were located at the constant distance defined by the parameter of inter-antenna angular spacing shown in Figure 108 (c). This parameter was analyzed to obtain the greatest PA in the desired target without compromising the impedance matching of individual antennas. A maximum acceptable value of S_{11} for each antenna element (including coupling with other elements) was set to -8.5 dB. Larger spacing between antennas decreases the ability to focus energy, while the smaller inter-antenna spacing generates near-field interferences that would compromise the impedance matching of the system. Smaller inter-antenna angular spacing allows the implementation of a larger number of antennas with the potential for good control of steerable power deposition profiles, at the expense of increased system complexity.

8.2.3. Evaluation of Proposed Designs

The PA was evaluated in the target volumes and in the full breast volume using Equation 21 [207], [287];

$$PA = \frac{\sigma|\mathbf{E}|^2}{2} \ [\mathrm{W/m^3}] \qquad (21)$$

where σ is the effective electrical conductivity of the tissue in S/m and $|\mathbf{E}|$ is the complex electric field (E-field) vector in V/m. The system performance is expressed in terms of the average power absorption (aPA) ratio as defined in Equation 22;

$$\alpha PA = \frac{\frac{PA_{targ}}{targ\_volume}}{\frac{PA_{breast}}{breast\_volume}} \qquad (22)$$

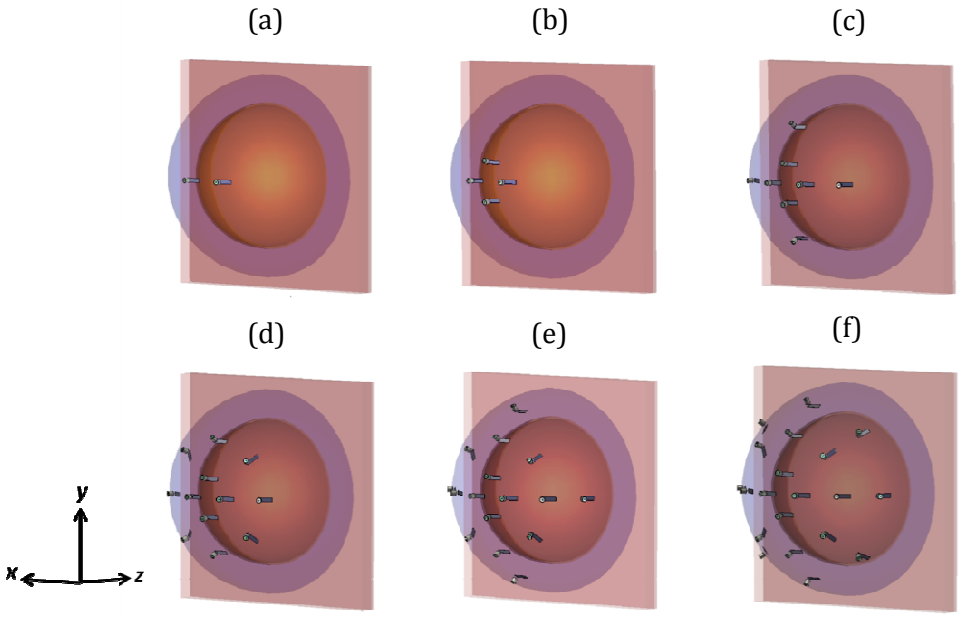

Figure 109. 3D view of array configurations with 2 (a), 4 (b), 8 (c), 12 (d), 16 (e) and 20 (f) antennas positioned on the applicator circumference along orthogonal arcs (the x-axis, the y-axis) and located in the diagonal between the x-axis and y-axis.

where PA_{targ} is the power absorbed in the target volume, $targ\_volume$ is the volume of the target, PA_{breast} is the power absorbed in the entire breast volume, and $breast\_volume$ is the cubic volume that encloses the breast.

8.2.4. Phase Adjustment to Steer Power Deposition Profiles

The objective function described in Wu *et al.* [273] was employed to determine the optimal phases of the signal applied to each antenna that results in E-field maximization at points within the tumor. The total E-field in the tumor center was defined as superposition of the individual E-field of N antennas, and computed as in Equation 23;

$$|\mathbf{E}(x,y,z)| = \left|\sum_{n=1}^{N} \mathbf{U_n}(x,y,z) I_n\right| \qquad (23)$$

where $\mathbf{U_n}$ is the E-field produced by the n_{th} antenna with unit input excitation and I_n is a complex number that represents the amplitude and the phase of the n_{th} antenna. A focus is generated when the individual E-field components constructively interfere at a defined location, and the highest interference is achieved when the magnitude squared of the total E-field is maximized relative to the sum of the squared input magnitudes as in Equation 24 [273].

$$|\mathbf{E}|^2 = \sum_{m=1}^{N}\sum_{n=1}^{N}(\mathbf{U_m}I_m)\ (\mathbf{U_n}I_n)^* \qquad (24)$$

When the amplitude of the antenna inputs is defined in advance, Equation (24) is a nonlinear function with the antenna input phases as variables [273]. Then, the magnitude squared of the total E-field in the tumor region can be obtained as a nonlinear objective function as shown in Equation 25;

$$\begin{aligned}\sum_{n=1}^{N-2}\sum_{m=n+1}^{N-1} & |I_n||I_m|\{|U_n^X||U_m^X|cos(\theta_n^X-\theta_m^X+\emptyset_n-\emptyset_m)\\ &+|U_n^Y||U_m^Y|cos(\theta_n^Y-\theta_m^Y+\emptyset_n-\emptyset_m)\\ &+|U_n^Z||U_m^Z|cos(\theta_n^Z-\theta_m^Z+\emptyset_n-\emptyset_m)\}\\ &+\sum_{n=1}^{N-1}|I_n||I_N|\{|U_n^X||U_N^X|cos(\theta_n^X-\theta_N^X+\emptyset_n)\\ &+|U_n^Y||U_N^Y|cos(\theta_n^Y-\theta_N^Y+\emptyset_n)\\ &+|U_n^Z||U_N^Z|cos(\theta_n^Z-\theta_N^Z+\emptyset_n)\}\end{aligned} \qquad (25)$$

where θ_n and θ_m are the arguments of the E-field U_n and U_m, respectively, and ϕ_n and ϕ_m are the phases of the excitations I_n and I_m, respectively. The reference phase of the N element is set to $\phi_N = 0°$. We first computed the E-field of each antenna independently and we specified constant magnitude of the excitations with the electromagnetic simulation. The technique used to solve the optimization problem was the iterative Nelder–Mead simplex algorithm [288]. Maximizing the objective function the algorithm generates the phases ϕ_n that produce a constructive E-field interference in the tumor region. The termination criterion for the algorithm was a tolerance of 1×10^{-8} between iterations.

Electromagnetic simulations were performed using CST Microwave Studio [171] on a 3.0 GHz PC with 16 GB RAM. Memory requirements and simulation times ranged from 691MB and ~40 min for the small breast model with the 2-antenna array configuration to 13 GB and ~8 h for the large breast model with the 20-antenna array configuration. Phased array computations were performed using Matlab (R2015).

8.2.5. Experimental Evaluation and Validation

A 4-antenna array configuration with inter-antenna angular spacing of 45° and hemispherical groundplane was fabricated for experimental evaluation in a small breast model. The patches and groundplane were implemented with 0.127 mm-thick copper sheets (McMaster-Carr, Elmhurst, Illinois) and the antennas were fed with 50 Ω SMA female connectors (PE4099, Pasternack Enterprise, Irvine,

California). Figure 110 (a) shows a photograph of the fabricated applicator showing the 4-antenna array configuration. The broadband reflection coefficient of the 4-antennas was measured when loaded with a tissue phantom of *ex-vivo* chicken breast. Tissue samples were stored in a refrigerator at a temperature of ~4 °C. Before performing the heating experiments, the sample was enclosed in sealed bags and heated up to 32 °C in a controlled bath. Just before performing the experiment, the samples were removed from the plastic bags and positioned in a 3D-printed 1.5 mm-thick PTFE fixture to perform the heating experiments. Figure 110 (b) shows a photograph of the 3D-printed fixture. Fiber-optic temperature probes (Neoptix RFX- 04-1, Canada) were placed within the *ex-vivo* chicken breast phantom as shown Figure 110 (c). Room temperature (20 °C) water was circulated through the system at a flow rate of 5 ml/s with a peristaltic pump (Cole-Parmer, 7554-90, IL).

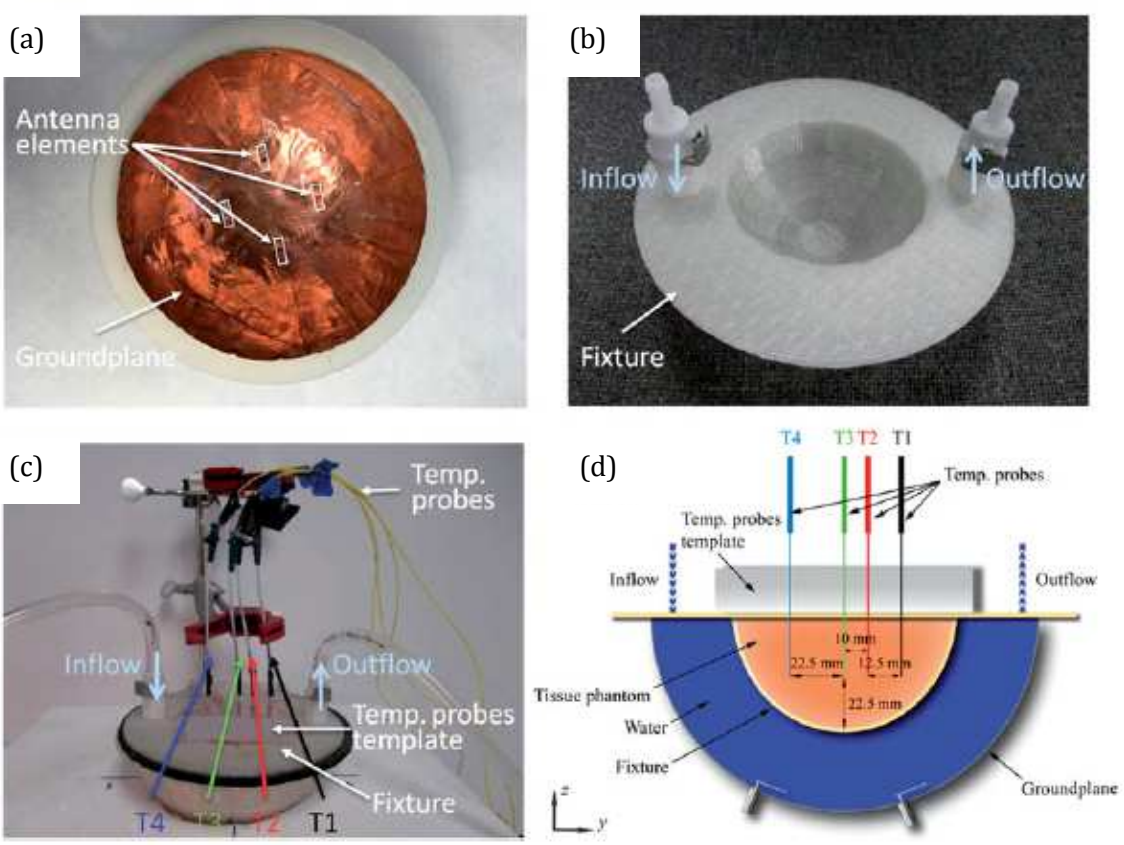

Figure 110. Fabricated applicator and experimental setup with a photograph of the fabricated applicator showing the 4-antenna array configuration (a), a photograph of the PTFE fixture (b), a photograph of the measurement setup (c) and schematic representation of the antenna setup measurement detailing the position of the temperature probes for the fabricated array configuration on the yz-plane (d).

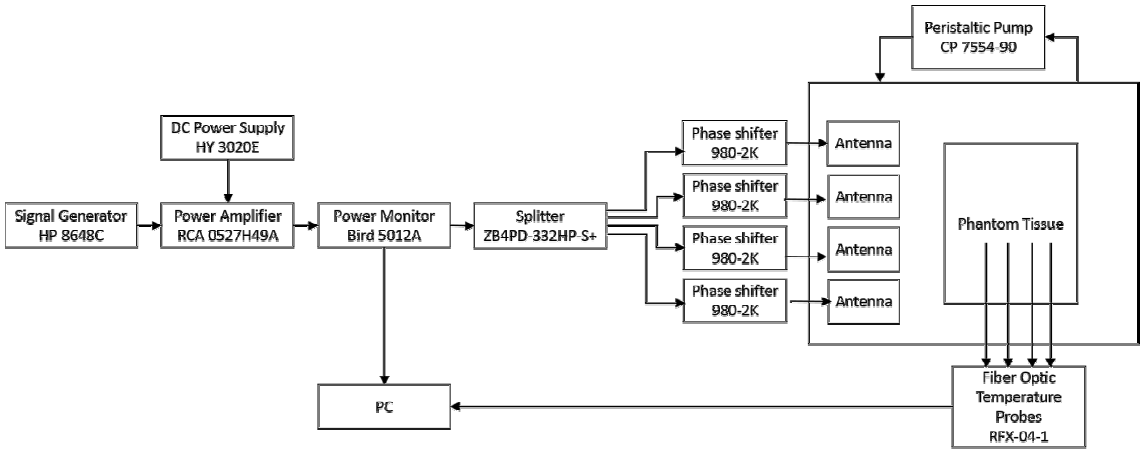

Figure 111. Setup for experimental assessment of phased array applicator in *ex-vivo* tissue phantom.

Experiments were performed with constant input power of 50 W, as measured with the power meter (7.5 W per antenna), for 10 min. Reflected power on each antenna was monitored before performing the heating experiments and it was in all cases below 2 % of the forward power measured by the power meter. One set of experiments employed equal phase to all antennas (to focus the energy in a target located 22.5 mm deep, along the midline of the tissue phantom, i.e. the tip of T3 in Figure 110 (d)), while the second set employed phases identified with the optimization technique (to focus the energy with an offset 22.5 mm from the midline of the tissue phantom, i.e. the tip of T1 in Figure 110 (d)).

The microwave hyperthermia system consists of a signal generator, power amplifier, power monitor, 4-channel power divider, 4 manually controlled phase shifters and the applicator. Heating experiments in the tissue phantom were performed with the setup illustrated in Figure 111 to measure the transient temperature profiles induced by the proposed applicator. Heating experiments were performed in triplicate. A computational model mimicking the experimental setup was implemented. This model comprised the tissue fixture and temperature template with dielectric properties as in Arunachalam *et al.* [289] and *ex-vivo* chicken breast phantom (ε_r=57.75 and σ=1.49 S/m) as in Curto *et al.* [181].

8.3. Results

8.3.1. Effect of Angular Spacing between Antennas

Figure 112 illustrates the aPA ratio for a 4-, 8- and 12-antenna array as a function of the inter-antenna angular spacing for the targets located at the center and close to the chest wall of the small breast model. The small breast model (90mm diameter) was selected as an example for illustrating the impact of antenna element spacing on aPA. The evaluated inter-antenna angular spacing are 20°, 22.5°, 45°, 75.5°, 90°, 112.5° and 135° for the 4-antenna array and 20°, 22.5° and 45° for the 8- and 12-antenna array (these are the largest angular spacing possible for this hemispherical applicator).

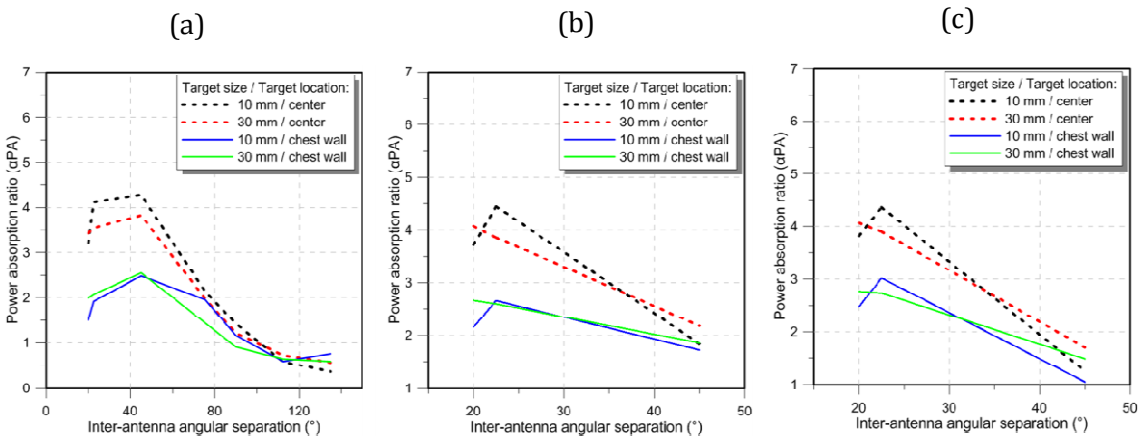

Figure 112. Average power absorption ratio of the 4-antenna array (a), 8-antenna array (b) and the 12-antenna array configuration (c) for the 10 mm edge length target and 30 mm edge length target located at the centre and near the chest wall of the small breast model for different inter-antenna angular spacing.

8.3.2. Effect of Number of Antennas in the Array Configuration

Figure 113 illustrates the aPA ratio as a function of number of antennas for the targets located at the center and close to the chest wall of the small breast model for configurations with inter-antenna angular spacing of 22.5°. Array configurations of 2, 4, 8, 12, 16 and 20-antennas (with configurations shown in Figure 109) were evaluated. The specific absorption rate (SAR) cross-sections on the yz-plane in the small breast model and array configurations of 2, 4, 8, 12, 16 and 20 antennas with constant phase is shown in Figure 114.

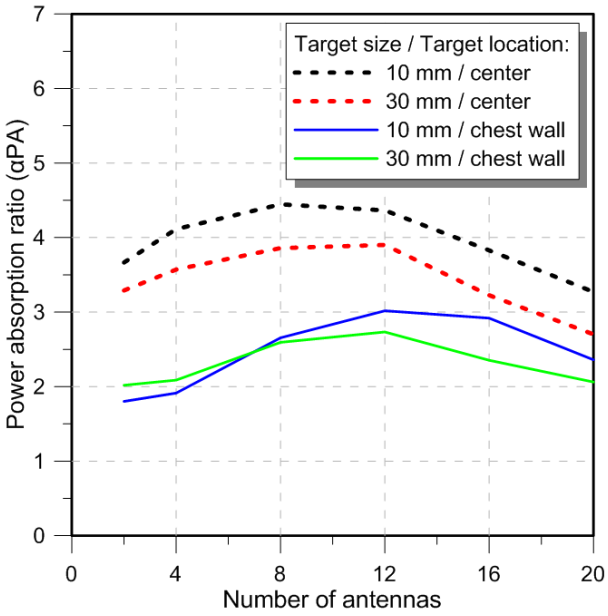

Figure 113. Average power absorbed ratio for the 10 mm edge length target and 30mm edge length target located at the centre and near the chest wall of the small breast model for different number of antenna configuration (2, 4, 8, 12, 16 and 20) and inter-antenna angular spacing 22.5°.

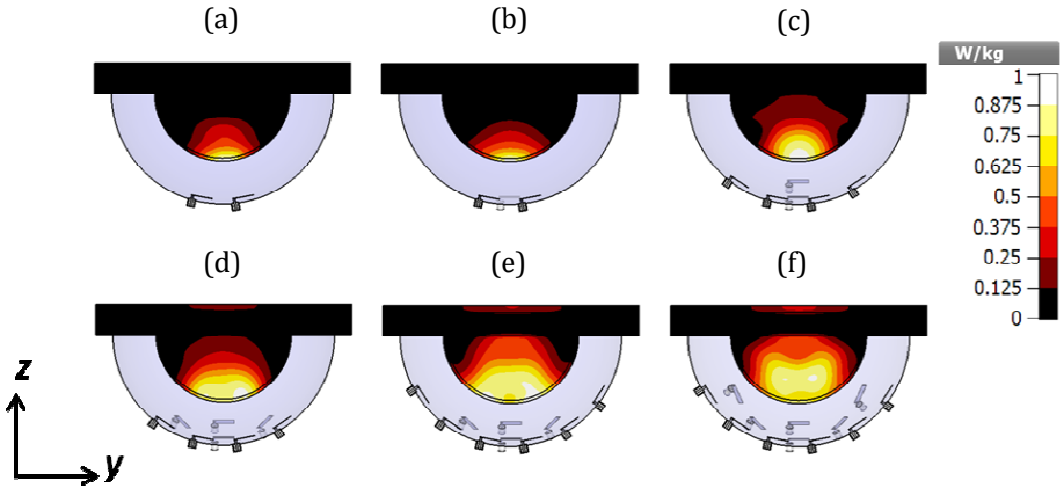

Figure 114. SAR cross-sections on the yz-planes of the small breast model and antenna array configurations of 2 (a), 4 (b), 8 (c), 12 (d), 16 (e) and 20 (f) antennas with constant phase. SAR normalized to the maximum value on the system.

8.3.3. Evaluation of a Largest Breast Model

Figure 115 illustrates the aPA ratio as a function of number of antennas for the targets located at the center and close to the chest wall of the large breast model for configurations with angular spacing of 22.5°. Array configurations of 2, 4, 8, 12, 16 and 20-antenna as shown in Figure 109 were evaluated.

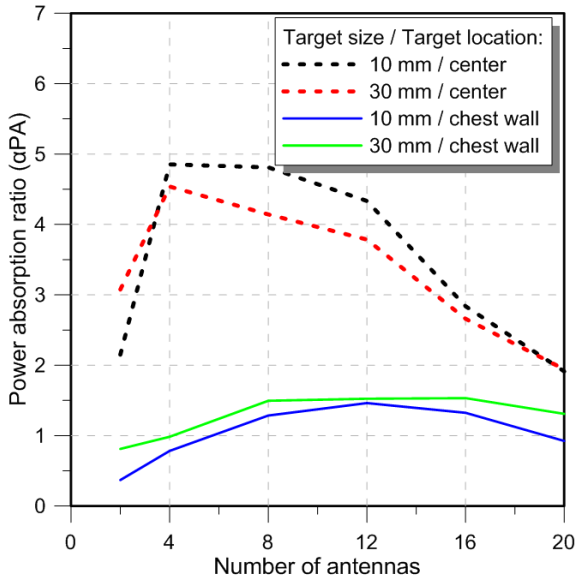

Figure 115. Power absorbed ratio for the 10 mm edge length target and 30 mm edge length target located at the center and near the chest wall of the large breast model for different number of antenna configuration (2, 4, 8, 12, 16 and 20) and inter-antenna angular spacing 22.5°.

8.3.4. SAR Distribution of the 4-Antenna Array with Optimized Phases

The simulated SAR distribution in the yz-plane for the 4-antenna array configuration with constant phase with the objective of generating a focus in a centrally located target (indicated with a symbol × in the figure) at the midline of the breast is shown in Figure 116 (a) and in the simulated experimental setup is shown in Figure 116 (c). The SAR distribution in the yz-plane with optimized phases (84.5°, 84.5°, 123°, 0°) with the objective of steering the energy deposition to a target (indicated with a symbol × in the figure) located in the right lobe of the breast with and offset of 22.5 mm from the breast midline is shown in Figure 116 (b) and at the same location of the simulated experimental setup is shown in Figure 116 (d).

8.3.5. Experimental Results

Figure 117 shows the simulated S_{11} with the simplified human breast model and the *ex-vivo* chicken breast model and experimentally measured S_{11} with the *ex-vivo* chicken breast phantom. Figure 118 shows experimentally measured (n=3) transient temperature profiles during heating experiments performed in *ex-vivo* tissue phantom, while applying a input power of 7.5 W per antenna with all the antennas fed with constant phase (Figure 118 (a)) and with optimized phase to steer the energy in a target 22.5 mm offset from the breast midline (Figure 118 (b)).

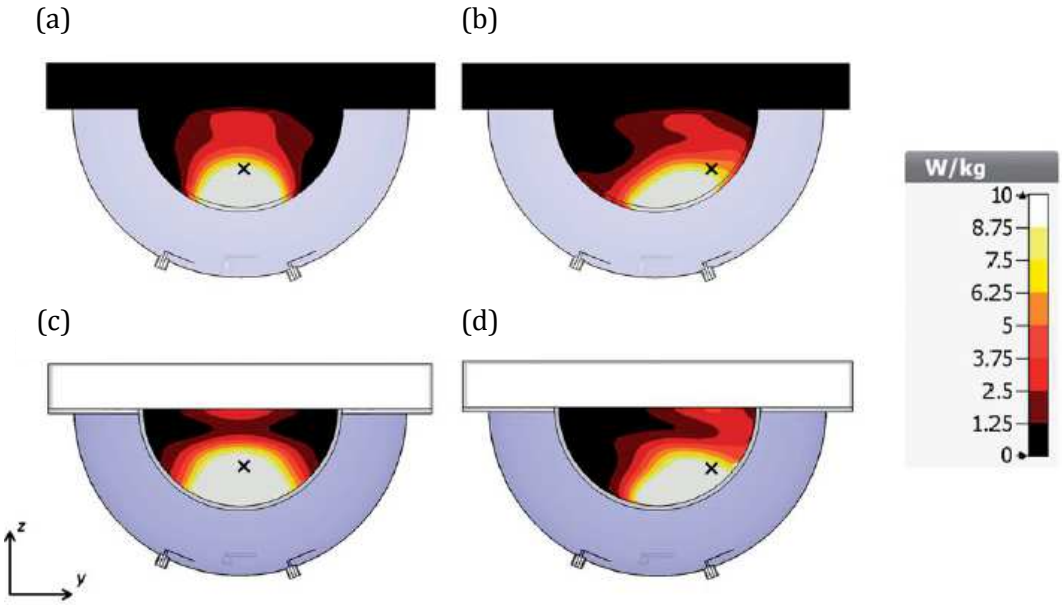

Figure 116. SAR cross-sections on the yz-plane with the 4-antenna array on the small breast model with all the antennas with constant phase (a) and phases optimized to create a focus in a laterally located target on the right lobe of the breast (b) and on the experimental setup with all the antennas with constant phase (c) and phases optimised to create a focus in a laterally located target on the right lobe (d). The symbol x indicates the location of the focus target.

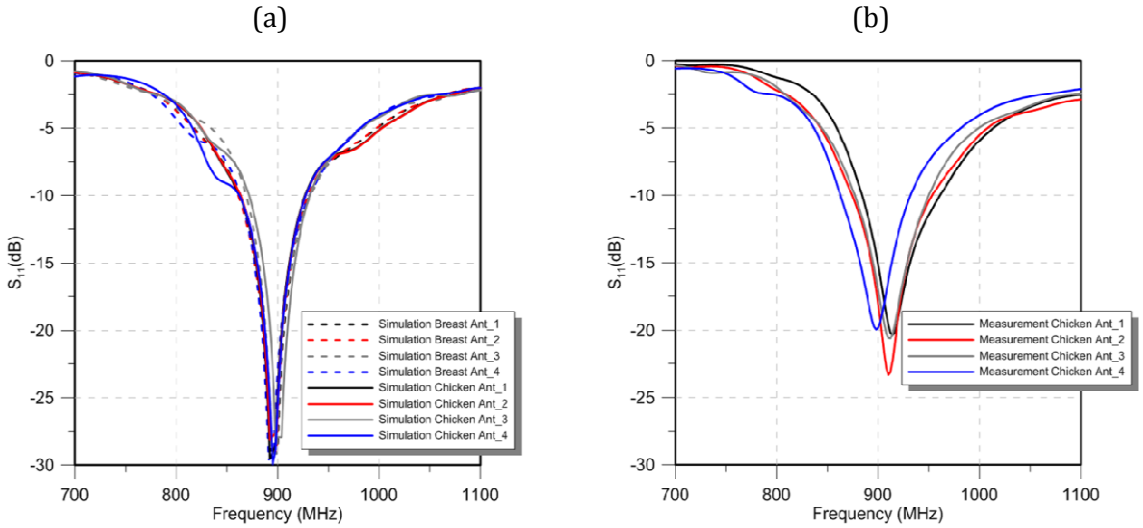

Figure 117. Simulated S_{11} values of the 4-antenna array the with simplified human breast model and *ex-vivo* chicken breast model (simulation of the experimental setup) (a) and S_{11} values of measurements with ex-vivo chicken breast (b).

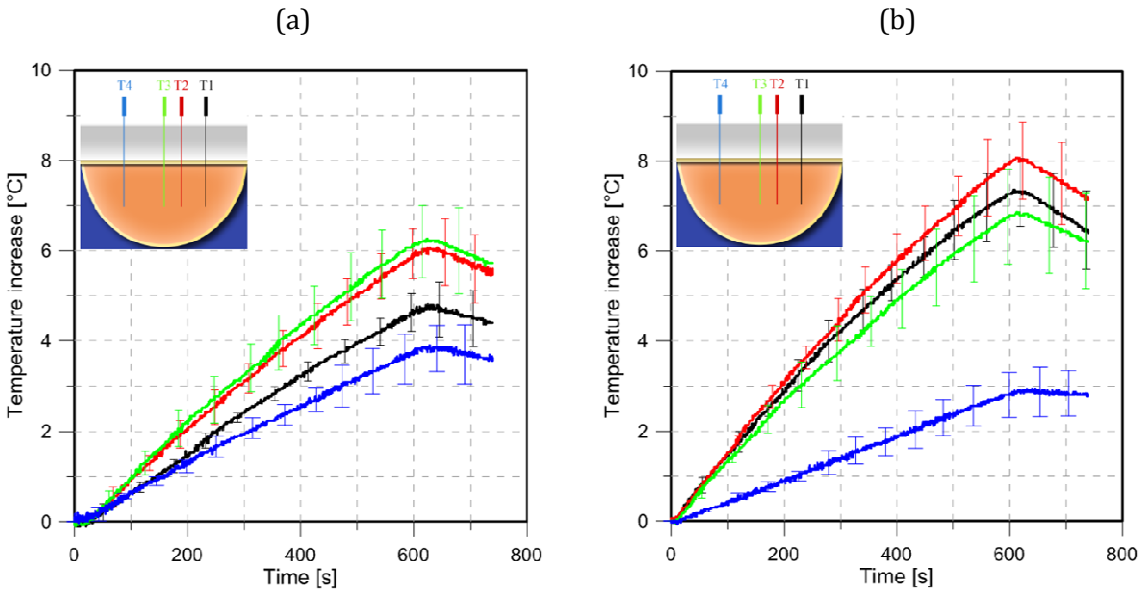

Figure 118. Experimentally measured (n=3) transient temperature profiles with the 4-antenna phased array with constant phase (a), and phased optimized (b) to have the focus with an offset of 22.5 mm from the breast midline. Solid lines represent the mean value, error bars represent the range (maximum/minimum values). Temperature probes T1, T2, T3 and T4 positioned in the *ex-vivo* tissue phantom. See Figure 110 for further details about the position of the temperature probes.

8.4. Discussion

8.4.1. Effect of Antenna Spacing on Energy Deposition Patterns

When considering a small breast, for a 4-antenna array configuration, simulations indicated moderate increases in aPA values as inter-antenna spacing increased from 20° to 45° within both small and large targets (see Figure 112 (a)). However, further increases in inter-antenna angular spacing yielded sharp decreases in aPA values. For 8- and 12-antenna arrays, the highest aPA was found with inter-antenna spacing of 22.5° for the small target and at 20° for the large target (see Figure 112 (b, c)). Positioning the antenna with an inter-antenna angular spacing of less than 20° generated nearfield interferences, which degraded the antenna impedance matching (i.e. S_{11}>-8.5 dB). In general, these results suggest that a good focusing effect can be achieved with inter-antenna spacing of 22.5° (or inter-antenna circumferential distance of ~27.4 mm) for arrays incorporating 4-12 antennas.

8.4.2. Effect of Number of Antennas on Energy Deposition Patterns

Considering an inter-antenna spacing of 22.5°, simulations were employed to assess the quality of focusing effect within small and large targets, positioned centrally or at depth (close to the chest wall) within the small breast, of 90 mm in diameter. As illustrated in Figure 113, for central targets, a similar performance was achieved with arrays employing 4–12 antennas, in which aPA ranged between 4.1 and 4.4 for small targets and 3.5 and 3.9 for large targets. Although increasing the number of antennas beyond 12 yielded intense energy deposition within the target, aPA values decreased more with the greater energy deposition outside the target, which could be seen in the SAR profiles illustrated in Figure 114. The aPA curve shifted to the right for deep-seated targets positioned near the chest wall, and good performance was achieved when using 8–16 antennas (Figure 113). This rightward shift can be explained by the effects of greater attenuation of the E-field due to the increased distance between the target volume and the antennas. Collectively, these results suggest that arrays incorporating 8–12 antennas with an inter-antenna angular spacing of 22.5° provide sufficient flexibility to achieve good focusing within cubic target volumes of 1 cm^3 and 27 cm^3 positioned centrally or at depth (close to the chest wall) within the breast.

Simulations with the large breast model showed that for an inter-antenna spacing of 22.5°, a good focusing effect (aPA ~4–5) was achieved with 4–8 antennas for central targets (Figure 115). Similar to the results with the small breast model, a larger number of antennas yielded the best focusing quality (aPA ~1.5 with 8–16 antennas) for deep targets. Similar aPA values were achieved for central targets in the small breast and large breast. This finding may be attributed to the reduced energy deposition in the target for the large breast being balanced by reduced energy deposition within the rest of the breast volume. However, for deep-seated targets, an optimum aPA value of ~3 was achieved in the small breast compared to ~1.5 in the large breast. This can be explained by the attenuation of heating effect due to the longer distances between the deep-seated target and antenna in the large breast than in the small breast.

8.4.3. Experimental Evaluation

A 4-antenna array configuration with inter-antenna angular spacing of 45° was fabricated for experimental evaluation. The antenna reflection coefficients measured in an *ex-vivo* chicken breast phantom were in good agreement with simulations of the simplified human breast model and the *ex-vivo* chicken breast (Figure 117). Positions of experimentally measured heating focal spots were in good agreement with SAR simulations. When using antennas with constant phase, the measured temperature profiles illustrated the capability of delivering energy to central targets with the proposed applicator (Figure 116 (a, c) and Figure 118

(a)) using relatively low input power levels (7.5 W per antenna). By adjusting the relative phase of signals fed to individual antennas, as determined using the focusing algorithm presented in Wu *et al.* [273], simulations and experiments indicated the feasibility of electrically steering focal spots ((Figure 116 (b, d) and Figure 118 (b)).

Table 42 shows the ratio of the experimentally measured temperature rise for the case with focus at the center compared to the lateral focus, following 60 s of heating at locations T1–T4. Also shown are the ratios of simulated SAR at the same locations. Both simulations and measurements indicate that, compared to lateral focusing (i.e. adjusted phases), central focusing (i.e. equal phase) yields: reduced heating at location T1, moderate increases in heating at locations T2 and T3, and large increases at T4. Discrepancies between experiment and simulation may be due to uncertainty in the location of temperature sensors during experiments, mismatch in tissue properties between experiment and simulation, and phase discrepancies along cables.

Table 42. Measured temperature and simulated SAR ratio center/lateral focusing at the locations T1, T2, T3 and T4.

Evaluated Location	Ratio of measured temperature	Ratio of simulated SAR
T1	0.89	0.58
T2	1.26	1.09
T3	1.66	1.84
T4	3.48	6.08

These simulation and experimental results suggest good potential for heating targets in diverse locations within the breast. In particular, for central targets, the ratio of power deposition within the target volumes was approximately five times larger than in the full breast volume. While this study focused on the analysis of parameters that affect the quality of electromagnetic focusing within target volumes, further investigations are necessary to assess the thermal profiles in simulation and experiment. Thermal analyses will be important for assessing the ability of the water bolus to effectively avoid heating the skin and non-targeted tissue between the target and the antennas. Another limitation of this study was that it did not consider dielectric heterogeneity between the target tissue and surrounding non-target regions. It is anticipated that dielectric contrast (especially effective conductivity) between the target and non-target tissue may yield increased power deposition within targets [207], [283].

Several studies have reported phased antenna arrays positioned within a cylindrical geometry for delivering hyperthermia to breast targets [272], [290].

Although the proposed system will require a water bolus for coupling electromagnetic energy to the breast while thermally sparing surface tissues, it will not require compression of the breast as in Dooley *et al.* [291]. Due to the use of a hemispherical groundplane, the antennas can be positioned close to the breast target. Thus, the power levels required per antenna for achieving adequate heating are lower than in other applicators [272], [273]. Hemispherical breast models and hemispherical groundplane applicators, with 25 mm-thick water bolus, were considered for this study. Future evaluations of this applicator will incorporate patient-specific models with variable water bolus thickness, e.g., for patients in prone position with pendant breast. Differences in water bolus thickness, and in general, path length and heterogeneity of interfacing tissues between the antenna elements and the actual tumor will be compensated by individualized patient treatment planning, in which specific power and phase could be applied for each antenna element. This study considers the antenna located at a variable angular separation along the orthogonal axis and in the diagonals between the axes as an initial approximation. Future studies will further investigate antenna distribution across the breast hemisphere with uniform solid angle; they should also assess the impact of heterogeneous tissue properties [292], as well as extend the biothermal modelling efforts for assessment of the array design presented [181].

8.5. Conclusions

This chapter presented a novel microwave hyperthermia applicator based on a phased array for the breast cancer treatment. The design incorporated a hemispheric groundplane and a bolus full of flowing cold water to maintain the temperature of the biologic tissues at safe levels. Phased arrays of 2, 4, 8, 12, 16 and 20 rectangular patch antennas were tested to assess the focusing of the delivered power.

Simulations were carried out in CST software, and the reflection coefficient, SAR levels and the aPA were assessed. Results illustrated that an angular spacing of 22.5° between antennas presented the best results in terms of aPA. Results also showed that an 8-antenna array achieved the highest aPA at centrally located targets, while a 12-antenna array achieved the highest aPA at deep seated targets for both small and large breast models.

An experimental model comprising 4-antennas with optimized phases was manufactured. The reflection coefficient measurements of the four antennas were in good agreement with simulations. The measured results showed a favorable temperature increase of 7 °C on laterally located targets 22.5 mm off from the center, compared with a temperature increase of only 3 °C on the opposite side. These results suggest that the applicator might be suitable for creating diverse energy deposition patterns at different locations within the intact breast.

9. General Discussion, Conclusions and Future Work

The research performed in this thesis was carried out under the framework of the oncoming P4 medicine paradigm, where the focus of the healthcare is placed on the patient. P4 medicine aims to quantify wellness and prevent diseases in order to reduce hospital costs and enhance the quality of life of the general population. In this context, biomedical devices with RF play a crucial role, as they can provide individualized treatments and/or long-term remote physiological data. One of the main challenges in the current research into biomedical devices with RF is the improvement of the design and characterization of the antennas in the presence of the human body.

The insights provided in this thesis are geared towards the development of antennas in biomedical device, for two main applications: wireless biotelemetry and microwave hyperthermia. For the former, the improved understanding of the interaction between EM and biological tissues has led to the design, development and implementation of novel in-body multilayered PIFA-based antennas that overcome some of the current problems. New contributions regarding miniaturization methods, phantom influence, bandwidth enhancement, manufacturing, characterization, packaging and RFID integration have been presented and discussed. With regard to microwave hyperthermia, a new approach to the applicator led to the design of a novel on-body, compact, comfortable, low-cost and configurable device for the treatment of breast cancer.

This thesis was divided in two parts. In the first, I presented the theoretical framework of antennas in the presence of a human body and the research developed to achieve the first manufactured in-body prototypes. In the second, I presented three antenna demonstrators that contribute to the current applications of biotelemetry and microwave hyperthermia.

9.1. Thesis Assessment

The achievements and elements discussed in this thesis can be classified under the following headings:

9.1.1. Antenna Design

In this thesis, I focused my study of the antenna design mainly on the in-body scenario. As identified in Chapter 2, several aspects of in-body antennas still remain under development, such as miniaturization, biocompatibility, operating frequency, antenna performance, powering, packaging, antenna modeling, manufacturing and experimental characterization. According to the literature, PIFA designs are suitable structures for in-body applications as they provide a good balance between miniaturization and antenna performance. Thus, in Chapter 3, the miniaturization issue was addressed through the exploration of different square PIFA size reduction methods, such as meanders, fractals, spirals and multilayer structures. The results showed that 3D spiral miniaturization techniques presented the best compromise between volume and efficiency. In addition, folding down the main radiator of the antenna, and separating the radiator ending as far as possible from the tissue, was found to optimize gain for a given antenna volume. Indeed, the ratio between volume and efficiency of the final 3D PIFA was twice that of the final 2D PIFA.

It is worth mentioning that the substrate thickness was limited to 2 mm because of the selected technology and the available facilities. However, thicker and narrower antenna designs (more similar to cubic structures) could increase the ratio between volume and efficiency, since it would make more efficient use of the available space. In any case, the final shape of the substrate depends on the application for which the antenna will be used. Other parameters of the designs analyzed were also limited by technology constraints, such as the radiator width or the distance between layers. Further development in the manufacturing technology will allow smaller designs.

The MedRadio frequency band was selected for most of the antenna designs. Some designs at other frequencies were also developed. In Chapter 4, square spiral PIFAs at 866 MHz and 2.45 GHz were obtained by reducing the length of the radiator. Chapter 7 presented a new antenna design for an UHF-RFID tag. This design was based on a square spiral PIFA with an inductor line to match the IC capacitive impedance. As regards antenna design, Chapter 8 proposed an array of rectangular patch antennas operating at 915 MHz for an on-body microwave hyperthermia applicator. A bolus full of water surrounding the antenna array helped to miniaturize the radiating patches, making the device more compact and configurable. The frequency detuning caused by the heterogeneity of the biological tissues was addressed in Chapter 6, where the design of a novel multilayer implantable broadband PIFA was proposed. The enlargement of the bandwidth was obtained by the coupling between two radiators, which provided two resonant peaks in close proximity.

Regarding the antenna modeling, several commercially available software packages were used during the development of the thesis, depending on the application, the available facilities and the stage of the design. The use of more than one EM computational tool in certain cases increased the confidence in the results.

Although the powering of the antenna and the electronics required in an IMD were not specifically assessed in this thesis, an integration technology was selected for future developments of complete devices (see Subsection 9.1.3). In Chapter 6, I presented a study of the influence of the electronics in the antenna performance. In Chapter 7, a passive in-body RFID tag was proposed as a solution for powering and integration. The results indicated a limited tag range of 10 cm, which may be enough for certain applications.

The manufacture of the antennas and their experimental characterization are discussed in Subsections 9.1.4 and 9.1.5 respectively.

9.1.2. The Human Body

As seen in Chapter 2, several human body models were found in the literature, either for computational simulations or experimental validation. The geometry, volume, materials and realism of the phantom selected depend mainly on the application and the design stage. Although it has previously been demonstrated in the literature that phantoms strongly influence the radiated EM fields of an antenna, a quantitative analysis was carried out in Chapter 4 for in-body square spiral PIFA-based antennas at different frequencies. It was found that, apart from size, implant depth and biological tissues, the EM field regions and the antenna orientation also significantly affected antenna performance. Some guidelines were therefore proposed to select the appropriate operating frequency band depending on the implant placement. For shallow implants, antennas operating at higher frequencies can show better performance (an increase of up to ~20 dB in gain), mainly due to the reduction of the near-field region, which can compensate for the higher losses. In contrast, for deeper implants, low frequencies are generally recommended.

Most of the simulations performed in this thesis were carried out in canonical phantoms. However, the heterogeneity of the tissues and the variations of the phantom sizes significantly alter antenna performance, such as the gain (see Chapter 4) or the operating frequency. In Chapter 6, a broadband antenna for in-body applications was presented to mitigate this frequency detuning. Its performance was evaluated when implanted into four different sites (head, chest, torso and arm), showing satisfactory results. For the assessment of a breast cancer hyperthermia treatment, in Chapter 8, the influence of breast size as well as the

target size and target location within the breast were taken into consideration in the assessment of the device.

In order to compare the antenna performance of different in-body antennas found in the literature or designed by oneself, in Chapter 4 I proposed an antenna characterization protocol based on the near-field regions, which aims to provide the same characterization scenario depending on the operating frequency. This standardization is indicated for antenna engineers seeking for an in-body antenna design that efficiently operates inside the body, without knowing the specific application in advance.

9.1.3. Integration Technology

In this thesis LTCC technology was selected as a promising multilayer ceramic-based technology for the integration of implantable antennas with the other components of an IMD. The advantages of LTCC include a final hermetic block as a monolithic structure (thus avoiding air gaps between layers or the use of glue to fix them), the inclusion of opened and closed cavities to integrate other components, the interconnection of components from the surface to the inner layers, biocompatible low-loss substrates with high permittivity and durability. The in-body antenna designs proposed in Chapters 3, 4, 5, 6 and 7 were based on LTCC technology in order to take advantage of these features. In Chapter 6, an initial assessment of the influence of the integration of electronics on antenna performance was made. The electronic components were modeled as embedded metallic boxes of varying sizes and placements. The results showed a good level of integration robustness. Chapter 7 took advantage of the cavities allowed in the LTCC substrate to isolate the RFID IC from the lossy surrounding media.

9.1.4. Manufacturing Process

Most of the representative antenna designs that I presented in this thesis were manufactured. For in-body antenna designs, LTCC technology was selected because of the features mentioned above. I had the opportunity to manufacture them at the FAE SAU company facilities. The analysis of the manufacturing process is important because, as shown in Chapter 2, the fabrication of multilayer antennas often produces layer misalignments or other imperfections that may produce significant changes in the antenna performance. Therefore, in Chapter 5, I addressed the manufacturing process of implantable antennas in LTCC technology from the industrial point of view. Possible sources of error in the fabrication stages were identified and discussed (such as misalignment of vias and cavities, unwanted shrinkage, substrate ruptures, etc.). In addition, sensitivity tests were

carried out, showing that the substrate permittivity and the horizontal size are the most sensitive parameters in terms of antenna performance. A threshold of a relative frequency detuning up to 2% was considered as acceptable. The free-sintering method was considered more suitable for in-body antenna fabrication since the scaling factor allows more control and homogeneity than the zero-shrinkage method. Radiator thickness up to 0.3 mm was successfully achieved.

The manufacturing of the microwave applicator for hyperthermia, described in Chapter 8, was performed using 3D printed models for both the hemispherical groundplane and the breast mold. Copper sheets were used for the antennas and also the groundplane. Despite being only a first prototype, the results showed good agreement between the EM computational model and the manufactured prototype.

Regarding the manufacturing of phantoms, in Chapter 5 I described the development of *in-vitro* phantoms for the experimental validation of in-body antennas. The recipes used were simple and easy to manufacture, as only three ingredients were needed: salt, sugar and distilled water. In general, the dielectric properties obtained were in satisfactory agreement with simulations. However, experimental phantoms at 2.45 GHz presented variations in the dielectric properties, which led to inaccuracies in the experimental results of antennas operating at that frequency, especially for the bandwidth. As shown in the sensitivity tests in Chapter 5, slight variations in phantom permittivity do not lead to significant differences in the operating frequency. It can therefore be said that the manufacturing process of the antenna is more sensitive than the manufacturing process of the phantom.

Chicken breast was selected as the *ex-vivo* phantom for hyperthermia. In this case, the development of *in-vitro* phantoms was not proposed because analysis of the thermal behavior was also needed.

9.1.5. Characterization and Experimental Validation

Once the antennas were manufactured, experimental characterization was required in order to validate the results. Nevertheless, according to the literature presented in Chapter 2, few investigations have described *in-vitro, ex-vivo* or *in-vivo* antenna measurements for in-body applications, especially for far-field features. This is mainly due to the complications that arise when using an unbalanced coaxial cable to feed ESAs, especially in an in-body scenario. As detailed in Chapter 5, currents flowing from the back side of the groundplane to the outer conductor of the cable produce unwanted radiated fields. Moreover, if the antenna is surrounded by a lossy medium, these currents on the cable couple with the medium and generate new dissipated fields, distorting the characterization of the antenna. Therefore, I presented two measurement

techniques in Chapter 5 to suppress or at least mitigate these undesirable effects: the use of a splitter that acts as a balun and the use of a fiber optic link to remove metallic parts. Measurements of the reflection coefficient with the splitter were found to be in good agreement with simulations. However, far-field measurements were only considered for the horizontal plane due to the distortions in the vertical plane. A measurement setup based on fiber optics was also proposed. Although an initial version of this measurement setup showed promising results, further development was required to establish it as a reliable system for in-body antenna characterization (the power, the feeding of the receiver module and the sealing).

Another issue concerning the characterization of certain types of antennas, like PIFAs, is the connection of the feeding when the radiator is surrounded by the substrate. To facilitate the soldering of the SMA connector in this case, a coplanar launcher was presented. Despite distorting the radiation pattern, especially at higher frequencies, it was proposed for frequencies at the MedRadio band. The direct connection was then suggested for implementations at higher frequencies.

The measurement setup used to experimentally validate the microwave applicator for the hyperthermia treatment of breast cancer consisted of a signal generator, a power amplifier, a power monitor, a 4-channel power divider, four manually controlled phase shifters and the applicator. The results gathered from the validation showed similar EM behavior between the heterogeneous phantom (piece of chicken breast) used in the experiments and the homogeneous phantoms employed in simulations.

9.1.6. Antenna Demonstrators

In the second part of the thesis I proposed three antenna demonstrators, which were based on the data and results presented in the previous chapters. The first one, presented in Chapter 6, was a novel multilayered broadband PIFA for compact embedded implantable medical devices. The miniaturization of this antenna was achieved by combining two radiators: a meander and a spiral. According to previous chapters, two spirals might have had a greater degree of miniaturization, but the coupling needed to enlarge the bandwidth (at least 70 MHz) could not be achieved. The antenna was tested in different realistic scenarios, showing a strong robustness in frequency. The internal cavity for electronics and powering was set up to 10 × 10 × 0.5 mm. This volume was enough for current passive ICs, like RFID ICs. However, for active powering circuits with a battery, it would take more space. The antenna was manufactured and experimentally validated. Compared to other similar designs found in the literature, this antenna achieved good levels of miniaturization, bandwidth, gain and integration.

The second antenna demonstrator, presented in Chapter 7, consisted of a multilayered implantable UHF-RFID tag for the remote monitoring of patients. The impedance matching and the broadband performance were achieved mainly through the addition of an inductive line, which compensated for the capacitive behavior of the RFID IC. The square spiral and the multilayered structure helped to miniaturize the device. In addition, an internal cavity allowed the integration of the IC. The experimental validation presented an enlargement of the 6 dB bandwidth of 45 MHz, basically because of the addition of the sealing material in the IC, which was not considered in simulations. Inaccuracies in the manufactured prototypes, the variations between simulated and real parameters and the unwanted effects of the measurement setup also contributed to the differences between simulations and measurements. However, both results exhibited enough bandwidth to operate in the European UHF-RFID band. A tag range of 10 cm was measured when implanted in a cubic skin phantom. Although for some applications this might be enough, for the remote monitoring of patients the tag range needs to be higher. It can be achieved mainly by increasing the size of the tag (and thus the gain) or by adding an active RFID IC. The same structure of the tag could be used to develop RFID tags with sensing capabilities thanks to the development of new ICs.

In Chapter 8 the third application is presented, consisting of a microwave applicator for the treatment of breast cancer through hyperthermia. The applicator is based on an array of simple patch antennas that share the same hemispherical groundplane. Thus, a compact, wearable and comfortable device is achieved. In addition, the phase variation of the antenna feedings allows focusing of the power deposition in different locations, meaning that the applicator can be used in different scenarios. However, the amplitude tuning would allow a higher level of configurability and selectivity. The effect of angular spacing between antennas was assessed, and 22.5° was shown to be the spacing that shows the best results. This number was constrained basically by the operating frequency of 915 MHz, which determines the near field regions of each antenna. The number of antennas in the array was also evaluated. Results showed that an 8-antenna array is the most suitable configuration for centrally located targets, while a 12-antenna array achieved the best results at deep seated targets for both small and large breast models. Higher frequencies could allow an increase in the number of antennas, but at the same time might also cause an increase in the losses. An experimental prototype of four antennas was manufactured and the temperature increase in different locations was monitored, showing a difference in the increase in temperature of about 4 °C between the target and the healthy tissue.

9.2. Final Conclusions

To sum up, the final conclusions of the thesis are the following:

PART 1. FRAMEWORK AND DEVELOPMENT

- Several challenges remain in various aspects of the use of radiofrequency in biomedical devices, such as the development of antennas in the presence of a human body.
- In wireless biotelemetry, the main challenges for in-body devices are in the fields of miniaturization, antenna performance, frequency detuning, biocompatibility, powering, packaging, manufacturing and experimental characterization.
- For miniaturization, multilayer PIFA designs are good candidates due to their size and efficiency.
- In the 2D miniaturization, the square spiral PIFA is a more efficient structure than the meander and fractal antennas.
- 3D miniaturization techniques achieve better results than 2D miniaturization because of their more efficient use of space.
- For the in-body 3D square spiral PIFA, folding down the main radiator of the antenna is the best procedure for optimizing gain for a given antenna volume.
- The depth of the implant, the phantom dimensions and the antenna orientation significantly modify antenna performance. A quantitative analysis is presented.
- The interaction between the air-tissue interface and the near field region is critical in the antenna performance.
- For shallow implants, square spiral PIFAs should be perpendicularly oriented to achieve greater gain values. For deep implants, the antenna orientation is less sensitive.
- For shallow implants, antennas operating at higher frequencies can achieve higher values of gain, especially due to their relatively larger size. For deep implants, lower frequencies are recommended.
- The development of a standard characterization protocol for in-body antennas is suggested. This could assist antenna engineers to determine the most suitable antenna for an in-body application from among all the designs and proposals provided by researchers and companies.
- A proposal for this protocol is to characterize the in-body antennas in the center of a cubic phantom, the dimensions of which are determined by the operating frequency.
- For the manufacturing of in-body antennas, LTCC technology is suggested because of the features it provides: biocompatibility, high permittivity, low loss tangent, multilayer structures, implementation of internal cavities and vias, possibility of embedding integrated microstructures and durability.

- Sensitivity tests of the LTCC manufacturing process indicate that the substrate permittivity and the scale factor are the most relevant parameters in terms of frequency detuning. A limit of a relative detuning up to 2% is considered as acceptable.
- The experimental characterization of in-body antennas is extremely complicated, due to the presence of unwanted radiated and dissipated fields when connecting a coaxial cable.
- The use of a coplanar launcher is suggested for the characterization of in-body antennas operating at the MedRadio band. The launcher facilitates the soldering of the SMA connector.
- For higher frequencies, the direct connection is preferable because the coplanar launcher compromises the radiation pattern.
- The use of a power splitter as a balun improves the measurement of the reflection coefficient for in-body antennas operating up to 900 MHz.
- Only the horizontal plane of the radiation pattern can be measured with the splitter; in the vertical plane, too many distortions appear.
- A preliminary setup of the radiation pattern measurement through a fiber optic link is proposed in order to remove the coaxial cable distortions. However, further development is needed to overcome the challenges that remain in an in-body scenario, such as the power, the receiver feeding and the sealing.
- Experimental characterization of 2D antennas presents a stronger agreement between simulations and measurements due to their lower level of complexity.
- Antennas operating at 2.45 GHz present variations between simulations and measurements, for two main reasons: (1) differences between the dielectric properties of the simulated and measured phantoms, and (2) the impossibility of using the splitter.

PART 2. ANTENNA DEMONSTRATORS

- A multilayered broadband PIFA for implantable medical devices is presented. The antenna is based on the LTCC technology and operates at the MedRadio band.
- The main advantages of this novel antenna are: (1) a strong miniaturization level, (2) a large bandwidth that mitigates the frequency detuning caused by the heterogeneity of the tissues, and (3) integration with the other electronic components.
- The broadband behavior is achieved thanks to the coupling of two radiators.
- Simulated results of the broadband antenna show a suitable operational behavior of the antenna in most of the scenarios studied (several locations in the body and different sizes of the embedded electronics).

- Measurements of the broadband antenna show a reliable communication link of a few meters, which are in satisfactory agreement with simulations.
- A new multilayered implantable UHF-RFID tag for the remote monitoring of patients is presented.
- The RFID tag is based on the PIFA structure and on the LTCC technology to allow integration with the RFID IC.
- An inductor line is used for impedance matching and the enlargement of the bandwidth.
- A manufactured prototype shows a tag range of 10 cm, which is in good agreement with simulations. However, further development is needed to reach larger distances of communication.
- A novel microwave hyperthermia applicator based on a phased array for the breast cancer treatment is presented.
- The design incorporates a shared hemispheric groundplane and a bolus full of flowing cold water to maintain the temperature of the biologic tissues at safe levels.
- Phased arrays of different numbers of rectangular patch antennas are tested to assess the focusing of the power delivered in different scenarios (different tumor sizes and locations and different breast sizes).
- Results showed that by changing the phases of the antennas it is possible to modify the target of the power deposition.
- An experimental prototype of four antennas with optimized phases is manufactured and experimentally validated. Measurements of the temperature increase in different locations show favorable results, thus indicating the ability of the device to create diverse energy deposition patterns at different locations within the intact breast.

9.3. Future Work and Perspectives

Although several issues related to antennas in biomedical applications have been addressed in this thesis, some important topics still need further development.

9.3.1. Wireless Biotelemetry

- IMD research seeks constant improvements in miniaturization in order to decrease invasiveness. However, the need for new technological capabilities and the improvement of antenna performance push in the opposite direction. In this thesis these aspects have been addressed. However, there is still room for improvement in this field: more efficient antenna designs

and the optimization of the available space in the IMD integration and packaging.

- The development of anatomical-based phantoms for *in-vitro* experimental validation is still an open field of research. While in the virtual world accurate phantoms are already available, this is not so in the real world, making the comparison of simulations and measurements in a realistic scenario a complex task. Other options involve *ex-vivo* or *in-vivo* measurements, already found in the literature, which should be taken into account as future steps for the research carried out in this thesis.
- Further development of a characterization protocol could be an interesting tool for classifying and categorizing in-body antennas.
- Improvements in the powering of IMD consist of extending the power life time, reducing the size of internal batteries or introducing wireless power transfer.
- Passive in-body RFID tags with sensing capabilities arise as a promising technology for wireless biotelemetry. Nevertheless, from the industrial point of view, an increase in the read range is needed.
- Most of the LTCC antennas presented in this thesis have a space available for the integration of electronic components. Apart from the UHF-RFID solution presented in Chapter 7, other alternatives are the use of a Voltage-Controlled Oscillator or other configurations with sensing capabilities.
- The enhancement of the resolution in the manufacturing process of in-body LTCC antennas may lead to smaller prototypes and more accurate results. However, it should be borne in mind that reducing the size also reduces the radiation efficiency.
- Far-field measurement setups have to be improved in order to avoid the distortions that appear because of the coaxial cable.
- The antenna characterization through a fiber optics link still requires further development in the receiver optical module: more available power, a FO-based DC feeding, and the sealing of all the module.

9.3.2. Microwave Hyperthermia for Breast Cancer Treatments

- Computational simulations in realistic models are required as well as thermal simulations.
- Further investigations should analyze the antenna distribution across the breast hemisphere with a uniform solid angle.
- The development of an algorithm with the optimization of both the feeding phases and the feeding amplitudes should be considered in order to enhance the focusing capabilities of the device.

- Another focusing algorithm based on the time-reversal method will be developed.
- For the control of the temperature increase in the biological tissues, a non-invasive monitoring system should be developed. This would prevent unwanted hotspots and the feedback of the system.
- A better control of the water circuit to cool the skin would make the results more accurate.
- A manufactured 3D-printed prototype, also for the metallic parts, can increase the device resolution, robustness and reliability.

References

[1] A. Rosen, M. A. Stuchly, and A. Vander Vorst, "Applications of RF/microwaves in medicine," *IEEE Trans. Microw. Theory Tech.*, vol. 50, no. 3, pp. 963–974, 2002.

[2] D. Kissinger and J.-C. Chiao, "Medical Applications of Radio-Frequency and Microwaves-Sensing, Monitoring, and Diagnostics [From the Guest Editors' Desk]," *IEEE Microw. Mag.*, vol. 16, no. 4, pp. 34–38, May 2015.

[3] K. S. Nikita, *Handbook of Biomedical Telemetry*. John Wiley & Sons, 2014.

[4] United Nations and Department of Economic and Social Affairs, *World population ageing, 2015 highlights*. 2015.

[5] L. Hood, R. Balling, and C. Auffray, "Revolutionizing medicine in the 21st century through systems approaches," *Biotechnol. J.*, vol. 7, no. 8, pp. 992–1001, Aug. 2012.

[6] M. Flores, G. Glusman, K. Brogaard, N. D. Price, and L. Hood, "P4 medicine: how systems medicine will transform the healthcare sector and society," *Pers. Med.*, vol. 10, no. 6, pp. 565–576, Aug. 2013.

[7] J. Gubbi, R. Buyya, S. Marusic, and M. Palaniswami, "Internet of Things (IoT): A vision, architectural elements, and future directions," *Future Gener. Comput. Syst.*, vol. 29, no. 7, pp. 1645–1660, Sep. 2013.

[8] G. Guarin, M. Hofmann, J. Nehring, R. Weigel, G. Fischer, and D. Kissinger, "Miniature Microwave Biosensors: Noninvasive Applications," *IEEE Microw. Mag.*, vol. 16, no. 4, pp. 71–86, May 2015.

[9] C. Pang, C. Lee, and K.-Y. Suh, "Recent advances in flexible sensors for wearable and implantable devices," *J. Appl. Polym. Sci.*, vol. 130, no. 3, pp. 1429–1441, Nov. 2013.

[10] Y.-L. Zheng *et al.*, "Unobtrusive Sensing and Wearable Devices for Health Informatics," *IEEE Trans. Biomed. Eng.*, vol. 61, no. 5, pp. 1538–1554, May 2014.

[11] B. G. Celler and R. S. Sparks, "Home Telemonitoring of Vital Signs—Technical Challenges and Future Directions," *IEEE J. Biomed. Health Inform.*, vol. 19, no. 1, pp. 82–91, Jan. 2015.

[12] P. J. Soh, G. A. E. Vandenbosch, M. Mercuri, and D. M. M.-P. Schreurs, "Wearable Wireless Health Monitoring: Current Developments, Challenges, and Future Trends," *IEEE Microw. Mag.*, vol. 16, no. 4, pp. 55–70, May 2015.

[13] A. Darwish and A. E. Hassanien, "Wearable and Implantable Wireless Sensor Network Solutions for Healthcare Monitoring," *Sensors*, vol. 11, no. 6, pp. 5561–5595, May 2011.

[14] F. Merli, "Implantable antennas for biomedical applications," 2011.

[15] J. Hayward, G. Chansin, and H. Zervos, *Wearable Technology 2016-2026: Markets, players and 10-year forecast*. IDTechEx, 2016.

[16] R. Elmgvist, J. Landegren, S. O. Pettersson, Å. Senning, and G. William-Olsson, "Artificial pacemaker for treatment of Adams-Stokes syndrome and slow heart rate," *Am. Heart J.*, vol. 65, no. 6, pp. 731–748, Jun. 1963.

[17] M. Yuce and T. Dissanayake, "Easy-to-swallow antenna and propagation," *IEEE Microw. Mag.*, vol. 14, no. 4, pp. 74–82, Jun. 2013.

[18] E. Chow, M. Morris, and P. Irazoqui, "Implantable RF Medical Devices: The Benefits of High-Speed Communication and Much Greater Communication Distances in Biomedical Applications," *IEEE Microw. Mag.*, vol. 14, no. 4, pp. 64–73, Jun. 2013.

[19] A. Kiourti and K. S. Nikita, "A Review of In-Body Biotelemetry Devices: Implantables, Ingestibles, and Injectables," *IEEE Trans. Biomed. Eng.*, vol. 64, no. 7, pp. 1422–1430, Jul. 2017.

[20] E. Moradi *et al.*, "Miniature implantable and wearable on-body antennas: towards the new era of wireless body-centric systems [antenna applications corner]," *IEEE Antennas Propag. Mag.*, vol. 56, no. 1, pp. 271–291, Feb. 2014.

[21] W. Yao, C.-H. Chu, and Z. Li, "The adoption and implementation of RFID technologies in healthcare: a literature review," *J. Med. Syst.*, vol. 36, no. 6, pp. 3507–3525, Dec. 2012.

[22] AMS, "SL900A EPC Class 3 Sensory Tag Chip - For Automatic Data Logging." 2014.

[23] S.-W. Wang, W.-H. Chen, C.-S. Ong, L. Liu, and Y.-W. Chuang, "RFID application in hospitals: a case study on a demonstration RFID project in a Taiwan hospital," in *System Sciences, 2006. HICSS'06. Proceedings of the 39th Annual Hawaii International Conference on*, 2006, vol. 8, p. 184a–184a.

[24] A. M. Wicks, J. K. Visich, and S. Li, "Radio frequency identification applications in hospital environments," *Hosp. Top.*, vol. 84, no. 3, pp. 3–8, 2006.

[25] S. Parlak, A. Sarcevic, I. Marsic, and R. S. Burd, "Introducing RFID technology in dynamic and time-critical medical settings: requirements and challenges," *J. Biomed. Inform.*, vol. 45, no. 5, pp. 958–974, Oct. 2012.

[26] K. S. Pasupathy and T. R. Hellmich, "How RFID Technology Improves Hospital Care," Harvard Business Review, 2015.

[27] J. A. Fisher and T. Monahan, "Evaluation of real-time location systems in their hospital contexts," *Int. J. Med. Inf.*, vol. 81, no. 10, pp. 705–712, Oct. 2012.

[28] M. McKee, "Reducing hospital beds: what are the lessons to be learned?," European Observatory on Health Systems and Policies, 2004.

[29] E. Drazen and J. Rhoads, "Using Tracking Tools to Improve Patient Flow in Hospitals," California Health Care Foundation, 2011.

[30] M. Franckena *et al.*, "Radiotherapy and hyperthermia for treatment of primary locally advanced cervix cancer: results in 378 patients," *Int. J. Radiat. Oncol. Biol. Phys.*, vol. 73, no. 1, pp. 242–250, Jan. 2009.

[31] J. van der Zee, D. González González, G. C. van Rhoon, J. D. van Dijk, W. L. van Putten, and A. A. Hart, "Comparison of radiotherapy alone with radiotherapy plus hyperthermia in locally advanced pelvic tumours: a prospective, randomised, multicentre trial. Dutch Deep Hyperthermia Group," *Lancet Lond. Engl.*, vol. 355, no. 9210, pp. 1119–1125, Apr. 2000.

[32] P. K. Sneed *et al.*, "Survival benefit of hyperthermia in a prospective randomized trial of brachytherapy boost +/- hyperthermia for glioblastoma multiforme," *Int. J. Radiat. Oncol. Biol. Phys.*, vol. 40, no. 2, pp. 287–295, Jan. 1998.

[33] E. L. Jones *et al.*, "Randomized trial of hyperthermia and radiation for superficial tumors," *J. Clin. Oncol. Off. J. Am. Soc. Clin. Oncol.*, vol. 23, no. 13, pp. 3079–3085, May 2005.

[34] N. R. Datta *et al.*, "Local hyperthermia combined with radiotherapy and-/or chemotherapy: Recent advances and promises for the future," *Cancer Treat. Rev.*, vol. 41, no. 9, pp. 742–753, Nov. 2015.

[35] M. Hurwitz and P. Stauffer, "Hyperthermia, Radiation and Chemotherapy: The Role of Heat in Multidisciplinary Cancer Care," *Semin. Oncol.*, vol. 41, no. 6, pp. 714–729, Dec. 2014.

[36] K.-J. Lee, J.-Y. Kim, S.-H. Son, and S. Kang, "MR images-Based Microwave Focusing for Thermal Therapy," 2017, pp. 126–131.

[37] N. R. Datta *et al.*, "Magnetic nanoparticle-induced hyperthermia with appropriate payloads: Paul Ehrlich's 'magic (nano)bullet' for cancer theranostics?," *Cancer Treat. Rev.*, vol. 50, pp. 217–227, Nov. 2016.

[38] C. M. Furse, "Biomedical telemetry: Today's opportunities and challenges," in *Antenna Technology, 2009. iWAT 2009. IEEE International Workshop on*, 2009, pp. 1–4.

[39] R. W. P. King, *Antennas in matter : fundamentals, theory and applications*. MIT Press, 1981.

[40] C. Gabriel, S. Gabriel, and E. Corthout, "The dielectric properties of biological tissues: I. Literature survey," *Phys. Med. Biol.*, vol. 41, no. 11, p. 2231, 1996.

[41] "Electromagnetic Fields in Biological Systems," *CRC Press*, 11-Oct-2011. [Online]. Available: https://www.crcpress.com/Electromagnetic-Fields-in-Biological-Systems/Lin/p/book/9781439859995. [Accessed: 17-Apr-2017].

[42] G. J. Rubin, R. Nieto-Hernandez, and S. Wessely, "Idiopathic environmental intolerance attributed to electromagnetic fields (formerly 'electromagnetic hypersensitivity'): An updated systematic review of provocation studies," *Bioelectromagnetics*, vol. 31, no. 1, pp. 1–11, Jan. 2010.

[43] "IEEE Standard for Safety Levels with Respect to Human Exposure to Radio Frequency Electromagnetic Fields, 3 kHz to 300 GHz," *IEEE Std C951-2005 Revis. IEEE Std C951-1991*, pp. 1–238, Apr. 2006.

[44] H. H. Pennes, "Analysis of Tissue and Arterial Blood Temperatures in the Resting Human Forearm," *J. Appl. Physiol.*, vol. 1, no. 2, pp. 93–122, Aug. 1948.

[45] International Commission on Non-Ionizing Radiation Protection, "ICNIRP statement on the 'Guidelines for limiting exposure to time-varying electric, magnetic, and electromagnetic fields (up to 300 GHz),'" *Health Phys.*, vol. 97, no. 3, pp. 257–258, Sep. 2009.

[46] "Important differences between The ICNIRP and IEEE standards and the FCC standard for cell phones. | EMFacts Consultancy," 2012. .

[47] L. J. Chu, "Physical Limitations of Omni-Directional Antennas," *J. Appl. Phys.*, vol. 19, no. 12, pp. 1163–1175, Diciembre 1948.

[48] H. Wheeler and others, "Fundamental limitations of small antennas," *Proc. IRE*, vol. 35, no. 12, pp. 1479–1484, 1947.

[49] A. K. Skrivervik, J.-F. Zurcher, O. Staub, and J. R. Mosig, "PCS antenna design: The challenge of miniaturization," *Antennas Propag. Mag. IEEE*, vol. 43, no. 4, pp. 12–27, 2001.

[50] L. J. Roca, M. Martinez-Vasquez, and R. Serrano, *Handbook on Small Antennas*. EurAAP AISBL, 2012.

[51] H. Wheeler, "Fundamental limitaions of a small VLF antenna for submarines," *IRE Trans. Antennas Propag.*, vol. 6, no. 1, pp. 123–125, Jan. 1958.

[52] H. Li, Y.-X. Guo, C. Liu, S. Xiao, and L. Li, "A Miniature-Implantable Antenna for MedRadio-Band Biomedical Telemetry," *IEEE Antennas Wirel. Propag. Lett.*, vol. 14, pp. 1176–1179, 2015.

[53] J. Kim and Y. Rahmat-Samii, "Planar inverted-F antennas on implantable medical devices: Meandered type versus spiral type," *Microw. Opt. Technol. Lett.*, vol. 48, no. 3, pp. 567–572, Mar. 2006.

[54] P. Soontornpipit, C. M. Furse, and Y. C. Chung, "Design of Implantable Microstrip Antenna for Communication With Medical Implants," *IEEE Trans. Microw. Theory Tech.*, vol. 52, no. 8, pp. 1944–1951, Aug. 2004.

[55] A. Kiourti and K. S. Nikita, "Miniature Scalp-Implantable Antennas for Telemetry in the MICS and ISM Bands: Design, Safety Considerations and Link Budget Analysis," *IEEE Trans. Antennas Propag.*, vol. 60, no. 8, pp. 3568–3575, Aug. 2012.

[56] L. J. Xu, Y. X. Guo, and W. Wu, "Bandwidth Enhancement of an Implantable Antenna," *IEEE Antennas Wirel. Propag. Lett.*, vol. 14, pp. 1510–1513, 2015.

[57] A. Kiourti and K. S. Nikita, "Meandered versus spiral novel miniature PIFAs implanted in the human head: Tuning and performance," in *Wireless Mobile Communication and Healthcare*, Springer, 2012, pp. 80–87.

[58] S. Jacobsen, H. O. Rolfsnes, and P. R. Stauffer, "Characteristics of microstrip muscle-loaded single-arm archimedean spiral antennas as investigated by FDTD numerical computations," *IEEE Trans. Biomed. Eng.*, vol. 52, no. 2, pp. 321–330, Feb. 2005.

[59] K. Gosalia, M. S. Humayun, and G. Lazzi, "Impedance matching and implementation of planar space-filling dipoles as intraocular implanted antennas in a retinal prosthesis," *IEEE Trans. Antennas Propag.*, vol. 53, no. 8, pp. 2365–2373, Aug. 2005.

[60] S. Bakogianni and S. Koulouridis, "Design of a novel compact printed folded dipole antenna for biomedical applications," in *Antennas and Propagation (EuCAP), 2014 8th European Conference on*, 2014, pp. 3178–3182.

[61] J. Abadia, F. Merli, J.-F. Zurcher, J. R. Mosig, and A. K. Skrivervik, "3D-spiral small antenna design and realization for biomedical telemetry in the MICS band," *Radioengineering*, vol. 18, no. 4, pp. 359–367, 2009.

[62] M. Z. Azad and M. Ali, "A Miniature Implanted Inverted-F Antenna for GPS Application," *IEEE Trans. Antennas Propag.*, vol. 57, no. 6, pp. 1854–1858, Jun. 2009.

[63] S. R. Best and J. D. Morrow, "On the significance of current vector alignment in establishing the resonant frequency of small space-filling wire antennas," *IEEE Antennas Wirel. Propag. Lett.*, vol. 2, no. 1, pp. 201–204, 2003.

[64] J. Kim and Y. Rahmat-Samii, "Implanted Antennas Inside a Human Body: Simulations, Designs, and Characterizations," *IEEE Trans. Microw. Theory Tech.*, vol. 52, no. 8, pp. 1934–1943, Aug. 2004.

[65] J. Ha, K. Kwon, and J. Choi, "Compact zeroth-order resonance antenna for implantable biomedical service applications," *Electron. Lett.*, vol. 47, no. 23, pp. 1267–1269, Nov. 2011.

[66] C. J. Sanchez-Fernandez, O. Quevedo-Teruel, J. Requena-Carrion, L. Inclan-Sanchez, and E. Rajo-Iglesias, "Dual-band microstrip patch antenna based on short-circuited ring and spiral resonators for implantable medical devices," *Antennas Propag. IET Microw.*, vol. 4, no. 8, pp. 1048–1055, Agosto 2010.

[67] C. Liu, Y. X. Guo, and S. Xiao, "Capacitively Loaded Circularly Polarized Implantable Patch Antenna for ISM Band Biomedical Applications," *IEEE Trans. Antennas Propag.*, vol. 62, no. 5, pp. 2407–2417, May 2014.

[68] C. m Lee, T. C. Yo, C. H. Luo, C. H. Tu, and Y. Z. Juang, "Compact broadband stacked implantable antenna for biotelemetry with medical devices," *Electron. Lett.*, vol. 43, no. 12, pp. 660–662, Jun. 2007.

[69] C. Liu, Y. X. Guo, and S. Xiao, "A Hybrid Patch/Slot Implantable Antenna for Biotelemetry Devices," *IEEE Antennas Wirel. Propag. Lett.*, vol. 11, pp. 1646–1649, 2012.

[70] C. Liu, Y. X. Guo, and S. Xiao, "Compact Dual-Band Antenna for Implantable Devices," *IEEE Antennas Wirel. Propag. Lett.*, vol. 11, pp. 1508–1511, 2012.

[71] W.-C. Liu, F.-M. Yeh, and M. Ghavami, "Miniaturized implantable broadband antenna for biotelemetry communication," *Microw. Opt. Technol. Lett.*, vol. 50, no. 9, pp. 2407–2409, 2008.

[72] A. Kiourti, M. Christopoulou, and K. S. Nikita, "Performance of a novel miniature antenna implanted in the human head for wireless biotelemetry," in *Antennas and Propagation (APSURSI), 2011 IEEE International Symposium on*, 2011, pp. 392–395.

[73] F.-J. Huang, C.-M. Lee, C.-L. Chang, L.-K. Chen, T.-C. Yo, and C.-H. Luo, "Rectenna Application of Miniaturized Implantable Antenna Design for Triple-Band Biotelemetry Communication," *IEEE Trans. Antennas Propag.*, vol. 59, no. 7, pp. 2646–2653, Jul. 2011.

[74] L. J. Xu, Y. X. Guo, and W. Wu, "Dual-Band Implantable Antenna With Open-End Slots on Ground," *IEEE Antennas Wirel. Propag. Lett.*, vol. 11, pp. 1564–1567, 2012.

[75] T. Karacolak, A. Z. Hood, and E. Topsakal, "Design of a Dual-Band Implantable Antenna and Development of Skin Mimicking Gels for Continuous Glucose Monitoring," *IEEE Trans. Microw. Theory Tech.*, vol. 56, no. 4, pp. 1001–1008, Apr. 2008.

[76] S. Bakogianni and S. Koulouridis, "Performance of a novel miniature antenna implanted into the human trunk for medical telemetry applications," in *2015 9th European Conference on Antennas and Propagation (EuCAP)*, 2015, pp. 1–5.

[77] M. S. Islam, K. P. Esselle, S. Sabrin, K. M. Morshed, and L. Matekovits, "A serpentine PIFA antenna for implantable RFID tag," in *Antennas and Propagation (ISAP), 2015 International Symposium*, 2015, pp. 1–3.

[78] C.-M. Lee, T.-C. Yo, F.-J. Huang, and C.-H. Luo, "Dual-resonant π-shape with double L-strips PIFA for implantable biotelemetry," *Electron. Lett.*, vol. 44, no. 14, pp. 837–839, 2008.

[79] W.-C. Liu, S.-H. Chen, and C.-M. Wu, "Bandwidth enhancement and size reduction of an implantable PIFA antenna for biotelemetry devices," *Microw. Opt. Technol. Lett.*, vol. 51, no. 3, pp. 755–757, Mar. 2009.

[80] Z. Duan, Y.-X. Guo, M. Je, and D.-L. Kwong, "Design and in Vitro Test of a Differentially Fed Dual-Band Implantable Antenna Operating at MICS and ISM Bands," *IEEE Trans. Antennas Propag.*, vol. 62, no. 5, pp. 2430–2439, May 2014.

[81] P. Soontornpipit, C. M. Furse, and You Chung Chung, "Miniaturized biocompatible microstrip antenna using genetic algorithm," *IEEE Trans. Antennas Propag.*, vol. 53, no. 6, pp. 1939–1945, Jun. 2005.

[82] C.-M. Lee, T.-C. Yo, F.-J. Huang, and C.-H. Luo, "Bandwidth enhancement of planar inverted-F antenna for implantable biotelemetry," *Microw. Opt. Technol. Lett.*, vol. 51, no. 3, pp. 749–752, Mar. 2009.

[83] F. Merli, L. Bolomey, J. F. Zurcher, G. Corradini, E. Meurville, and A. K. Skrivervik, "Design, Realization and Measurements of a Miniature Antenna for Implantable Wireless Communication Systems," *IEEE Trans. Antennas Propag.*, vol. 59, no. 10, pp. 3544–3555, Oct. 2011.

[84] M. S. Islam, K. P. Esselle, D. Bull, and P. M. Pilowsky, "Converting a Wireless Biotelemetry System to an Implantable System Through Antenna Redesign," *IEEE Trans. Microw. Theory Tech.*, vol. 62, no. 9, pp. 1890–1897, Sep. 2014.

[85] T. F. Chien, C. M. Cheng, H. C. Yang, J. W. Jiang, and C. H. Luo, "Development of Nonsuperstrate Implantable Low-Profile CPW-Fed Ceramic Antennas," *IEEE Antennas Wirel. Propag. Lett.*, vol. 9, pp. 599–602, 2010.

[86] H. Bahrami, S. A. Mirbozorgi, L. A. Rusch, and B. Gosselin, "Biological Channel Modeling and Implantable UWB Antenna Design for Neural Recording Systems," *IEEE Trans. Biomed. Eng.*, vol. 62, no. 1, pp. 88–98, Enero 2015.

[87] C. H. Kang, S. J. Wu, and J. H. Tarng, "A Novel Folded UWB Antenna for Wireless Body Area Network," *IEEE Trans. Antennas Propag.*, vol. 60, no. 2, pp. 1139–1142, Feb. 2012.

[88] D. Valderas, C. Schmidt, and X. Chen, "Broadband implanted UHF RFID antenna," in *2010 IEEE Antennas and Propagation Society International Symposium*, 2010, pp. 1–4.

[89] L. J. Xu, Y. X. Guo, and W. Wu, "Miniaturized Dual-Band Antenna for Implantable Wireless Communications," *IEEE Antennas Wirel. Propag. Lett.*, vol. 13, pp. 1160–1163, 2014.

[90] M. L. Scarpello *et al.*, "Design of an Implantable Slot Dipole Conformal Flexible Antenna for Biomedical Applications," *IEEE Trans. Antennas Propag.*, vol. 59, no. 10, pp. 3556–3564, Oct. 2011.

[91] A. Faul and J. Naber, "A novel 915 MHz, RFID-based pressure sensor for glaucoma using an electrically small antenna," *Analog Integr. Circuits Signal Process.*, vol. 85, no. 1, pp. 167–180, Oct. 2015.

[92] H. Yu *et al.*, "Printed capsule antenna for medication compliance monitoring," *Electron. Lett.*, vol. 43, no. 22, Oct. 2007.

[93] Z. N. Chen, G. C. Liu, and T. S. P. See, "Transmission of RF Signals Between MICS Loop Antennas in Free Space and Implanted in the Human Head," *IEEE Trans. Antennas Propag.*, vol. 57, no. 6, pp. 1850–1854, Jun. 2009.

[94] R. S. Alrawashdeh, Y. Huang, M. Kod, and A. A. B. Sajak, "A Broadband Flexible Implantable Loop Antenna With Complementary Split Ring Resonators," *IEEE Antennas Wirel. Propag. Lett.*, vol. 14, pp. 1506–1509, 2015.

[95] P. Anacleto, P. M. Mendes, E. Gultepe, and D. H. Gracias, "3D small antenna for energy harvesting applications on implantable micro-devices," in *Antennas and Propagation Conference (LAPC), 2012 Loughborough*, 2012, pp. 1–4.

[96] C. Schmidt, F. Casado, A. Arriola, I. Ortego, P. D. Bradley, and D. Valderas, "Broadband UHF Implanted 3-D Conformal Antenna Design and Characterization for In-Off Body Wireless Links," *IEEE Trans. Antennas Propag.*, vol. 62, no. 3, pp. 1433–1444, Mar. 2014.

[97] A. L. Chlebowski, E. Y. Chow, C. Ellison, and P. P. Irazoqui, "Integrated LTCC packaging for use in biomedical devices," *Biomed. Mater. Eng.*, vol. 22, no. 6, pp. 361–372, 2012.

[98] E. Y. Chow, C.-L. Yang, A. Chlebowski, W. J. Chappell, and P. P. Irazoqui, "Miniature antenna for RF telemetry through ocular tissue," in *Microwave Symposium Digest, 2008 IEEE MTT-S International*, 2008, pp. 1309–1312.

[99] E. Y. Chow, Chin-Lung Yang, A. Chlebowski, Sungwook Moon, W. J. Chappell, and P. P. Irazoqui, "Implantable Wireless Telemetry Boards for In Vivo Transocular Transmission," *IEEE Trans. Microw. Theory Tech.*, vol. 56, no. 12, pp. 3200–3208, Dec. 2008.

[100] L. Golonka, P. Bembnowicz, D. Jurkow, K. Malecha, H. Roguszczak, and R. Tadaszak, "Low temperature co-fired ceramics (LTCC) microsystems," *Opt. Appl.*, vol. 41, no. 2, pp. 383–388, 2011.

[101] K. A. Psathas, A. Kiourti, and K. S. Nikita, "Biocompatibility of implantable antennas: Design and performance considerations," in *The 8th European Conference on Antennas and Propagation (EuCAP 2014)*, 2014, pp. 1566–1570.

[102] "FAE - Fabricante de componentes eléctricos y electrónicos - Francisco Albero S.A.U." [Online]. Available: http://www.fae.es/. [Accessed: 30-Aug-2016].

[103] D. M. Pozar, *Microwave Engineering*, 4 edition. Hoboken, NJ: Wiley, 2011.

[104] A. Kiourti and K. S. Nikita, "Implantable Antennas: A Tutorial on Design, Fabrication, and In Vitro\/In Vivo Testing," *IEEE Microw. Mag.*, vol. 15, no. 4, pp. 77–91, Jun. 2014.

[105] J. G. Webster, *Design of Cardiac Pacemakers*. IEEE, 1995.

[106] "Medical Device Radiocommunications Service (MedRadio)," *Federal Communications Commission*, 09-Dec-2011. [Online]. Available: https://www.fcc.gov/medical-device-radiocommunications-service-medradio. [Accessed: 04-Oct-2017].

[107] T. Houzen, M. Takahashi, K. Saito, and K. Ito, "Implanted planar inverted F-antenna for cardiac pacemaker system," in *Antenna Technology: Small Antennas and Novel Metamaterials, 2008. iWAT 2008. International Workshop on*, 2008, pp. 346–349.

[108] W.-C. Liu, S.-H. Chen, and C.-M. Wu, "Implantable broadband circular stacked PIFA antenna for biotelemetry communication," *J. Electromagn. Waves Appl.*, vol. 22, no. 13, pp. 1791–1800, 2008.

[109] S. I. Kwak, K. Chang, and Y. J. Yoon, "The helical antenna for the capsule endoscope," in *Antennas and Propagation Society International Symposium, 2005 IEEE*, 2005, vol. 2, pp. 804–807.

[110] A. Kiourti, M. Christopoulou, S. Koulouridis, and K. S. Nikita, "Design of a novel miniaturized implantable PIFA for biomedical telemetry," in *Wireless Mobile Communication and Healthcare*, Springer, 2011, pp. 127–134.

[111] N. Vidal, S. Curto, J. M. Lopez-Villegas, J. Sieiro, and F. M. Ramos, "Detuning study of implantable antennas inside the human body," *Prog. Electromagn. Res.*, vol. 124, pp. 265–283, 2012.

[112] T. Karacolak, R. Cooper, J. Butler, S. Fisher, and E. Topsakal, "In Vivo Verification of Implantable Antennas Using Rats as Model Animals," *IEEE Antennas Wirel. Propag. Lett.*, vol. 9, pp. 334–337, 2010.

[113] T. Karacolak, R. Cooper, and E. Topsakal, "Electrical Properties of Rat Skin and Design of Implantable Antennas for Medical Wireless Telemetry," *IEEE Trans. Antennas Propag.*, vol. 57, no. 9, pp. 2806–2812, Sep. 2009.

[114] T. Yilmaz, T. Karacolak, and E. Topsakal, "Characterization and Testing of a Skin Mimicking Material for Implantable Antennas Operating at ISM Band (2.4 GHz-2.48 GHz)," *IEEE Antennas Wirel. Propag. Lett.*, vol. 7, pp. 418–420, 2008.

[115] P. Valdastri, A. Menciassi, A. Arena, C. Caccamo, and P. Dario, "An implantable telemetry platform system for in vivo monitoring of physiological parameters," *IEEE Trans. Inf. Technol. Biomed.*, vol. 8, no. 3, pp. 271–278, Sep. 2004.

[116] E. A. Johannessen, L. Wang, C. Wyse, D. R. S. Cumming, and J. M. Cooper, "Biocompatibility of a Lab-on-a-Pill Sensor in Artificial Gastrointestinal Environments," *IEEE Trans. Biomed. Eng.*, vol. 53, no. 11, pp. 2333–2340, Nov. 2006.

[117] J. Gemio, J. Parron, and J. Soler, "Human body effects on implantable antennas for ISM bands applications: Models comparison and propagation losses study," *Prog. Electromagn. Res.*, vol. 110, pp. 437–452, 2010.

[118] A. Sani, M. Rajab, R. Foster, and Y. Hao, "Antennas and Propagation of Implanted RFIDs for Pervasive Healthcare Applications," *Proc. IEEE*, vol. 98, no. 9, pp. 1648–1655, Sep. 2010.

[119] M. Norris, J.-D. Richerd, and D. Raynes, "Sub miniature antenna design for wireless implants," 2007.

[120] C. Roopnariane, M.-R. Tofighi, C. M. Collins, and others, "Radiation performance of small implanted antennas in head at MICS, ISM, and GPS bands," in *Bioengineering Conference, Proceedings of the 2010 IEEE 36th Annual Northeast*, 2010, pp. 1–2.

[121] C. Occhiuzzi, G. Contri, and G. Marrocco, "Design of Implanted RFID Tags for Passive Sensing of Human Body: The STENTag," *IEEE Trans. Antennas Propag.*, vol. 60, no. 7, pp. 3146–3154, Jul. 2012.

[122] R. Lodato and G. Marrocco, "Close Integration of a UHF-RFID Transponder Into a Limb Prosthesis for Tracking and Sensing," *IEEE Sens. J.*, vol. 16, no. 6, pp. 1806–1813, Mar. 2016.

[123] C.-K. Wu, T.-F. Chien, C.-L. Yang, and C.-H. Luo, "Design of Novel S-Shaped Quad-Band Antenna for MedRadio/WMTS/ISM Implantable Biotelemetry Applications," *Int. J. Antennas Propag.*, vol. 2012, p. e564092, Jul. 2012.

[124] W. Xia, K. Saito, M. Takahashi, and K. Ito, "Performances of an Implanted Cavity Slot Antenna Embedded in the Human Arm," *IEEE Trans. Antennas Propag.*, vol. 57, no. 4, pp. 894–899, Apr. 2009.

[125] E. Y. Chow, Yuehui Ouyang, B. Beier, W. J. Chappell, and P. P. Irazoqui, "Evaluation of Cardiovascular Stents as Antennas for Implantable Wireless Applications," *IEEE Trans. Microw. Theory Tech.*, vol. 57, no. 10, pp. 2523–2532, Oct. 2009.

[126] U. Kawoos, M.-R. Tofighi, R. Warty, F. A. Kralick, and A. Rosen, "In-Vitro and In-Vivo Trans-Scalp Evaluation of an Intracranial Pressure Implant at 2.4 GHz," *IEEE Trans. Microw. Theory Tech.*, vol. 56, no. 10, pp. 2356–2365, Oct. 2008.

[127] G. Collin, A. Chami, C. Luxey, P. Le Thuc, and R. Staraj, "Small electrical antenna for SAW sensor biotelemetry," *Microw. Opt. Technol. Lett.*, vol. 51, no. 10, pp. 2286–2293, Oct. 2009.

[128] R. Warty, M.-R. Tofighi, U. Kawoos, and A. Rosen, "Characterization of Implantable Antennas for Intracranial Pressure Monitoring: Reflection by and Transmission Through a Scalp Phantom," *IEEE Trans. Microw. Theory Tech.*, vol. 56, no. 10, pp. 2366–2376, Oct. 2008.

[129] K. M. S. Thotahewa, J. M. Redouté, and M. R. Yuce, "SAR, SA, and Temperature Variation in the Human Head Caused by IR-UWB Implants Operating at 4 GHz," *IEEE Trans. Microw. Theory Tech.*, vol. 61, no. 5, pp. 2161–2169, May 2013.

[130] S. Soora, K. Gosalia, M. S. Humayun, and G. Lazzi, "A Comparison of Two and Three Dimensional Dipole Antennas for an Implantable Retinal Prosthesis," *IEEE Trans. Antennas Propag.*, vol. 56, no. 3, pp. 622–629, Mar. 2008.

[131] M. R. Yuce, T. Dissanayake, and H. C. Keong, "Wireless telemetry for electronic pill technology," in *Sensors, 2009 IEEE*, 2009, pp. 1433–1438.

[132] E. Y. Chow, A. Kahn, and P. P. Irazoqui, "High Data-Rate 6.7 GHz Wireless ASIC Transmitter for Neural Prostheses," in *2007 29th Annual International Conference of the IEEE Engineering in Medicine and Biology Society*, 2007, pp. 6580–6583.

[133] Y. Ahmed, Y. Hao, and C. Parini, "A 31.5 GHz Patch Antenna Design for Medical Implants," *Int. J. Antennas Propag.*, vol. 2008, p. e167980, Sep. 2008.

[134] A. K. Skrivervik, "Implantable antennas: The challenge of efficiency," in *Antennas and Propagation (EuCAP), 2013 7th European Conference on*, 2013, pp. 3627–3631.

[135] A. Kiourti and K. S. Nikita, "Detuning issues and performance of a novel implantable antenna for telemetry applications," in *Antennas and Propagation (EUCAP), 2012 6th European Conference on*, 2012, pp. 746–749.

[136] Z. Duan, Y.-X. Guo, R.-F. Xue, M. Je, and D.-L. Kwong, "Differentially Fed Dual-Band Implantable Antenna for Biomedical Applications," *IEEE Trans. Antennas Propag.*, vol. 60, no. 12, pp. 5587–5595, Dec. 2012.

[137] C. Liu, Y. X. Guo, H. Sun, and S. Xiao, "Design and Safety Considerations of an Implantable Rectenna for Far-Field Wireless Power Transfer," *IEEE Trans. Antennas Propag.*, vol. 62, no. 11, pp. 5798–5806, Nov. 2014.

[138] S. Bakogianni and S. Koulouridis, "Design of a novel miniature implantable rectenna for in-body medical devices power support," in *2016 10th European Conference on Antennas and Propagation (EuCAP)*, 2016, pp. 1–5.

[139] L. Marnat, M. H. Ouda, M. Arsalan, K. Salama, and A. Shamim, "On-Chip Implantable Antennas for Wireless Power and Data Transfer in a Glaucoma-Monitoring SoC," *IEEE Antennas Wirel. Propag. Lett.*, vol. 11, pp. 1671–1674, 2012.

[140] M. Kiani and M. Ghovanloo, "A 13.56-Mbps Pulse Delay Modulation Based Transceiver for Simultaneous Near-Field Data and Power Transmission," *IEEE Trans. Biomed. Circuits Syst.*, vol. 9, no. 1, pp. 1–11, Feb. 2015.

[141] G. Slaughter and T. Kulkarni, "Enzymatic Glucose Biofuel Cell and its Application," *J. Biochips Tissue Chips*, vol. 5, no. 1, Jul. 2015.

[142] A. Zebda *et al.*, "Single Glucose Biofuel Cells Implanted in Rats Power Electronic Devices," *Sci. Rep.*, vol. 3, p. 1516, Mar. 2013.

[143] A. Cadei, A. Dionisi, E. Sardini, and M. Serpelloni, "Kinetic and thermal energy harvesters for implantable medical devices and biomedical autonomous sensors," *Meas. Sci. Technol.*, vol. 25, no. 1, p. 012003, 2014.

[144] M. Deterre, E. Lefeuvre, Y. Zhu, M. Woytasik, B. Boutaud, and R. D. Molin, "Micro Blood Pressure Energy Harvester for Intracardiac Pacemaker," *J. Microelectromechanical Syst.*, vol. 23, no. 3, pp. 651–660, Jun. 2014.

[145] B. M. G. Rosa and G. Z. Yang, "Active implantable sensor powered by ultrasounds with application in the monitoring of physiological parameters for soft tissues," in *2016 IEEE 13th International Conference on Wearable and Implantable Body Sensor Networks (BSN)*, 2016, pp. 318–323.

[146] E. Moon, D. Blaauw, and J. D. Phillips, "Subcutaneous Photovoltaic Infrared Energy Harvesting for Bio-implantable Devices," *IEEE Trans. Electron Devices*, vol. PP, no. 99, pp. 1–6, 2017.

[147] C. W. L. Lee, A. Kiourti, and J. L. Volakis, "Miniaturized Fully Passive Brain Implant for Wireless Neuropotential Acquisition," *IEEE Antennas Wirel. Propag. Lett.*, vol. 16, pp. 645–648, 2017.

[148] H. N. Schwerdt, F. A. Miranda, and J. Chae, "Wireless Fully Passive Multichannel Recording of Neuropotentials Using Photo-Activated RF Backscattering Methods," *IEEE Trans. Microw. Theory Tech.*, vol. 63, no. 9, pp. 2965–2970, Sep. 2015.

[149] Z. Xiao *et al.*, "An Implantable RFID Sensor Tag toward Continuous Glucose Monitoring," *IEEE J. Biomed. Health Inform.*, vol. 19, no. 3, pp. 910–919, May 2015.

[150] H. Talleb, S. Faci, D. Lautru, V. F. Hanna, and J. Wiart, "Investigation on an RFID planar coil for a wireless communicative aortic stent," *Comptes Rendus Phys.*, vol. 14, no. 5, pp. 438–446, May 2013.

[151] R. Lodato, P. P. Valentini, and G. Marrocco, "A structural antenna for UHF-RFID implant into limb prosthesis," in *2015 IEEE International Symposium on Antennas and Propagation USNC/URSI National Radio Science Meeting*, 2015, pp. 1568–1569.

[152] A. K. Skrivervik and F. Merli, "Design strategies for implantable antennas," in *Proc. Loughborough Antennas & Propagation Conference 2011 (LAPC 2011)*, 2011.

[153] S. H. Lee and Y. J. Yoon, "Fat arm spiral antenna for wideband capsule endoscope systems," in *Radio and Wireless Symposium (RWS), 2010 IEEE*, 2010, pp. 579–582.

[154] T. Baras and A. F. Jacob, "Manufacturing Reliability of LTCC Millimeter-Wave Passive Components," *IEEE Trans. Microw. Theory Tech.*, vol. 56, no. 11, pp. 2574–2581, Nov. 2008.

[155] W. Smetana, B. Balluch, G. Stangl, E. Gaubitzer, M. Edetsberger, and G. Köhler, "A multi-sensor biological monitoring module built up in LTCC-technology," *Microelectron. Eng.*, vol. 84, no. 5–8, pp. 1240–1243, May 2007.

[156] J. Luo and R. E. Eitel, "A Biocompatible Low Temperature Co-fired Ceramic Substrate for Biosensors," *Int. J. Appl. Ceram. Technol.*, vol. 11, no. 3, pp. 436–442, May 2014.

[157] H. Permana, Q. Fang, and W. S. Rowe, "Hermetic implantable antenna inside vitreous humor simulating fluid," *Prog. Electromagn. Res.*, vol. 133, pp. 571–590, 2013.

[158] J. W. Hand, "Modelling the interaction of electromagnetic fields (10 MHz–10 GHz) with the human body: methods and applications," *Phys. Med. Biol.*, vol. 53, no. 16, pp. R243–R286, Aug. 2008.

[159] K. Yee, "Numerical Solution of Initial Value Problems of Maxwells Equations," *IEEE Trans Antennas Propag*, vol. 14, no. 3, pp. 302–307, May 1966.

[160] K. L.-L. Roman, G. Vermeeren, A. Thielens, W. Joseph, and L. Martens, "Characterization of path loss and absorption for a wireless radio frequency link between an in-body endoscopy capsule and a receiver outside the body," *EURASIP J. Wirel. Commun. Netw.*, vol. 2014, no. 1, pp. 1–10, 2014.

[161] H.-Y. Lin, M. Takahashi, K. Saito, and K. Ito, "Performance of implantable folded dipole antenna for in-body wireless communication," *Antennas Propag. IEEE Trans. On*, vol. 61, no. 3, pp. 1363–1370, 2013.

[162] K. Gosalia, G. Lazzi, and M. Humayun, "Investigation of a Microwave Data Telemetry Link for a Retinal Prosthesis," *IEEE Trans. Microw. Theory Tech.*, vol. 52, no. 8, pp. 1925–1933, Aug. 2004.

[163] D. Rucker, A. Al-Alawi, R. Adada, and H. M. Al-Rizzo, "A miniaturized tunable microstrip antenna for wireless communications with implanted medical devices," in *Proceedings of the ICST 2nd international conference on Body area networks*, 2007, p. 1.

[164] K. M. S. Thotahewa, J. M. Redoutè, and M. R. Yuce, "Propagation, Power Absorption, and Temperature Analysis of UWB Wireless Capsule Endoscopy Devices Operating in the Human Body," *IEEE Trans. Microw. Theory Tech.*, vol. 63, no. 11, pp. 3823–3833, Nov. 2015.

[165] A. Garcia-Miquel, B. Medina-Rodríguez, N. Vidal, F. M. Ramos, E. Roca, and J. M. Lopez-Villegas, "Design and characterization of a miniaturized implantable UHF RFID tag based on LTCC technology," in *Antennas and Propagation (EUCAP), 2017 11th European Conference on*, 2017, pp. 1024–1026.

[166] R. Xu, H. Zhu, and J. Yuan, "Circuit-coupled FEM analysis of the electric-field type intra-body communication channel," in *2009 IEEE Biomedical Circuits and Systems Conference*, 2009, pp. 221–224.

[167] H. Bahrami, B. Gosselin, L. Rusch, and others, "Design of a miniaturized UWB antenna optimized for implantable neural recording systems," in *New Circuits and Systems Conference (NEWCAS), 2012 IEEE 10th International*, 2012, pp. 309–312.

[168] D. B. Davidson, *Computational Electromagnetics for RF and Microwave Engineering*. Cambridge University Press, 2010.

[169] J.-P. Berenger, "A perfectly matched layer for the absorption of electromagnetic waves," *J. Comput. Phys.*, vol. 114, no. 2, pp. 185–200, Oct. 1994.

[170] "SIM4LIFE » zurich med tech." [Online]. Available: https://www.zurichmedtech.com/sim4life/. [Accessed: 26-Apr-2017].

[171] "CST Microwave Studio." [Online]. Available: https://www.cst.com/. [Accessed: 30-Aug-2016].

[172] "Advanced Design System." [Online]. Available: http://www.keysight.com/. [Accessed: 30-Aug-2016].

[173] K. Ito, "Human Body Phantoms for Evaluation of Wearable and Implantable Antennas," in *The Second European Conference on Antennas and Propagation, EuCAP 2007*, 2007, pp. 1–6.

[174] A. Kiourti and K. S. Nikita, "A review of implantable patch antennas for biomedical telemetry: Challenges and solutions [wireless corner]," *Antennas Propag. Mag. IEEE*, vol. 54, no. 3, pp. 210–228, 2012.

[175] "Dielectric Properties of Body Tissues: Home page." [Online]. Available: http://niremf.ifac.cnr.it/tissprop/. [Accessed: 25-Apr-2017].

[176] "Dielectric Properties » IT'IS Foundation." [Online]. Available: https://www.itis.ethz.ch/virtual-population/tissue-properties/database/dielectric-properties/. [Accessed: 05-Oct-2017].

[177] A. K. Skrivervik, M. Bosiljevac, and Z. Sipus, "Propagation Considerations for Implantable Antennas," in *Antennas and Propagation (EUCAP), 2017 11th European Conference on*, 2017, pp. 1573–1577.

[178] T. Dissanayake, K. P. Esselle, and M. R. Yuce, "Dielectric Loaded Impedance Matching for Wideband Implanted Antennas," *IEEE Trans. Microw. Theory Tech.*, vol. 57, no. 10, pp. 2480–2487, Oct. 2009.

[179] S. Bakogianni and S. Koulouridis, "An Implantable Planar Dipole Antenna for Wireless MedRadio-Band Biotelemetry Devices," *IEEE Antennas Wirel. Propag. Lett.*, pp. 1–1, 2015.

[180] H. Permana, Q. Fang, and I. Cosic, "3-layer implantable microstrip antenna optimised for retinal prosthesis system in MICS band," in *Bioelectronics and Bioinformatics (ISBB), 2011 International Symposium on*, 2011, pp. 65–68.

[181] S. Curto and P. Prakash, "Design of a compact antenna with flared groundplane for a wearable breast hyperthermia system," *Int. J. Hyperthermia*, vol. 31, no. 7, pp. 726–736, Oct. 2015.

[182] D. A. Iero, L. Crocco, T. Isernia, and E. Korkmaz, "Optimal focused electromagnetic hyperthermia treatment of breast cancer," in *2016 10th European Conference on Antennas and Propagation (EuCAP)*, 2016, pp. 1–2.

[183] C. Miry, R. Gillard, and R. Loison, "An application of the multi-level DG-FDTD to the analysis of the transmission between a dipole in free-space and an implanted antenna in a simplified body model with various positions," in *2009 3rd European Conference on Antennas and Propagation*, 2009, pp. 67–70.

[184] Z. Živković, E. Vujević, D. Poljak, K. E. K. Drissi, and A. Šarolić, "Computation of SAR in the simplified model of a pregnant woman exposed to RF radiation from 10 MHz to 1800 MHz," in *2013 21st International Conference on Software, Telecommunications and Computer Networks - (SoftCOM 2013)*, 2013, pp. 1–5.

[185] A. Garcia-Miquel, S. Curto, N. Vidal, J. M. Lopez-Villegas, F. M. Ramos, and P. Prakash, "Multilayered Broadband Antenna for Compact Embedded Implantable Medical Devices: Design and Characterization," *Prog. Electromagn. Res.*, vol. 159, pp. 1–13, 2017.

[186] A. Peyman and C. Gabriel, "Cole–Cole parameters for the dielectric properties of porcine tissues as a function of age at microwave frequencies," *Phys. Med. Biol.*, vol. 55, no. 15, p. N413, Jul. 2010.

[187] C. Rossmann and D. Haemmerich, "Review of temperature dependence of thermal properties, dielectric properties, and perfusion of biological tissues at hyperthermic and ablation temperatures," *Crit. Rev. Biomed. Eng.*, vol. 42, no. 6, pp. 467–492, 2014.

[188] J. Wang, O. Fujiwara, and S. Watanabe, "Approximation of aging effect on dielectric tissue properties for SAR assessment of mobile telephones," *IEEE Trans. Electromagn. Compat.*, vol. 48, no. 2, pp. 408–413, May 2006.

[189] W. Huang and A. A. Kishk, "Embedded Spiral Microstrip Implantable Antenna," *Int. J. Antennas Propag.*, vol. 2011, p. e919821, Aug. 2011.

[190] "The National Library of Medicines Visible Human Project." [Online]. Available: https://www.nlm.nih.gov/research/visible/visible_human.html. [Accessed: 26-Apr-2017].

[191] T. Nagaoka *et al.*, "Development of realistic high-resolution whole-body voxel models of Japanese adult males and females of average height and weight, and application of models to radio-frequency electromagnetic-field dosimetry," *Phys. Med. Biol.*, vol. 49, no. 1, pp. 1–15, Jan. 2004.

[192] A. Christ *et al.*, "The Virtual Family—development of surface-based anatomical models of two adults and two children for dosimetric simulations," *Phys. Med. Biol.*, vol. 55, no. 2, pp. N23–N38, Jan. 2010.

[193] "Virtual Classroom » IT'IS Foundation." [Online]. Available: https://www.itis.ethz.ch/news-events/news/virtual-population/virtual-classroom/. [Accessed: 26-Apr-2017].

[194] B. B. Beard *et al.*, "Comparisons of computed mobile phone induced SAR in the SAM phantom to that in anatomically correct models of the human head," *IEEE Trans. Electromagn. Compat.*, vol. 48, no. 2, pp. 397–407, May 2006.

[195] A. Alomainy and Y. Hao, "Modeling and Characterization of Biotelemetric Radio Channel From Ingested Implants Considering Organ Contents," *IEEE Trans. Antennas Propag.*, vol. 57, no. 4, pp. 999–1005, Apr. 2009.

[196] W. G. Scanlon, B. Burns, and N. E. Evans, "Radiowave propagation from a tissue-implanted source at 418 MHz and 916.5 MHz," *IEEE Trans. Biomed. Eng.*, vol. 47, no. 4, pp. 527–534, Apr. 2000.

[197] J. H. Jung, S. W. Kim, Y. S. Kim, and S. Y. Kim, "Electromagnetic Propagation From the Intestine-Ingested Source in the Human Body Model," *IEEE Trans. Antennas Propag.*, vol. 58, no. 5, pp. 1683–1688, May 2010.

[198] A. Sani, A. Alomainy, and Yang Hao, "Numerical Characterization and Link Budget Evaluation of Wireless Implants Considering Different Digital Human Phantoms," *IEEE Trans. Microw. Theory Tech.*, vol. 57, no. 10, pp. 2605–2613, Oct. 2009.

[199] V. D. Santis and M. Feliziani, "Intra-body channel characterization of medical implant devices," in *10th International Symposium on Electromagnetic Compatibility*, 2011, pp. 816–819.

[200] T. Hikage, Y. Kawamura, T. Nojima, and E. Cabot, "Numerical assessment methodology for active implantable medical device EMI due to magnetic resonance wireless power transmission antenna," in *International Symposium on Electromagnetic Compatibility - EMC EUROPE*, 2012, pp. 1–6.

[201] M. E. Jalil, M. K. A. Rahim, N. A. Samsuri, N. A. Murad, N. Othman, and H. A. Majid, "On-body investigation of dual band diamond textile antenna for wearable applications at 2.45 GHz and 5.8 GHz," in *2013 7th European Conference on Antennas and Propagation (EuCAP)*, 2013, pp. 414–417.

[202] C. Liu, Y. X. Guo, X. Liu, and S. Xiao, "An Integrated On-Chip Implantable Antenna in CMOS Technology for Biomedical Applications," *IEEE Trans. Antennas Propag.*, vol. 64, no. 3, pp. 1167–1172, Mar. 2016.

[203] M. T. Islam, M. R. I. Faruque, and N. Misran, "Design Analysis of Ferrite Sheet Attachment for SAR Reduction in Human Head," *Prog. Electromagn. Res.*, vol. 98, pp. 191–205, 2009.

[204] C. J. Panagamuwa, W. G. Whittow, R. M. Edwards, and J. C. Vardaxoglou, "Experimental Verification of a Modified Specific Anthropomorphic Mannequin (SAM) Head used for SAR Measurements," in *2007 Loughborough Antennas and Propagation Conference*, 2007, pp. 261–264.

[205] E. Zastrow, S. K. Davis, M. Lazebnik, F. Kelcz, B. D. Van Veen, and S. C. Hagness, "Database of 3D Grid-Based Numerical Breast Phantoms for use in Computational Electromagnetics Simulations."

[206] P. T. Nguyen, A. Abbosh, and S. Crozier, "Microwave Hyperthermia for Breast Cancer Treatment Using Electromagnetic and Thermal Focusing Tested on Realistic Breast Models and Antenna Arrays," *IEEE Trans. Antennas Propag.*, vol. 63, no. 10, pp. 4426–4434, Oct. 2015.

[207] S. Curto, G. Ruvio, M. J. Ammann, and P. Prakash, "A wearable applicator for microwave hyperthermia of breast cancer: Performance evaluation with patient-specific anatomic models," in *Electromagnetics in Advanced Applications (ICEAA), 2015 International Conference on*, 2015, pp. 1159–1162.

[208] A. Garcia-Miquel, S. Curto, N. Vidal, J. M. Lopez-Villegas, and P. Prakash, "Antenna Array for Hyperthermia Treatment of Breast Cancer," in *XXXI Simposium Nacional de la Unión Científica Internacional de Radio*, Madrid, Spain, 2016.

[209] "iSEG - Medical Image Segmentation Tool Set." [Online]. Available: https://www.zurichmedtech.com/sim4life/modules/iseg/. [Accessed: 26-Apr-2017].

[210] "ALBA 3D Segmentation Tool (ALBA-3Dseg)." [Online]. Available: http://www.albahyperthermia.com/ALBA-3Dseg.html. [Accessed: 26-Apr-2017].

[211] "Poser » zurich med tech." [Online]. Available: https://www.zurichmedtech.com/sim4life/modules/poser/. [Accessed: 26-Apr-2017].

[212] T. Nagaoka and S. Watanabe, "Postured voxel-based human models for electromagnetic dosimetry," *Phys. Med. Biol.*, vol. 53, no. 24, pp. 7047–7061, Dec. 2008.

[213] C. H. Li *et al.*, "Influence of the Hand on the Specific Absorption Rate in the Head," *IEEE Trans. Antennas Propag.*, vol. 60, no. 2, pp. 1066–1074, Feb. 2012.

[214] "POPEYE-V5.5 » SPEAG, Schmid & Partner Engineering AG." [Online]. Available: https://www.speag.com/products/em-phantom/phantoms/popeye-v5-5/. [Accessed: 26-Apr-2017].

[215] "SAM-V4.5BSE » SPEAG, Schmid & Partner Engineering AG." [Online]. Available: https://www.speag.com/products/em-phantom/phantoms/sam-v4-5bse/. [Accessed: 26-Apr-2017].

[216] M. Y. Kanda, M. Ballen, S. Salins, C.-K. Chou, and Q. Balzano, "Formulation and characterization of tissue equivalent liquids used for RF densitometry and dosimetry measurements," *IEEE Trans. Microw. Theory Tech.*, vol. 52, no. 8, pp. 2046–2056, Agosto 2004.

[217] N. Joachimowicz, C. Conessa, T. Henriksson, and B. Duchêne, "Breast Phantoms for Microwave Imaging," *IEEE Antennas Wirel. Propag. Lett.*, vol. 13, pp. 1333–1336, 2014.

[218] B. Tuong and I. Gardiner, "Development of a novel breast MRI phantom for quality control," *AJR Am. J. Roentgenol.*, vol. 201, no. 3, pp. W511-515, Sep. 2013.

[219] S. Curto, A. Garcia-Miquel, M. Suh, N. Vidal, J. M. Lopez-Villegas, and P. Prakash, "Design and characterisation of a phased antenna array for intact breast hyperthermia," *Int. J. Hyperthermia*, pp. 1–11, Jun. 2017.

[220] S. Curto, M. Taj-Eldin, D. Fairchild, and P. Prakash, "Microwave ablation at 915 MHz vs 2.45 GHz: A theoretical and experimental investigation," *Med. Phys.*, vol. 42, 2015.

[221] F. Merli *et al.*, "Example of Data Telemetry for Biomedical Applications: An In Vivo Experiment," *IEEE Antennas Wirel. Propag. Lett.*, vol. 11, pp. 1650–1654, 2012.

[222] C. Liu, Y. X. Guo, R. Jegadeesan, and S. Xiao, "In Vivo Testing of Circularly Polarized Implantable Antennas in Rats," *IEEE Antennas Wirel. Propag. Lett.*, vol. 14, pp. 783–786, 2015.

[223] A. Kiourti, K. A. Psathas, J. R. Costa, C. A. Fernandes, and K. S. Nikita, "Dual-band implantable antennas for medical telemetry: a fast design methodology and validation for intra-cranial pressure monitoring," *Prog. Electromagn. Res.*, vol. 141, pp. 161–183, 2013.

[224] A. Kiourti and K. S. Nikita, "Miniaturization vs gain and safety considerations of implantable antennas for wireless biotelemetry," in *Antennas and Propagation Society International Symposium (APSURSI), 2012 IEEE*, 2012, pp. 1–2.

[225] J. M. Gonzalez-Arbesu, S. Blanch, and J. Romeu, "Are space-filling curves efficient small antennas?," *IEEE Antennas Wirel. Propag. Lett.*, vol. 2, no. 1, pp. 147–150, 2003.

[226] C.-L. Yang, C.-L. Tsai, and S.-H. Chen, "Implantable High-Gain Dental Antennas for Minimally Invasive Biomedical Devices," *IEEE Trans. Antennas Propag.*, vol. 61, no. 5, pp. 2380–2387, May 2013.

[227] A. Kiourti and K. S. Nikita, "Performance of miniature implantable antennas for medical telemetry at 402, 433, 868 and 915 MHz," in *Wireless Mobile Communication and Healthcare*, Springer, 2013, pp. 122–129.

[228] F. Merli and A. K. Skrivervik, "Design and measurement considerations for implantable antennas for telemetry applications," in *Proceedings of the Fourth European Conference on Antennas and Propagation*, 2010, pp. 1–5.

[229] F. M. Ramos, "Integración de la tecnología multicapa," Universitat de Barcelona, 2014.

[230] Q. Duan *et al.*, "Characterization of a dielectric phantom for high-field magnetic resonance imaging applications," *Med. Phys.*, vol. 41, no. 10, p. n/a-n/a, Oct. 2014.

[231] "Dielectric phantom recipes for MRI." [Online]. Available: https://amri.ninds.nih.gov/cgi-bin/phantomrecipe. [Accessed: 30-Aug-2016].

[232] S. A. Kumar and T. Shanmuganantham, "Design and analysis of implantable CPW fed bowtie antenna for ISM band applications," *AEU - Int. J. Electron. Commun.*, vol. 68, no. 2, pp. 158–165, Feb. 2014.

[233] "Mini Circuits - Global Leader of RF and Microwave Components." [Online]. Available: https://ww2.minicircuits.com/homepage/homepage.html. [Accessed: 16-Nov-2017].

[234] M. Alexander, T. H. Loh, and A. L. Betancort, "Measurement of electrically small antennas via optical fibre," in *2009 Loughborough Antennas Propagation Conference*, 2009, pp. 653–656.

[235] "SPINNER Group - Home." [Online]. Available: http://www.spinner-group.com/en/. [Accessed: 05-Aug-2017].

[236] "Broadcom Limited | Connecting Everything." [Online]. Available: https://www.broadcom.com/. [Accessed: 05-Aug-2017].

[237] A. Kiourti, K. A. Psathas, and K. S. Nikita, "Implantable and ingestible medical devices with wireless telemetry functionalities: A review of current status and challenges: Implantable/Ingestible Medical Devices," *Bioelectromagnetics*, vol. 35, no. 1, pp. 1–15, Jan. 2014.

[238] K. A. Psathas, A. P. Keliris, A. Kiourti, and K. S. Nikita, "Operation of ingestible antennas along the gastrointestinal tract: Detuning and performance," in *Bioinformatics and Bioengineering (BIBE), 2013 IEEE 13th International Conference on*, 2013, pp. 1–4.

[239] M. D. Weiss, J. L. Smith, and J. Bach, "RF Coupling in a 433-MHz Biotelemetry System for an Artificial Hip," *IEEE Antennas Wirel. Propag. Lett.*, vol. 8, pp. 916–919, 2009.

[240] D. Crescini, E. Sardini, and M. Serpelloni, "Design and test of an autonomous sensor for force measurements in human knee implants," *Sens. Actuators Phys.*, vol. 166, no. 1, pp. 1–8, Mar. 2011.

[241] U. Kawoos, X. Meng, M.-R. Tofighi, and A. Rosen, "Too Much Pressure: Wireless Intracranial Pressure Monitoring and Its Application in Traumatic Brain Injuries," *IEEE Microw. Mag.*, vol. 16, no. 2, pp. 39–53, Mar. 2015.

[242] E. Y. Chow, A. L. Chlebowski, S. Chakraborty, W. J. Chappell, and P. P. Irazoqui, "Fully Wireless Implantable Cardiovascular Pressure Monitor Integrated with a Medical Stent," *IEEE Trans. Biomed. Eng.*, vol. 57, no. 6, pp. 1487–1496, Jun. 2010.

[243] Federal Communications Comission, "Evaluating compliance with FCC guidelines for human exposure to radiofrequency electromagnetic fields. Washington, DC," 2001.

[244] A. Yakovlev, S. Kim, and A. Poon, "Implantable biomedical devices: Wireless powering and communication," *IEEE Commun. Mag.*, vol. 50, no. 4, pp. 152–159, Apr. 2012.

[245] G. Marrocco, "RFID Antennas for the UHF Remote Monitoring of Human Subjects," *IEEE Trans. Antennas Propag.*, vol. 55, no. 6, pp. 1862–1870, Jun. 2007.

[246] A. Sani, M. Rajab, R. Foster, and Y. Hao, "Antennas and Propagation of Implanted RFIDs for Pervasive Healthcare Applications," *Proc. IEEE*, vol. 98, no. 9, pp. 1648–1655, Sep. 2010.

[247] H. Aubert, "RFID technology for human implant devices," *Comptes Rendus Phys.*, vol. 12, no. 7, pp. 675–683, Sep. 2011.

[248] "Higgs 4 RFID IC | Alien Technology." .

[249] "Alien Technology Readers." [Online]. Available: http://www.alientechnology.com/products/readers/. [Accessed: 30-Aug-2016].

[250] P. V. Nikitin and K. V. S. Rao, "Antennas and propagation in UHF RFID systems," *challenge*, vol. 22, p. 23, 2008.

[251] R. Siegel, D. Naishadham, and A. Jemal, "Cancer statistics, 2013.," *CA Cancer J Clin*, no. 63, pp. 11–30, 2013.

[252] "Cancer Prevention & Early Detection| American Cancer Society." [Online]. Available: https://www.cancer.org/research/cancer-facts-statistics/cancer-prevention-early-detection.html. [Accessed: 23-Aug-2017].

[253] S. A. Narod, "Tumour size predicts long-term survival among women with lymph node-positive breast cancer," *Curr. Oncol.*, vol. 19, no. 5, pp. 249–253, Oct. 2012.

[254] M. Morrow *et al.*, "Standard for Breast Conservation Therapy in the Management of Invasive Breast Carcinoma," *CA. Cancer J. Clin.*, vol. 52, no. 5, pp. 277–300, Sep. 2002.

[255] R. R. Bitton, E. Kaye, F. M. Dirbas, B. L. Daniel, and K. B. Pauly, "Toward MR-guided high intensity focused ultrasound for presurgical localization: focused ultrasound lesions in cadaveric breast tissue," *J. Magn. Reson. Imaging JMRI*, vol. 35, no. 5, pp. 1089–1097, May 2012.

[256] T. M. Zagar *et al.*, "Hyperthermia combined with radiation therapy for superficial breast cancer and chest wall recurrence: A review of the randomised data," *Int. J. Hyperth. Off. J. Eur. Soc. Hyperthermic Oncol. North Am. Hyperth. Group*, vol. 26, no. 7, pp. 612–617, 2010.

[257] N. R. Datta, E. Puric, D. Klingbiel, S. Gomez, and S. Bodis, "Hyperthermia and Radiation Therapy in Locoregional Recurrent Breast Cancers: A Systematic Review and Meta-analysis," *Int. J. Radiat. Oncol. Biol. Phys.*, vol. 94, no. 5, pp. 1073–1087, Apr. 2016.

[258] C. D. Landon, J.-Y. Park, D. Needham, and M. W. Dewhirst, "Nanoscale Drug Delivery and Hyperthermia: The Materials Design and Preclinical and Clinical Testing of Low Temperature-Sensitive Liposomes Used in Combination with Mild Hyperthermia in the Treatment of Local Cancer," *Open Nanomedicine J.*, vol. 3, pp. 38–64, Jan. 2011.

[259] S. S. Evans, E. A. Repasky, and D. T. Fisher, "Fever and the thermal regulation of immunity: the immune system feels the heat," *Nat. Rev. Immunol.*, vol. 15, no. 6, pp. 335–349, Jun. 2015.

[260] A. H. S. Lee, "Why is carcinoma of the breast more frequent in the upper outer quadrant? A case series based on needle core biopsy diagnoses," *Breast Edinb. Scotl.*, vol. 14, no. 2, pp. 151–152, Apr. 2005.

[261] P. D. Darbre, "Recorded quadrant incidence of female breast cancer in Great Britain suggests a disproportionate increase in the upper outer quadrant of the breast," *Anticancer Res.*, vol. 25, no. 3c, pp. 2543–2550, Jun. 2005.

[262] A. American Cancer Society, "Detailed Guide: Breast Cancer," 2014.

[263] J. Van Der Zee *et al.*, "Reirradiation combined with hyperthermia in breast cancer recurrences: overview of experience in Erasmus MC," *Int. J. Hyperth. Off. J. Eur. Soc. Hyperthermic Oncol. North Am. Hyperth. Group*, vol. 26, no. 7, pp. 638–648, 2010.

[264] E. G. Moros, J. Peñagaricano, P. Novàk, W. L. Straube, and R. J. Myerson, "Present and future technology for simultaneous superficial thermoradiotherapy of breast cancer," *Int. J. Hyperth. Off. J. Eur. Soc. Hyperthermic Oncol. North Am. Hyperth. Group*, vol. 26, no. 7, pp. 699–709, 2010.

[265] D. S. Shimm *et al.*, "Regional hyperthermia for deep-seated malignancies using the BSD annular array," *Int. J. Hyperth. Off. J. Eur. Soc. Hyperthermic Oncol. North Am. Hyperth. Group*, vol. 4, no. 2, pp. 159–170, Apr. 1988.

[266] G. Shi and W. T. Joines, "Design and analysis of annular antenna arrays with different reflectors," *Int. J. Hyperth. Off. J. Eur. Soc. Hyperthermic Oncol. North Am. Hyperth. Group*, vol. 20, no. 6, pp. 625–636, Sep. 2004.

[267] A. J. Fenn and G. A. King, "Adaptive radiofrequency hyperthermia-phased array system for improved cancer therapy: phantom target measurements," *Int. J. Hyperth. Off. J. Eur. Soc. Hyperthermic Oncol. North Am. Hyperth. Group*, vol. 10, no. 2, pp. 189–208, Apr. 1994.

[268] D. Fatehi and G. C. van Rhoon, "SAR characteristics of the Sigma-60-Ellipse applicator," *Int. J. Hyperth. Off. J. Eur. Soc. Hyperthermic Oncol. North Am. Hyperth. Group*, vol. 24, no. 4, pp. 347–356, Jun. 2008.

[269] R. F. Verhaart *et al.*, "Accurate 3D temperature dosimetry during hyperthermia therapy by combining invasive measurements and patient-specific simulations," *Int. J. Hyperth. Off. J. Eur. Soc. Hyperthermic Oncol. North Am. Hyperth. Group*, vol. 31, no. 6, pp. 686–692, 2015.

[270] P. R. Stauffer *et al.*, "Conformal Microwave Array (CMA) Applicators for Hyperthermia of Diffuse Chestwall Recurrence," *Int. J. Hyperth. Off. J. Eur. Soc. Hyperthermic Oncol. North Am. Hyperth. Group*, vol. 26, no. 7, pp. 686–698, 2010.

[271] A. J. Fenn, G. L. Wolf, and R. M. Fogle, "An adaptive microwave phased array for targeted heating of deep tumours in intact breast: animal study results," *Int. J. Hyperth. Off. J. Eur. Soc. Hyperthermic Oncol. North Am. Hyperth. Group*, vol. 15, no. 1, pp. 45–61, Feb. 1999.

[272] J. Stang, M. Haynes, P. Carson, and M. Moghaddam, "A Preclinical System Prototype for Focused Microwave Thermal Therapy of the Breast," *IEEE Trans. Biomed. Eng.*, vol. 59, no. 9, pp. 2431–2438, Sep. 2012.

[273] L. Wu, R. J. McGough, O. A. Arabe, and T. V. Samulski, "An RF phased array applicator designed for hyperthermia breast cancer treatments," *Phys. Med. Biol.*, vol. 51, no. 1, p. 1, 2006.

[274] M. Asili *et al.*, "Flexible Microwave Antenna Applicator for Chemo-Thermotherapy of the Breast," *IEEE Antennas Wirel. Propag. Lett.*, vol. 14, pp. 1778–1781, 2015.

[275] G. Chakaravarthi and K. Arunachalam, "Design and characterisation of miniaturised cavity-backed patch antenna for microwave hyperthermia," *Int. J. Hyperth. Off. J. Eur. Soc. Hyperthermic Oncol. North Am. Hyperth. Group*, vol. 31, no. 7, pp. 737–748, 2015.

[276] W. C. Choi, K. J. Kim, J. Kim, and Y. J. Yoon, "Compact Microwave Radiator for Improving Heating Uniformity in Hyperthermia System," *IEEE Antennas Wirel. Propag. Lett.*, vol. 13, pp. 1345–1348, 2014.

[277] M. Converse, E. J. Bond, B. D. Veen, and C. Hagness, "A computational study of ultra-wideband versus narrowband microwave hyperthermia for breast cancer treatment," *IEEE Trans. Microw. Theory Tech.*, vol. 54, no. 5, pp. 2169–2180, May 2006.

[278] D. A. M. Iero, L. Crocco, and T. Isernia, "Thermal and Microwave Constrained Focusing for Patient-Specific Breast Cancer Hyperthermia: A Robustness Assessment," *IEEE Trans. Antennas Propag.*, vol. 62, no. 2, pp. 814–821, Feb. 2014.

[279] E. Zastrow, S. C. Hagness, and B. D. Van Veen, "3D computational study of non-invasive patient-specific microwave hyperthermia treatment of breast cancer," *Phys. Med. Biol.*, vol. 55, no. 13, pp. 3611–3629, Jul. 2010.

[280] M. Haynes, J. Stang, M. Moghaddam, M. Haynes, J. Stang, and M. Moghaddam, "Microwave Breast Imaging System Prototype with Integrated Numerical Characterization, Microwave

Breast Imaging System Prototype with Integrated Numerical Characterization," *Int. J. Biomed. Imaging Int. J. Biomed. Imaging*, vol. 2012, 2012, p. e706365, Mar. 2012.

[281] S. Gabriel, R. W. Lau, and C. Gabriel, "The dielectric properties of biological tissues: III. Parametric models for the dielectric spectrum of tissues," *Phys. Med. Biol.*, vol. 41, no. 11, p. 2271, 1996.

[282] U. Kaatze, "Reference liquids for the calibration of dielectric sensors and measurement instruments," *Meas. Sci. Technol.*, vol. 18, no. 4, pp. 967–976, Apr. 2007.

[283] E. Zastrow, S. K. Davis, M. Lazebnik, F. Kelcz, B. D. Van Veen, and S. C. Hagness, "Development of anatomically realistic numerical breast phantoms with accurate dielectric properties for modeling microwave interactions with the human breast," *IEEE Trans. Biomed. Eng.*, vol. 55, no. 12, pp. 2792–2800, Dec. 2008.

[284] A. Christ, A. Klingenbock, T. Samaras, C. Goiceanu, and N. Kuster, "The dependence of electromagnetic far-field absorption on body tissue composition in the frequency range from 300 MHz to 6 GHz," *IEEE Trans. Microw. Theory Tech.*, vol. 54, no. 5, pp. 2188–2195, May 2006.

[285] A. Garcia-Miquel, S. Curto, N. Vidal, J. M. Lopez-Villegas, and P. Prakash, "Compact Microwave Applicator for Thermal Therapy of Breast Cancer: Comparative Assessment of Arrays Operating at 434 and 915 MHz," in *European Conference on Antennas and Propagation*, Davos, Switzerland, 2016.

[286] H. Bahramiabarghouei, E. Porter, A. Santorelli, B. Gosselin, M. Popović, and L. A. Rusch, "Flexible 16 Antenna Array for Microwave Breast Cancer Detection," *IEEE Trans. Biomed. Eng.*, vol. 62, no. 10, pp. 2516–2525, Oct. 2015.

[287] M. M. Paulides, J. F. Bakker, A. P. M. Zwamborn, and G. C. van Rhoon, "A head and neck hyperthermia applicator: Theoretical antenna array design," *Int. J. Hyperthermia*, vol. 23, no. 1, pp. 59–67, Jan. 2007.

[288] J. Lagarias, J. Reeds, M. Wright, and P. Wright, "Convergence Properties of the Nelder--Mead Simplex Method in Low Dimensions," *SIAM J. Optim.*, vol. 9, no. 1, pp. 112–147, Jan. 1998.

[289] K. Arunachalam, P. F. Maccarini, and P. R. Stauffer, "A thermal monitoring sheet with low influence from adjacent waterbolus for tissue surface thermometry during clinical hyperthermia," *IEEE Trans. Biomed. Eng.*, vol. 55, no. 10, pp. 2397–2406, Oct. 2008.

[290] K.-C. Ju, L.-T. Tseng, Y.-Y. Chen, and W.-L. Lin, "Investigation of a scanned cylindrical ultrasound system for breast hyperthermia," *Phys. Med. Biol.*, vol. 51, no. 3, p. 539, 2006.

[291] W. Dooley, H. Vargas, and A. Fenn, "Randomized Study of Preoperative Focused Microwave Phased Array Thermotherapy for Early-Stage Invasive Breast Cancer," *Cancer Ther*, no. 6, pp. 395–408.

[292] C. M. van Leeuwen *et al.*, "3D radiobiological evaluation of combined radiotherapy and hyperthermia treatments," *Int. J. Hyperth. Off. J. Eur. Soc. Hyperthermic Oncol. North Am. Hyperth. Group*, pp. 1–10, Oct. 2016.

Appendices

Appendix A. Characterization of LTCC In-body Antennas

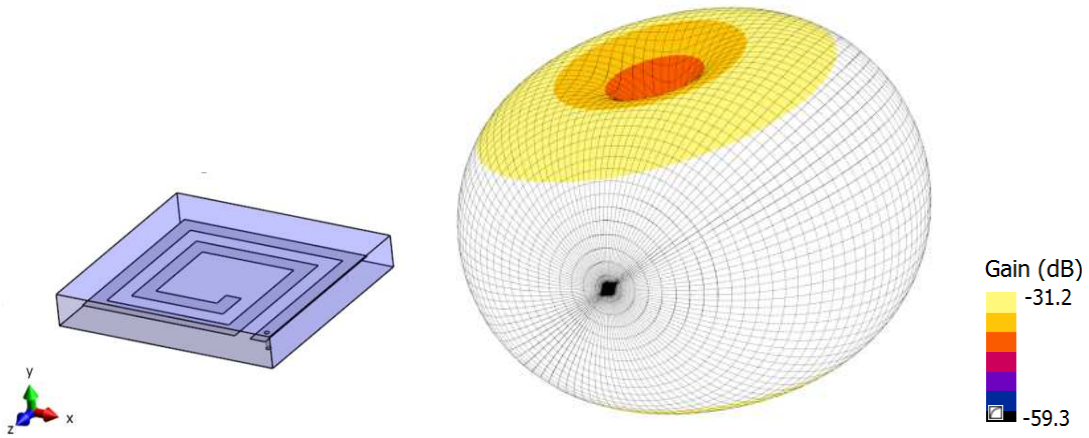

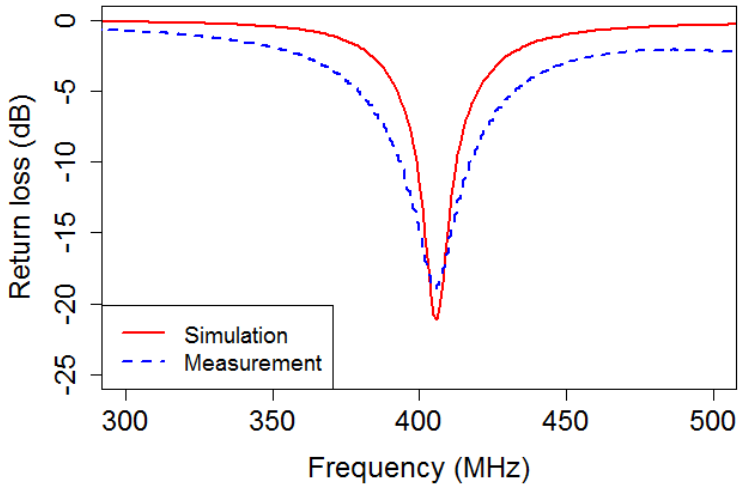

Figure 119. Perspective view, gain radiation pattern and reflection coefficient of the 2d403 antenna.

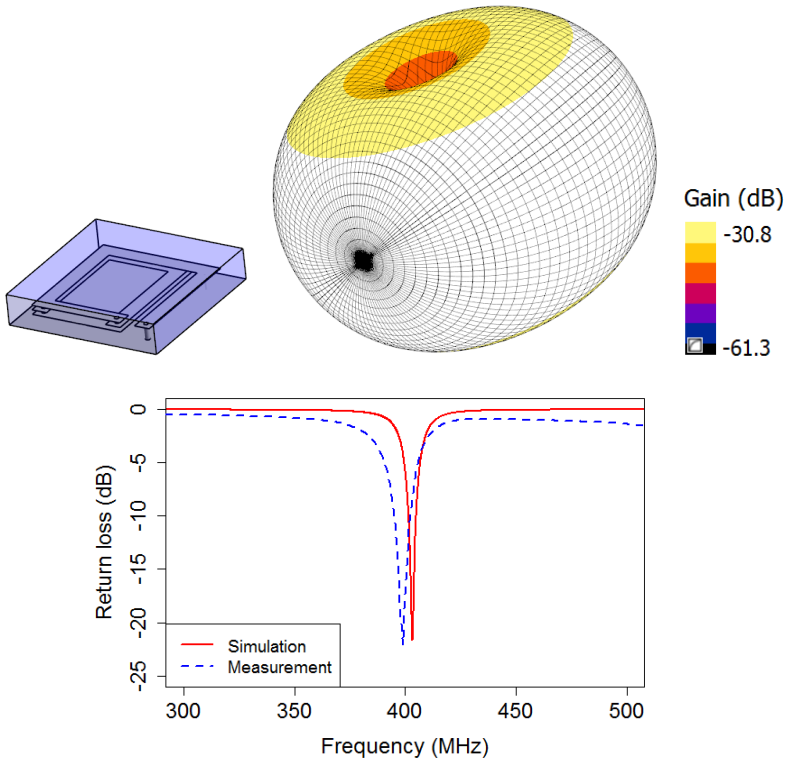

Figure 120. Perspective view, gain radiation pattern and reflection coefficient of the 3d403 antenna.

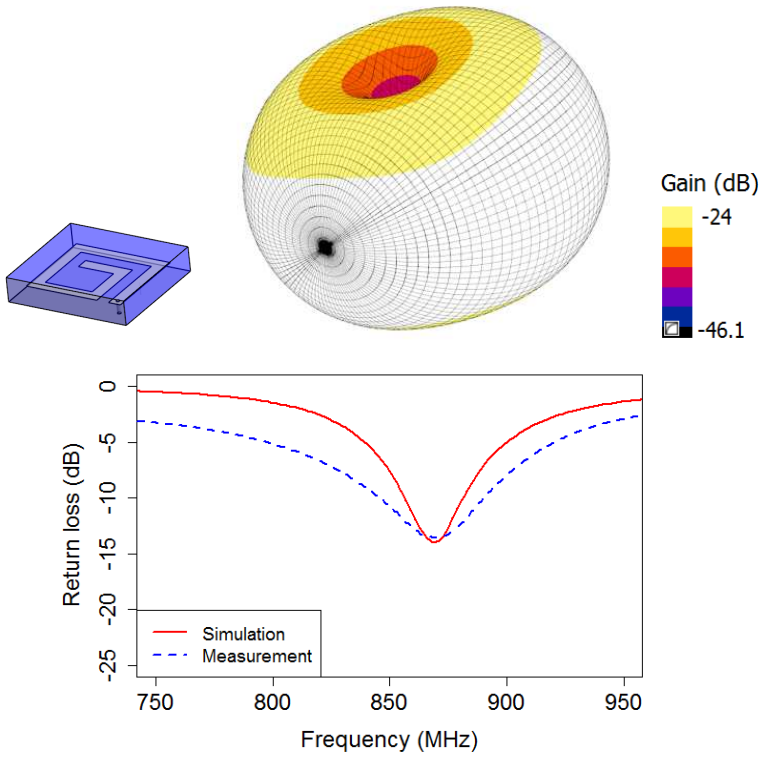

Figure 121. Perspective view, gain radiation pattern and reflection coefficient of the 2d866 antenna.

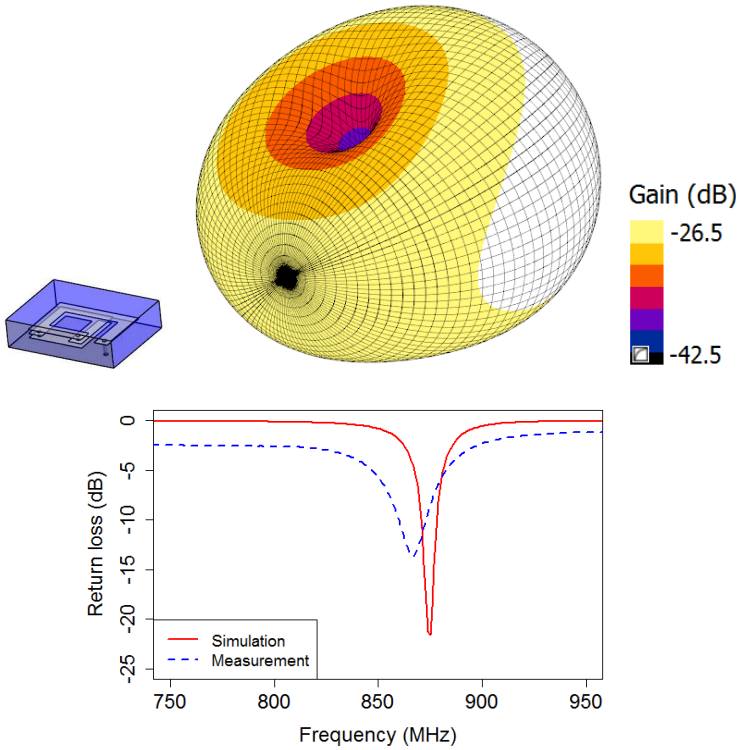

Figure 122. Perspective view, gain radiation pattern and reflection coefficient of the 3d866 antenna.

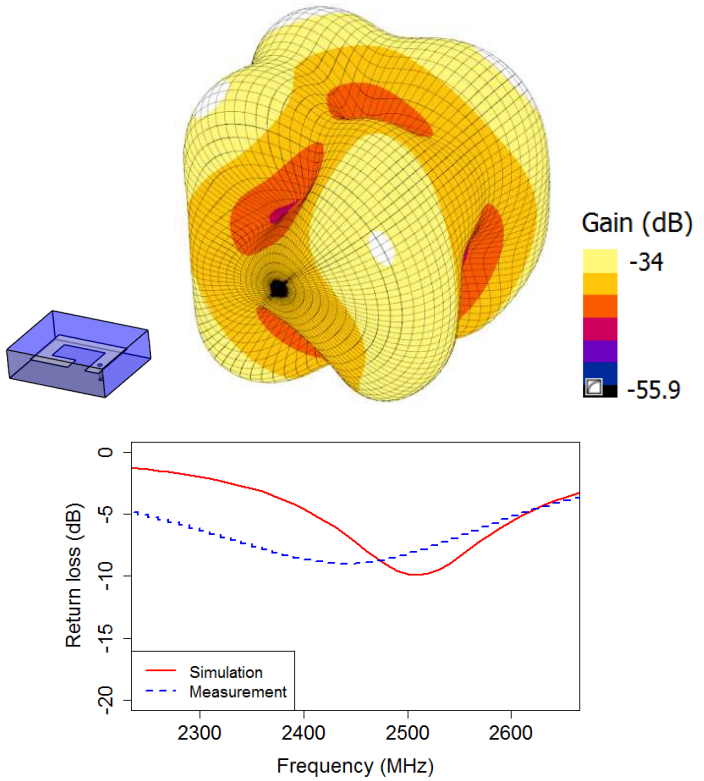

Figure 123. Perspective view, gain radiation pattern and reflection coefficient of the 2d2450 antenna.

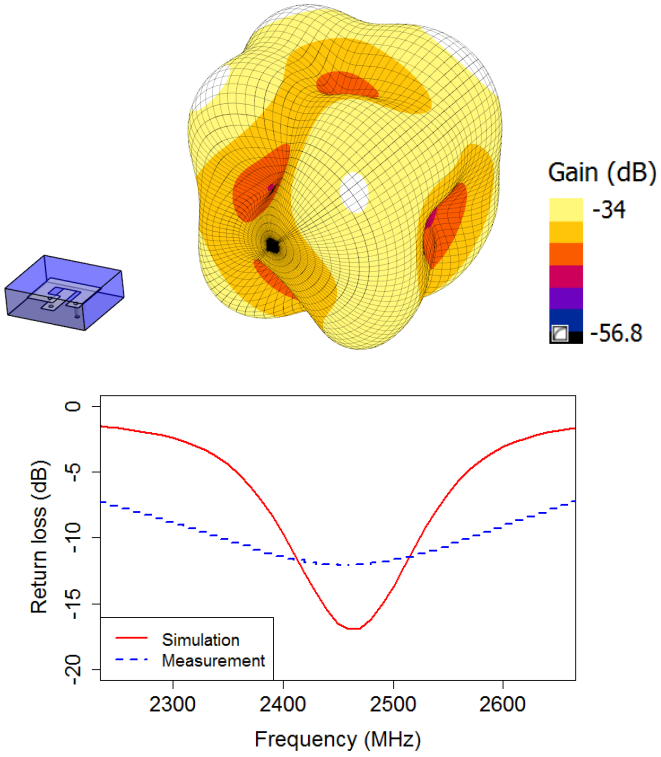

Figure 124. Perspective view, gain radiation pattern and reflection coefficient of the 3d2450 antenna.

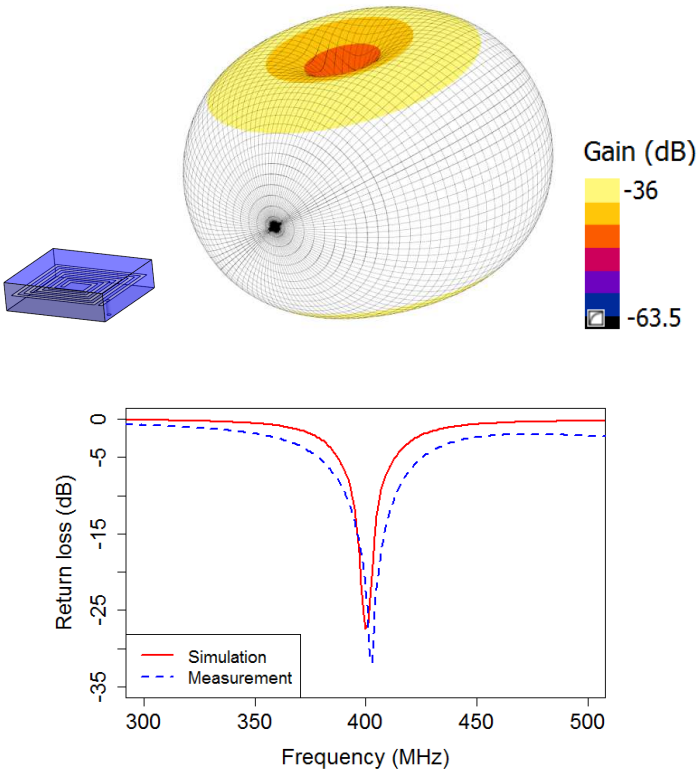

Figure 125. Perspective view, gain radiation pattern and reflection coefficient of the 2d403t antenna.

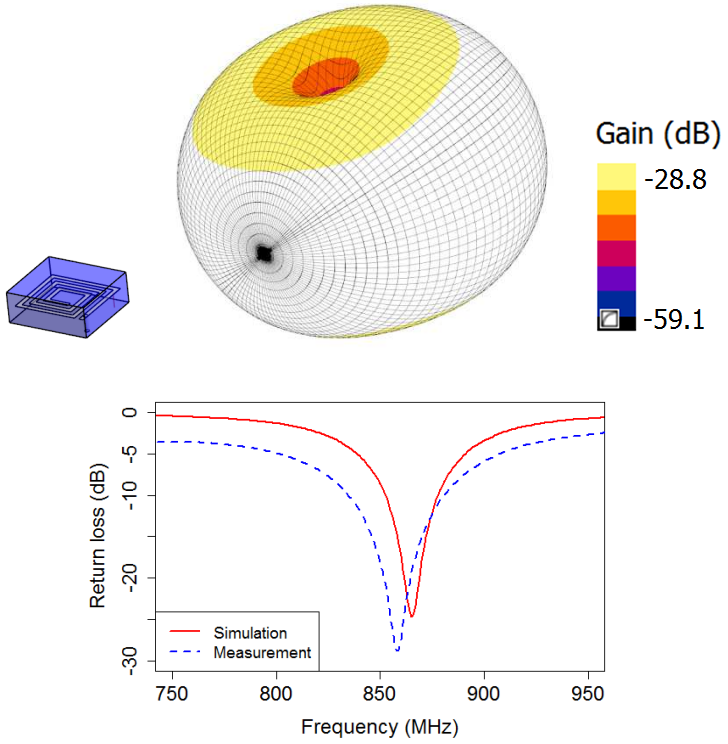

Figure 126. Perspective view, gain radiation pattern and reflection coefficient of the 2d866t antenna.

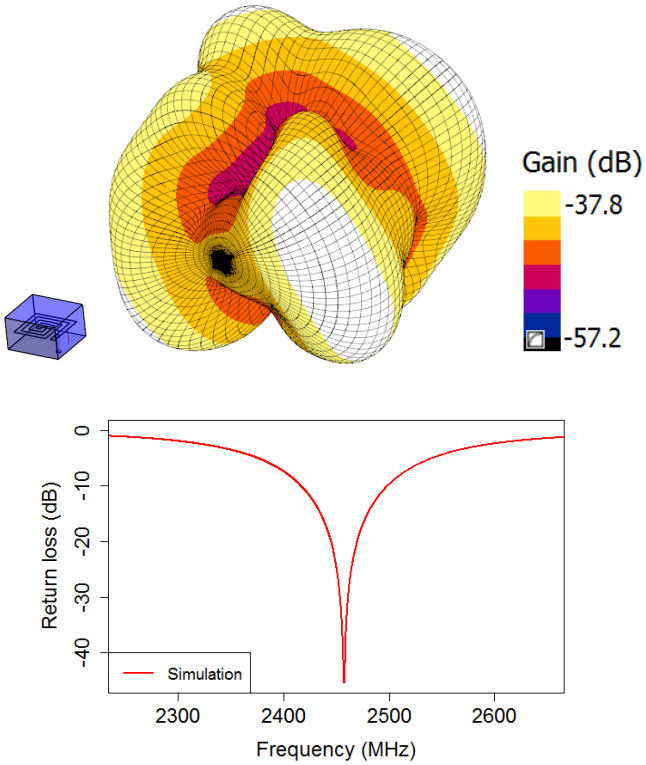

Figure 127. Perspective view, gain radiation pattern and reflection coefficient of the 2d2450t antenna.

Appendix B. Scientific C*urriculum Vitae* of the Author

Academic Degrees

- **MSc. in Biomedical Engineering**
  Universitat of Barcelona (UB), Universitat Politècnica de Catalunya (UPC). September 2013. Barcelona

- **Telecommunications Engineer**
  Universitat Politècnica de Catalunya (UPC). June 2009. Barcelona
  Erasmus at Delft University of Technology (TUDelft)

Outcomes and Contributions

Publications

- A. Garcia-Miquel, S. Curto, N. Vidal, J. M. Lopez-Villegas, F. M. Ramos, and P. Prakash, "Multilayered Broadband Antenna for Compact Embedded Implantable Medical Devices: Design and Characterization," Prog. Electromagn. Res., vol. 159, pp. 1–13, 2017.

- S. Curto, A. Garcia-Miquel, M. Suh, N. Vidal, J. M. Lopez-Villegas, and P. Prakash, "Design and characterization of a phased antenna array for intact breast hyperthermia," Int. J. Hyperthermia, pp. 1–11, Jun. 2017.

- A. Garcia-Miquel, B. Medina-Rodríguez, N. Vidal, F. M. Ramos, E. Roca, and J. M. Lopez-Villegas, "Design and characterization of a miniaturized implantable UHF RFID tag based on LTCC technology," in 11th European Conference on Antennas and Propagation (EUCAP), Paris, France, 2017.

- A. Garcia-Miquel, S. Curto, N. Vidal, J. M. Lopez-Villegas, and P. Prakash, "Compact Microwave Applicator for Thermal Therapy of Breast Cancer: Comparative Assessment of Arrays Operating at 434 and 915 MHz," in 10th European Conference on Antennas and Propagation (EUCAP), Davos, Switzerland, 2016.

- N. Vidal, A. Garcia-Miquel, A. Rios, J. M. Lopez-Villegas, E. Roca, "Personal Exposure to Radiofrequency Electromagnetic Fields: University of Barcelona Survey", in 10th European Conference on Antennas and Propagation (EUCAP), Davos, Switzerland, 2016.

- A. Garcia-Miquel, S. Curto, N. Vidal, J. M. Lopez-Villegas, and P. Prakash, “Antenna Array for Hyperthermia Treatment of Breast Cancer,” in XXXI Simposium Nacional de la Unión Científica Internacional de Radio (URSI), Madrid, Spain, 2016.

- A. Garcia-Miquel, S. Curto, N. Vidal Martínez, J.M. Lopez-Villegas, P. Prakash, "Evaluación Térmica de un Sistema Radiante de Microondas para el Tratamiento del Cáncer de Mama Mediante Hipertermia", in XXXIV Congreso Anual de la Sociedad Española de Ingeniería Biomédica (CASEIB), Valencia, Spain, 2016.

- M. Gómez, A. Garcia-Miquel, N. Vidal, "Development of a 3D-Printed Robotic Prosthetic Arm", in XXXIV Congreso Anual de la Sociedad Española de Ingeniería Biomédica (CASEIB), Valencia, Spain, 2016.

- A. Garcia-Miquel, N. Vidal, J.M. Lopez-Villegas, J.J. Sieiro, F.M. Ramos, "Miniaturization Effects on Implantable Antennas for Biomedical Applications,” in 9th European Conference on Antennas and Propagation (EUCAP), Lisbon, Portugal, 2015.

- N. Vidal, A. Garcia-Miquel, J.M. Lopez-Villegas, J.J. Sieiro, F.M. Ramos, "Influence of Phantom Models on Implantable Antenna Performance for Biomedical Applications,” in 9th European Conference on Antennas and Propagation (EUCAP), Lisbon, Portugal, 2015.

- A. Garcia-Miquel, N. Vidal, J.M. Lopez-Villegas, J.J. Sieiro, S. Curto, "Miniaturización de PIFAs Implantables Basadas en Tecnología LTCC", in *XXX Simposium Nacional de la Unión Científica Internacional de Radio (URSI)*, Pamplona, Spain, 2015.

- N. Vidal, J.M. Lopez-Villegas, S. Curto, J. Colomer, S. Ahyoune, A. Garcia, J.J. Sieiro, F.M. Ramos, "Design of an Implantable Broadband Antenna for Medical Telemetry Applications,” in *7th European Conference on Antennas and Propagation (EUCAP)*, Gothenburg, Sweden, 2013.

- A. Garcia-Miquel, “UWB Antenna Design for Underwater Communications”. Master Thesis, 2009.

Conferences

- 11th European Conference on Antennas and Propagation, EUCAP 2017

  Poster presentation: A. Garcia-Miquel, B. Medina-Rodríguez, N. Vidal, F. M. Ramos, E. Roca and J.M. Lopez-Villegas, “Design and characterization of a miniaturized implantable UHF RFID tag based on LTCC technology”

- 5th Jornada d'Investigadors Predoctorals Interdisciplinària, JIPI 2017

  Poster presentation: A. Garcia-Miquel, S. Curto, N. Vidal, J.M. Lopez-Villegas, P. Prakash, "Microwave Hyperthermia: Enhancing the Conventional Breast Cancer Treatments with Thermal Therapies"

- 1st International IEEE EMBS Summer School on Computer Modeling in Medicine. 2017

  Poster presentation: A. Garcia-Miquel, S. Curto, N. Vidal, J.M. Lopez-Villegas, P. Prakash, "Compact Antenna Array for the Thermal Treatment of Breast Cancer: Design, Characterization and Preliminary Ex-vivo Validation"

- 10th European Conference on Antennas and Propagation, EUCAP 2016

  Poster presentation: A. Garcia-Miquel, S. Curto, N. Vidal, J.M. Lopez-Villegas, P. Prakash, "Compact Microwave Applicator for Thermal Therapy of Breast Cancer: Comparative Assessment of Arrays operating at 434 and 915 MHz"

  Poster presentation: N. Vidal, A. Garcia-Miquel, A. Rios, J. M. Lopez-Villegas, E. Roca, "Personal Exposure to Radiofrequency Electromagnetic Fields: University of Barcelona Survey"

- 1st Biomed PhD Day Symposium 2016

  Oral presentation: "Experimental Thermal Validation of a Microwave Hyperthermia Applicator for the Breast Cancer Treatment"

- XXXIV Congreso Anual de la Sociedad Española de Ingeniería Biomédica, CASEIB 2016

  Poster presentation: A. Garcia-Miquel, S. Curto, N. Vidal Martínez, J.M. Lopez-Villegas, P. Prakash, "Evaluación Térmica de un Sistema Radiante de Microondas para el Tratamiento del Cáncer de Mama Mediante Hipertermia"

- XXXI Simposium Nacional de la Unión Científica Internacional de Radio, URSI 2016

  Oral presentation: "Antenna Array for Hyperthermia Treatment of Breast Cancer"

- 4th Jornada d'Investigadors Predoctorals Interdisciplinària, JIPI 2016

  Oral presentation: "Microwave Hyperthermia for Breast Cancer Treatment"

- International Congress of Hyperthermic Oncology, ICHO 2016

  Poster presentation: S. Curto, A. Garcia-Miquel, N. Vidal, J.M. Lopez-Villegas, P. Prakash, "A Phased Antenna Array for the Treatment of Cancer Malignancies in the Intact Breast"

- XXX Simposium Nacional de la Unión Científica Internacional de Radio, URSI 2015

  Poster presentation: A. Garcia-Miquel, N. Vidal, J. M. Lopez-Villegas, J.J. Sieiro, S. Curto, "Miniaturización de PIFAs Implantables Basadas en Tecnología LTCC"

- 9th European Conference on Antennas and Propagation, EUCAP 2015

  Poster presentation: A. Garcia-Miquel, N. Vidal, J.M. Lopez-Villegas, J.J. Sieiro, F.M. Ramos, "Miniaturization Effects on Implantable Antennas for Biomedical Applications"

  Poster presentation: N. Vidal, A. Garcia-Miquel, J.M. Lopez-Villegas, J.J. Sieiro, F.M. Ramos, "Influence of Phantom Models on Implantable Antenna Performance for Biomedical Applications"

- 7th European Conference on Antennas and Propagation, EuCAP 2013

  Poster presentation: N. Vidal, J.M. Lopez-Villegas, S. Curto, J. Colomer, S. Ahyoune, A. Garcia, J.J. Sieiro, F.M. Ramos, "Design of an Implantable Broadband Antenna for Medical Telemetry Applications"

Teaching Experience

- Assistant Professor in Electronic Engineering of Telecommunications degree, Biomedical Engineering Degree and Biomedical Engineering Master:
  - Bioelectricity and Bioelectromagnetics
  - Electronic Components
  - Clinical Engineering
  - Electronic Circuits Analysis
  - High-Frequency Electronics
  - Modeling of Biological Systems
  - ICT Support Systems
  - Wireless Body Area Networks
  - Biophotonics

- Project Manager in 7 Final Graduate/Master Projects:
  - Stents as Implantable Antennas
  - Implementation of an eHealth platform based on Arduino for WBAN applications
  - Design and Manufacturing of On-body Antennas
  - On-Body RFID Solution for Hospital Patient Tracking
  - Wearable Device for Continuous Non-Invasive Blood Pressure Monitoring
  - Development of a 3D-Printed Robotic Prosthetic Arm
  - Development of a web platform for an RFID-based RTLS system in a hospital environment

Training Courses

- *Summer School on Computer Modeling in Medicine.* IEEE Engineering in Medicine and Biology Society. Charleston, USA. September 2017.
- *Summer School on Compact Antennas.* European School of Antennas (ESoA). Barcelona, Spain. June 2016
- *Learning Teaching.* University of Barcelona. 2013

Project Collaborations

- Development of low-cost circulators for microwaves modules (LOCCIMIM). (TEC2010-21484)
- Development of passive RF components based on ferrite in LTCC technology for medium power applications (TEC2013-40430-R)
- Design and manufacture through 3D printing of passive components and circuits for RF applications (TEC2017-83524-R)
- Professional learning in the field of Engineering and Medicine (2016PID-UB/005)
- Design, manufacturing and characterization of a compact RFID system in LTCC technology. (Code: 308811)

Honors and Awards

- *PhD Fellowship:* APIF (Grants for Predoctoral Research Personnel in Training). University of Barcelona (2016-2018)
- *Student Research grant*: University of Barcelona. IEEE EMBS International Summer School on Computer Modeling in Medicine (Charleston, USA, 2017)
- *Award*: Best technological conference "MICROWAVE HYPERTHERMIA FOR BREAST CANCER" at the 4th Jorrnada d'Investigadors Predoctorals Interdisciplinària (JIPI 2016)
- *Student Research award*: CST Microwave Studio. EsoA Summer school on Compact Antennas (Barcelona, 2016)
- *Student Research grant*: University of Barcelona. XXX Simposium Nacional de la Unión Científica Internacional de Radio (URSI 2015)
- *Student Research grant*: University of Barcelona. 9th European Conference on Antennas and Propagation (EUCAP 2015)

Memberships

- Student Member of the Spanish Society of Biomedical Engineering (SEIB). 2016.
- Organizing Committee Member of the 1st Biomed PhD Day Symposium. 2016.
- Organizing Committee Member of the 5th Jorndada d'Investigadors Predoctorals Interdisciplinàira JIPI. 2017.